FERMILAB-PROPOSAL-0823

10/18/9

D0 D0 D0

D0 D0 D0 D0 D0 D0

UPGRADE

D0 D0 D0 D0 D0 D0

D0 D0 D0

D0

D0 D0 D0 D0 D0 D0

Table of Contents

THE D0 COLLABORATION

J. Chen, G. Forden, E. Jenkins, K. Johns, M. Li, A. Milder,
J. Rutherfoord, M. Shupe and J. Zeng
University of Arizona

S. Aronson, M. Fatyga, B. Gibbard, H. Gordon, J. M. Guida, W. Guryn, S. Kahn,
S. Protopopescu, and P. Yamin
Brookhaven National Laboratory

D. Cullen-Vidal, D. Cutts, J. Hoftun, R. Lanou, F. Nang, D. Nesic,
R. Partridge, H. Xu and R. Zeller
Brown University

K. Bazizi, J. Ellison, D. Franks, R. Hall, T. Huehn, D. Joyce,
A. Kernan, A. Klatchko, S.J. Wimpenny, and M.-J. Yang
University of California, Riverside

P. Franzini and P.M. Tuts
Columbia University

S. Abachi, S. Ahn, N. Amos, J.F. Bartlett, P. Bhat, D. Bogert, F. Borcherding,
A. Bross, J. M. Butler, J. Christenson, W.E. Cooper, T. Diehl, R. Dixon,
G. Dugan, D. Eartly, D. Finley, H.E. Fisk, S. Fuess, C.S. Gao, N. Graf,
D. Green, H. Greenlee, H. Haggerty, S. Igarashi, A.S. Ito, M. Johnson,
A. Jonckheere, H. Jostlein, B. Klima, S. Krzywdzinski, R. Li, R. Lipton,
P. Lucas, H.S. Mao, P. Martin, X.C. Meng, W. Merritt, H. Montgomery,
C.T. Murphy, N. Oshima, C.H. Park, H. Prosper, R. Raja, A.L. Read,
W. Smart, R.P. Smith, C. Stewart, A. Taketani, M. Tartaglia,
R. Yamada, and Y.H. Zhou
Fermi National Accelerator Laboratory

W. Dharmaratna, S. Hagopian, V. Hagopian, S. Linn, H. Piekarz, H. Wahl,
S. Youssef, and J. Womersley
Florida State University

J. Walker, A. White, Z. Wolf
University of Florida

R. Cence, M. Peters, C. Yoshikawa
University of Hawaii

J. Li, T. Marshall, J. Martin, D. Zieminska and A. Zieminski
Indiana University

H. Aihara, A. Clark, O. Dahl, P. Grudberg, L. Kerth, S. Loken, R. Madaras, E. Oltman, N. Roe, A. Spadafora, M.L. Stevenson, M. Strovink, T. Trippe, and W. Wenzel
Lawrence Berkeley Laboratory

A. Baden, N. Hadley, S. Kunori, D. Norman, T.M.L. Ren and K. Streets
University of Maryland

R. Ball, K. De, T. Geld, R. Gustafson, M. Marcin, H. Neal and G. Snow
University of Michigan

M. Abolins, R. Astur, R. Brock, D. Edmunds, J. Linnemann, P. Mooney, D. Owen, B. Pi, B. Pope, S. Tisserant, H. Weerts, and X. Yi
Michigan State University

J. Kourlas, J. Kotcher, A. Mincer, M. Mudan, P. Nemethy, J. Sculli, J. Yang, and Q. Zhu
New York University

M. Fortner, J. Green, D. Hedin, R. Morphis, S. Repond and S. Willis
Northern Illinois University

R. Avery, J. Bantley, S. Blessing, D. Buchholz, B. Gobbi, S. Rajagopalan, and H. Schellman
Northwestern University

B. Baumbaugh, N. Biswas, J. Piekarz, P. Kenney, R. Ruchti
University of Notre Dame

D. Koltick, R. McIlwain
Purdue University

G. Blazey, J. Borders, P. Draper, S. Durston, G. Fanourakis, T.Ferbel,
R. Hirosky, F. Lobkowicz, and P. Slattery
University of Rochester

Y. Ducros, J. Glicenstein, R. Hubbard, P. Mangeot, B. Mansoulie,
J. Teiger, and A. Zylberstejn
CEN Saclay, France

Y. Antipov, B. Baldin, S. Chekulaev, S. Cherny, D. Denisov, S. Denisov,
A. Efimov, O. Eroshin, V. Glebov, E. Kistenev, V. Klyukhin,
V. Kochetkov, E. Kozlovsky, N. Mokhov, Y. Pischalnikov,
V. Riadovikov, V. Sirotenko, and A. Vorobiev
Institute for High Energy Physics, Protvino, USSR

J. Cochran, M. Demarteau, R. Engelmann, S. Feher, G. Finocchiaro, M.L. Good,
P. Grannis, J. A. Guida, T. Heuring, W. Karsh, C. Klopfenstein,
J. Lee-Franzini, Q.Z. Li-Demarteau, S. Lokos, M. Marx, R. McCarthy,
K. Ng, M. Paterno, D. Pizzuto, L. Rasmussen, M. Rijssenbeek,
P. Rubinov, R.D. Schamberger, F. Stocker,
J. Thompson, and J. Yu
State University of New York - Stony Brook

B. Acharya, M. Krishnaswamy, N. Mondal, V. Narasimham, P. Ramanamurthy,
M. Rao, and P. Vishwanath
Tata Institute of Fundamental Research, Bombay India

R. Huson, J.T. White, J. Wightman
Texas A&M University

M. Zeller
Yale University

1. Introduction

1.1 Context of the DØ Upgrade

The original proposal for the DØ detector was made in 1983 and put forward a coherent view that emphasis on the detection of the fundamental entities – e's, μ's, quarks and gluons materialized as jets, and ν's inferred from missing E_T – would optimize the study of physics at the smallest distances and largest masses. We believe that this concept has stood up well. Most of the specific studies identified in 1983 are still topical (measure m_W/m_Z, find the top, seek supersymmetry, etc).

The DØ collaboration is now engaged in the final preparations for its first run in the Collider. In addition to gathering data on a variety of large mass and high p_T phenomena, we will learn for the first time what special surprises life in the Tevatron Collider has in store for us. It may seem odd therefore to bring forward a proposal for upgrading the detector at this moment. It is obvious that what we learn in the first DØ run, both in physics and concerning the detector, must be folded into the final upgrade plan. However, external events argue for a DØ upgrade proposal now. Fermilab is in the process of upgrading the Tevatron complex. The CDF collaboration is examining needed improvements to their detector and pointing the way to new physics opportunities. The U.S. High Energy Physics community has been engaged in considerable self-examination to guide the choice of opportunities for the 1990's. In the context of these developments, it seems natural and even necessary that the planning for DØ evolution be made specific. The DØ program is a central feature of the U.S. High Energy Physics program for the next decade.

Some features of the DØ upgrade proposal are driven by the change in conditions at the evolving Tevatron and are extended by the parameters after the addition of the Main Injector. As the luminosity rises far above the $10^{30} cm^{-2} s^{-1}$ for which the detector was originally designed, some changes will become necessary to handle the increased average particle rate and radiation dose. The shortened interval between crossings, expected in the second DØ run, will have an impact upon the trigger design since there is less time for early decision making without dead-time penalty. The present bunch interval, ΔT_b, is $3.5\mu s$ but by 1995 it is expected to decrease to 400 ns.

Added impetus for the DØ upgrade comes from new physics opportunities. We are confident that the search for the top and study of its properties will crucially depend on the increase in luminosity. We may however expect some change of emphasis in the later years of Collider operation; in an era of mere doubling of event samples, some of the searches for new states will give rather marginal improvement. Many new opportunities will presumably come for studies at less than the maximum p_T. The beautiful studies of the past few years on the production and decay of b-quark states at ARGUS[1] , UA1[2] , CLEO[3] , CUSB[4] , and CDF[5] have led us to believe that the study of production, decay and time-evolution of states containing b-quarks would be a profitable new area of physics which DØ could attack.

This upgrade proposal therefore takes as its the guiding principle that the DØ detector should retain its excellent power for studying large p_T processes involving jets, e's and μ's with uniform detection over the full solid angle. In addition, we will seek to add the capability needed to study the production of b-quarks and the decays of B hadrons into as large a set of interesting final states as is possible. In particular, we would aim to make significant progress toward finding CP violation in B_d (B_s) decays.

1.2 The Present DØ Detector

The main features of the present DØ detector are summarized in this section, with some indication of the problems which might arise as the luminosity increases or the bunch-crossing interval decreases.

The DØ detector as it is being built for the 1991 run is shown in Fig. 1.1. It consists of the three nested shells of tracking/TRD detectors, calorimeters, and muon detectors. Level 0 trigger scintillators mounted on the end calorimeters signal the presence of an inelastic beam-beam collision. The detector rests upon a moveable platform which allows translation of the detector between the assembly hall and the collision region. The shaping electronics resides on the detectors or under the platform. A Moving Counting House (MCH) follows the detector, but remains outside the radiation enclosure. All digitizing and fast trigger electronics are in the MCH. Digital signals from all detectors and the hardware level 1 trigger are transported to the second floor of the fixed counting area, where event building and μprocessor event filtering (level 2 trigger) is performed.

1.2.1 Tracking Detectors

Figure 1.2 shows the layout of the existing DØ tracking and transition radiation detectors. Vertex Drift Chamber (VDC), Transition Radiation Detector (TRD) and Central Drift Chambers (CDC) give track coordinates and electron identification in the large angle region. The VDC and CDC are 'jet' chambers with 8 or 7 wires, coaxial with the beams, in each of 3 or 4 cells. The TRD contains three sections of polypropylene foils followed by a Xenon-filled radial drift cell for X-ray detection. The small-angle regions are covered by the Forward Drift Chambers (FDC) which contain three multiwire sections measuring respectively θ, ϕ, and θ coordinates.

Since the DØ design has assumed a $3.5\mu s$ minimum time between interactions, these chambers have been built with relatively long drift cells (up to $\sim 2\mu s$) to minimize the channel count. Thus bunch crossing times of less than $3.5\mu s$ will result in event pileup in the present chambers. In addition, the low wire density means that the accumulated charge on the wires is large; the inner sense wires of VDC and FDC approach 1 C/cm for a one year run at $\mathcal{L}= 10^{31} cm^{-2} s^{-1}$. These values are likely to cause degradation of the chambers.

Consideration of both event pileup and radiation damage imply that the DØ tracking chambers will need to be replaced as the luminosity grows. We have long estimated that this transition should occur when the average luminosity exceeds $\mathcal{L}= 10^{31} cm^{-2} s^{-1}$. With the presently expected luminosity growth at the Tevatron, it would seem that this threshold will be exceeded by the 1995 run, with or without the Main Injector Upgrade. Since new tracking chambers will be needed in any case, we take the opportunity to re-examine the optimization of the physics issues in the latter portion of the 1990's. The understanding that the study of B-physics will be an important added ingredient to our program leads us to design the new tracking with these goals in mind.

1.2.2 Calorimeters

The layout of the DØ calorimeters is shown in Fig. 1.3. Three large liquid argon devices, each within their own cryostat, span the rapidity range $|\eta| < 4$ with a single, radiation-hard technology. The Central Calorimeter (CC) contains rings of electromagnetic ($3mm$ U), fine sampling ($6mm$ U) hadronic and coarse sampling hadronic ($47mm$ Cu) modules axisymmetric with the beams. The End Calorimeters (EC) have electromagnetic and hadronic fine and coarse modules which come to within $2°$ of the beams as well as an intermediate ring of hadronic modules and an outer ring of coarse modules at successively larger radii. The transverse segmentation is $\Delta\eta = \Delta\phi = 0.1$, except at the smallest angles. Typically there are 4 independent readout layers of the electromagnetic calorimeter; 4 layers of the fine-sampling hadronic calorimeter and 1 layer of the coarse hadronic calorimeters. A system of massless gaps on the ends of CC modules and fronts of EC modules, together with a scintillator/ wavelength-shifting fiber Intercryostat Detector, monitor the energy flow through the structural material at the CC/EC interface.

Liquid argon calorimetry is expected to be extremely radiation hard, so no change is necessary at the upgraded Tevatron. Even the internal cabling and signal boards will withstand far more dose than will be delivered. No change to the mechanical aspects of the calorimeters is envisioned.

The argon gaps in DØ are $2.3mm$, corresponding to a drift time across the full cell of $\sim 450ns$ (3/4 of the collected charge is available in $200ns$). The rise-time of the charge-sensitive preamplifiers mounted just outside the cryostats is of order $1\mu s$. Each readout segment of the calorimeter is sampled just before the beam crossing time and again $2.2\mu s$ later to give a measure of the charge deposited during that crossing. Rise times and sampling times were chosen to optimize the two dominant sources of noise at $\mathcal{L}= 10^{30} cm^{-2} s^{-1}$: electronics noise, predominantly from the preamplifiers, and the noise from random charge deposited in the cells due to uranium radioactive decays. For the high $\mathcal{L}$ upgrade conditions, an added component of noise enters due to the pileup of charge from events overlapped within the time resolution of the calorimeter readout system. We need to re-optimize the various time constants in the system to bring the contributions to the total noise back into balance for the high $\mathcal{L}$ situation.

1.2.3 Muon Detection

The elements of the DØ muon detection system are shown in Fig. 1.4. In each of 5 angular regions, iron toroidal magnets give fields of $\sim$ 1.9T. The muon tracks are recorded in sets of chambers before and after the toroids; at angles larger than $\sim 10°$ there are typically 4 cells just before the toroids and 2 sets of 3 cells separated by about $1m$ after the magnets. These large angle detector cells ($5cm$ half-cell width) have a drift time of just over 1 μsec with the Ar/CO_2 gas to be used initially. The large angle chambers measure the coordinate parallel to the wire by determining the pulse area of the induced pulse in a pair of cathodes shaped in a 'diamond' pattern, such that the ratio of pulses from the two cathode segments gives a measure (to within a few mm) of the distance along the wire.

The μ's in the small angle region ($< 10°$) are recorded before and after the toroid in x-y-u triplets of $30mm$ diameter drift tube planes. Each x,y, or u measurement consists of two overlapped planes of tubes. The drift time in these tubes is about $200ns$.

For the initial run of DØ, there will be a scintillator cover over the top of the detector only. The function of this scintillator is to give a more accurate time than is available from the chamber hardware for tracks in the vertical direction; in particular, the scintillator offers the basis for rejecting cosmic ray triggers at an early stage.

Although high $\mathcal{L}$ running with small ΔT_b will open the possibility that overlaps could occur in the large angle chambers for events from adjacent bunch crossings, the mean occupancy in the large angle muon chambers is expected to be small enough that the chambers can be kept in the upgraded detector. The occupancies in the small angle chambers will however be large enough that some upgrade will be necessary, particularly at the trigger level. In addition, the smaller ΔT_b gives an increase in the fraction of time that the detector is live; this suggests that some improvement in the rejection of cosmic rays will be necessary in the upgrade.

1.3 Summary of Main Elements of the DØ Upgrade

The various upgrades to the DØ Detector are discussed in some detail in the later chapters of this proposal. Some of these will be made for the second DØ run in 1993. Others of them are associated with the addition of a central magnetic field; we anticipate that these changes will be made for the third DØ collider run, presently scheduled to begin in Winter '94-'95. We give here a capsule summary of the various proposed upgrades, and indicate the DØ run (II or III) for which they are to be completed.

We expect that for the 1993 run, the DØ tracking and TRD detectors will withstand the radiation from beam-beam collisions. However, the decrease planned for the bunch interval, ΔT_b (to $800ns$ or $400ns$), means that faster collection of the charge is necessary. Even with faster drift, there will be some overlap of information from events in adjacent crossings due to the time required to collect the delay-lines bearing the z-coordinates.

- **We propose to change to a faster drift gas for the tracking and TRD chambers for the 1993 run.** [Run II]

DØ will need to replace its tracking detectors, probably by the 1995 run regardless of the Main Injector timetable. Since we recognize that in the second half of the decade further extensions of large mass searches will be minimal, and that new studies of B-particle production and decay will be of increased interest, it is natural to optimize the new tracking detectors to capitalize on B-physics. We take as a ground rule that the current DØ strengths for high p_T phenomena should not be compromised.

One of the most exciting (and difficult) aspects of the study of b-quarks is the potential for finding CP violation in the $B^0 - \overline{B}^0$states. Many authors have emphasized the importance of such a search in decays of the neutral B's into CP-eigenstates. Prominent among these is the final state $\psi\ K_S$ which may be taken as a bellwether for such studies. The ability to isolate this final state, as distinct, for example, from the state $\psi\ K^{*0}$, *requires* that magnetic measurement of the μ's (from ψ) and π's (from K_S) be made to adequate precision. The only magnetic field consistent with the existing DØ calorimeter geometries confining the tracking volume is a solenoid.

• **We propose to add a 1.5T superconducting solenoid magnet within the 75 cm inner bore of the DØ Central Calorimeter. [Run III]**

The study of B^0 decays, $B^0 - \overline{B}^0$ mixing, CP violation etc, as well as some of the topics from the large p_T list, are aided by measurements of the decay vertex location of long-lived particles (B's, D's, τ's). In addition, DØ requires efficient tracking in the forward direction since our muon detection (a central part of our B-physics capability) is most efficient at small angles. Such small angle tracking is difficult to provide with detectors whose elements are parallel to the beams.

• **We propose a set of silicon tracking devices with both a large-angle barrel section and sets of disks perpendicular to the beams at small angles. [Run III with possible tests in Run II]**

DØ needs to develop a new tracking system with finer segmentation than the present system simply to handle the increased radiation dose. The new tracking system requires especially good resolution in the $r - \phi$ coordinate to make use of the magnetic bending; however, the z coordinate is of interest as well, both for the measurement of production and decay vertex locations and for matching to the η-ϕ cells in the calorimeters. The need for much finer cells than the several *cm* in the present tracking means that the constraints due to mechanical support, signal pre-amplifiers, gas and high voltage service distributions, and cooling will tend to disfavor wire chambers or straw tubes with large numbers of wires. An alternative which removes several of these drawbacks is based upon a scintillating fiber tracking detector; this approach brings its own uncertainties concerning readout devices.

• **We propose as our primary option, a scintillating fiber tracking system with ribbons of axial and large-angle stereo fibers in the radial space between 20 and 55 cm. Clear fibers would transport the light to transducers outside of the tracking volume. [Run III]**

Electron identification is currently provided in DØ through a combination of fine longitudinal and transverse segmentation of the liquid argon calorimetry and the Transition Radiation Detector in the tracking volume. In the upgrade, the proposed magnetic field can provide a portion of the tools needed for e identification; however, measurement of E/p is not expected to be sufficient to control backgrounds for e's from $\gamma - \pi^{\pm}$ overlaps or from generalized charge-exchanges in the calorimeters. Without the TRD in the upgrade, added protection against these backgrounds is necessary.

• **We propose a preshower detector following the solenoid coil and before the calorimeter. We expect this detector to be similar in technology to the main outer tracking system. [Run III]**

The increase in luminosity at the improved Tevatron will mean that added quasi-random energy will be added to the calorimeter cells due to events close in time to any event of interest. This can be treated approximately as another noise contribution (added to electronic and uranium noise) and a re-optimization of the several noise components can be made. This results in a shorter time between *'before'* and *'after'* sampling and lower noise preamps to compensate the increased bandwidth. We also would modify the shaping circuitry to improve the baseline restoration properties. We strongly prefer to keep the overall calorimeter electronics framework unchanged. Modification of crates, backplanes, power distribution, etc. would cause far more perturbation than replacement of the active circuits.

• **We propose to replace the 50,000 preamplifier and base line subtractor hybrids but to retain the motherboards, crates, and backplanes for these electronics. We are pursuing a scheme in which modification, but not replacement, of both preamp and BLS power supplies will be made. [Run III]**

The decreasing time between bunch crossings means that there is insufficient time for a deadtime-less trigger decision (between crossings) to be made. We will need to save the analog calorimeter information for approximately 2 μsec while a first level trigger decision can be made.

• **We propose to add lumped delay lines to the input stage of the base-line-subtractor hybrids. [Run III]**

The addition of a solenoid magnet will increase the ambient field at the location of the Intercryostat detectors to several hundred gauss.

• **We propose to add new PM tube shielding or replace the present fiber readout system with a new one which transports the light to the phototubes outside the muon magnets. [Run III]**

Since the drift cells for the muon system have larger drift times than the bunch crossing interval, we need to tag each event of interest with a time-stamp registered to the crossing number.

• **We propose to increase the scintillator cover, now employed over the top of DØ, to all six sides of the detector. [Run II]**

Increased speed for signal collection in the large angle μ PDT's is desirable for trigger formation.

• **We propose to use a faster gas (Ar CO_2 CF_4) and to add necessary gas-handling facilities. [Run III]**

The small angle region of muon detection and triggering will be under severe pressure from the increased rate of particle production. Some learning from experience will be necessary to finalize plans for upgrade. We presently envision the need for trigger improvements using small cell scintillator or propotional chamber tiles.

• **We propose a 2-dimensional overlay of chambers to give a better approximation of space-point elements for triggering on small angle μ's. [Run II]**

Increased rates in the small-angle muon system necessitates adding double-hit capability to the drift-time measurements, increased spatial resolution at the trigger level, and increased speed in the digitizing system.

• **We propose upgrade extensions to the shapers, trigger latches and ADC's for the small angle muon system. [Run II]**

The lowest level of DØ triggers is given by scintillators mounted on the front face of the End Calorimeters. In the presence of the magnetic field, the phototubes for these counters will not work.

• **We propose to replace the Level 0 readout with either fiber extensions to remote phototubes or photodiodes. [Run III]**

Increase in the raw collision rate by a factor of nearly 2 orders of magnitude, and the introduction of new physics objectives, dictate significant extensions in the trigger capability of DØ. We anticipate improvements in all levels of the existing trigger systems, based upon the hooks designed into these systems originally. The present classification of hardware triggers is based on the distinction of those which operate without deadtime (i.e. within the present 3.5 μsec crossing time) and those which proceed with some, presumably small, deadtime. This distinction will be further blurred with the upgraded accelerator due to the decrease in crossing interval and the need to introduce more sophisticated triggering algorithms operating at the hardware level. We have noted the plan to make analog storage of calorimeter and muon signals at the front ends to allow time for the simpler portions of the trigger to occur. Additions to to the existing hardware trigger will enable decisions based upon calorimeter cluster information, on the energy isolation for electrons, on improved determination of the z-coordinate of the primary vertex, and on more precise EM/Hadronic energy ratios. We will improve the granularity and timing for the muon triggers to improve the rejection of backgrounds at the hardware level. New sections of the trigger framework are proposed which will allow requiring pre-determined topological correlations of μ 's, e's, or jets – for example requiring certain mass intervals of $e - \mu$ combinations or of multi-jet systems. In addition, we will increase the bandwidth for event transfer to the subsequent Level 2 μprocessor farm.

• **We propose a collection of extensions to the existing hardware triggers to allow more complete characterization of events. [Run II and III]**

There will be increasing pressure on the Level 2 μprocessors to cope with higher input event rate and increasing event complexity. We expect that the input bandwidth for the Level 2 system will increase twofold to 1 KHz. We expect the output bandwidth to increase to about 10 Hz. The detailed Level 2 upgrades must be evaluated after experience with DØ running in each successive collider cycle and as improvements in computing hardware become available. We need to increase the input bandwidth to Level 2 by upgrading the data cable bandwidth by increasing the number of data cables. We propose to enhance the power of the Level 2 farm by combinations of increasing the number of nodes, upgrading the CPU's in the farms, and/or adding co-processors to the existing multiport memory busses.

- **We propose enhancement of the power of the Level 2 trigger through expansion and improved processors. [Run II and III]**

1.4 Conclusion

The remainder of this document covers the proposed upgrades to the DØ Detector and their physics motivation in more detail. Chapter 2 reviews the physics themes which we expect to form the basis for the DØ program in the later part of the 1990's. Chapter 3 discusses the major proposed upgrades for tracking. Chapters 4 and 5 present the modifications proposed for the calorimeter and muon detection respectively. The additions to the various levels of triggering necessitated by the larger $\mathcal{L}$ are described in Chapter 6.

We point out that, although much work has been already been done in seeking the appropriate optimizations of the upgrade detectors, this work will continue through the coming year. Several components of the upgrade proposal rest upon an R&D program which is now beginning. Finally, we recognize that some aspects of the DØ upgrade will depend strongly on the experience gained in the first Collider run with DØ. All of these factors lead us to realize that this proposal will of necessity continue to evolve with time.

We expect that the Physics Advisory Committee and the Laboratory will wish to pose its own questions to be added to the list that the DØ collaboration has regarding details of the upgrade. We do however hope that there will be a dialogue in the next few months that will enable the DØ collaboration to gauge the suitability in scope and in direction for what is proposed herein.

Chapter 1 References

1. ARGUS results on B properties. e.g. H. Albrecht *et al.* Phys. Lett. B, 245 (1987) for mixing.
2. C. Albajar *et al.* Phys. Lett.**B213**, 405 (1988).
3. "B Meson Decays", B. Gittelman and S. Stone, Cornell Preprint, CLNS 87/81 and B. Gittelman, "Spectroscopy and Decay of Heavy Flavors", talk at XXV ICHEP Conference, Singapore 1990.
4. P.M. Tuts, "Upsilon Spectroscopy: A Review of Recent Results", Proceedings of the 1989 International Symposium on Heavy Quark Physics, AIP Conference Proceedings 196, ed. by P.S. Drell and D.L. Rubin, (AIP, New York, 1989) p.299.
5. L. Pondrom, talk at XXV ICHEP Conference, Singapore 1990; A.R. Baden, "Heavy Flavor Physics with CDF", talk at the 1990 SLAC Summer Institute on Particle Physics, SLAC 1990.

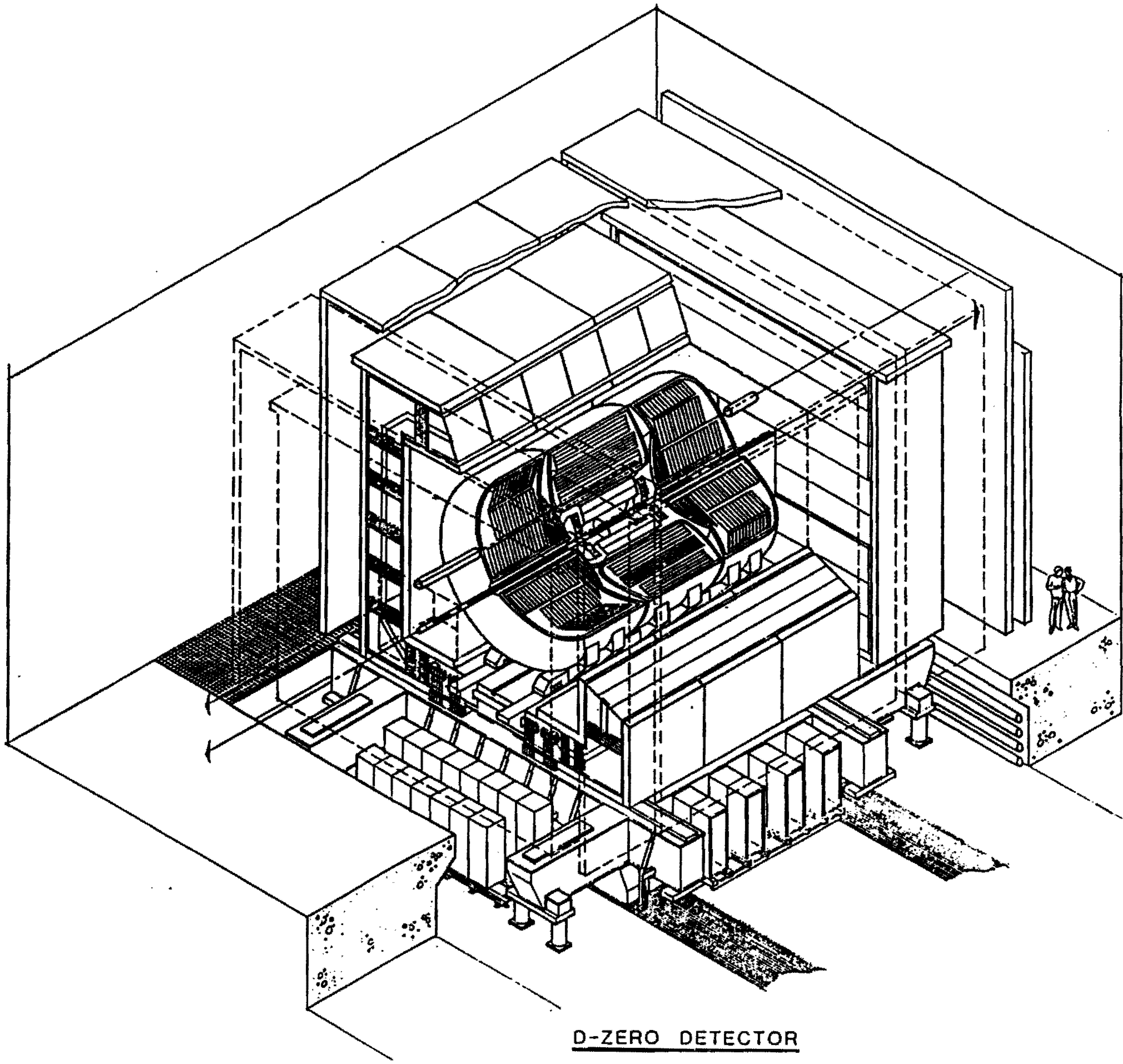

Figure 1.1 The present DØ Detector – Isometric view.

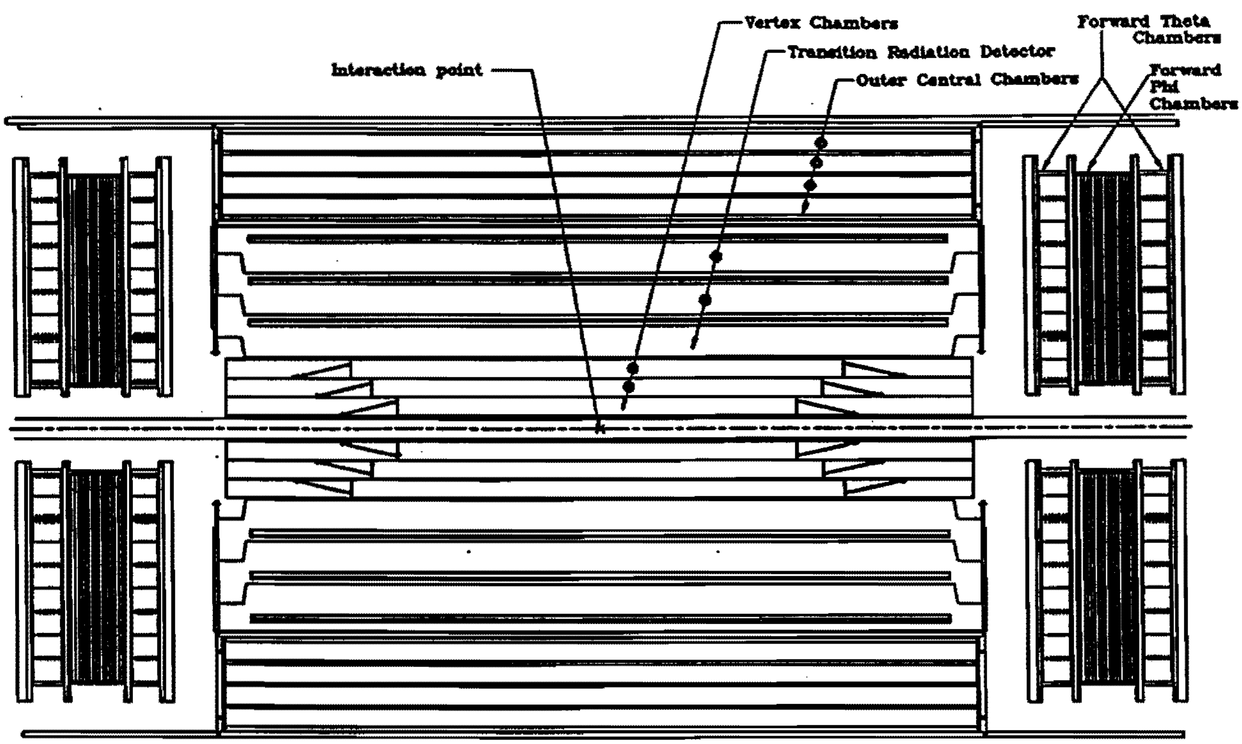

Figure 1.2 Layout of the Tracking/TRD detectors for the present DØ Detector.

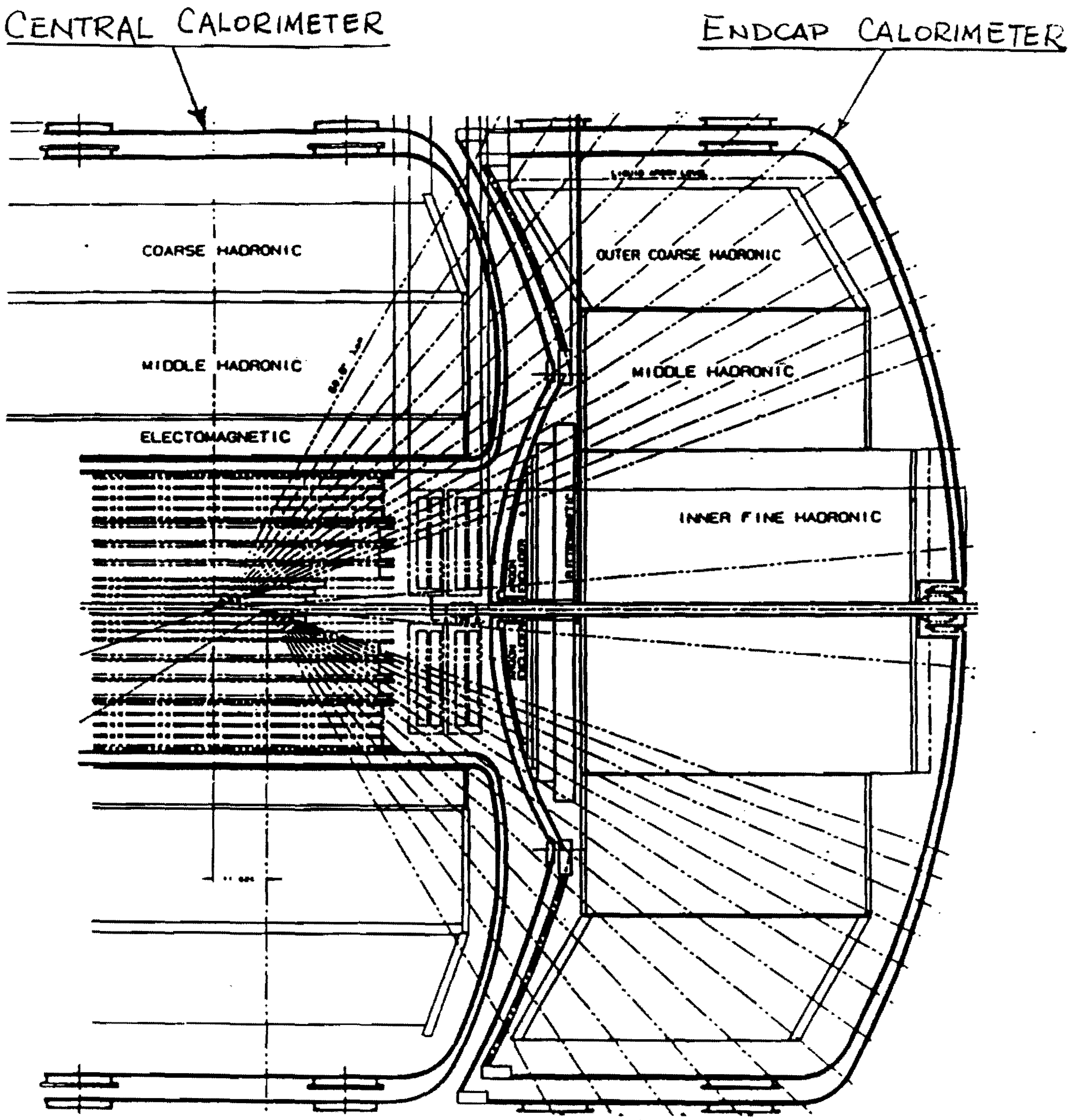

Figure 1.3 Layout of the Calorimeters. Only one hemisphere of the calorimeter system is shown.

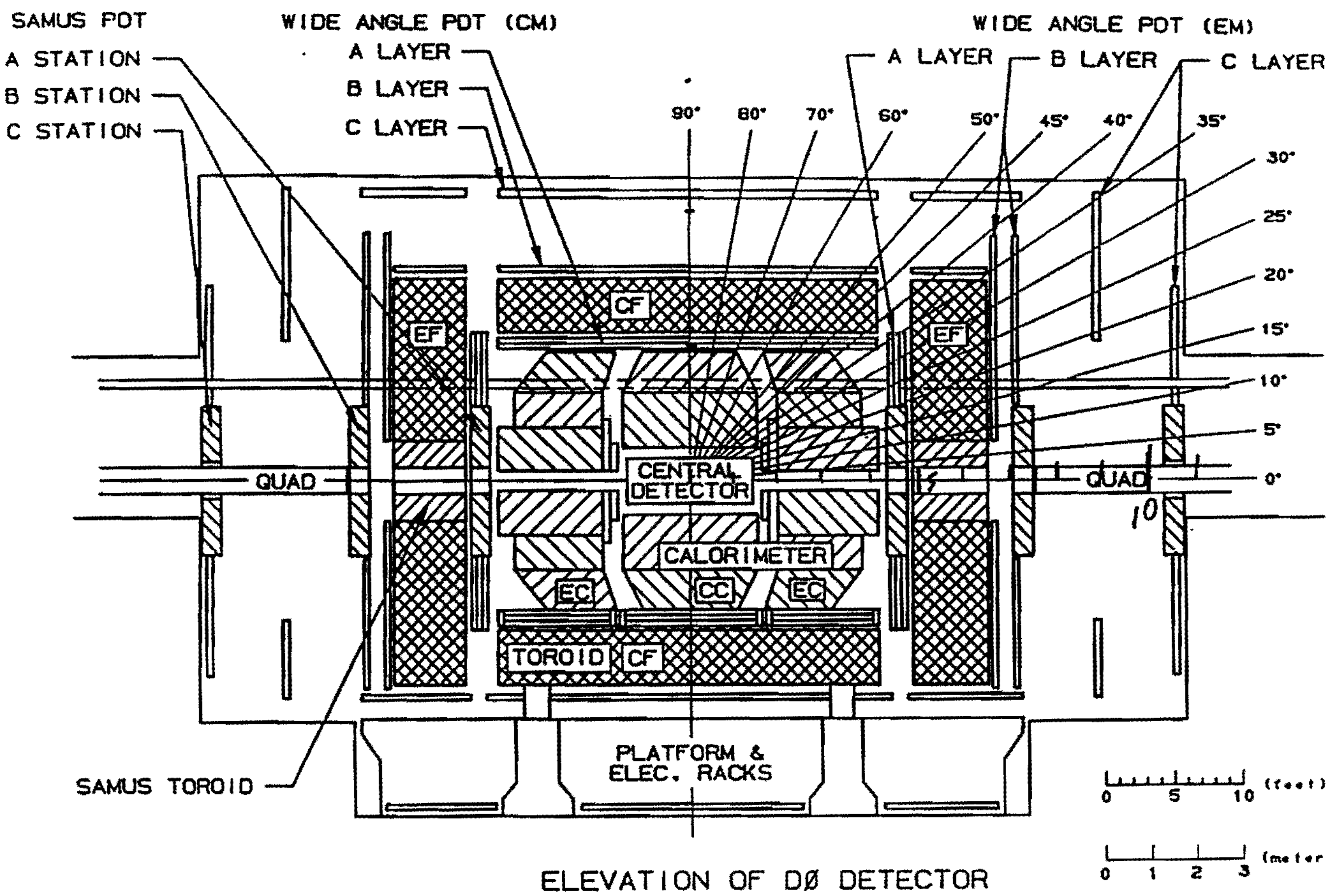

Figure 1.4 Muon detectors layout.

2. Physics Goals

2.1 Top Physics

A major goal for the Tevatron in the 1990's is the discovery of the top quark and the comparison of its mass and decay properties with the Standard Model. Since the currently allowed mass range exceeds the present collider capability, the top search provides one of the strongest justifications for the upgrade of the collider itself. Now that the top mass is found to be above the W mass,[1] the top signatures are fairly straightforward ($t \rightarrow Wb$, yielding isolated leptons and jets from W decays) and the present DØ detector is well optimized to detect them. The increased luminosity will be essential for finding the top if its mass is near the upper end of the currently predicted range.[2] The present DØ detector with its good lepton, jet and missing E_T capabilities should be a superb instrument for discovery and study of the top quark. The proposed upgrade of the central tracking will not compromise those features and will improve the b-jet tagging, providing additional confirmation of a top signal and improving the ability to measure the top mass.[3]

Table 2.1 gives the expected top cross sections[4] .

Table 2.1

Cross Sections (in pb) for various m_t and $\sqrt{s}$

$m_t =$	90 GeV	120 GeV	150 GeV	180 GeV	210 GeV	240 GeV
$\sqrt{s} = 1.8$ TeV	140	35	10	3.6	1.4	0.57
$\sqrt{s} = 2.0$ TeV	200	50	14	4.8	2.0	0.89

Through about 1995, a luminosity of $\sim 50\ pb^{-1}$ will have been accumulated. Top will have been discovered in the cleanest channel (isolated e and μ with jets with a branching ratio of 2.5%) if the mass is 140 GeV or less and in the lepton (e or μ) +jets (branching ratio 30%) if the mass is 160 GeV or less. (The assumptions here are that 10 events are needed in the $e - \mu$ channel and 100 in the lepton+jets and that the acceptances are about 50% and 70% respectively.) Increasing the integrated luminosity by a factor of 10 and increasing the energy from 1.8 to 2.0 TeV would give about 1500 lepton+jets events if the top mass is 150 GeV.

The top mass may be directly measured to within 10 GeV or less in the lepton+jets channel since there is only one ν. The effective mass of the W ($\rightarrow l\nu$) + b jet will show a peak at the top mass, providing that the backgrounds can be controlled and that the correct choice for the b-jet can be made. Choosing the b-jet candidate can be done by vertex tagging or a high p_T muon tag, but at the expense of large inefficiency. We believe that an alternative method of tagging the b-jet by topological means will also work. Figure 2.1 shows the effective (W+b) mass for a 150 GeV top quark in an ISAJET analysis in which the most likely b-jet in the event was selected. The backgrounds for this channel are the QCD W + multijet production; although troublesome, we expect that they will not dominate the signal.

In addition to a making a mass measurement one can look for other decay modes besides W+b. No other easily observed decay mode is expected in the standard model but, for example, in some technicolor models[5] it is possible for top to decay to Z + c (or γ + c or gluon + c) with relatively large branching ratios (10% or more). Given the 6% branching ratio of Z into ee and $\mu\mu$ these decays become observable at high luminosity.

If the top mass is above 160 GeV its discovery will have to wait until the collider is upgraded to higher luminosity. Assuming that in 2 years of running at the higher luminosity, we can accumulate 1000 events/pb at 2.0 TeV center of mass with the same efficiency as at lower luminosity, then the discovery limit is 240 GeV in the $e-\mu$ channel and over 260 GeV in the lepton+jets channel. This is well above current theoretical upper limits,[2] assuring either discovery of the standard model top quark or the indication of an important departure from the standard model.

The discovery limits[6] for top in $e-\mu$ or lepton + jet channels are summarized in Fig. 2.2.

2.2 B Physics

As long as the Tevatron remains the highest energy hadron machine, there will continue to be interesting searches for new phenomena at the largest mass. However, as the Tevatron program matures, the rate at which the search frontiers are pushed back will diminish. To keep the program at the Collider strong in this period, we need seek new opportunities – particularly among the copious processes at lower p_T. The programatic study of B-particles is a particularly attractive example of these 'low-p_T' studies for the DØ upgrade era; indeed CDF[7] has already shown some of the potential for B-physics at the Tevatron. The b-quark mass is large enough that there is a large ($\sim 10^3$) increase in cross section between the Fermilab fixed target regime and the collider. The B particles are expected to have a collection of very interesting medium rare decays which offer opportunity to explore some fundamental issues concerning the origin of mass differences and of CP violation.

Many of the features which have given DØ an excellent capability for large mass physics questions translate into strengths for the study of B states. These assets of DØ are radiation-hard, hermetic, fine grained calorimetry; excellent muon and electron identification with large solid angle coverage and good trigger capabilities; and a flexible multi-level trigger with an associated high bandwidth data acquisition system. With the addition of the magnetic field for reconstructing exclusive decay channels of B's and a system of silicon strip detectors to measure separated decay vertices, we believe that DØ will become a superior instrument for the study of a wide range of b-quark topics.

The $B\overline{B}$ cross section ($\sigma \sim 50\ \mu$b) is about 0.1% of the total inelastic cross section. For annual exposures of 500 pb^{-1} after the Tevatron upgrade there are $\sim 2.5 \times 10^{10}$ produced b pairs per collider detector per year. The fraction of events with b-quarks ($\sim 10^{-3}$) is similar to that for fixed target charm production where large data sets of fully reconstructed decays have been collected. We expect that the introduction of secondary vertex tagging and good mass resolution will be similarly beneficial for collider studies of B's.

The selection of an interesting sample of B particles requires particular attention be given to the non-trivial problem of triggering, and in many cases to tagging the B or $\overline{B}$ character of at least one of the pair-produced hadrons. The first line of attack is given by the fact that high p_T ($\geq$ 3 GeV/c) e's or μ's are dominantly due to B semileptonic decays; this is simply due to the relatively harder fragmentation function for b $\rightarrow$ B than for c $\rightarrow$ D. Observation of a relatively non-isolated lepton will also serve to tag the beauty content through the determination of lepton sign.

Observation of the B semileptonic decay products is constrained by the DØ detector. Figure 2.3 shows the effect of the range requirement on muon p_T and η. Figure 2.4 indicates how an isolation requirement (less than 10% of the electron energy deposited within ΔR=0.1 of the electron) affects the electron acceptance.

In many cases, added features will be needed to limit rates at trigger or early analysis levels to select useful samples of interesting events. Among those which could be useful in various contexts are (a) observation of some modest missing E_T, (b) indication of separated production and decay vertices, and (c) presence of ψ's seen as dimuons or dielectrons in the appropriate mass interval. In the case of the missing E_T, DØ will need to retain its excellent hermetic calorimetry. The separated vertex information requires a silicon tracking system at small radii and strongly benefits from a magnetic field in which the tracks can be weighted by their multiple scattering errors.

For both muon and electron triggers, some minimum E_T will be required for detection; setting this threshold will require experience with operating the DØ detector and in evolving the trigger capabilities. The other b-quark decay in the event will still tend to be at low p_T and there is thus a premium on being able to find it efficiently to avoid large extrapolation to p_T =0.

Some argument can be made that particle identification would be useful for B-tagging; for example, flagging the K^- in an event with a $D^0 \rightarrow K^-\pi^+$ would indeed reduce combinatorics. However, we regard particle identification with somewhat lower priority for B physics in DØ, especially in light of the compact region that is available for tracking. We note that the silicon vertex detection will give its own large reduction in the combinatorics of particles to be included in B or D mass plots while Cerenkov tagging will only reduce the background by factors of a few. Finally, we point out that the strong magnetic field will aid the particle identification; good mass resolution allows kinematical restriction; for example, by assigning a trial kaon mass and seeing if that assignment leads to a D/D_s mass peak. Efficient B particle reconstruction also requires good V^0 pattern recognition efficiency and resolution. The K_s and Λ particles thus found extend the strange particle identification.

An ensemble of B physics topics, possible with the increased luminosity and the DØ upgrade, is summarized below. The order is roughly that of increasing difficulty. The goal of much of the B-physics portion of the upgrade is to trigger and reconstruct the tagged exclusive final states efficiently and cleanly. We note that many of these topics will have been studied by CDF and e^+e^- machines, as well as the original incarnation of DØ, before the upgraded DØ comes on line. However, detailed analyses of the topics given below will still remain to be done, particularly given the significantly increased luminosity at the Tevatron after 1995.

2.2.1 Production Cross-Sections

We expect to measure the production cross sections for B^0, B^0_s, χ, χ_b: The initial goal is a study of the production dynamics of b quarks in both "open" and "onium" channels. We will trigger on 1 good muon, with $p_T > 3$ Gev. Subsidiary requirements are a modest missing p_T and a second (lower quality) muon or electron. These events will allow one to compare to theoretical predictions, while making only a modest extrapolation to $p_T = 0$. Added measurements include differentiation of $2 \rightarrow 2$ gluon fusion as opposed to $2 \rightarrow 3$ gluon splitting, sorted using the dimuon correlations. In addition, ψ from decays of B may be differentiated from ψ from directly produced χ using the associated γ's as a tag, as indicated in recent CDF studies[1] . Obviously there is a premium on hermetic, high resolution, well segmented calorimetry–a DØ strength. A follow-on would be to explore χ_b production dynamics using dileptons + a soft photon candidate. The rates are quite large, and should yield large data samples.

2.2.2 Find the B_c

A trilepton signature exists in the Cabibbo favored decay $B_c \rightarrow \psi + \mu + \nu$. Since the small-x sea quarks are more accessible at the high energies of the collider, the production rates are expected to be large. The trilepton mass is expected to be unmistakable evidence for B_c. Note that this mode is not accessible in e^+e^- experiments at the Upsilon(4S) resonance. If the signature of ψ + lepton + missing p_T is not sufficiently clean, the rate is copious enough so that one can require an additional lepton (e or μ) tag. This study places a premium on lepton identification.

2.2.3 Mixing of B_d or B_s

Mixing of B^0, B_s^0 can be studied using $\mu^\pm\mu^\pm/\mu^+\mu^-$ final states. The existence of like-sign dileptons is a signature for mixing in the B system. Separation of B_d and B_s mixing can be accomplished in the DØ Upgrade using the semileptonic decays to D and D_s respectively. The D_s and D would be reconstructed using all charged particle final states such as $D \rightarrow K + \pi$, $D_s \rightarrow \phi + \pi$. This distinction between B_d^0 and B_s^0 is important in testing the Standard Model prediction for x_d/x_s which is expected to be small, and proportional to (V_{td}/V_{ts}).

2.2.4 Observation of the Cabibbo Favored Decays

The decays $B^0 \rightarrow \psi + K_S$, $B_s \rightarrow \psi + \phi$, $\Lambda_b \rightarrow \psi + \Lambda$, $\Lambda_{bs} \rightarrow \psi + \Xi$ are all expected to occur with moderate branching ratios. These decays are likely to be the exclusive province of LEP detectors and the Tevatron. The decay modes are very well matched to the DØ Upgrade, especially the forward muon $\psi \rightarrow \mu^+\mu^-$ trigger. These are all Cabibbo favored hadronic, exclusive decays. The meson decays are good candidates for study of CP effects. In the past, heavy quark baryon spectroscopy has been the province of hadron machines and the modes listed here are a reasonable basis for the search of B baryons. The rates are expected to be comparable to those for B^0 and B_s.

2.2.5 Rare decays

The decays $B \rightarrow \mu^+\mu^-$ and $B \rightarrow \mu e$ have an extremely simple topology. Limits will be placed on the branching ratios, given the lepton capabilities of DØ, which are competitive with those from e^+e^- machines.

2.2.6 Flavor changing neutral currents in 1 loop Electroweak penguins

Such decays are an extension of the studies mentioned in item (2.2.4) above. They include $B \rightarrow K_S + l^+ + l^-$, $\Lambda_b \rightarrow \Lambda + l^+ + l^-$, and $\Lambda_{bs} \rightarrow \Xi + l^+ + l^-$. These decays modes are quite clearly well suited to the superior lepton detection of DØ.

2.2.7 Tagged B pairs in CP eigenstates and CP violation

One of the most favorable modes for searching for CP violation in the B-sector is in the asymmetry between B and $\overline{B}$ decays into a final state CP eigenstate. The theoretical interpretation is straightforward, and the asymmetries are often moderately large (of order 10%).[8] One of the simplest self conjugate final states occurs in the decay $B \rightarrow \psi + K_S$. This mode has become a paradigm for the reconstruction of CP eigenstates. Such studies will come last, after some experience is obtained on simpler topics. In addition to reconstructing ψK_S, an additional lepton from the other B ($\overline{B}$) is needed for the tag. These studies will require the full Upgrade to both the Tevatron and DØ if they are to be performed successfully. Some preliminary estimate of the capability of the upgraded DØ for measuring CP violation has been made.[9] One wishes to determine of the angle β in the B^0 decay unitarity triangle that characterizes CP violation.[10] We estimate that, with the dilutions caused by integration over decay time and wrong-sign tags due to mixing, the μ-tagged events can reach a $3-\sigma$ determination of the value of $\sin(2\beta)$ after accumulation of between ~100 - 2500 pb^{-1}, depending upon where the value of $\sin(2\beta)$ is found within the currently allowed range.

2.3 *W* and *Z* Physics

The SU(3)×SU(2)×U(1) Standard Model (SM) has been extensively tested using both e^+e^- and $\overline{p}$-p data and is found to give a good description of all of the processes studied to date. Despite its considerable success, the model fails to answer many questions, such as how the mass hierarchy is set up and what generates the angles of the KM matrix. Attempts to resolve these and other questions using extensions of the SM introduce new physics at a characteristic mass scale of around a TeV. To date we have no evidence for the existence of such particles.

The luminosity available at the upgraded Tevatron will enable significantly more stringent tests of these models than have been possible so far. The direct search for particles in the TeV range will be difficult since such particles have both complicated decay topologies and very small cross- sections. A more promising approach is an indirect search via studies of the electroweak sector, SU(2)×U(1) of the SM. Since new mass scales will enter via virtual loop graphs to the radiative corrections to the W and Z masses, precision studies of these quantities will provide stringent constraints on any new physics. In the following sections we discuss this and other electroweak studies which are possbile using the upgraded DØ detector.

2.3.1 W Boson Mass Determination

A very important test of the validity of the electroweak interaction in the SM comes from comparing the physical value of the Z^0 and $W^{\pm}$ masses. In the SM, the gauge boson masses are calculable to higher order in term of measured low energy parameters such as α, G_F, $\sin^2\theta_W$, and finally the top and Higgs masses. (There are many different definitions of $\sin^2\theta_W$, depending upon which quantities, at which scale, are chosen as fundamental parameters of the theory.)

At LEP the Z^0 mass has been measured to be $91177\pm31\pm30$ MeV,[11] an accuracy of $\sim$0.03% at 90 GeV. From this value one obtains $\sin^2\theta_w|_Z = 0.23147 \pm 0.00039$,[12] where $\theta_W|_Z$ is defined by taking the Z^0 mass as the fundamental physical quantity, accounting for all "known" physics by using $\alpha(m_Z^2) = 1/128.80\pm0.12$[13] and including the remaining radiative corrections in $\sin^2\theta_w$ resulting in the relation $\sin^2\theta_W|_Z = \sqrt{(4\pi\alpha(m_Z^2))/(\sqrt{2}G_F m_Z^2)}$.

One way to put the SM to strict test is to check whether other calculable observables lead to the same value for $\sin^2\theta_w$. While this approach was already well known when the original DØ was being proposed, the situation today has become even more interesting. The discovery of significant $B^0-\overline{B}^0$ mixing by ARGUS[14] gave the first indication that the mass of the top quark might be very high.[15] Experimental lower bounds are now around 89 GeV[1] and from the LEP results $m_t = 150$ ($\pm$few10's) GeV is obtained. The radiative correction to the W/Z masses, usually introduced through the parameter Δr, is rather large at low m_t (Δr=0.07 for m_t=45 GeV) but vanishes at m_t=245 GeV. Since Δr appears in the mass as $1/\sqrt{1-\Delta r}$, $\delta M/M$ changes by $\sim$3.5% for $45 < m_t < 245$ GeV. Roughly, a mass measurement of 0.03% accuracy determines the mass of the top to 2 GeV (modulo the value of $\sin^2\theta_w$ and the Higgs mass).

We can thus look forward to the possibility of a complete self consistent check of the electroweak sector, coming entirely from measurements at Fermilab. If in addition, the Z^0 mass is included together with forward-backward and polarization asymmetries, neutral to charged current ratios in neutrino scattering etc., one might finally indicate a way in which to go beyond the SM. In particular Peskin and Takeuchi[12] recently have shown how the precise determination of parameters of what we should call low energy phenomenology, imposes constraints on technicolor models.

Figure 2.5, from Peskin,[16] shows a possible comparison of results from Z^0 mass ($\delta M_Z = 30$ MeV), W mass ($\delta M_W = 50$ MeV), polarization asymmetry, A_{LR} in e^+e^- annihilations into fermion pairs ($\delta A_{LR} = 0.003$), and $R_{\bar{\nu}}$, the neutral to charged current ratio in $\bar{\nu}(A, Z)$ scattering , ($\delta R = 0.003$) plotted in the $\sin^2\theta_w$, m_t plane. Note that M_W and M_Z determine the top mass to $\sim\pm 10$ GeV – twice as well as a polarization asymmetry measurement to a third of 1%. We thus observe that a very complete and highly significant test requires finding the top and measuring the $W^\pm$ mass to ± 50 MeV.

The $W^\pm$ mass measurement is ultimately limited by the accuracy with which one can fix the absolute scale of the energy measurement. The quantity of physical relevance here is the mass *difference* between $W^\pm$ and Z^0. This difference is of the order of 10% of the W/Z masses and calibrating the energy scale with Z^0 decays offers the best method for keeping systematic errors to a minimum, especially for DØ whose response linearity has been proved to be exceptionally good.[17] Because of the high precision required, only $W^\pm \rightarrow e\nu$ and $Z^0 \rightarrow e^+e^-$ events are of practical interest. For an accumulated luminosity of 500 pb^{-1} one can collect, after cuts, sample's of 50,000 Z^0's and 500,000 $W^\pm$'s, decaying in the modes of interest. With the DØ electromagnetic calorimeter resolution of $16\%/\sqrt{E}$ resolution and the Z^0 width of 2.5 GeV, we obtain a statistical error on the determination of the Z^0 mass of $\sim$16 MeV. By that time LEP will have calibrated its energy scale to better than few MeV by using depolarizing resonance methods and with improved statistics the Z^0 mass will be known to better than 10 MeV. We can therefore assume an absolute scale calibration of the DØ detector to $\sim$15 MeV accuracy.

While systematic uncertainties will undoubtedly be considerably larger, they largely cancel in the mass difference measurement. For the $W^\pm$ case, one cannot measure the mass but must use instead the transverse mass, which requires measurements of the transverse energies of recoil hadrons. This implies that the hadronic resolution and calibration of the detector become important, as well as knowledge of the $W^{\pm}$ transverse momentum distributions and of the structure functions. Calculations show that the statistical uncertainty is again about 15 MeV and all other effects combined can be controlled so that a final total uncertainty of perhaps 30 MeV,[18] can be achieved, satisfying the accuracy requirements for a critical confrontation of the standard model. Figure 2.6(a) below shows the transverse mass distribution for decays of $W^{\pm}$'s produced in $p\bar{p}$ collisions before smearing due to detector resolution. From such a spectrum one determines the $W^{\pm}$ mass to a statistical accuracy of $3.2/\sqrt{N}$ GeV, for N events. Including the DØ detector resolution broadens the spectrum as shown in Fig 2.6(b). The $W^{\pm}$ mass can now be measured to an accuracy of $5.8/\sqrt{N}$ GeV. For $N = 500\,000$, the statistical error is 11.6 MeV.

2.3.2 Asymmetry in Z^0 Leptonic Decays

Another way to obtain an independent measurement of $\sin^2\theta_w$ is through measurements of the asymmetry in l^+ emission angle with respect to the incident $\bar{p}$ direction in leptonic Z^0 decays. This asymmetry depends on the quantity $(0.25 - \sin^2\theta_w)$.

The asymmetry is only weakly dependent on poorly known physics, such as structure functions and transverse momentum distributions. With an accumulated luminosity of 500 pb^{-1}, it is estimated that one can reach an accuracy of 0.002 with DØ.[19]

2.3.3 Cross Section Times Branching Ratio

The very precise direct measurements of the Z^0 width at LEP, $\Gamma(Z^0) = 2496 \pm 16$ MeV,[18] allows for a very accurate measurement of the $W^{\pm}$ width via the measurement of the ratio of cross section$\times$leptonic branching ratio, with the advantage of cancellations of uncertainties in both theoretical calculations and experimental measurement. This measurement opens a small window for discovery of particles which couple to W's but not Z^0's. While this is very unlikely, especially after recent LEP limits on neutral and charged Higgs and so on, it is still an interesting measurement if enough accuracy can be achieved.

Measurements of the cross section-branching ratio product become interesting at $\int \mathcal{L}dt \sim 500$ pb^{-1}, giving measurements of the widths to $\sim 1\%$ accuracy. Direct measurements from the transverse mass analysis as described above, with such large samples give in fact more precise answers. Thus for large accumulated luminosity, this measurement can be used to make an interesting check on the cross-section measurements.

2.3.4 More Gauge Bosons?

The first lesson we learned from the UA1 and UA2 experiments at the CERN collider, was how easy it was to observe essentially background-free samples of $W^{\pm}$'s and Z^0's. At Fermilab the reach of such easy discovery is extended to considerably heavier Z^0's gauge bosons required, for instance, in some SUSY extensions of the SM.

The sensitivity of searches for $Z^{0\prime}$ bosons is very good for low masses and extends to around M=500 GeV. While this is the limit reachable with 500 pb^{-1}, the limit varies very slowly with statistics. In contrast doubling the collision energy would raise the reachable mass to 700 GeV.

Likewise W bosons up to similar masses can be discovered, if production and decay into clean channels remain as favorable, with respect to the Z^0 case, as was the case for the *standard*, observed boson. Some caution might be necessary here since the couplings of these extra bosons[20] could be extremely small depending on the particular way in which the SM emerges as a remnant of some broken higher symmetry.

2.3.5 Gauge Boson Pairs

The production of $W^{\pm}\gamma$ pairs to measure the gauge coupling was discussed in the original DØ proposal and was found to be marginal statistically with $\int \mathcal{L}dt$=5pb^{-1}. With the much larger luminosity of the upgrade, study of the angular distribution with its characteristic amplitude zero should become possible.

We can, in principle, look for $W^{\pm}$ pairs, which come from several sources of interest: the gauge coupling, and for heavy Higg's and top, both from $H \rightarrow W^+W^-$ and the cascade $H \rightarrow t\bar{t} \rightarrow W^+W^-$. The signal is acceptable, the background probably overwhelming.

The detection of $W^{\pm}$ pairs will be severely impaired by the $W^{\pm}$+jet background, some three order of magnitudes larger. It is difficult to predict at present our ability to extract a signal. It is probably best to say that we will have to try, and perhaps we will learn how to do it. If so we will be able to study very interesting new physics.

It has been recently pointed out[21] that the study of $Z^0W^{\pm}$ pairs might be considerably less obscured by the many sources of possible background, giving us additional and cleaner informations on predicted, as well as new, physics.

2.4 QCD Studies

From the theoretical and experimental work done over the past years, the general agreement between perturbative QCD predictions and experimental data can be claimed to be good, if not excellent. This comparison should be expanded in the Tevatron Collider upgrade. The higher luminosities should open interesting new possibilities in two broad categories: 1) measurements of parts of parton distributions not accessible in previous experiments and 2) tests of precise predictions of perturbative QCD and if possible extraction of the strong coupling constant. We give examples below for such experiments.

2.4.1 Inclusive Jet Cross-Section

With the advent of QCD calculations for inclusive jet cross sections up order α_s^3 [22] , the theoretical errors have been greatly reduced. These predictions for the first time take 3 parton final states into account and predict the size of a jet in η-ϕ space around the parton. We can test experimentally how how the jet cross-section (at a fixed p_T) depends on ΔR. The higher p_T range is enabled by larger $\mathcal{L}$. Although there are final state fragmentation contributions to this dependence, it is believed that most of the dependence comes from perturbative QCD. With their fine η and ϕ segmentation, the DØ calorimeters will be in a good position to measure the R–dependence of the cross section.

Comparing the total jet cross section to the theoretical predictions as a function of E_T will give information about the parton distributions. Several parton distribution parametrizations are being used now and this measurement should help discrimate among them. In particular, the extrapolations into the low-x and high-x, high-Q^2

regions can be tested this way. The high x,Q^2 region is explored by the large E_T part of the jet E_T distribution. With an integrated luminosity of 1000 pb^{-1} one will be able to explore jet E_T up to 600 GeV. Measuring the η dependence of the cross-section at low E_T will probe the small x region of the parton distributions. With its uniform calorimeter coverage out to $\eta = 3.0$, DØ will be able to contribute significantly here.

2.4.2 Direct Photons

The gluon distribution of the proton can only be probed directly by direct photon production,[23] through the Compton scattering of a quark and a gluon, which dominates at small E_T and/or large η. Of special interest is the exploration of the very small-x region of the gluon distribution ($x < 0.01$), accessible at Collider energies, but not with any fixed target experiments. The sensitivity to the low-x part of the gluon distribution is limited to the E_T region 10–30 GeV, in which one needs to measure η-dependence of the cross-section for $|\eta| \leq 3$. These measurements distinguish between different parametrizations of the gluon distributions allowed by deep inelastic lepton-nucleon scattering. Figure 2.7 shows the predicted direct γ cross-sections for several allowed gluon structure functions. Since the final state photon is not affected by uncertainties in fragmentation models, the prediction of the cross section by QCD is considered to be more reliable than jet cross-sections and therefore allows a better test of perturbative QCD.

2.4.3 High p_T $W^\pm$ and Z^0 Production

The W and Z production mechanisms are similar to the direct photon process since there is a non-colored object in the final state which does not hadronize. At an upgraded Collider we expect hundreds of thousands of leptonic W's and Z's. Measuring the relative cross section of W/Z production measures the u/d ratio in the proton; at Tevatron energies one also becomes sensitive to the charm contribution in the proton.[24] The E_T spectrum for W's and Z's is predicted[25] to order α_s^2. With the above statistics it will be possible to measure E_T out to 250 GeV/c which will enable a significant test of QCD predictions. The shape of the E_T spectrum has also some sensitivity to the choice of the scale for α_s and there is a possibility that certain scales can be ruled out with this kind of statistics.[26] The ratio of W +n jet production to total W production (and similarly for Z's) is a measure of the strong coupling constant as has been shown by UA2[27] with small statistics. With the large expected W+ n jets, these ratios should be measured very accurately and a measurement of α_s will be possible.

2.4.4 Searches for New Phenonema

The increased luminosity of the upgraded Collider will enable extension of the search for new phenomena at large p_T. The comparison of QCD prediction of high p_T jets and the data will allow sensitivity to parton compositeness out to $\Lambda \sim 2.5$ TeV. The search for supersymmetric objects will be continued; standard SuSy objects such as $\tilde{g}$ and $\tilde{q}$ should be found if the masses are less than ~ 250 GeV/c^2. Important connections and constraints should exist between the searches for sleptons, charginos and neutralinos at LEP and the strongly-interacting sector of SuSy at the Tevatron.

With the addition of a magnetic field, DØ will gain the capability to recognize τ's as low multiplicity jets. The τ signals will be useful for seeking departures from lepton universality and as signatures for new particles such as charged Higgs, leptoquarks or top.

Chapter 2 References

1. CDF Collaboration, L. Pondrom, in Proceedings of the XXV International Conference on High Energy Physics, Singapore, August 1990.
2. V. Barger, J.L. Hewett, T.G. Rizzo, Phys Rev. Lett. 1313, **65** (1990).
3. S. Snyder, DØ Note #1031.
4. G. Altarelli *et al.* Nucl. Phys. **B308** 724 (1988). The specific values in the table are taken from ISAJET; these values fall in the middle of a range of theoretical predictions with an uncertainty of $\sim$ 30%.
5. B. Dutta-Roy et. al., Phys. Rev. Lett.,827 **65** (1990).
6. S. Abachi *etal* "Prospects for Top at the Tevatron Collider in the 1990's", in Proceedings of the Workshop on Physics at Fermilab in the 1990's, Breckenridge Colorado, 1989, E. Fisk and A. Slaughter eds.
7. A.R. Baden, "Heavy Flavor Physics With CDF", talk at the 1990 SLAC Summer Institute on Particle Physics, SLAC, August 1990.
8. I.I. Bigi and A.I. Sanda, Nucl.Phys. 237, **281** (1987).
9. D. Hedin, DØ Note 666. N. Roe, "Measuring CP Violation at the Upgraded Tevatron" DØ Note (September 1990). J.G. Heinrich and K.T. McDonald, "B-Physics Options at TeVI",Princeton University preprint DOE/ER/3072-61 (August 10, 1990).
10. C. Dib, I. Dunietz, F. Gilman and Y. Nir, Phys Rev. 1522, **D41** (1990).
11. F. Dydak, Review Talk at the XXV ICHEP Conference, Singapore, Aug. 1990.
12. M. E. Peskin and T. Takeuchi, Phys. Rev. Lett. 964, **65** (1990).
13. M. Consoli and W. Hollik in *Z Physics at LEP 1*, G. Altarelli *et al.*, eds. (CERN–89–08, 1989); see also P. Langacker, in Review of Particle Properties, Phys. Lett. B **204**, 102 (1988).
14. H. Albrecht *et al.* (ARGUS), Phys. Lett. B, 245 (1987)
15. See for instance G. Altarelli and P. J. Franzini, Z. Phys. C **37**, 271 (1988).
16. M. E. Peskin, 1989 SLAC Summer Institute, SLAC-PUB-5210 (1990).
17. The DØ Calorimetry Group, Nucl. Inst. and Meth. A280 (1990) 36.
18. R. Raja, DØ note # 798, Nov. 1988 and Proceedings of the 1988 $\bar{p}$-p Workshop, Fermilab, (1988).

19. "Physics at Fermilab in the 1990's", Workshop at Breckenridge Colo. June 1989 , E. H. Fisk and J. Slaughter Eds.
20. P. J. Franzini, XXI Rencontre de Moriond, Progress in Electroweak Interactions, J. Tran Thanh Van Editor, Editions Frontières, (1986), p. 242.
21. R. Gatto, private communication.
22. See the review by R.K. Ellis and W.J. Stirling, "QCD and Collider Physics", Fermilab preprint 090-164-T (August, 1990).
23. For a review see for example: Owens, J.F., Rev. Mod. Phys. **59**, 465(1987) Aurenche, P. et al, Nucl. Phys., **B297**, 661(1988)
24. "Physics at Fermilab in the 1990's", Breckenridge, June 1989, p.128.
25. P.Arnold and M.H.Reno, FNAL -Pub-88/168 (1988)
26. See reference 19, p.222.
27. R.Ansari et al, Phys. Lett. **B215**, 175(1988)

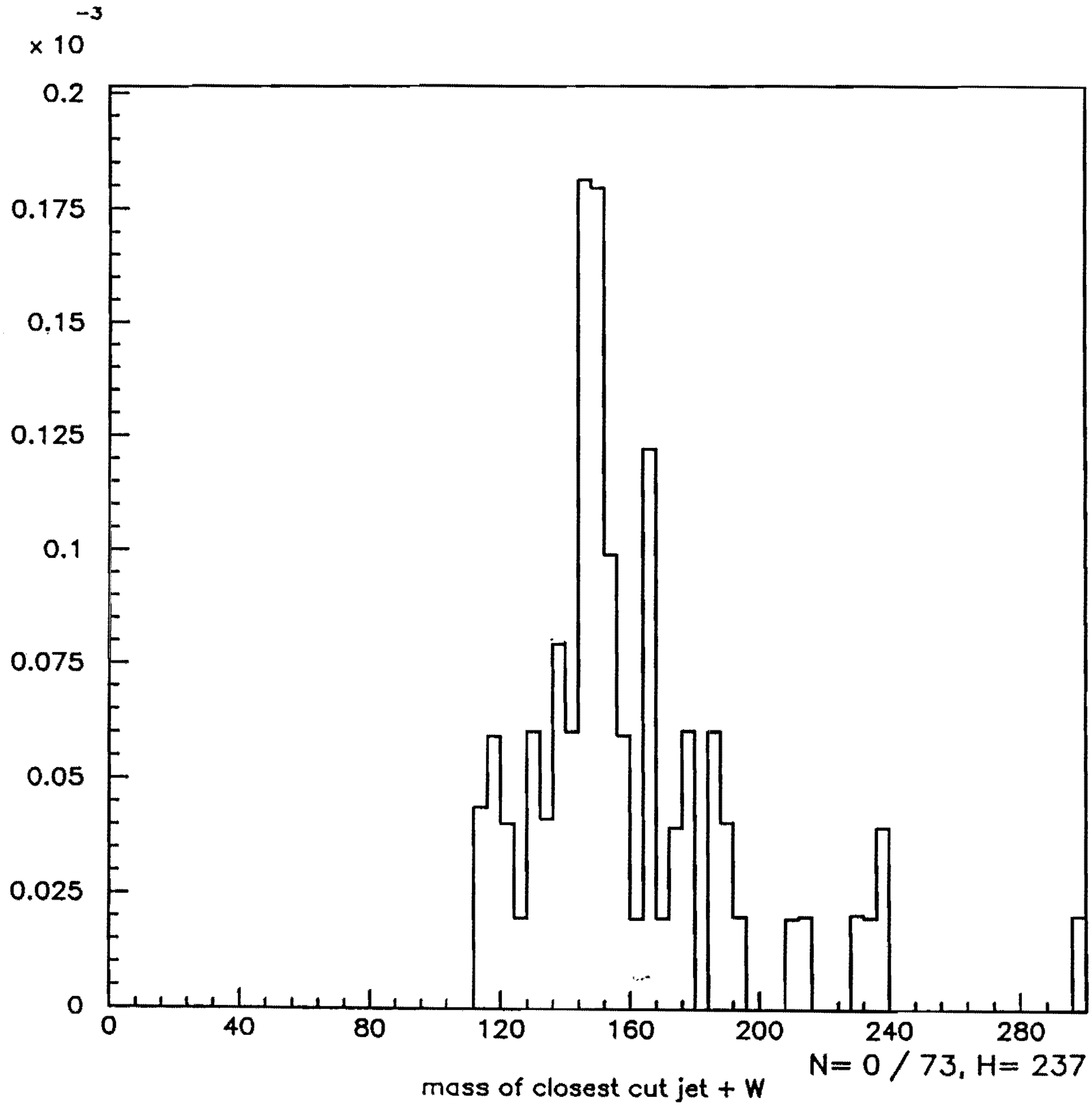

Figure 2.1 Effective W-b mass for a 150 GeV top. The b-jet to be paired with the W has been chosen on the basis of a modified nearest neighbor algorithm.

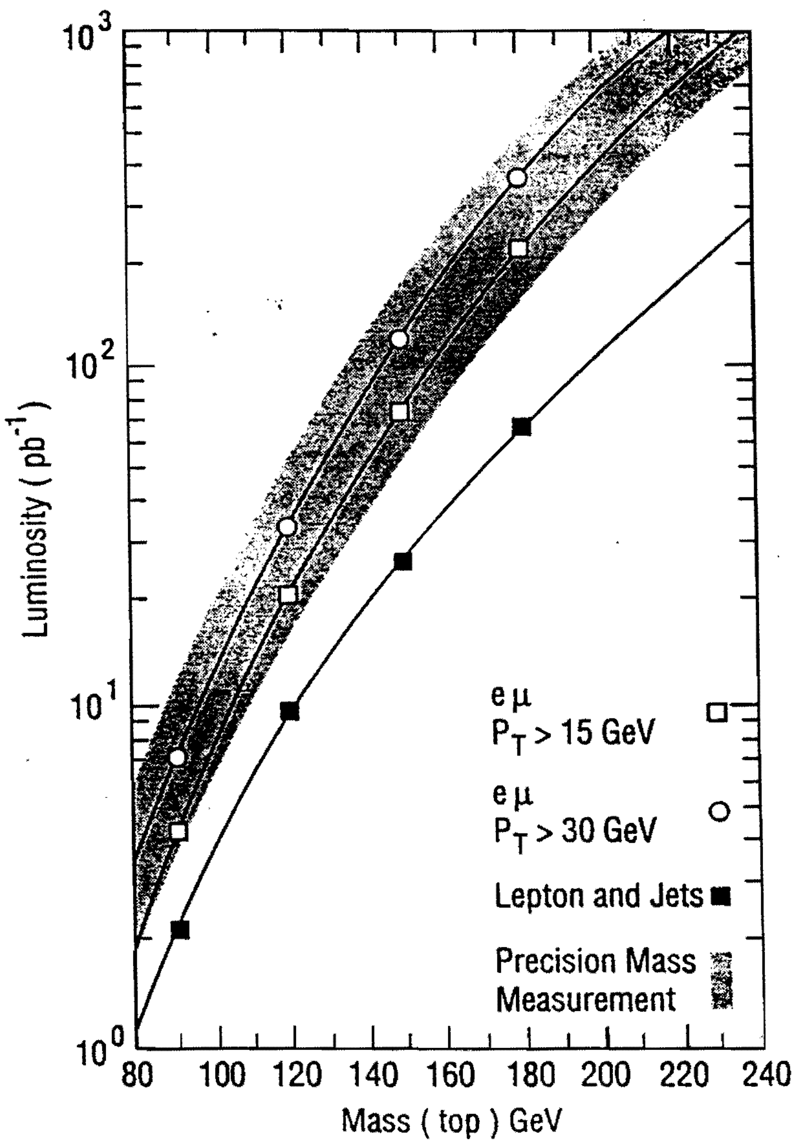

Figure 2.2 Required Luminosity to discover top at 1.8 TeV in dilepton and lepton plus jet channels.

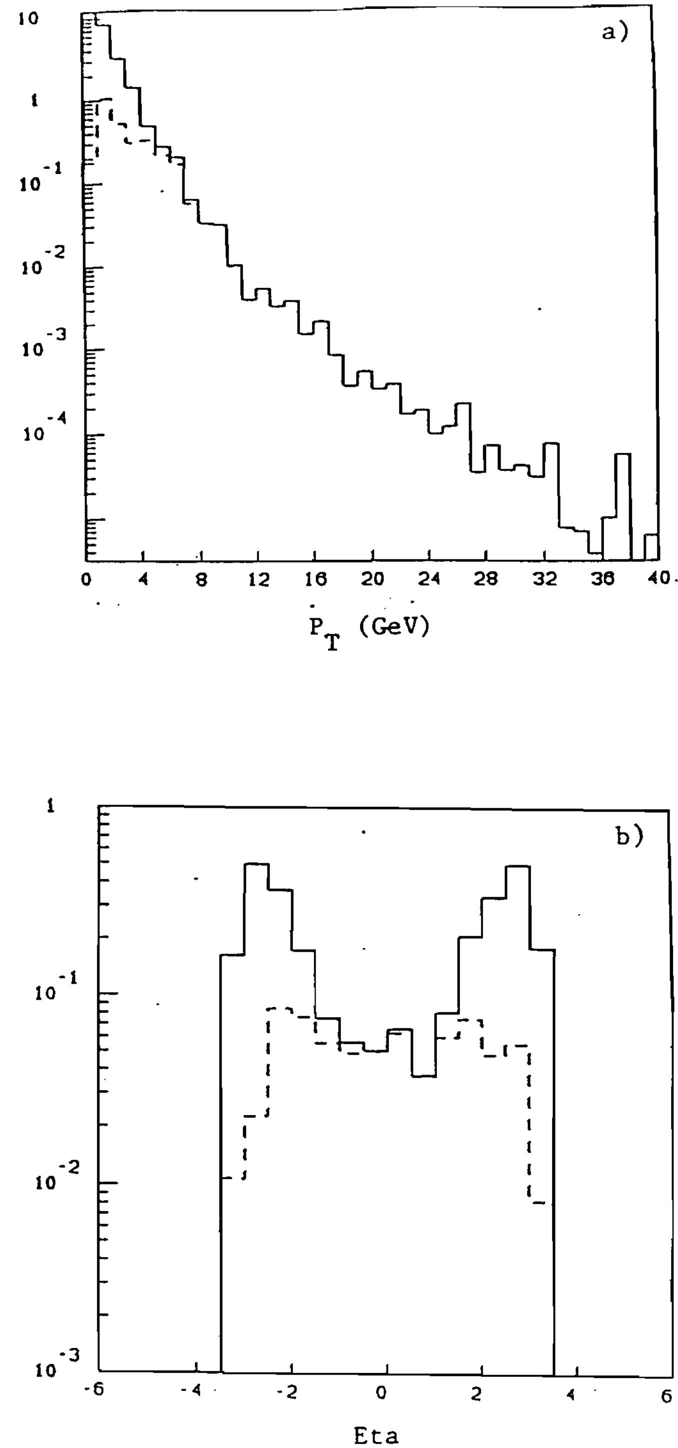

Figure 2.3 (a) Single muon rates as a function of p_T before (solid) and after (dashed) muon trigger requirements based on the range requirements in calorimetry and toroids. (b) The η distributions for all triggered muons (solid) and those with $p_T > 4$ GeV/c (dashed).

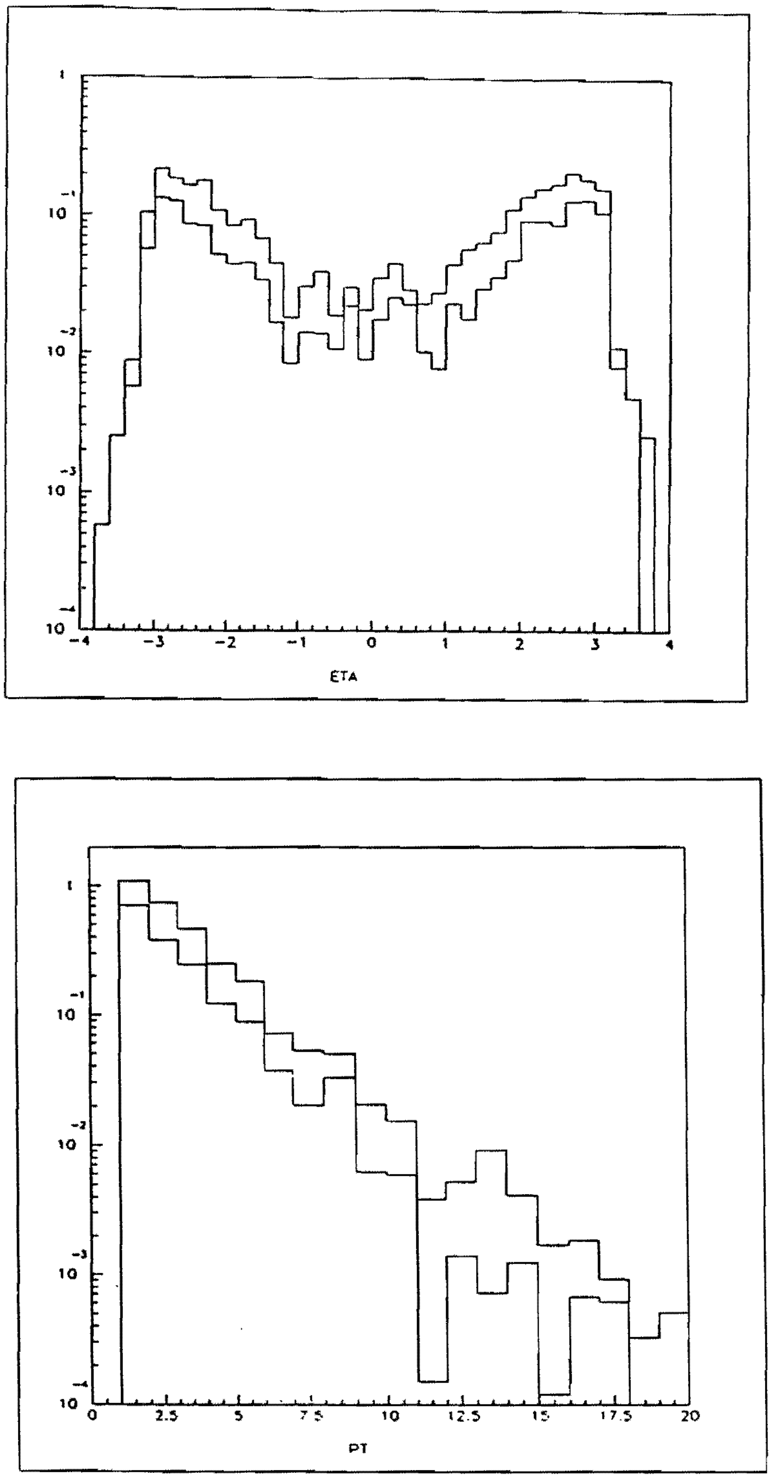

Figure 2.4 **(a) Rapidity and (b) p_T distributions for electrons before and after application of isolation requirements in the calorimeters (less than 10% of the electron energy in a $\Delta R \leq 0.2$ with respect to the electron).**

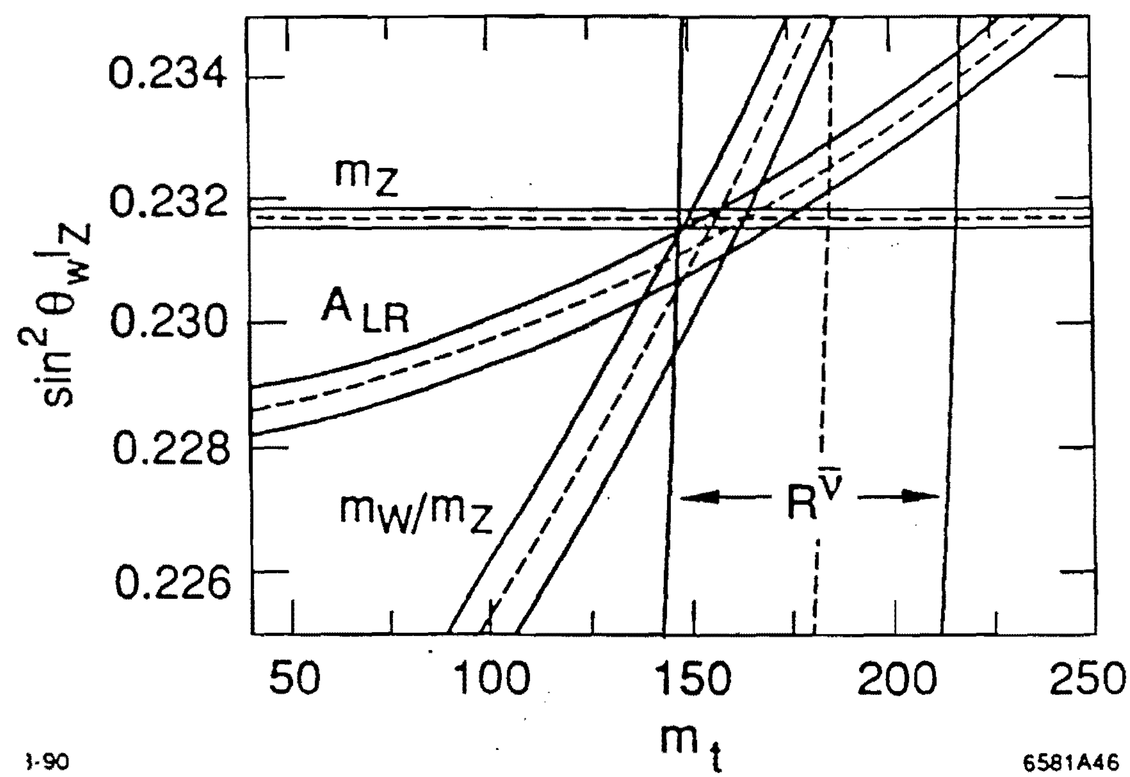

Figure 2.5 Prospects for constraints on $\sin^2\theta|_Z$ versus m_t. The 1σ confidence intervals come from M_Z, M_W/M_Z, A_{LR} and $R^{\bar{\nu}}$, with uncertainties as described in the text. The central values are arbitrary. From Peskin.[16]

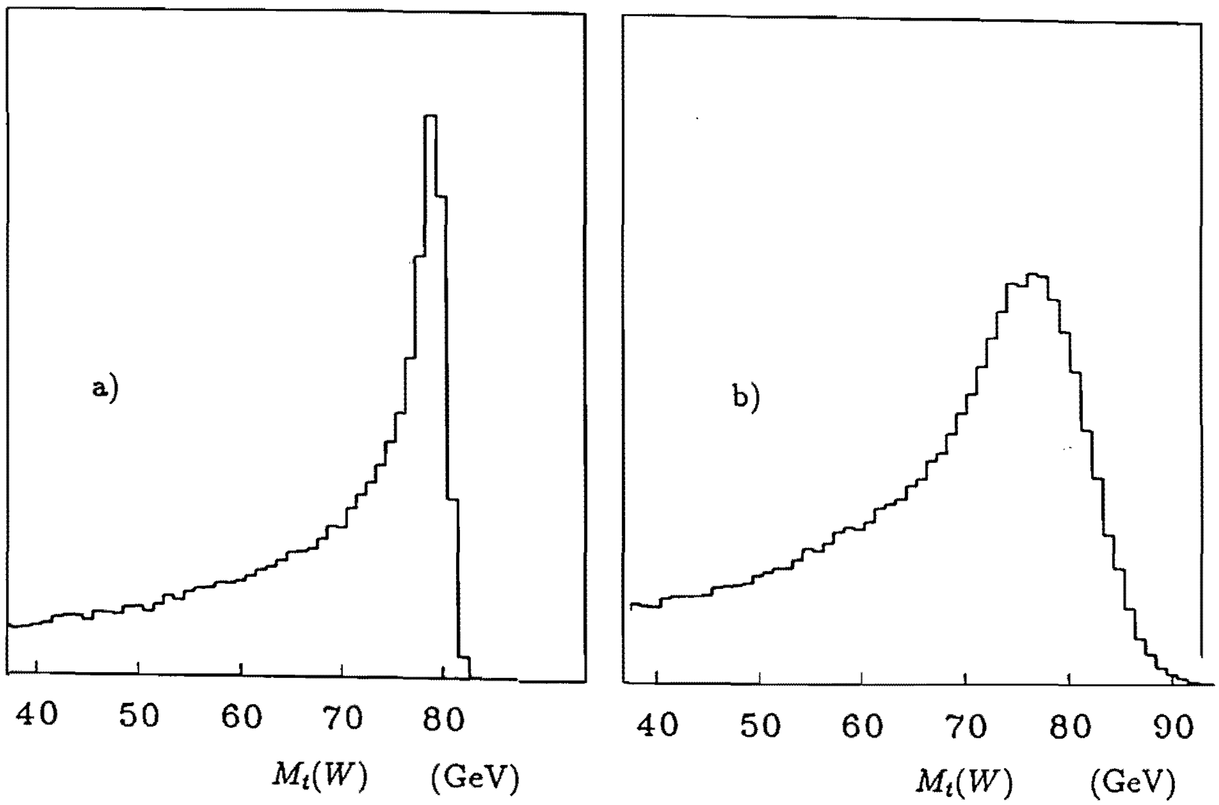

Figure 2.6 Transverse mass distribution for the e-ν from W decay: a) Perfect resolution. and (b) DØ resolution.

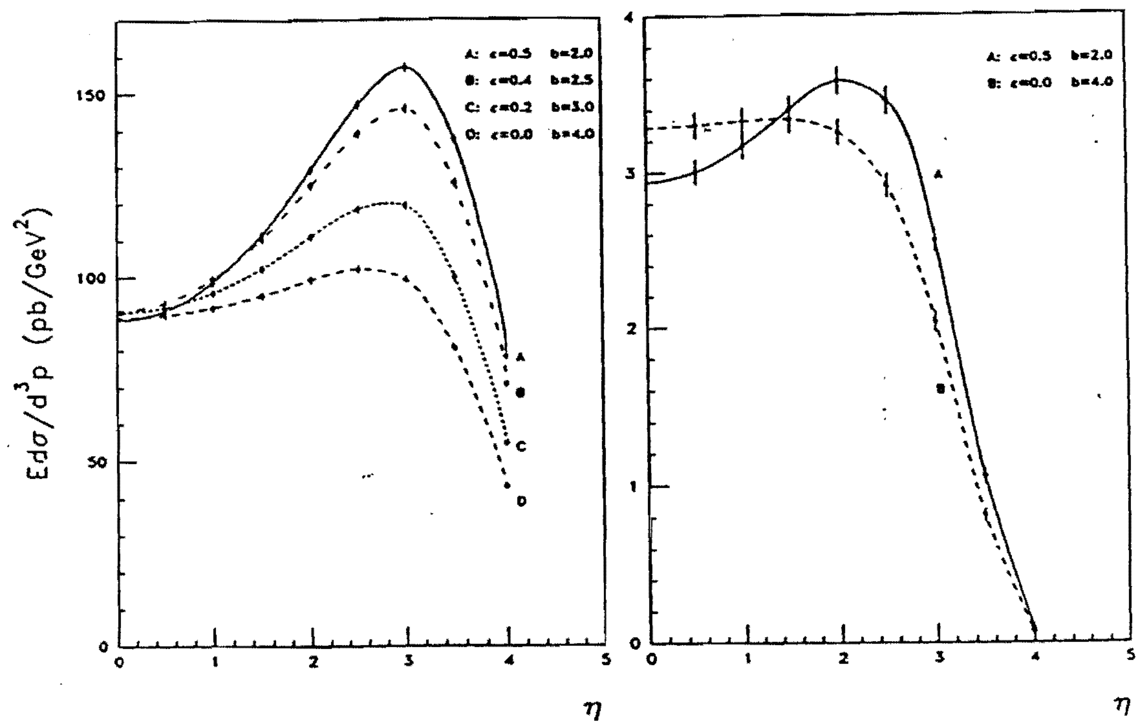

Figure 2.7 Rapidity dependence of the direct γ production cross-section in $\bar{p}$-p collisions for a range of allowable gluon structure functions of the form $xG(x) = x^{-\epsilon}(1-x)^b$. The p_T of the γ is (a) 10 GeV/c and (b) 20 GeV/c.

3. Tracking Detector Upgrades

3.1 Modifications for the 1993 Run

The upgrade to the central detector will be staged in two phases. For the first phase in the 1993 Collider run, the initial luminosity is expected[1] to exceed $10^{31} cm^{-2} s^{-1}$ with 36 (or 18) bunches and $\Delta T_b \sim 400$ (or 800) ns between crossings. Increasing the number of bunches in the Collider will require modifications to the existing DØ central tracking detector. The current detector (see Fig. 1.2 in Chapter 1) is optimized for 6 bunch operations with $3.5\mu s$ between the crossings. Table 3.1 lists the properties of the central tracking detector as it is expected to run in 1991 with the assumption of an initial luminosity of $5 \times 10^{30} cm^{-2} s^{-1}$ and considering only inelastic collisions.

Table 3.1

Operating Conditions for DØ Central Tracking Detectors in 1991

	VTX	TRD	CDC	FDC
Max drift distance (mm)	16	20	70	53
gas	CO_2/C_2H_6	Xe/C_2H_6	$Ar/CH_4/CO_2$	$Ar/CH_4/CO_2$
drift velocity (mm/μs)	10	35	34	34
max drift time (μs)	1.6	0.57	2	1.6
avg no. events/crossing	0.3	0.3	0.3	0.3
avg no. events/readout time	0.14	0.05	0.2	0.14

For 36 bunches and with no changes in the drift chambers, there would be up to four crossings during a readout period. To decrease this number we will replace the operating gas with a faster gas. Ar/CF_4 is an anticipated substitute gas for the CDC/FDC detectors. We have operated a test cell with Ar/CF_4 and a drift velocity of 120 mm/μs. Changing the gas and operating conditions for the 1993 run will allow us to operate with the conditions shown in Table 3.2. This table assumes that the initial luminosity will have increased to $10^{31} cm^{-2} s^{-1}$ and 36 bunches. With this gas the maximum drift time in the TRD, CDC, and FDC will still exceed the 400ns between beam crossings and there will be some overlap of subsequent interactions. In addition, the delays lines in the existing FDC and CDC detectors which provide the alternate coordinate will add to the overall time for signal collection. The maximum time for the delay line readout is the maximum drift time in the chamber plus the delay line progation time. For the CDC this is 580ns plus 800ns. The delay lines will be useful only for events where there are few subsequent interactions or the density of hits is small. Operation of the existing chamber system with minimal temporal overlap of events would benefit from keeping the number of bunches small (*e.g.* 18 instead of 36 bunches).

Table 3.2

Conditions in DØ Central Tracking Detector with Faster Gases

Assuming Initial Luminosity of $10^{31} cm^{-2} s^{-1}$

	VTX	TRD	CDC	FDC
gas	Ar/C_2H_6	Xe/C_2H_6	Ar/CF_4	Ar/CF_4
drift velocity (mm/μs)	50	35	120	120
max drift time (ns)	320	570	580	440
avg no. events/crossing	0.1	0.1	0.1	0.1
avg no. events/readout time	0.1	0.15	0.15	0.1

We will make further tests of these gases in a test beam to understand how their properties effect the chamber resolution. For example, the current FDC chamber signal with risetime of 15 ns in $Ar/CO_2/CH_4$ would be expected to have a risetime of 4 ns in Ar/CF_4. This means that, with the current 106 MHz FADC sampling, we would not be able to use the leading edge derivative method for hit finding. We would have to use an alternate method like pulse height above threshold. The effect of the loss in sampling rate and its affect on the chamber resolution should be measured this winter in the NWA test beam with a spare theta module of the FDC detector.

In phase 1 of the tracking modifications we do not anticipate changing the chamber preamps, cabling, or FADC readout system. The shaping functions may require modifications but this is a plug-in header board on the shaper cards. The zero suppression chip in the FADC readout was designed with enough programmability that it can adapt to an alternate amplitude above threshold scheme.

Another important consideration for a gas detector is the accumulated charge on the wires which is responsible for radiation damage. Considering only beam-beam collisions with a peak luminosity of $10^{31}cm^{-2}s^{-1}$ and running for a standard year (8×10^6s at peak luminosity), the innermost layer of the VTX detector would receive 0.2 Coulombs/cm. Although this is considerable, it is still within the range of successful operation of chambers.

3.2 Motivation and Overview of the Proposed Tracking Upgrade

In the preceding we have discussed what can be achieved with minor modifications to the existing DØ tracking system to accomodate a reduction in ΔT_b and a modest increase in luminosity. In this section we discuss a strategy for a major improvement in the DØ tracking for the 1995 run which preserves the stress on high p_T physics and allows extension toward B-physics.

3.2.1 Operational Constraints

In trying to achieve the goals for the upgrade, we identify the following boundary conditions.

a. The Tevatron luminosity will reach and perhaps exceed $\mathcal{L}=5 \times 10^{31}cm^{-2}s^{-1}$ with ΔT_b=400 nsec.

b. A magnetic field is necessary for good reconstruction of B meson decays. A solenoidal field appears to be the only option consistent with the current highly optimized layout of the DØ calorimetry.

c. The magnetic tracking detector system must provide good momentum determination for $|\eta| <3$ to be compatible with the current good muon trigger range. Detection of low p_T μ's from B's is most efficient at large η.

d. The tracking detector system must give sufficient resolution in vertex reconstruction to recognize tracks from separated vertices and to reconstruct the multiple vertices in a $B^0 - \overline{B}^0$ event. In fixed target charm experiments, dramatic progress was made when the charged particles were tracked with sufficient precision to permit identification of separated primary and secondary vertices. It is reasonable to expect a similar phenomenon with B physics at the collider.

e. Provision must be made for electron identification at least as good as that with the TRD system in the present DØ.

f. We are cognizant of the possibility of a reduction luminous region length from ±30cm to ±12cm which could be achieved by upgrading the Tevatron RF system. Such an improvement would greatly ease the design and optimization of a detector adequate for B physics. We have, in this proposal, allowed ourselves such a possibility and urge that the Fermilab Accelerator Division pursue this option agressively. Should this turn out not to be possible, some different optimization of detector deployment would likely result.

3.2.2 The Proposed Configuration

Figure 3.1 shows the layout of the proposed upgraded tracking region whose elements are discussed in subsequent sections. The superconducting solenoidal coil with 1.5T central field is required to allow discrimination between ψ K_S and ψ K_S π^0 decays of B^0. Silicon strip detectors are provided so as to identify separated vertices from b- and c-quark decays. Since the DØ muon triggering emphasizes the small angle region, we choose a silicon system which relies heavily on a set of disks mounted perpendicular to the beams. Outside the silicon tracking, we propose four sets of axial and small-angle stereo scintillating fiber superlayers. The fibers augment the momentum resolution for $|\eta| < 1.8$ and give crucial help to the pattern recognition for tracks. We propose to use the material of the superconducting coil to convert photons which are then detected in the 'preshower detector' station of scintillating fibers outside the coil. Electron identification is given by requiring $E/p \approx 1$, the preshower detector energy and position match to the inner tracking and by the calorimeter energy deposit profile.

3.2.3 Performance

The relative momentum resolution obtained in a simulation of this system is shown as a function of η in Fig 3.2. Both the multiple scattering term and the measurement resolution term are smaller in the small η region covered by both the silicon and the scintillating fiber system than for large η where there is the silicon system alone.

The resolution of the system has been further studied by tracking a sample of B$\rightarrow$ ψ K_S decays through the detectors in a uniform field, simulating the scattering and the measurement errors at the detectors. The momenta of the charged tracks are then recalculated and the resonance masses are computed. The results are shown in Fig. 3.3 for (a) the ψ mass ($\sigma = 38$ MeV); (b) the K^0 mass ($\sigma = 6$ MeV) and (c) the B mass. Imposing mass constraints on the intermediate K^0 and ψ improves the B mass resolution from about 68 MeV in Fig 3.3(c) to about 17 MeV in Fig 3.3(d).

A typical background to the measurement sketched above could be the decay B$\rightarrow$ J/ψ K^* where the K^* subsequently decays to K_S π^0 and the π^0 is missed. In Fig. 3.4 we superimpose the reconstructed "B" mass distribution from such events as that previously obtained for the J/ψ K_S decays. We observe that they contribute negligibly to the region under the B mass peak.

Finally we have calculated the significance of the measurement of the difference between the primary and B decay vertices. This is shown in Fig. 3.5. The measurement is clearly adequate to recognise a large fraction of the B decays as separate vertices.

3.2.4 Acceptance

Preliminary studies of the acceptance for B mesons in the upgraded DØ detector have been performed using ISAJET. Two-jet $B^0 - \overline{B}^0$events were generated with $4 \leq p_T(\text{jet}) \leq 50$ GeV/c; the total cross section for this process calculated by ISAJET was 16 μb. The contribution from gluon fragmentation was not calculated but is comparable.

Muons were required to have momentum greater than 3 GeV/c to roughly simulate the range requirement of the calorimeter and the muon detector, and to have $|\eta| < 3.1$, corresponding to the angular acceptance of the forward muon system and of the silicon disk system.

Using these criteria, the acceptance for muons from the semileptonic decay $B \rightarrow D^* \mu\nu$ is 45%. For the process $B^0 \rightarrow \psi K_S$, the total acceptance for both muons is 29%. Additionally requiring $|\eta| < 3.1$ for the K_S results in an acceptance of 26%. If one also requires a muon tag from the other B the acceptance is 13%, very close to the product of the individual tagging and ψK_S acceptances. This suggests that the acceptances are not strongly correlated.

One may be able to trigger on two μ's in the muon detector and reconstruct the third muon in the calorimeter. If we remove the requirement on momentum for the lowest energy muon the resulting acceptance increases from 13% to 41%.

Acceptance studies for these as well as other final states involving B mesons are continuing; these results should be taken as preliminary.

3.2.5 Optimization

These comments and the detailed descriptions below encourage us to believe that we are proposing a tracking design concept which is appropriate to the pursuit of B physics at the Tevatron. Nevertheless these studies are but a first step towards designing a detector which is optimally configured for the task at hand. In particular we can identify several topics which need more investigation.

a. Cost. We are investigating the dependence of performance on the most costly components of the system; for example we are examining the dependence of the cost of the superconducting coil on the field strength.

b. Multiple Scattering. In each of the tracking subsystems we are examining the tradeoffs between the numbers of planes and the multiple scattering errors to achieve a rational compromise.

c. Electrons. More detailed studies of electron identification without the TRD and of the energy and position resolution for electrons and γ's after the coil need to be done.

d. Uniformity of resolution. The B meson is light enough that its production spectrum is rather flat as a function of rapidity. It therefore seems to be an optimum to have a tracking system which is uniform as a function of rapidity. Within a constant budget this may imply tradeoffs between the inner and outer tracking systems.

e. Pattern Recognition. The considerations of momentum and mass resolution tend to underestimate the number of planes and the numbers of hits per track. This can lead to a detector that is inadequate for the intricate pattern recognition needed in the Tevatron environment. Studies of the performance of the detector design in these terms need to be extended.

f. Background Rejection. Notwithstanding the rather encouraging indications described above it is important that we establish with Monte Carlo simulation the ability of the tracking to reject backgrounds to the $B^0 - \overline{B}^0$ signals.

g. Triggering. Refined calculations for trigger efficiencies, both for B production modes and for QCD backgrounds need to be extended and refined. The data from the first DØ run will further aid in understanding these trigger rates.

h. Mechanical Services and Supports. The details of support structures for the solenoid and the services and connections to the coil and detectors remain to be worked out in detail.

3.3 Superconducting Solenoid

The upgraded tracking detector for DØ is based on the addition of a solenoidal magnetic field within the region inside the existing central calorimeter. The general requirements for the solenoid include:

1. A central field of 1.5T to provide good momentum and mass resolution.
2. A radially thin coil and cryostat to fit into the available space and still allow room for tracking devices.
3. A coil and cryostat that have a total thickness not exceeding about one radiation length so that they may be used as part of a pre-radiator electromagnetic shower detector.
4. A reasonably uniform field to allow the use of simple algorithms for track finding and pattern recognition without close iron for flux return.
5. Leads and cryogenic services that can fit into the 3 inch gap that exists between the end and central calorimeter to avoid introducing any deterioration of missing E_T resolution.

Table 3.3

Properties of the DØ Superconducting Coil

Magnetic Field at Center	1.50 T
at ± 1.25m	1.10 T
Cryostat Outer Radius	72.5 cm
Cryostat Inner Radius	56.7 cm
Total Thickness	15.8 cm
Thickness Outer Wall (Al)	1.25 cm
Thickness Inner (Al) Wall	0.5 cm
Overall Length	2.75 m
Coil Length	2.565 m
Coil Outer Radius	64.4 cm
Coil Inner Radius	60.7 cm
Winding	2 layers
Number of Turns	2×450=900
Conductor - NbTi/Cu	1.8 mm X 3.8 mm
Cu/SC Area Ratio	1.0
NbTi/Cu in extruded Al	4.35 mm × 18 mm (with insul.)
Insulation thickness turn to turn	0.38 mm kapton
Insulation thickness layer to layer	1.0 mm G-10
Nominal Operating Current	4200 A

The DØ superconducting solenoid will have a mean radius of 62.6 cm and a length of 2.57 m. This, coupled with the fact that an iron return yoke is not possible due to the location of the end calorimeters, would give an axial field that falls off to about half its central value at the ends of the winding if a uniform axial current density is assumed. The field profile is improved with a graded current density which makes the DØ design more similar to ZEUS[2] than to CDF.[3] The current distribution assumed in the calculation below is full density over the outer 28.25". In the central 43.5" region the winding is half density. The magnet design parameters are given in Table 3.3; Fig. 3.6 shows a cross section of the coil and cryostat.

This design will provide a field whose variation of B_z in the central tracking region of $\pm$ 1m is less than $\pm$ 10%. The conductor is to be wound in two layers with an axial distribution of current density that provides the desired field uniformity. A plot of the calculated field is shown in Figure 3.7. The DØ muon iron is far enough from the superconducting solenoid that only about half of the flux is returned through the iron. Effects of the field on the drift of ionization in the muon proportional drift tubes is not expected to be a problem. The coil decentering forces are expected to be straightforward to handle.

The hoop and axial stresses caused by the electromagnetic forces on the coil are taken up by an outer support cylinder. In the vacuum space between the outer cryostat walls and the captured coil there will be a 77K heat intercept, cooled by forced flow of LN_2 through tubes thermally attached to the *Al* nitrogen shield. The coil is cooled with forced flow He through tubes which are thermally and physically attached to the outer support cylinder. Although the stored magnetic energy of 3 MJ is well below the values for the CDF (30 MJ) and ZEUS (10 MJ) coils, the magnetic pressure on the coil and its support structure remains fairly high. The most critical stress is axial and this stress dictates the thickness of the outer support cylinder.

Table 3.4 gives the inventory of components that make up the material a particle exiting the interaction region will encounter at $\eta = 0$. Most of the contribution to the 1.1 radiation lengths is in the coil, the outer support cylinder and the outer vacuum shell. (The coil was assumed here to have uniform density at its higher value.)

Table 3.4

Contributions to coil thickness

Item	Material	in.	cm.	X_0	λ_{Abs}
Inner Vacuum Shell	Al	0.20	0.5	0.055	0.013
Inner N2 Shield	Al	0.06	0.15	0.017	0.0038
Conductor	Al/Cu/NbTi	1.42	3.6	0.561	0.104
Insulation	Epoxy/Fiberglass	0.12	0.30	0.017	0.006
Outer Suppt Cyl.	Al	0.63	1.6	0.179	0.043
Outer Shield	Al	0.08	0.20	0.022	0.0053
Outer Vacuum Shell	Al	0.50	1.25	0.141	0.034
Total		3.01	7.6	1.00	0.21

It is important that the superconducting coil not add so much material that the performance of the calorimeter outside is compromised. We note that in fact, this coil is comparable in radiation lengths (but not absorption lengths) with each of the 3 mm uranium absorber plates in the central calorimeter electromagnetic modules. We have performed a calculation using GEANT to examine the degradation in energy resolution for electrons and pions in a comparable coil to that described here. The result is shown in Fig. 3.8 for 10 and 50 GeV particles. There is no correction applied for energy loss in the coil in this analysis. In fact, as discussed in Section 3.6 below, the preshower detector will allow just this correction to be made for each isolated shower and thus we expect that the effect of the coil on energy resolution will be small.

3.4 Silicon Tracking

The silicon tracker serves two purposes: tracking and momentum measurement in a 1.5T solenoidal field up to $|\eta| < 3.1$, and tagging of secondary vertices. It consists of a 25 cm long $\times 16$ cm diameter barrel with four Si layers, capped at each end by eleven 30 cm diameter disks spaced over the full available length (Fig. 3.9). The total Si area is 2 m^2, divided into 800 double-sided wafers and read out by 10^6 electronics channels.

In the DØ tracker, 85% of the Si is in disks spaced along the beam axis over the full ($|z|$ <135 cm) tracking length available. Therefore the size of the DØ Si system is fixed primarily by the disk outer radius, which must be chosen carefully. In a solenoidal field, at forward angles, this system of disks will provide a roughly uniform resolution dp_T/p_T until η becomes so large that the highest $|z|$ disk is crossed at significantly less than its maximum radius. Beyond that point, dp_T/p_T increases with θ^{-2} if measuring error is most important, and with θ^{-1} if Coulomb scattering is dominant. We define the corner angle θ_c of the disk system using the track that crosses $z = 135$ cm at the maximum disk radius, and we define the useful angular range of the Si disk system by $\theta > 0.8\,\theta_c$. The disk radius R is then set by the useful range that is needed. Of course, enlarging the disks would not degrade the resolution at fixed θ, but the additional expense would be difficult to justify, especially considering that, for $\theta > \theta_c$, additional points on the track become available from the outer tracker.

One approach to establish R following the corner-angle argument given above emphasizes the desired tracking system acceptance. The DØ SAMUS muon system achieves an acceptance, averaged over azimuth, extending to η=3.2. Not accidentally, the DØ electromagnetic calorimeter retains a fine (0.1×0.1) segmentation out to the same η. A plot of the rapidity of muons with $p > 4$ GeV/c from decay of J/ψ arising from $B \to J/\psi\ K_S$ is peaked at $\eta \approx 2.1 \pm 0.9$, requiring good momentum measurement out to $\eta \approx 3$. So, for the Si disks, a useful angular range corresponding to $\eta \approx 3.1$ is required, or $\theta = 5.2°$; then $\theta_c = 6.4°$ and $R = 15$ cm.

Another approach considers the momentum resolution that is desired from the Si system alone (e.g. for corner tracks). As noted above, dp_T/p_T depends strongly on R: if $dp_T/p_T = Ap_T \oplus B$, A depends on R^{-2} and B on R^{-1}. For R =15 cm, for the Si alone in a 1.5T solenoidal field without beam constraint, $A = 0.02$ and $B = 0.06$ are achievable (c.f. Fig. 3.2). Detailed simulation[4] of the combined Si and outer tracker, including tracks near η=3 reconstructed only in the Si, confirms that this level of momentum resolution is adequate for reconstruction of exclusive b final states, e.g. separation of $\psi\ K_S$ from $\psi\ K^*$ (Fig. 3.4). Choice of R substantially below 15 cm would seriously degrade this capability.

The choice $R = 15$ cm also satisifies a practical constraint. With supports and services, a Si system with this active radius will fit inside the 17.5 cm inner radius of the existing DØ TRD. This will allow early testing of prototype disks in the DØ environment.

In considering the barrel Si detector for DØ, we have paid close attention to the SVX detector now being readied for CDF's 1991 run. The function of the two detectors is the same: identification of secondary vertices, e.g. from b decay, at central rapidity where tracks are detected in a powerful tracker outside, within a 1.5T solenoidal field. However, it would make no sense for DØ simply to copy the 1991 version of the CDF SVX. First, it is expected[5] that the 1991 CDF SVX must be replaced for later runs, for at least three reasons: readout chip ("SVXC") speed, SVXC radiation damage, and drift of SVXC bias due to radiation-induced strip leakage. Second, as noted above, we have been encouraged to assume that the luminous region will be of reduced 12 cm rms. For vertex tagging in the central region, a four-layer barrel with the same radii as the 1991 CDF SVX, but only half the length, would provide adequate acceptance and tracking capability if its ends are capped by Si disks. Provisionally, we have adopted the SVX barrel dimensions (save for shortening by half) in order to facilitate the possible development of common solutions for runs beyond 1991.

The number and placement of Si disks is set by requiring at least 5 double-sided Si wafers to be hit by tracks with $|\eta| < 3.1$ that are not geometrically accepted by the full outer tracking system. This allows a 2C fit in the bend view from Si information alone. If the track is geometrically accepted by the outer tracking system, only 4 hits are required. For tracks directed toward $+z$, these requirements are imposed for the 80% of primary interactions with $z < 10$ cm. The number of disks needed to satisfy these requirements is minimized at 11 per end provided that their spacing is set by a uniform progression in $log(z - 10\ \text{cm})$. The gross dimensions of the Si system are summarized in Table 3.5, and the number of hits per track for various track angles and interaction points is plotted in Fig. 3.10.

Table 3.5

Active dimensions of the Si system in cm.

Layer	z(min)		z(max)	r(min)		r(max)
Barrel 1	−12.75		12.75		2.90	
2	−12.75		12.75		4.05	
3	−12.75		12.75		5.41	
4	−12.75		12.75		8.06	
Disk 1		15.0		3.0		15.0
2		16.9		"		"
3		19.5		"		"
4		23.1		"		"
5		28.1		"		"
6		35.0		"		"
7		44.4		"		"
8		57.5		"		"
9		75.6		"		"
10		100.6		9.0		"
11		135.0		"		"

Though not finally optimized, these dimensions serve as a reasonable framework in which to assess possible choices for layout and readout of the Si wafers. Our aim is to minimize material, complexity, and cost required to achieve an adequate level of performance – mainly in the areas of momentum resolution, pattern recognition, and vertex resolution.

For Si wafer layout, the fundamental issues are strip orientation and strip length. First we consider the barrel geometry. For barrel layers in a solenoidal field, the natural strip orientation is axial. Double-sided wafers allow stereo strips at angles ranging from 5 mrad (one SSC conceptual design[6]) to 90°.

Because most of the DØ Si area is in the disks, and disk systems so far are uncommon,[7] we have directed most of our initial attention to them. The main choices of strip orientation are wedge shaped radial strips (usually with small-angle stereo), or rectangular strips parallel to one another in the plane of the disk. With rough knowledge of the track's polar angle, radial strips in a solenoidal field directly measure the momentum. Parallel strips measure the momentum only if 3D space points are constructed using local stereo layers. The latter method requires large stereo angles to minimize errors in the ϕ coordinate. Correspondingly, a larger number of stereo layers are required to overcome hit-matching confusion, which increases with the stereo angle. Since the stereo requirements appear to be much more relaxed for radial than for parallel strips, we have focused on the former. Pattern recognition using radial strips is also simplified by the fact that tracks emanating from the axis have exactly straight trajectories in ϕ *vs.* z regardless of their curvature in the solenoidal field. (Trajectories in ϕ *vs.* r or r *vs.* z are not straight.)

The choice of strip length can be debated. Many of the strip length issues are common to barrel and disk geometries, but there are some differences. Physically the length of (axial) barrel strips is limited only by the length of the barrel, while (radial) disk strips are limited in length to the difference between inner and outer radii. That difference is only 12 cm in the DØ Si disks, much shorter than the present SVX strip length of 25.5 cm.

At the other extreme, Spieler[8] has argued that optimizing for minimum power dissipation yields strip length closer to 1 cm. A detailed optimization for Tevatron as opposed to SSC conditions has not yet been performed but it is doubtful that strips as short as 1 cm could be justified for the Tevatron.

The choice of strip length is also affected by consideration of increased shot noise due to radiation-induced strip leakage. (We assume that the preamps will be AC coupled so that this leakage cannot influence the preamp bias.) Ellison[9] has calculated the radiation damage expected for axial strips at a variety of radii. For a 6 cm strip with a CR-RC shaping time of 200 nsec, exposed to 0.6 fb^{-1} at 3 cm radius, he computed a radiation-induced equivalent noise charge ("ENC") of $\approx$ 450 electrons, to be added in quadrature to the preamp noise, estimated to be $\approx$ 1100 electrons for 12 pF input capacitance. We infer that radiation-induced shot noise is an important consideration, but is unlikely to force the DØ design toward strips as short as 1 cm.

We have considered a particular layout of Si wafers to provide a framework for visualizing the detector and roughly estimating its cost. As in the CDF SVX, each barrel layer is made of 24 "ladders" (12 azimuthal sections $\times$ 2 ends). In DØ a ladder is only 12.8 cm long and might be composed of two 6.4 cm wafers, with strips that could be wire-bonded and read out at the end, or (perhaps in the innermost layer) read out individually. Then the barrel would contain 192 wafers and (allowing for stereo readout) at least 600 readout chips of 128 channels each.

The layout of disk wafers is displayed in Fig. 3.11. The upper left detail indicates the individual wafers inscribed in a circle of diameter of 8 cm. The detail in the upper right shows the radial strips with a factor of two change in pitch at the annular boundary. The lower details show radial (right) and 50 mrad stereo(left) strips, with no change of pitch at the annular boundary. The inner annulus ($3 \leq r \leq 9$ cm) consists of 10 wafers in the shape of isosceles pentagons, while the outer annulus ($9 \leq r \leq 15$ cm) consists of 20 wafers with an asymmetric trapezoidal shape. Both types of wafer can be cut from 4 inch diameter Si crystals. The analog to the barrel "ladder" is a "wedge" consisting of one inner and two adjoining outer wafers. Alternate wedges could be located in alternate z-planes, allowing overlap and simplifying relative alignment. Wafers with radial strips on one side and stereo strips with angles up to 3° are possible in the design shown. (The choice of stereo angle is a detailed optimization that weighs simplicity of pattern recognition against precise radial measurement.) If strips on the inner and outer wafers are wire-bonded together, all readout chips can be located outside a 15 cm radius, reducing material in the active volume and greatly simplifying the cooling. (Again, as an alternative, the wafers could be read out individually.) This disk system would contain 620 double-sided wafers and at least 7,480 readout chips.

Particularly for the disks, where the strips are not rectangular, the strip pitch must be considered carefully. Both the radial and small-angle stereo strips will have a spacing that depends linearly on radius. If standard readout chips are located at the maximum radius of 15 cm, it is natural to choose a $\approx 50\mu$ strip pitch there. The strip pitch would decrease to $\approx 30\mu$ at 9 cm radius, where wire-bonding to strips of the inner layer would occur. One straightforward scheme would be to choose the inner strip pitch to be $\approx 60\mu$ at 9 cm radius, decreasing to $\approx 20\mu$ at 3 cm. (Strips are readily manufacturable in the 20-60μ range.) Then every inner strip would be bonded to every other outer strip. The bonding pitch would be 60μ, again easily achievable. As read out, alternate strips would have a normal noise level (bonded to an inner strip) or an unusually low noise level (not bonded). Sparsification thresholds that were set for the normal-noise strips would work well also for the low-noise strips.

The DØ Si tracker is intended to be fully compatible with use of the existing SVXC readout chip, with the upgrades in radiation hardness and speed that are already planned[10] and underway for future CDF use. Conversely, the DØ Si tracker could take advantage of any benefits offered by a newly designed chip with characteristics appropriate to moderate strip lengths (5-10 cm) and risetimes ($\approx$ 200 nsec).

Preliminary work has been done on the pattern recognition for the silicon (and fiber) tracking. Fig. 3.12 shows, for a single $B^0 - \overline{B}^0$ event, a display of hits from the disk silicon (denoted crosses) and scintillating fibers (denoted diamonds) in a ϕ-z view. In this view, all tracks in a uniform solenoid are straight. The slope reflects the momentum of the track. One sees that single-view oriented pattern recognition gives a set of clearly recognizable tracks.

Matching the stereo view information in this geometry seems possible. Figure 3.13 is based on one of the tracks from Fig. 3.12 in a more than usually busy region. For that track, all of the stereo strips (angle = 50 mrad) crossing a struck radial strip which show hits are used to generate an r coordinate (by combining with the struck radial strip). The resultant candidate r coordinates are plotted vs the z of the disk. For this busy event, there are typically more than 2 candidate r-z pairs per disk; the average over a larger sample of $B^0 - \overline{B}^0$ events is 1.5 candidates. One sees from Fig. 3.13 that the correct choice of r-z pairings (a straight line) is apparent.

3.5 Outer Tracking Detector

For track detection at larger radius, we propose a scintillating fiber central detector to occupy the region $20 \leq r \leq 55$ cm. The scintillating fiber tracker will cover $|\eta| \leq 2.7$; it will measure particle momenta with good precision up to 20 GeV/c and provide a 3σ sign determination up to 60 GeV/c. The combination of good momentum and energy measurement relieves some of the need for the transition radiation detectors in the current DØ detector. We outline below a preferred design based upon solid state photomultipliers (SSPM/VLPC); R&D toward realizing these devices for high energy physics is being vigorously pursued. However, since these devices have not yet been demonstrated in experiments, we also discuss an alternative readout scheme.

3.5.1 Preferred Design

The overall layout for the scintillating fiber central tracker proposed for the DØ upgrade is shown schematically in Figure 3.1. The system is composed of 4 superlayers of scintillating fibers, spaced radially at 11.5 cm intervals beginning at 20 cm from the beam line. Each superlayer contains eight component layers: four parallel to the beam axis (x layers) and four at narrow angle stereo (2 u and 2 v layers). The fiber diameters are 750μ. The axial layers (x fibers) will have each successive component layer staggered by one quarter of a fiber diameter with respect to the previous component layer. This arrangement of x fibers will yield a high resolution measurement of the r-ϕ coordinate, and provides for the maximum possible resolution for charged tracks in a given superlayer. The stereo layers (u and v fibers) will be staggered by half of a fiber diameter. These u and v fibers will be deployed so as to measure narrow stereo angle coordinates, allowing the z-coordinate of the interaction vertex to be determined with reasonable precision.

The scintillating fibers themselves will be 2.8 meters in length, centered upon the interaction region. The scintillation light signal will be transmitted via clear polystyrene fiber waveguides from the scintillating fibers to Visible Light Photon Counters (VLPCs) (variants of the infrared sensitive Solid State Photomultiplier (SSPM) devices which were tested previously) situated outside the tracking and calorimetric volume. These VLPC/SSPM devices have high quantum efficiency (60%) at visible wavelengths as indicated in Fig. 3.14 and single photon detection capability as seen in Fig. 3.15. For effective operation, the VLPCs must be maintained at a temperature of 7K which is achieved by enclosing the devices in compact liquid helium cryostats located outside of the detector volume.

The core of the scintillating fibers will be a polystyrene-based ternary scintillator with emission in the yellow-green ($\lambda_{max} \sim 550nm$). This choice is made because light at this wavelength is transmitted with minimum attenuation in undoped polystyrene and because radiation damage to fibers that fluoresce or transmit light at this wavelength is not a big problem for the integrated luminosities expected at the Main Injector. With these choices, we expect to detect > 5 photoelectrons per fiber per minimum ionizing track. The actual performance of prototype fibers readout by VLPC/SSPM devices will be studied systematically during beam tests planned for Winter 1990-Spring 1991 at Fermilab. Table 3.6 lists the channel count for this system.

Table 3.6

Outer Tracking Dimensions

Layer no.	$< r >$ (cm)	Fiber count (VLPC)	Fiber count (MAPMT)
1	20	13400	4500
2	31.5	21100	7050
3	43	28800	9600
4	54.5	36500	12200
Total		99800	33350

The thickness of the tracker assuming 32 component layers, is $\approx 7\%$ X_0 at η =0, and $\approx 19\%$ X_0 at η =1.7. We estimate that an additional 0.3% X_0 per superlayer should be added to account for the composite material support structure. The estimated radiation lengths of material for the fiber tracker as a function of η is shown in Fig. 3.16.

We envision a scheme for fast triggering on high p_T tracks in which the hits in the outer superlayer are assumed to be associated with infinite momentum tracks. The line joining these hits is connected to the beam line in the $r - \phi$ view and compared with hits in intermediate superlayers. For example, the sagitta of a 1 GeV/c particle is 17 mm at the third superlayer so that with 750μ fibers so that its momentum can be determined to within 10% at the trigger level. This technique will be studied in the forthcoming beam tests.

3.5.2 Secondary Design

In the event that the VLPC/SSPM devices are unavailable at the time of construction, we require some alternate design for the outer tracking. We propose a fallback design based upon scintillating fibers, readout by Multi-Anode Photomultiplier Tubes (MAPMTs) operating at room temperatures.

The quantum efficiency of a typical vacuum transmission photocathode is substantially below that of the VLPC; it is down by a factor of 10 at λ= 550 nm and by a factor of 5 at 500 nm. To compensate for this loss, we must use fibers of greater diameter or mosaics of fibers of a same diameter to increase the total light collected onto the phototube. This leads to reduced resolution for momentum measurement and higher occupancy in a given layer of fiber detectors.

To take advantage of the better quantum efficiency at shorter wavelength, we require a scintillator which fluoresces at shorter wavelengths. There are several high efficiency scintillators with blue-green emission which are excellent candidates, but there is the disadvantage of a shorter attenuation length in the clear fiber waveguides which transmit the scintillation light to the phototubes. Radiation damage is not expected to be of major importance, even though the wavelength of emission is reduced.

The geometry of the fallback design is similar to the primary option except that the superlayers now contain four component layers rather than eight. Two are parallel to the beam axis (2 x layers) and two are at stereo angles of (1 u and 1 v layer). Each component is constructed of triplets of 750 μ fibers.

The core of the scintillating fibers will be a polystyrene-based ternary scintillator with emission in the blue-green to green ($\lambda_{max} \sim 480 - 500 nm$). The scintillation light signal will be transmitted via clear polystyrene fiber waveguides from the scintillating fibers to MAPMTs situated outside the tracking and calorimetric volume. These MAPMTs have typically 256 independent anodes and hence can read out 256 individual fiber triplets. With this configuration of scintillating fibers, clear optical waveguides, and MAPMTs, we expect to detect $\sim$ 3 photoelectrons per fiber triplet per minimum ionizing track. Performance of prototype fibers read out by MAPMT devices will be studied during the upcoming beam tests. The channel count for this configuration is given in Table 3.6.

3.6 Preshower Detector

The main backgrounds for electrons are charged hadron-photon overlaps, gamma conversions to electron positron pairs and charge exchange of energetic charged pions in the first few radiation lengths of the calorimeter. The present TRD fulfills the function of electron-tagger very well for electrons that are relatively isolated. We aim to reproduce this rejection for the upgraded tracking detector.

The preshower detector has two purposes. It serves as a first calorimeter sampling layer, making up for the additional dead material introduced by the superconducting coil. By having better position resolution than the calorimeter, it will allow us to distinguish showers from nearby tracks or other showers. The preradiator will thus reduce backgrounds from charged hadron-γ overlap, from conversion electron-positron pairs by detecting separated showers, and from early charge exchange, as the preradiator now acts as a first calorimeter layer with separate readout.

We may expect that the optimum thickness for the material before the preradiator is in the range of 1-2 X_0, so that it may be necessary to add some added material to the coil to increase and make more uniform the material traversed. We propose to use the same technology for the preradiator detector as for the tracking detector before the coil. The detector consists of by 3 staggered layer fiber pairs: one axial pair and 2 stereo layer pairs. The fibers are thick (1 mm diameter) to provide good light output while giving good position information. We expect resolution of about 0.5 mm in r-ϕ and 1 mm in z. The overall detector is 1.5 to 2 cm thick and could be self-supporting or fixed to the cryostat walls.

3.7 Electron Identification

For the existing DØ TRD, the measured pion rejection at 90% electron efficiency is about 55:1 (total energy likelihood). Since the upgraded tracking does not contain a TRD, we need to be assured that the electron identification performance will be adequate. We have studied the misidentification background for electrons from a study of QCD two-jet events. The primary background sources are expected from:

1. Overlaps: a low momentum charged hadron overlapping with one or more π^0's (of significant energy) in the calorimeter. Rejection can be obtained from a TRD, from matching the EM Calorimeter energy deposition with the measured momentum, or from a preshower detector of sufficient spatial resolution.
2. Early charge exchange: a charged pion can make an inelastic scatter in the early portion of the calorimeter which results in mostly energetic π^0's. Rejection can be obtained by a TRD, or to some extent, a preshower detector.
3. Internal and external conversions of energetic photons (from π^0's, η's etc.): Rejection can be made from dE/dx measurement in the tracking detector (when there is no B field) or seeing e^+e^- separately in a field when the pair is not too asymmetric. Of course the conversion point might be seen if it occurs outside the beam pipe.

A gradual transition exists between background sources 1 and 2; both are due to some rather rare type of fragmentation of QCD jets together with the chance of early charge exchange.

We generated 10,000 ISAJET QCD two-jet events with one fifth of the events in each of 5 p_T bins starting at 10 GeV/c and becoming progressively wider in order to keep adequate significance in the higher p_T range. Jets were generated in a narrow η range around zero for simplicity.

To obtain a background sample, we selected in every event those charged tracks which were isolated within a single $\Delta\eta\ \Delta\phi = 0.1 \times 0.1$ calorimeter cell, and required the energy fraction deposited in the surrounding 8 cells not to exceed 5% of the central tower's energy. In addition, charged particle isolation was required within a cone of $\Delta R < 0.15$. These tracks were then weighted by the calorimeter pion rejection (from GEANT, based on longitudinal shower profile only) of 500:1 . This weighting function is assumed to go linearly to 1 at 1 GeV for energies below 5 GeV, reflecting a guess of the decreasing pion rejection at lower energies.

A rough modelling of the rejection power of the E/p match or preshower detector is then factored in. For the E/p matching simulation, we assumed a particular tracking system, with an overall $dp_T/p_T = 8\% \times p_T + 2\%$ in a 1.5T magnetic field. Calorimeter (EM) resolution was set to $18\%/\sqrt{E}$. An E/p cut at 3σ was made to satisfy the energy-momentum match. The preshower rejection was done by calculating the conversion probability for each π^0, and if a conversion occurred (a random drawing according to the conversion probability) rejecting the event if the conversion shower occurs more than 3σ away from the charged track impact point. The combined resolution σ of the tracking and preshower detector is assumed to be 1 mm. The thickness of the radiator was taken as $2X_0$.

In Fig. 3.17 we show the distribution of the background, before any cuts and after preshower detector and E/p cuts. We see that an E/p match together with a preshower detector will do as well as the TRD, and that the magnetic field and preshower contribute about equally to the rejection. Some care should be taken with these conclusions, however, until a full simulation is done.

Chapter 3 References

1. G. Dugan "Tevatron Collider: Status and Prospects", Fermilab-CONF-89/182, Aug 1989, 14th Int. Conf. on High Energy Accelerators, Tsukuba, Japan.
2. A. B. Oliva, et.al., " ZEUS Magnet Tests" Proceedings of Magnet Technology Conference- 11 [1989], Japan, to be published.
3. R. Fast et.al, "Design Report for an Indirectly Cooled 3-m Diameter Superconducting Solenoid for the Fermilab Collider Detector Facility", FNAL (1982).

4 H. Schellman, private communication

5 D. Amidei, presented at Snowmass 1990.

6 J. Hylen *et. al.*, Santa Cruz Institute for Particle Physics preprint no. SCIPP 90/24 (September 1990).

7 Planned for HERA are Si disks for tagging small angle tracks, in which the strips are mainly azimuthal (at constant radius).

8 H. Spieler, presented at Snowmass 1990.

9. J. Ellison, private communication.

10 S. Kleinfelder and R. Yarema, private communications.

11. F. Abe *et. al.*, Phys. Rev. Letters 64, 157 (1990).

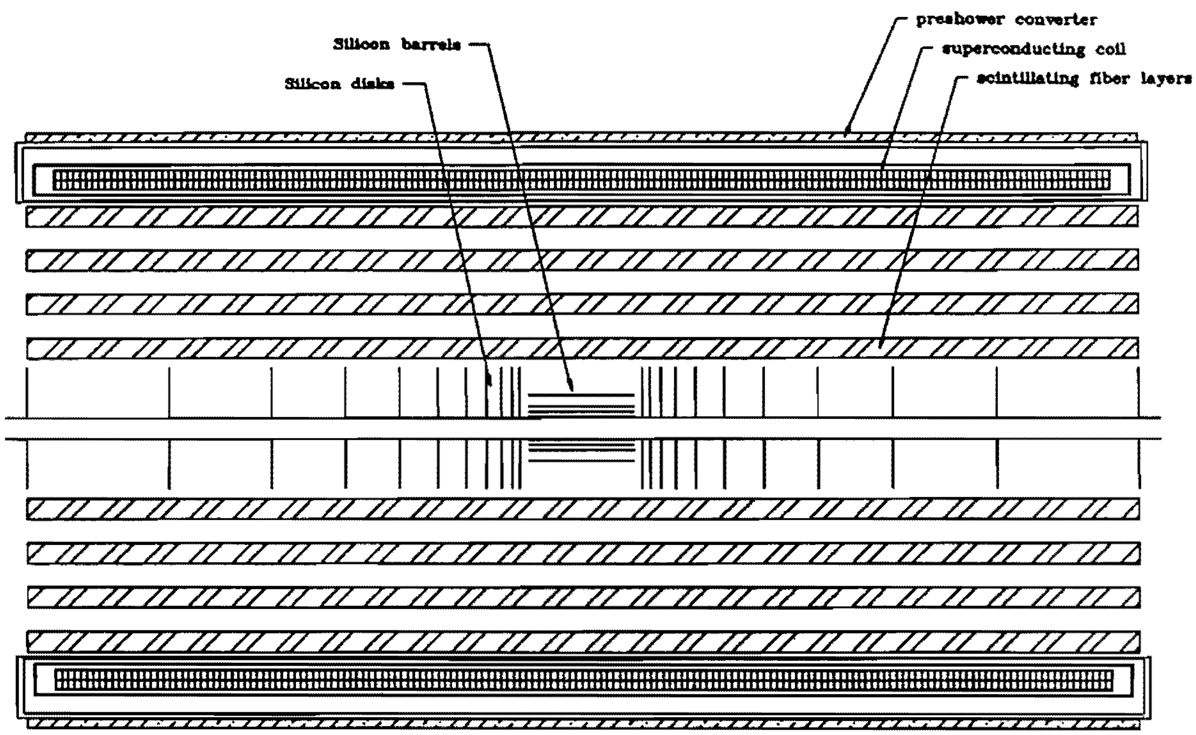

Figure 3.1 Overall Layout of Upgrade Tracking.

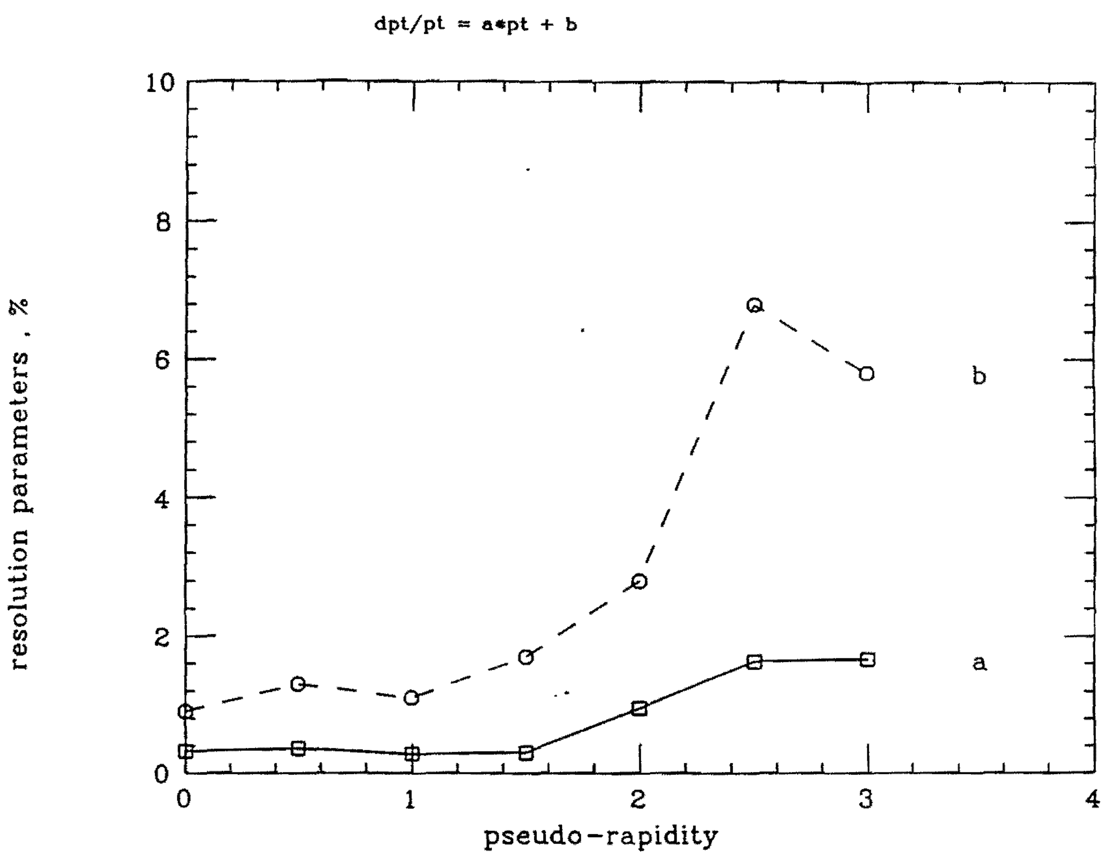

Figure 3.2 **Variation of the resolution term (*a*) and multiple scattering term (*b*) of the transverse momentum resolution as a function of eta.**

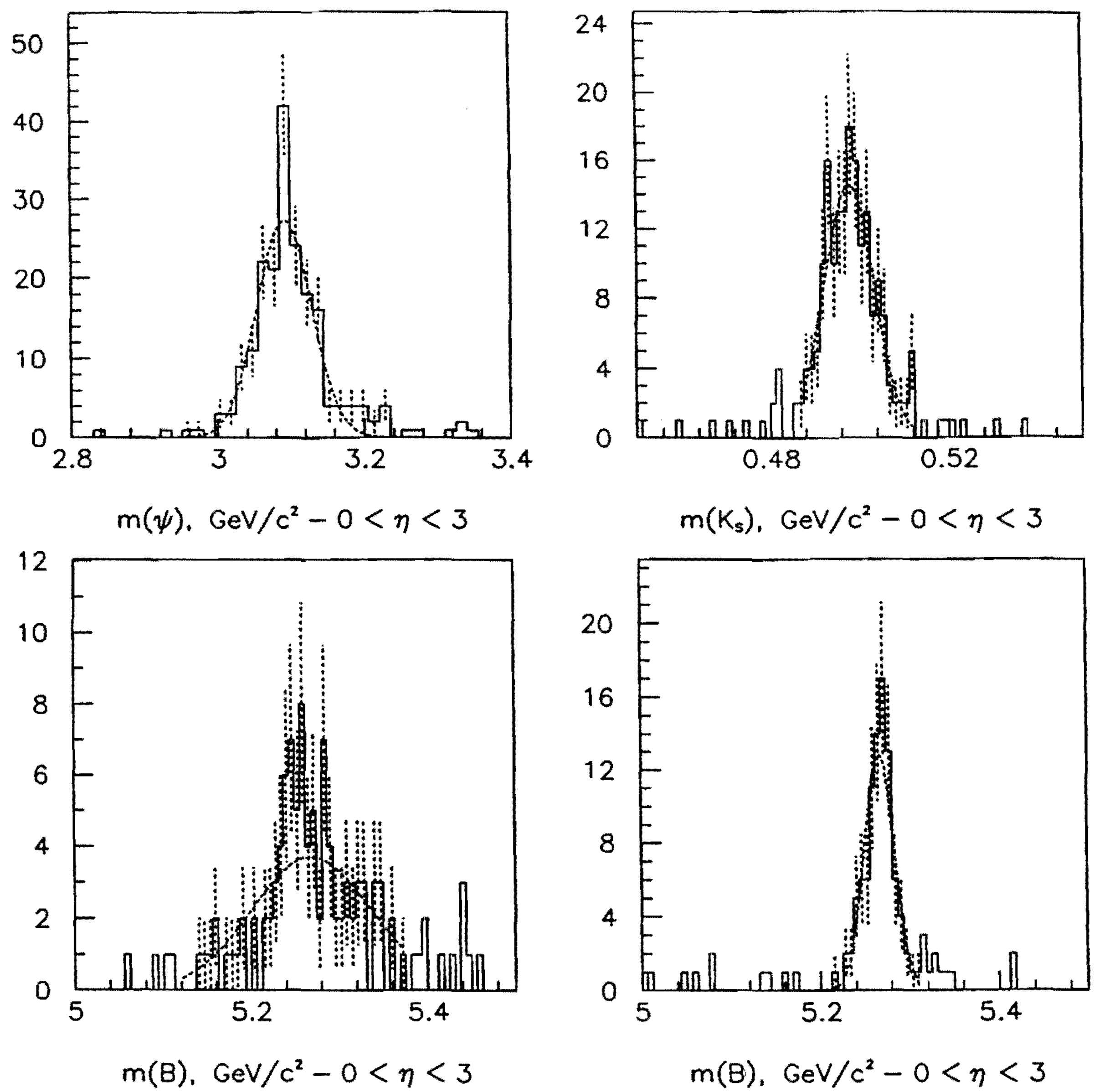

Figure 3.3 Simulation of mass resolutions in 1.5T field. a) ψ Mass Peak in B$\rightarrow$ ψ- K_S b) Kaon Mass Peak in B$\rightarrow$ ψ- K_S c) Unconstrained B Mass Peak in B$\rightarrow$ ψ- K_S d) Constrained Mass Peak in B$\rightarrow$ ψ- K_S

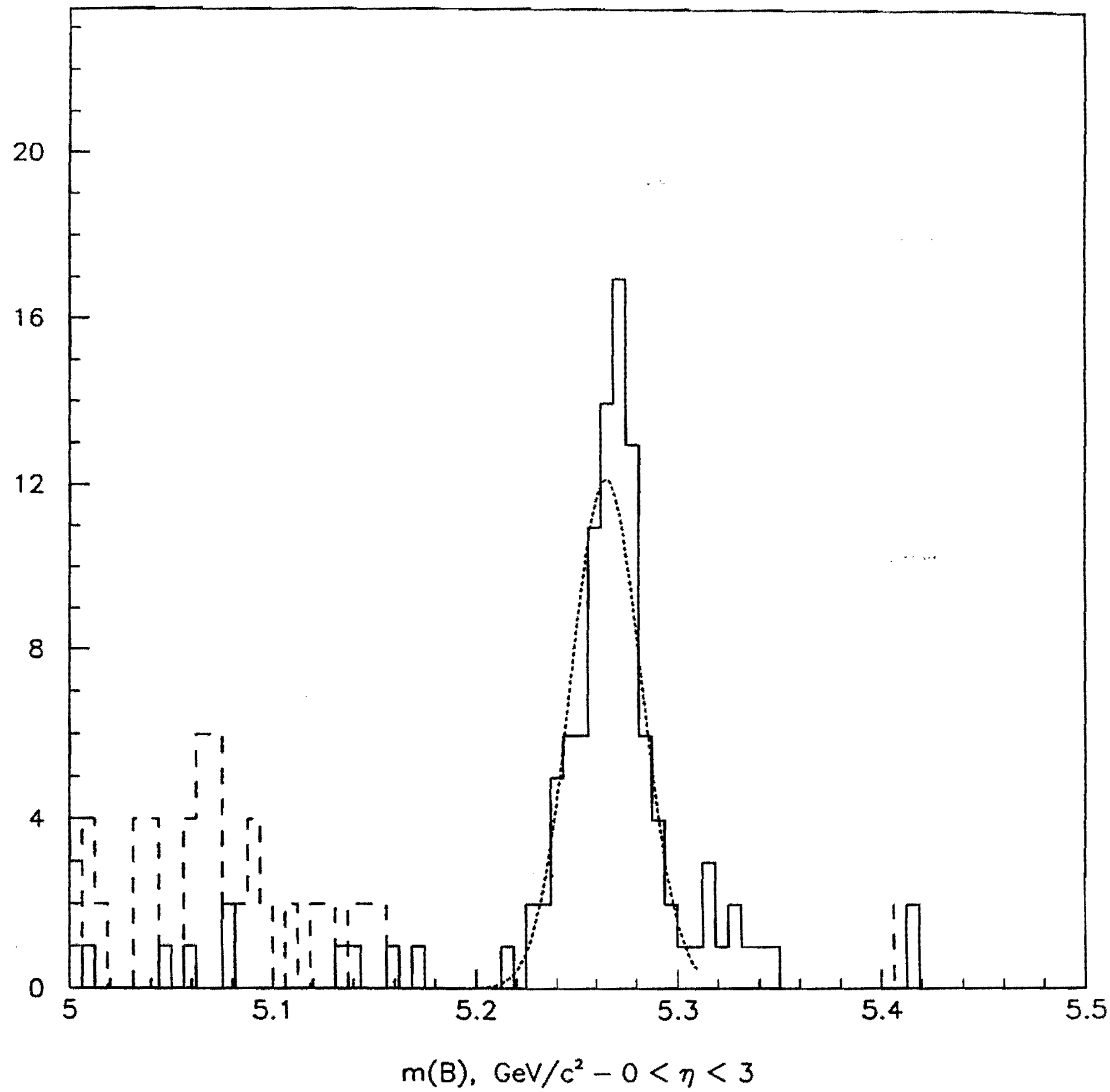

Figure 3.4 Mass distributions for the ψ K_S system from B^0 decays to ψ $K^* \rightarrow \psi$ $K_S\pi^0$ (dashed) and to ψ K_S (solid). Events are weighted appropriately to production ratios and decay fractions.

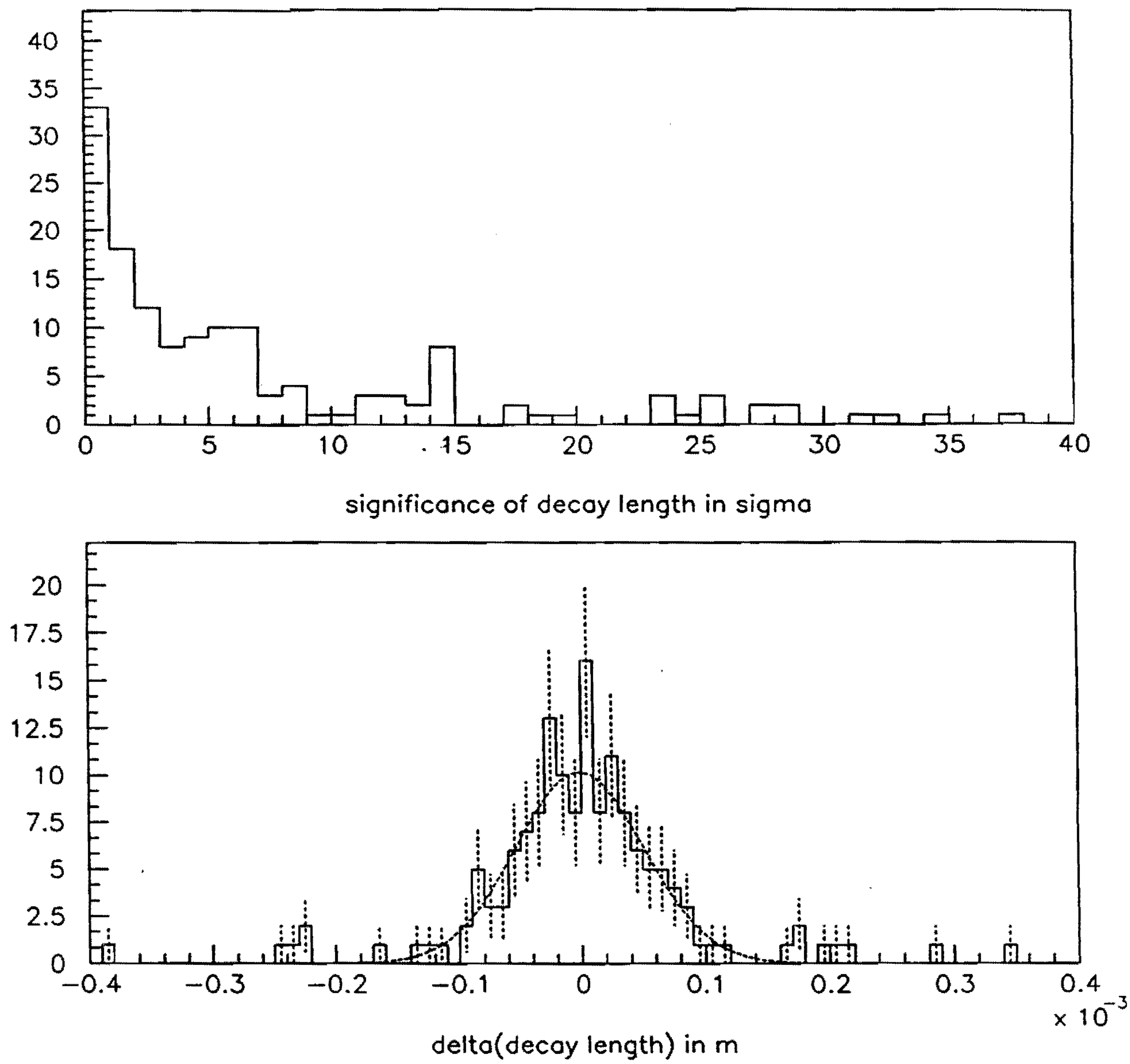

Figure 3.5 (a) Distribution of the significance of the B decay length measurement (in numbers of standard deviations); (b) difference in measured and true decay lengths.

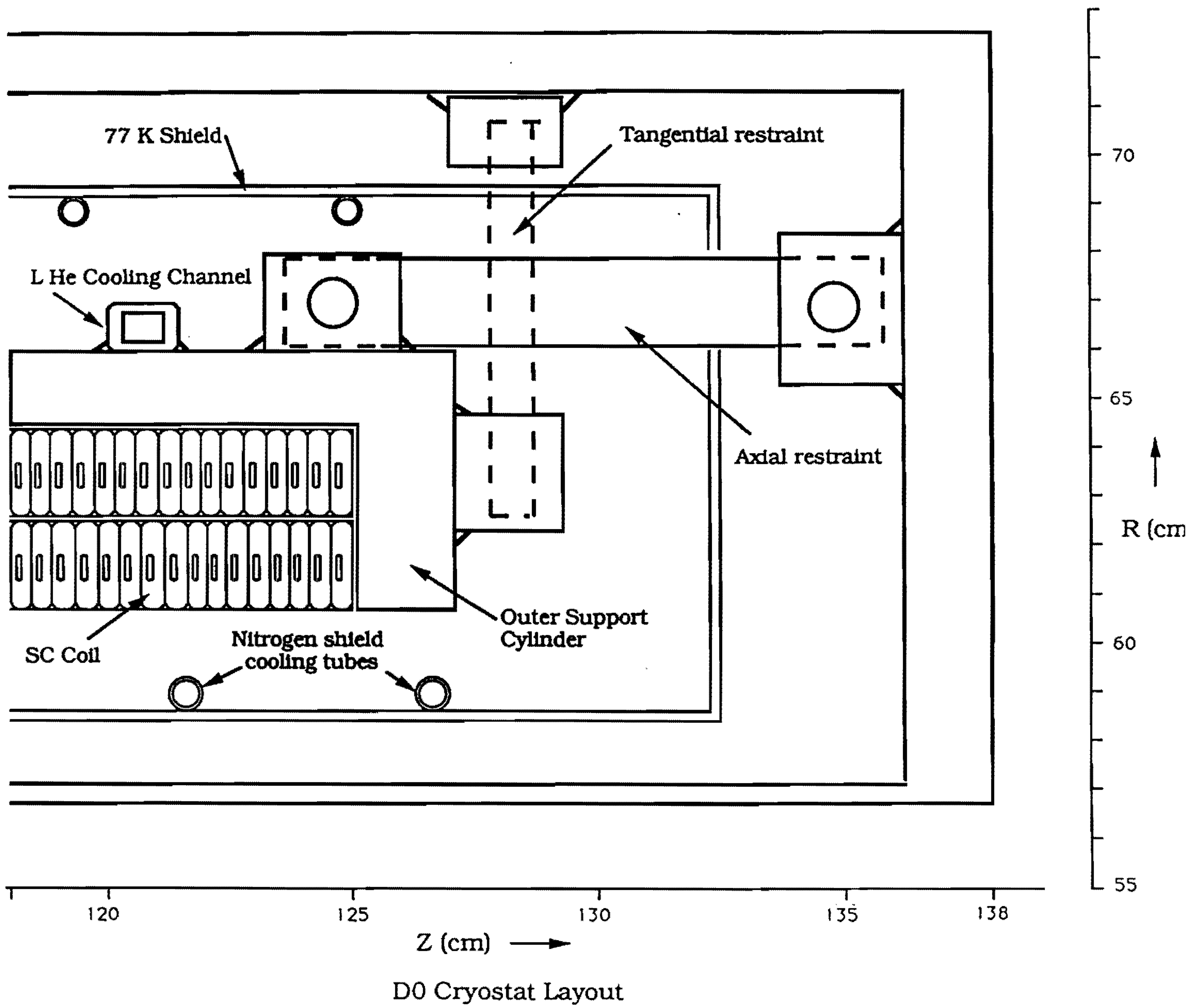

Figure 3.6 Cross-section of superconducting coil and cryostat.

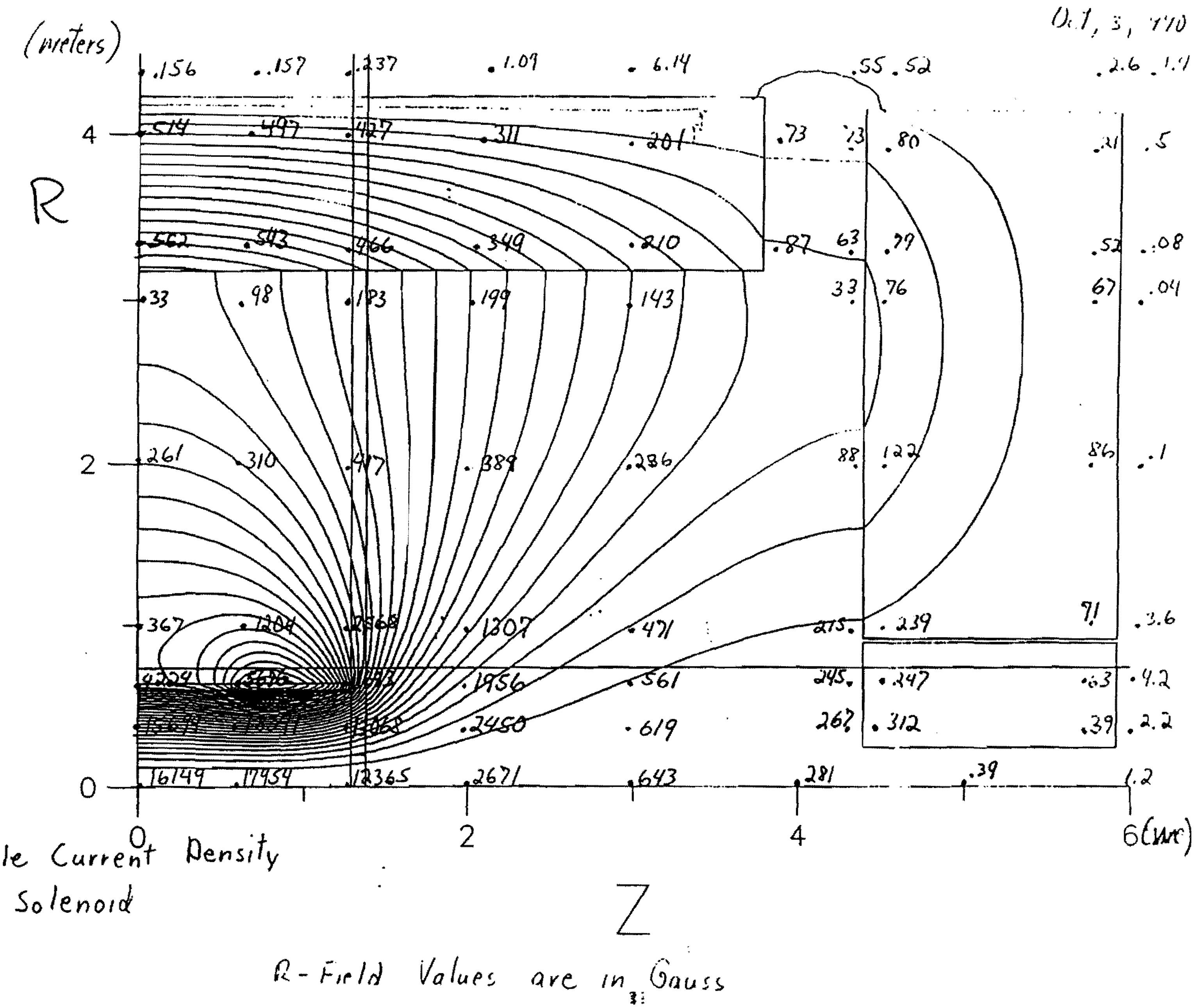

Figure 3.7 Field strength for proposed solenoid superimposed upon the outline of the DØ Detector.

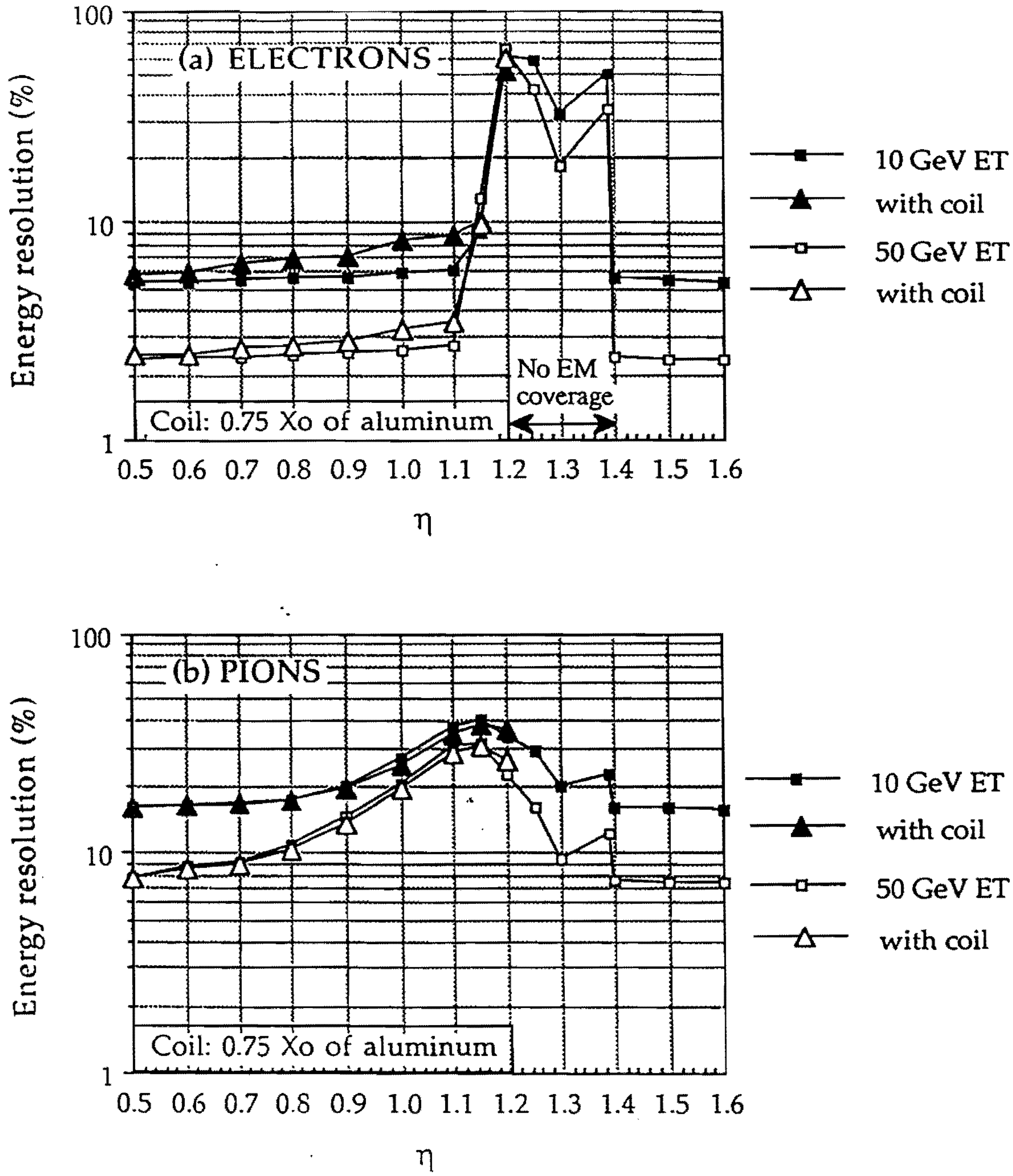

Figure 3.8 Fractional energy resolution for E_T= 10 and 50 GeV electrons and pions with and without a 0.75 X_0 aluminum coil before the calorimeter, taken from a GEANT simulation.

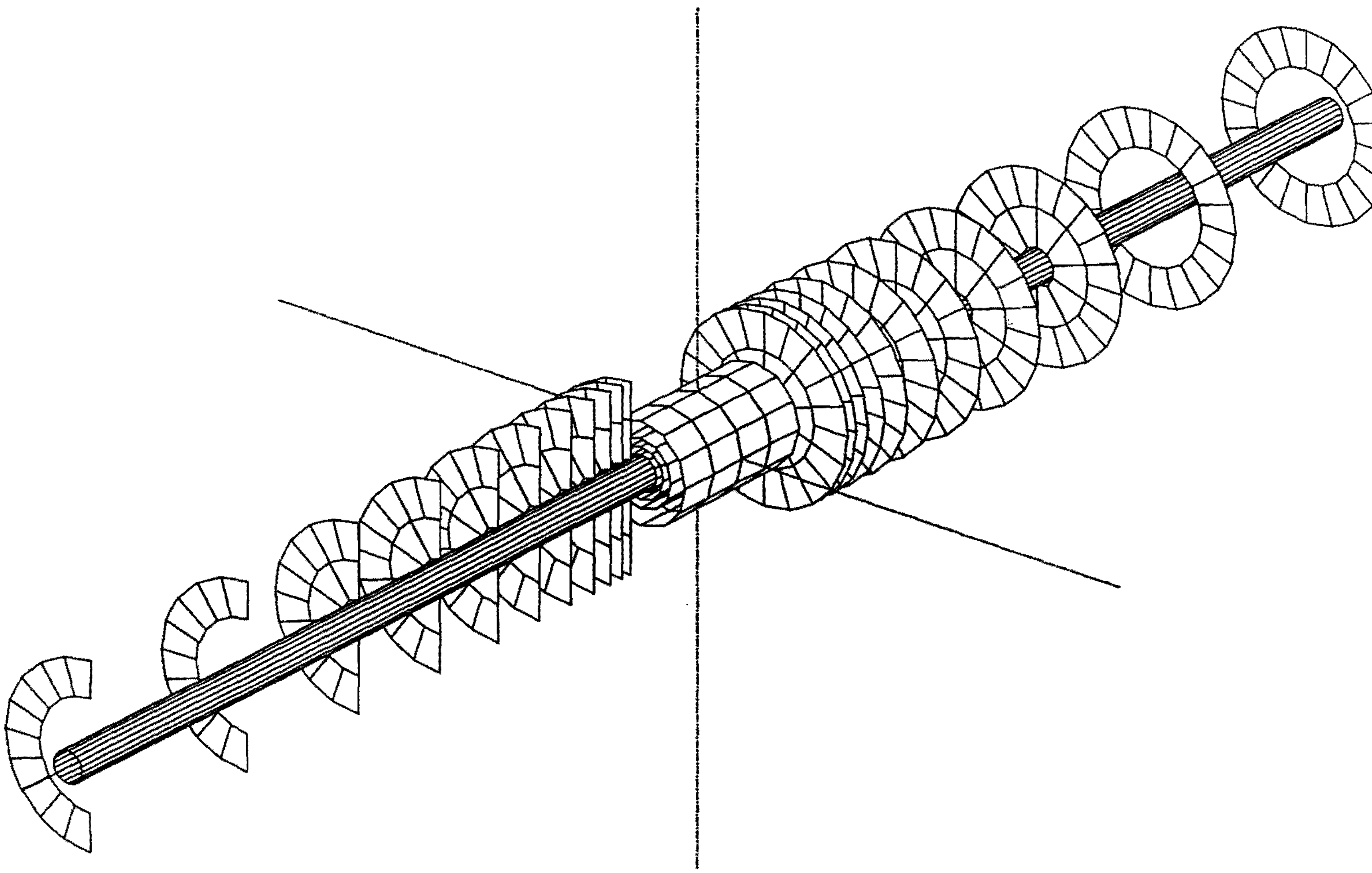

Figure 3.9 Layout of silicon barrels and disks

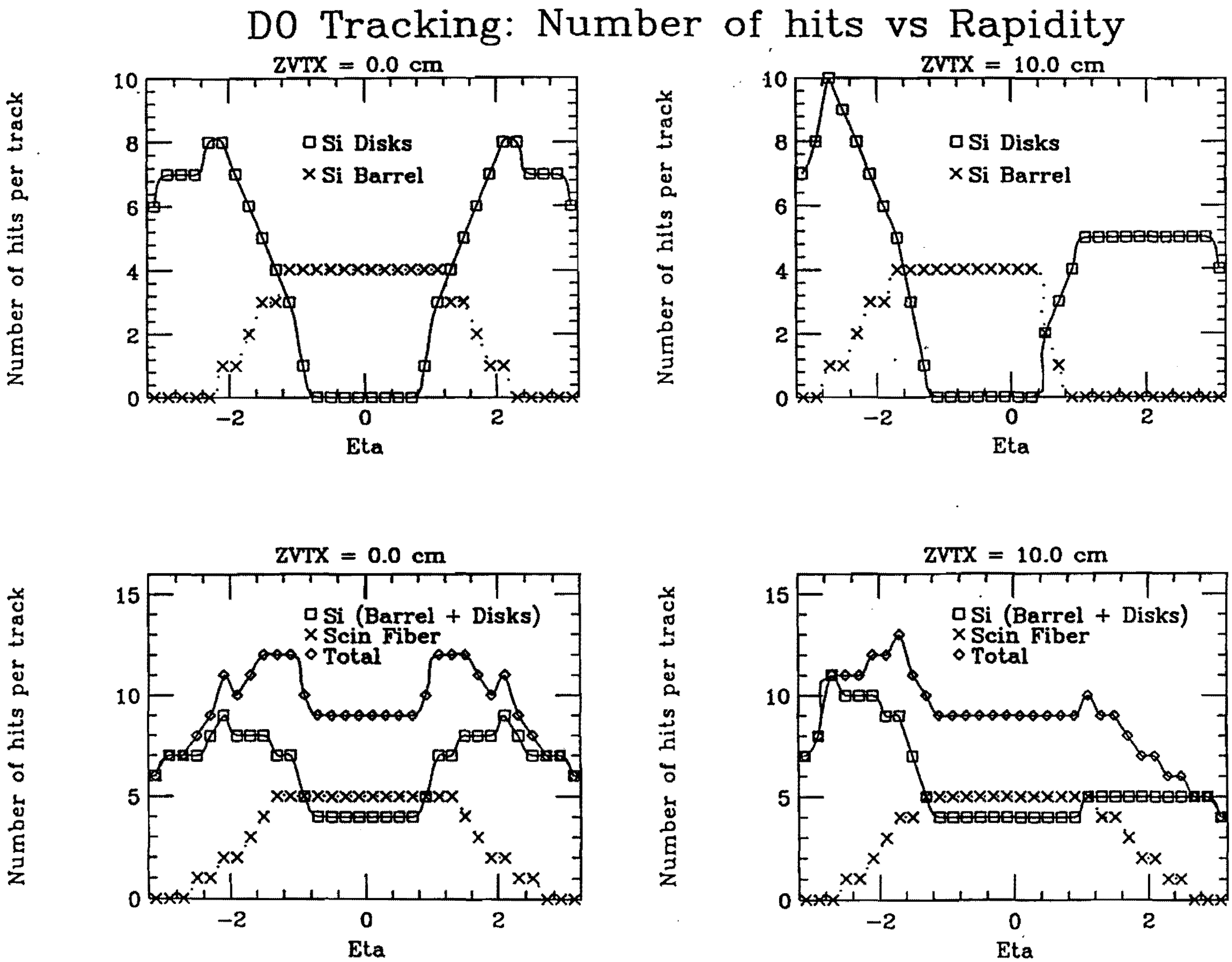

Figure 3.10 The number of hits per track for various track angles and interaction points.

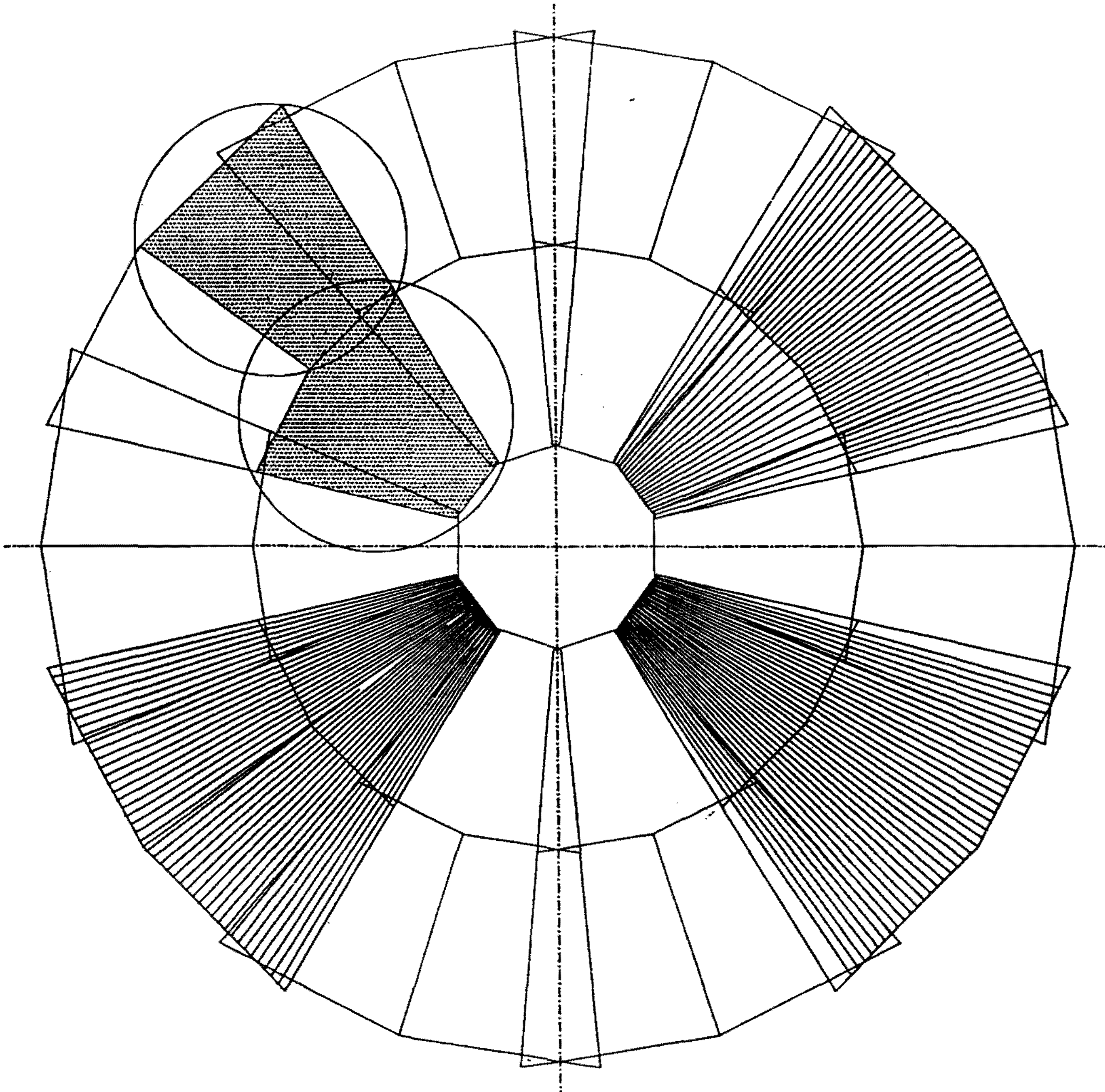

Figure 3.11 The layout of disk wafers. The significance of the four detailed sections is discussed in the text.

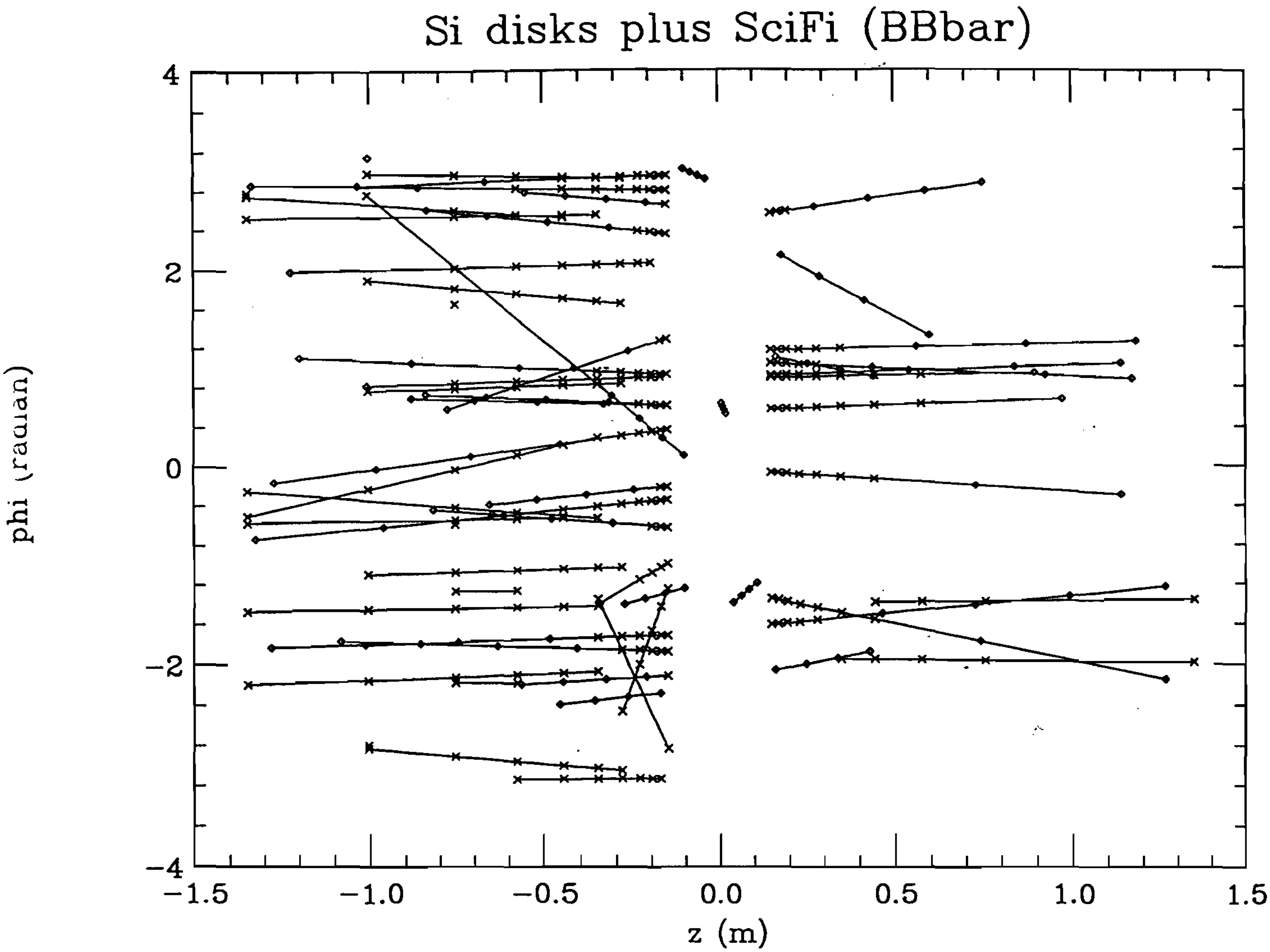

Figure 3.12 A single event display in the ϕ-z view for silicon disks ($\times$) and scintillating fibers (diamonds). Tracks in this view are expected to be straight lines in a pure solenoidal field, with slope dependent on momentum.

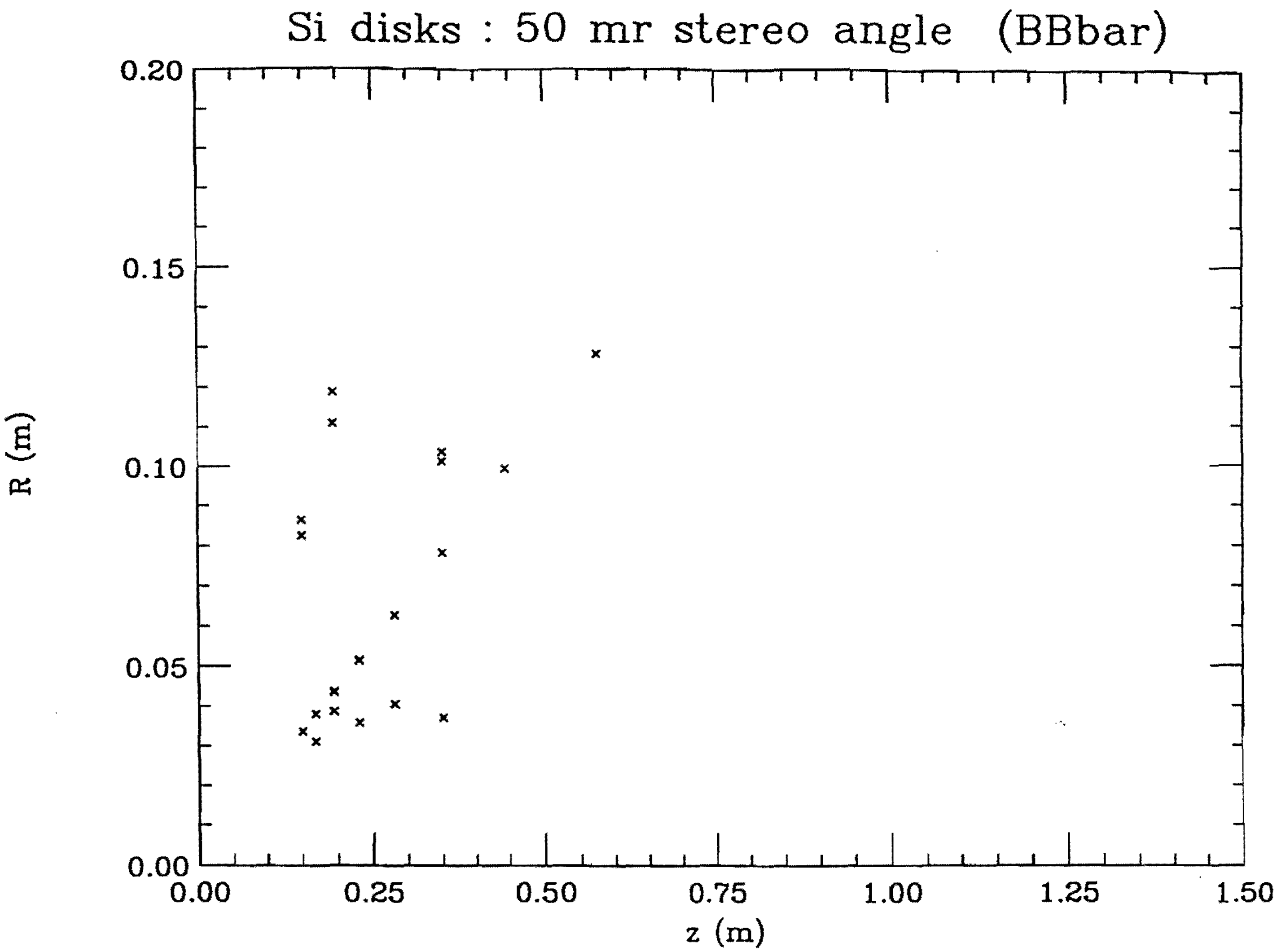

Figure 3.13 The r-z candidate points from all radial strip and stereo strip combinations for a single track in Fig. 3.12. The correct combination forming a straight line in this view is apparent.

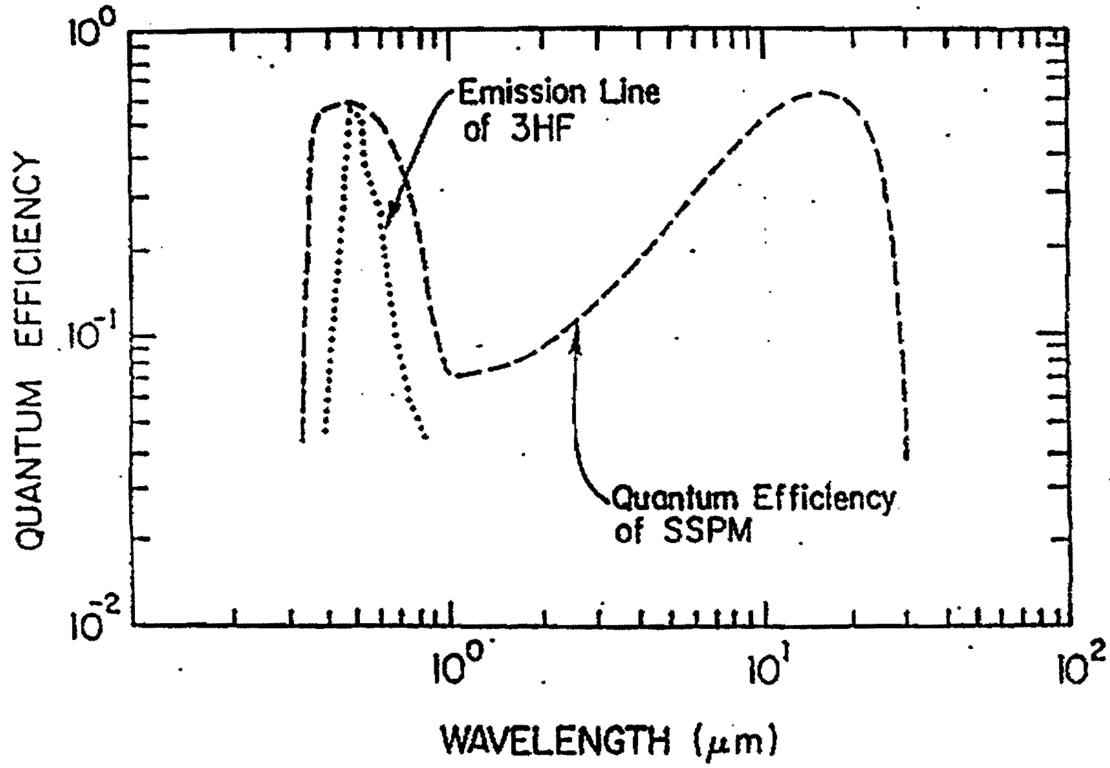

Figure 3.14 Quantum efficiency of SSPM devices as a function of wavelength.

(a)

(b)

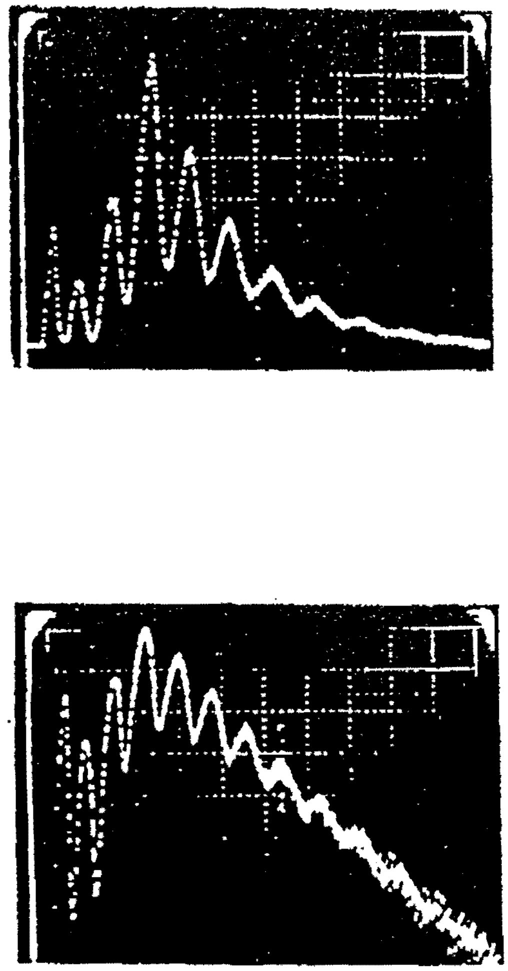

Figure 3.15 Pulse height spectra from a 0.5 mm scintillating fiber in a $625\mu\times 625\mu$ SSPM on a (a) linear and (b) logarithmic scale.

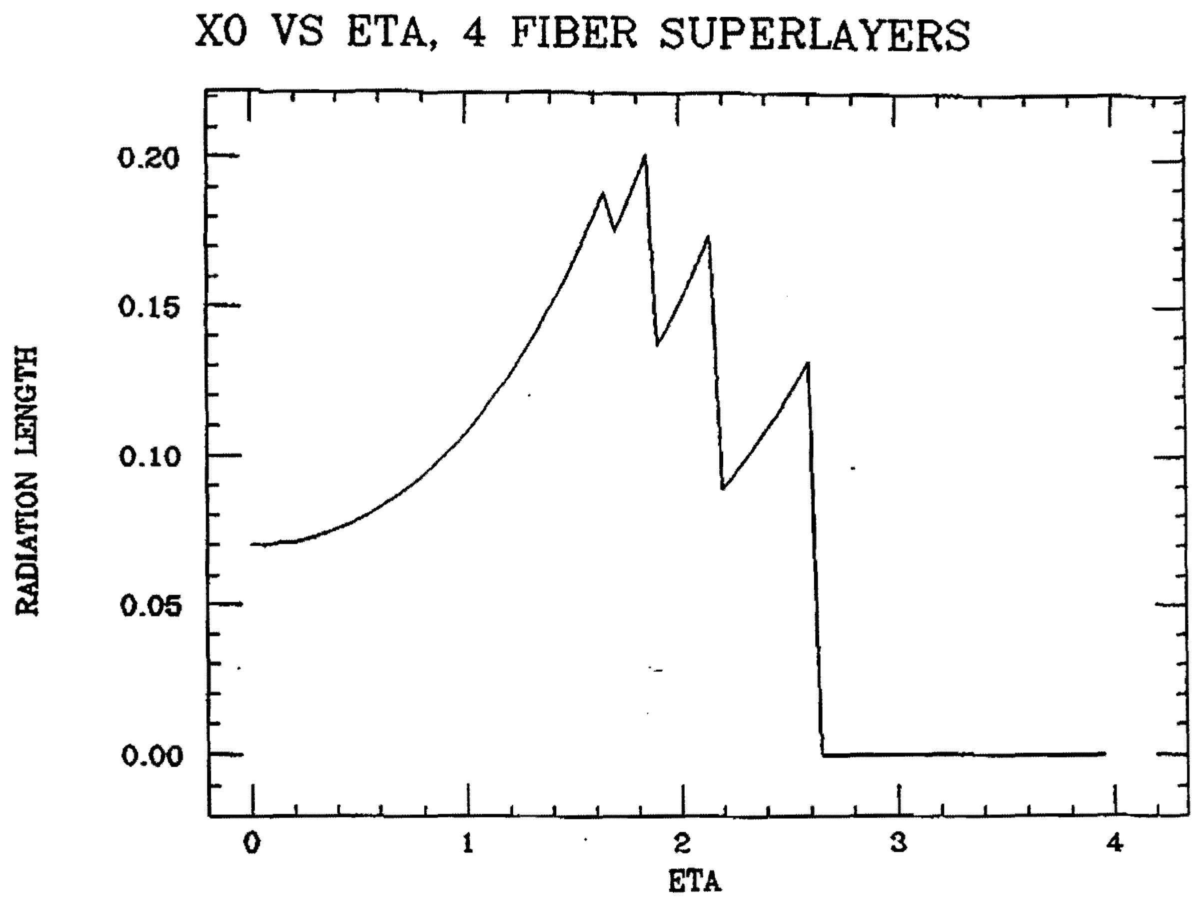

Figure 3.16 Estimated radiation lengths of material for the stand-alone fiber tracker as a function of pseudorapidity.

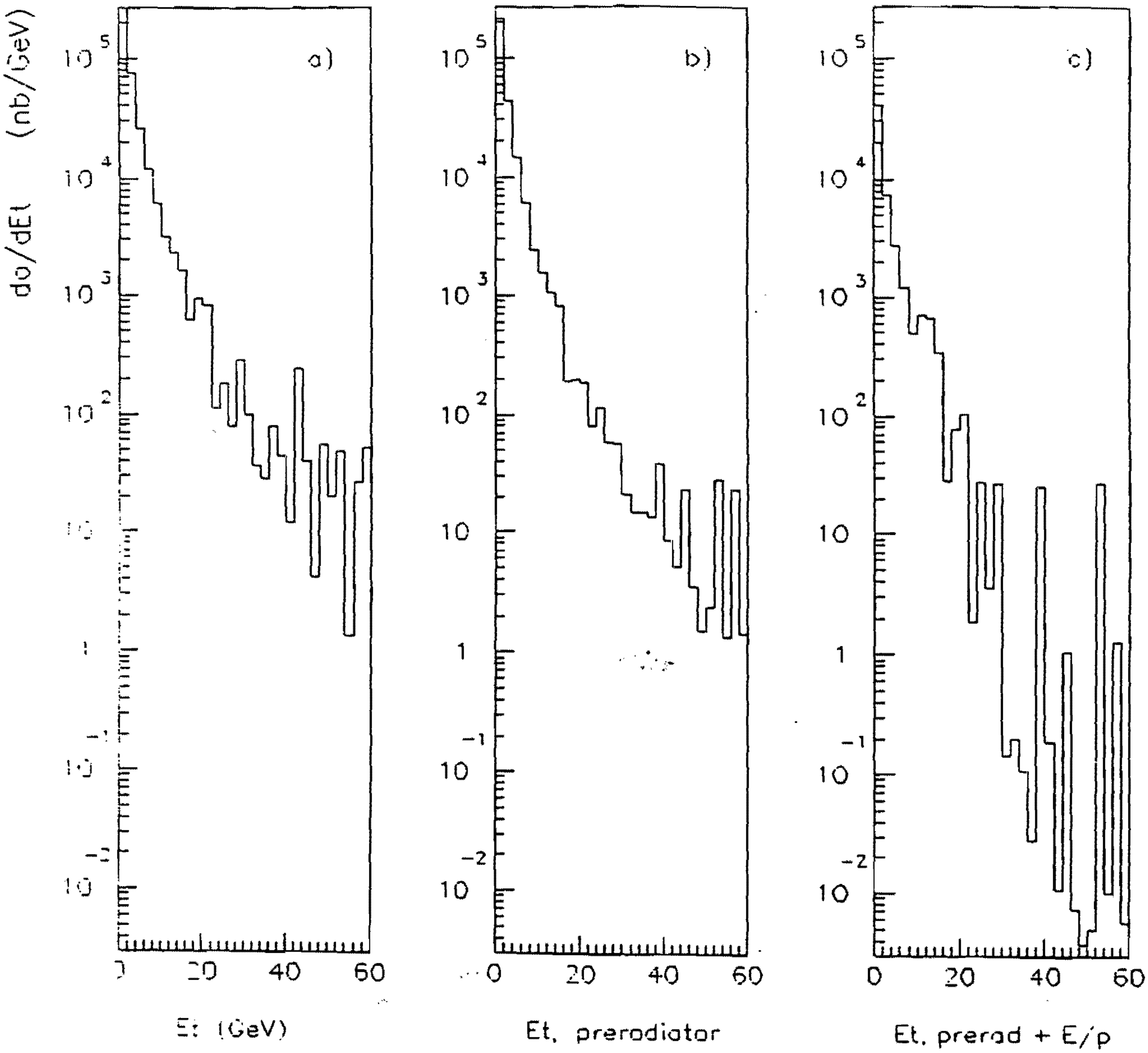

Figure 3.17 (a) p_T distributions for the full background (b) with preshower requirement only and (c) with preshower and E/p requirement.

4. Calorimeter and Inter–Cryostat Detector Upgrades

In this section we summarize[1] the planned upgrades for the DØ calorimeters and inter–cryostat detector (ICD). We note that the mechanical structure of the DØ calorimeters will *not* be changed in any of the upgrades. The maximum drift time in the liquid argon is of order 450 ns and is thus fairly well matched to the beam crossing times planned for the 1995 run. We will have to change the calorimeter shaping electronics which were designed for 3.5μs beam crossing times and luminosities of $10^{30} cm^{-2}s^{-1}$.

The ICD's are scintillators designed to measure energy deposited in the region between the central and endcap calorimeter cryostats. They are read out at present by phototubes. The addition of a magnetic field will require that the readout for the ICD be changed.

4.1 Calorimeter Electronics Upgrade

With the large increase in luminosity and the decrease in bunch time interval at the upgraded Tevatron, the DØ calorimeter will see a marked increase in the energy deposited from unwanted collisions close in time to a triggered event. This contribution is called 'pile-up' noise in the following and is an additive to other sources of noise in the calorimeters. We propose modifications to the calorimeter electronics to better achieve an overall noise minimization. The basic change is the reduction of the time interval between 'before' and 'after' sampling of the charge in a cell.

Since a ground-up redesign of the calorimeter and its readout is out of the question, we have assumed that everything within the cryostat remains unchanged and hence the first stage of electronics must be located outside the cryostat (in its present location). In order to implement an upgrade of the $\approx 50,000$ calorimeter electronics channels in a timely manner, we have opted for redesign in order to preserve as much as possible of the existing system. Ideally that would mean replacement or modification of only: (1) preamp hybrids, (2) preamp power supplies, (3) baseline subtracter (BLS) hybrids, (4) BLS power supplies, and (5) calibration pulser system.

The three main subsystems of the present calorimeter electronics[2] are the charge-sensitive preamplifiers (mounted on the outer cryostat shells), the baseline-subtractors which shape and multiplex the signals (mounted beneath the detector) and the digitizers (mounted in the moving counting house). One of the difficulties in implementing the minimal changes may be the impossibility of maintaining the same size footprint for both the preamp and BLS hybrids. A different size or a different pinout may require the design and construction of new motherboards for both those types of hybrids.

We have recently concluded a large scale ($\approx$ 5000 channels) test of the calorimeter electronics which has given valuable data on the system performance. Over the three month running period, few failures were observed (*e.g.* 2 preamp hybrids, 4 sample and hold hybrids, 7 analog drivers). Since infant mortality and unstable conditions exacerbated the problems, we extrapolate to very acceptable performance in DØ. Measurements have shown[3] for the intrinsic electronics noise $\sigma_{elect} = (2000 + 3100 \times C_D(\text{in nF}))$ electrons which is well within our specifications. Coherent noise was measured[4] at about 150 electrons per channel. Temperature coefficients for the front-end amplifiers are[5] about -0.1% $/°C$; we expect temperature stability in preamp enclosures to within 1 $°C$. No cross-talk has been seen in the standard readout path for signals, though a few percent cross-talk has been observed in the higher bandwidth trigger path. This effect will be studied further, but is not expected to give a problem for the upgraded electronics.

The proposed changes for the upgraded detector are all in either the preamplifier or BLS circuits. The fundamental change is the reduction (from about $\sim 2\mu s$ to 0.5 μs) of the sampling time interval at the BLS between the 'before' and 'after' crossing to make the contribution from pile-up noise less. This change then dictates changes in the preamplifier and the power supplies for both BLS and preamp. Table 4.1 summarizes the main changes; more detail follows below.

Table 4.1

Changes to Present Electronics

Feature	Present Value	Proposed Change
Preamp		
Input FET	$g_m = 40$mS	$g_m > 80$mS (2 FETs)
Power rail	± 6 volts	$+12, -6$ volts
Current	20mA	32mA
Output Driver	none	115Ω cable driver
BLS		
Shaping time	2μs	0.5μs
Filtering	Double sample	Unipolar (Sallen-Key)
Filter design	Op amps	Discrete transistor
Power rail	$+13, -5$ volts	± 12 volts
Current	$\approx$ 20mA	$\approx$ 30mA

Preamp

We propose a new preamplifier hybrid circuit in which there are two basic changes. The first is that the input will have two N-channel Toshiba 2SK369 JFET's instead of the present single FET. The higher g_m of the parallel FET's has been measured to provide an improvement of $\sqrt{2} = 1.4$ in the electronic noise slope. The improved noise performance will help to offset the increase in noise expected from going to shorter shaping times. A simpler solution to replace the present Toshiba FET with lower noise, higher transconductance FETs has been shelved due to the large cost, but will be kept as an option.

The second change is a driver stage which has been added to drive a terminated twisted pair line. This is necessitated by the higher bandwidth requirements of the shorter shaping times. The penalty for these improvements is an increase in power consumption of over a factor of two.

No new technology is required for these changes. We are confident that such a design can be implemented in the same footprint package with the same pinout. At present we have a surface mount prototype version that is only somewhat larger than our present preamp. Maintaining the same size and pinout translates of course into both money and manpower savings.

Preamp Power Supplies

We expect that more power will be needed because of the change from one to two FET's, and because of the addition of an output cable driver stage. In the proposed design the current requirements would increase by $\times 1.5$ to a little over 30mA, and the upper voltage rail would increase from +6V to +12V to allow for similar output voltage swings into a terminated line. At present, there are redundant power supplies for the preamps (due to their inaccessibility), so that a factor of two in power is readily available at the expense of redundancy.

BLS

The major changes to the calorimeter electronics come in the BLS (Sample and Hold) system, where the signal shaping is done. In the present design, some is done in the front end before the double sample is taken. By going to $0.5\mu s$ (from the present $2\mu s$) shaping time, we must increase the bandwidth of the input amplifier. At present, we do not know of any low-power monolithic solution, and have thus opted for discrete component shaping circuitry at the front end. We will also add an $\approx 2\mu s$ analog delay line following the receiver and trigger pickoff amplifiers. This delay line is present because the trigger signal is expected to be available after $1.6\mu s$, significantly longer than the 400ns bunch crossing time. Following the delay line is a unipolar $0.5\mu s$ shaping circuit, implemented by means of a Sallen-Key filter.[6] After shaping, the design follows the existing design, where we now propose to sample the baseline until such time as a trigger is received (this is now possible because all signals are delayed to wait for the trigger). On receipt of a trigger, the baseline would be held, and the peak of the filter output sampled. By retaining the baseline sampling, we greatly reduce the pile-up due to the small sinusoidal tails of the unipolar shaping. Maintaining the same footprint and pinout as the existing system is more complicated than in the preamp case, because many more components must be added. We are presently studying the feasibility of maintaining the same physical dimensions.

BLS Power Supplies

Again the need for higher bandwidth forces us to pay the price in power consumption and voltage level. With the proposed BLS design, we estimate that the current requirements will increase by about 50% from about 20 mA to about 30mA per BLS channel. The negative power rail would also need to be changed to -12V from the present -5V. It is probable that such a change would only require modification of the existing supplies, but that is presently under investigation.

Expected Performance

We have built prototypes of the new preamp design which have demonstrated a factor of 3 reduction in risetime at full detector capacitance. We are presently in the process of laying out a new BLS design. We have also ordered a series of delay lines from a variety of manufacturers in order to evaluate the delay line properties. However, we have individually tested multiple FET input preamps and have indeed verified the expected $1/\sqrt{N_{FET}}$ dependence of the electronic noise contribution. The three contributors to total stochastic noise (electronic, uranium decays, and pileup) scale with shaping time, τ, and $\mathcal{L}$ as follows: σ(Electronic)$\sim 1/\sqrt{\tau}$; σ(Uranium)$\sim \sqrt{\tau}$; and σ(Pileup)$\sim \sqrt{\tau\mathcal{L}}$.

The estimated effect of these contributions is given in Table 4.2.

Table 4.2

Noise in MeV as a Function of Luminosity

Luminosity	$\tau=2\mu s$ 1 FET			
($cm^{-2}sec^{-1}$)	σ_E	σ_U	σ_P	σ_{TOT}
1×10^{31}	50	100	67	130
1×10^{32}	50	100	211	240
Luminosity	$\tau=0.5\ \mu s$ 2 FET's			
($cm^{-2}sec^{-1}$)	σ_E	σ_U	σ_P	σ_{TOT}
1×10^{31}	71	50	34	93
1×10^{32}	71	50	106	137

These values represent only the average contributions to the noise. A study of what new physics might be "created" due to pile-up effects is underway.

We have also calculated (with SPICE) the effect of the detector capacitance ranges. The shorter shaping time makes one more sensitive to these differences. The shift in the shaped peak signal is about 125ns as can be seen in Fig. 4.1. We expect that there will be several different shaping circuits required to make the shaped signal peak at the same time.

Electron/Pion Response

One might worry that reduction in shaping time could adversely affect compensation; generally a shorter shaping time would lead to an increased e/π ratio due to decreased collection of charge from hadrons. Recent indications from Monte Carlo calculations suggest that the problem is not severe. Figure 4.2 shows results on compensation from the 1987 DØ calorimeter test beam[2] together with a detailed simulation[7] of the e/π expected for 50 ns and 250 ns integration times at 25 GeV. The simulation (by Alsmiller et al.) uses the CALOR89 nuclear physics code package. This work is still in progress and the actual DØ data (2300 ns integration time) have not yet been simulated, but if we assume that the CALOR89 result would be similar to the D0 data, then going to even a 250 ns integration time would degrade the e/π at 25 GeV from 1.03 to no more than 1.07. Thus there should be no problem with the situation foreseen for the upgrade.

4.2 Inter–Cryostat Detector Readout Upgrade

We are considering two options to allow the ICD photomultipliers to be compatible with the DØ magnetic field. We expect that the 1.5T solenoid will produce between 200 and 500 gauss at the site of these PM tubes. The first and simpler option is to add passive or active (bucking coils) magnetic shielding to the existing PM's. In this case the full system of scintillator, fiber readouts and mechanical housing could be retained intact.

If shielding is not viable, then the PM's must be removed from the ICD boxes and moved to a lower field region. The most likely position for them would then be between the central and end toroids. This option will require using new wavelength shifting fibers so that the terminal fluorescence from the tile/fiber system will be shifted to lower wavelength. This will allow for adequate light transmission in the clear fiber bundles that will couple the light from the waveshifting fibers to the PMT's. This distance can be as large as 3 to 4 meters. Although the current scintillator tiles could be reused by machining out the old wavelength shifting fiber, the better solution would be to start with new scintillator. New ICD boxes will be required in order to allow for a modified geometry that incorporates the clear fiber bundles.

Chapter 4 References

1. See "Calorimeter and ICD Upgrade", DØ Note # 1038, F. Borcherding et.al. (10/90) for a more complete description and circuit schematics.
2. M. Abolins et al., NIM 280, 36 (1989).
3. P. Franzini, NIM A289, 438 (1990); R.D. Schamberger, *Proceedings of the 2nd International Conference on Advanced Technology and Particle Physics*, Como, Italy, 11-15 June, 1990 (to be published in Nucl. Phys. B Proceedings Supplements Section), also DØ note 1026.
4. P. Franzini, DØ note 623 (1987).
5. L. Rasmussen, presented at the DØ upgrade workshop, Fermilab, August 17-18, 1990.
6. P. Franzini, DØ note 982 (1990).
7. G.S. Abrams et al., Progress report on Work Done in FY90 and Request for FY91 funding for R& D of a Liquid Argon Calorimeter for the SSC, Sept. 1990.

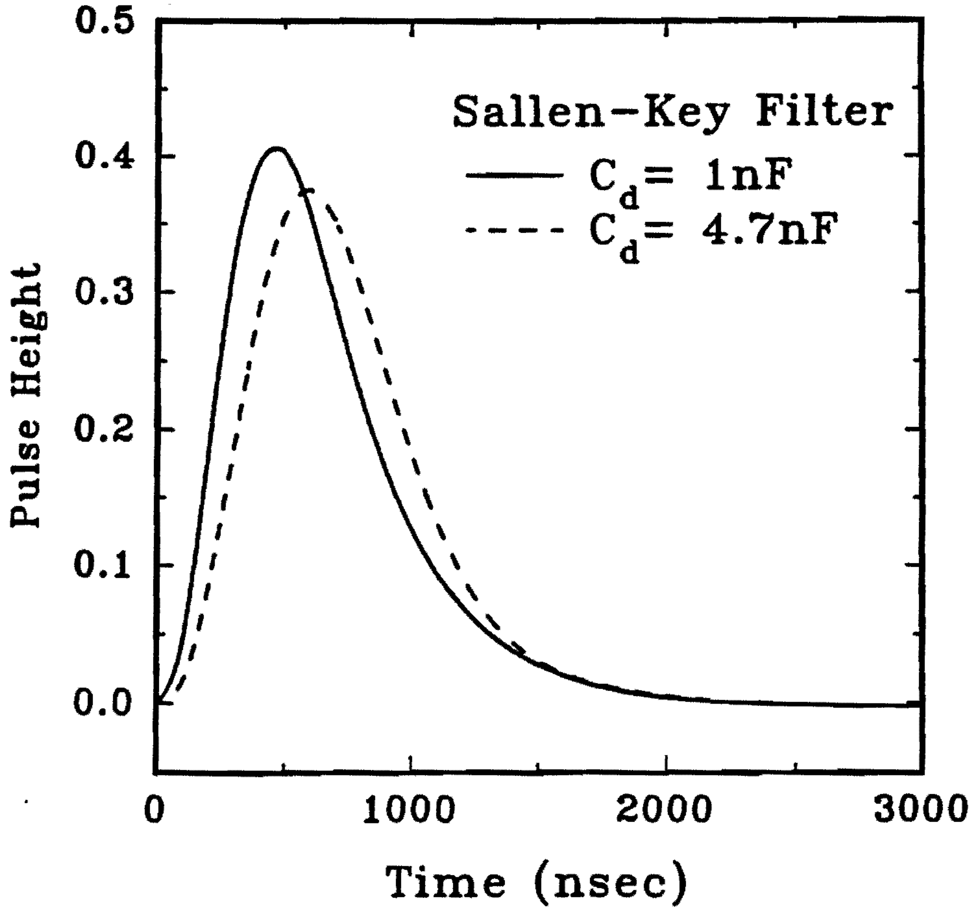

Figure 4.1 SPICE calculation for detector capacitances of 1nF and 4.7nF which span the range of DØ capacitances.

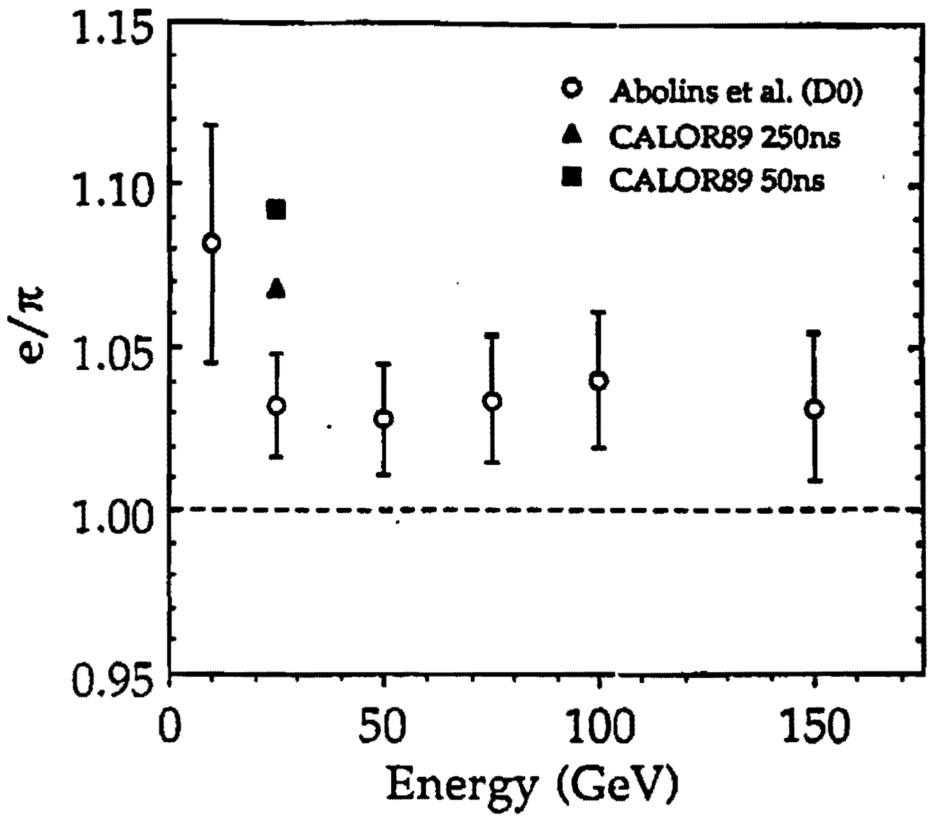

Figure 4.2 e/π as a function of energy for several integration times.

5. Muon System Upgrades

5.1 Introduction

Muon tracks are recorded in sets of chambers before and after magnetized iron toroids. There are typically three layers of muon chambers, one located just outside of the calorimeter and inside the toroids (the A layer) and the other two outside the toroids (the B and C layers). Angles larger than $\sim 10°$ are covered by the Wide Angle MUon System or WAMUS. WAMUS has 4 planes (called 'decks') of proportional drift tubes (PDT's) in the A layer just inside the toroids. The B and C layers are separated by about $1m$ outside the magnets, and each has 3 decks. The WAMUS PDT cells (5 cm half-cell width) have a drift time of just over 1 μs with the Ar/CO_2 gas to be used initially. These chambers measure the coordinate parallel to the wire by determining the pulse area of the induced pulse in a pair of cathodes shaped in a 'diamond' pattern, such that the ratio of pulses from the two cathode segments gives a measure (to within a few mm) of the distance along the wire. Coarse determination of which cathode segment has been struck is made by time differences on the two wire ends.

The μ's in the small angle region ($< 10°$) are recorded before and after the toroid in x-y-u triplets of $30mm$ diameter drift tube planes. Each x,y, or u measurement consists of two overlapped planes of tubes. The drift time in these tubes is about $200ns$. These chambers are called the SAMUS (Small Angle MUon System) chambers and cover $3°$ to $10°$.

5.2 Scintillator Coverage

The present WAMUS drift time of 1.2 μs becomes a problem for large bunch crossing frequency (ν_{cross}). The first problem is that the cosmic ray trigger rate scales as ($\mathcal{L}_{cosmic} \times \Delta T_{live} \times \nu_{cross}$) and becomes too large for the available trigger bandwidth.

Calculations suggest that the cosmic ray trigger rate will be manageable in the 1991 running period, but problematic with the proposed accelerator upgrades. Table 5.1 shows the calculated cosmic ray trigger rate without scintillator timing (ΔT_{live}=1.2 μs) and with scintillator timing (ΔT_{live}=50 ns). Since a cosmic ray rate of a few 100

Hz is acceptable, we see from Table 5.1 that the situation with the scintillator is viable. In order to make significant improvement in the cosmic ray problem, it is sufficient to cover only the top of the detector.

Table 5.1

Cosmic Ray trigger rates for 2 time resolutions

Luminosity	Without Scintillator	With Scintillator
$10^{30}\mathrm{cm}^{-2}\mathrm{s}^{-1}$	50 Hz	3 Hz
$5 \times 10^{31}\mathrm{cm}^{-2}\mathrm{s}^{-1}$	2500 Hz	150 Hz

The second problem is that for $\Delta T_b < 1.2\mu s$, one needs an independent indication of which bunch crossing initiated the trigger. The inclusion of a scintillator timing signal whose accuracy is a fraction of the bunch interval would automatically serve to give the time stamp needed to determine the time of arrival of PDT tracks. For this function, it would be necessary to cover all six sides of the detector.

In anticipation of the problems at higher $\mathcal{L}$, we have already installed large acrylic scintillators from experiment E733 in DØ. These scintillators are 100" × 50" and are read out on their edges by BBQ waveshifter bars. Only the central iron toroid is covered with these counters. Four counters cover each muon PDT. The PDT electronics are built to accomodate 4 decks per layer, but these outermost layers have only three decks. Therefore, a circuit has been designed which will amplify, discriminate, latch and time-digitize the scintillator signals so they may be integrated as the fourth deck of the outer layer.

In order to complete the total coverage of scintillator, the same counter design is proposed with sizes chosen in order to match the PDT chambers on which they would be mounted. Three additional standard sizes of scintillator counters are planned which match the C or B layer PDT's on the remainder of the top, sides and bottom.

The total coverage is $\sim$ 6000 ft^2 of which we have roughly 17% in hand for the first run. We would require the construction of 292 new counters with 584 new phototube channels. This, along with the existing system, will bring the total to 324 counters and 648 channels and a total scintillator blanket over all of the outer PDT surfaces. Sufficient phototubes have been reserved from a decommissioned BNL experiment.

5.3 Fast Gas

Using a faster gas in WAMUS is desirable in order to reduce the maximum drift time in the PDT chambers and to speed up the Level 1 (hardware) muon trigger. There are several requirements for gas choice: the plumbing requires a nonexplosive gas and given the electrostatics, the drift velocity must be relatively saturated to have a fairly uniform time to distance relation.[1] The most promising gas[1] for the upgrade is an $Ar:CO_2:CF_4$ (88:2:10) mixture which has a drift velocity approximately 1.8 times faster than the $Ar:CO_2$ (90:10).

The crucial issue for study with the $Ar:CO_2:CF_4$ mixtures is the possible degradation of resolution with the faster drift velocities. Using $Ar:CO_2$ we have achieved a resolution in the drift direction of 0.31 mm, to be compared with the diffusion limit of 0.225 mm. Tests of $Ar:CO_2:CF_4$ mixtures which will measure this resolution are underway.

Environmental restrictions on the use of CF_4 in WAMUS will necessitate changing the present single pass gas system into a recirculating system. The current plumbing needs little modification to go to a high flow rate recirculating system.

5.4 Additional Small Angle Muon Chambers

The small angle muon system, SAMUS, will use two triggering schemes; one is based on finely segmented, one-dimensional strips in x and y projections to give momentum information at the trigger level. The second requires coarser x-y-u coincidences. Both triggers will be fooled often at large $\mathcal{L}$ by the large rate of low energy hadrons.

The Level 2 trigger will probably be overwhelmed by the task of x-y-u matching. A trigger element that gives indication of the muon location in three dimensions would help the Level 2 algorithm tremendously.

To aid small angle muon triggers, we propose a system of small wire-spacing proportional chambers with cathode pad readout to give the desired 2D pattern of segmentation. These chambers would back the existing SAMUS B and C stations with an additional set midway between them.

We propose to copy E771 chambers with 8 mm wire spacing and cathode pad readout. The pads would be designed to have approximately equal occupancy; this would yield an accidental rate of about 0.1%. Detailed pad design would await experience in the next run. The existing SAMUS trigger could be required together with the new trigger to get a trigger dominated by real muons.

5.5 SAMUS Electronics Upgrade

The existing SAMUS front end electronics consists of ADLT (amplify, discriminate, latch and time) cards handling 32 drift tubes each and a control board to handle up to 6 ADLT cards. The ADLT is equipped for single hit drift time measurement with a common stop. The drift cells are latched in pairs on the ADLT and 'or'ed together on the control board to form bit patterns used in the Level 1 trigger. The SAMUS chambers already are expected to have an average of 6 hits per station per crossing at luminosities of $10^{30} cm^{-2}s^{-1}$.

The ADLTs need two upgrades to be fully useful at higher luminosities. The small size of the SAMUS tubes insure that the drifting will occur in a time less than the smallest time between crossings. However, the trigger will not be available within 400 ns, so analog delay chips will need to be added to each channel. Also, the ADLTs should be upgraded to provide second hit capability like the wide angle chambers. This will improve SAMUS rejection of noise from albedo and scraping as well as delta rays from good tracks.

The control boards already have provisions for a finer pattern from the SAMUS chambers for use in a fast trigger. Until data is available from the first DØ run, it is difficult to see if the provisions made in the system will be sufficient. If a higher resolution is needed from the control boards, they can be replaced and new Level 1 trigger logic added.

5.6 Muon Data Acquisition Upgrade

The current data acquisition system for the muon chambers consists of VME crates for raw data and for trigger information. In the data crates each chamber communicates through a module address card (MAC) that performs zero suppression by reporting only those cell that are tagged by a hit. On interrupt, a 68020–based microprocessor reads the lists of hits from all MACs and selects the hit cells one at a time for digitization by an in-crate ADC card. The complete event is transferred to the Level 2 processor farm by a VME buffer driver card once digitization is complete.

The processors and ADCs are not well matched to the needs of the muon system, since they are based on the calorimeter design. The 68020-based processors have a typical instruction time of 500 ns/operation and an interrupt time of up to 20 μs. Because the interrupt time is long, digitization cannot begin until the Level 1.5 trigger has confirmed the event, putting a delay of tens of microseconds into the muon event building process.

An average WAMUS crate will have typically 6 hit cells requiring 30 μs to digitize plus 500 μs in program overhead. The SAMUS small angle crates are much worse, with typically 20 hit cells requiring 100 μs to digitize with over a millisecond of program time. These are average figures and there will be large fluctuations. At the higher luminosities of an upgraded Tevatron, the number of hits in SAMUS will increase tenfold. The input to Level 2 will be increased to a maximum rate of 1000 Hz, so it is essential to upgrade the muon digitization cycle to match this rate requirement.

We propose to replace the existing processors and ADCs in the muon crates with a dedicated DSP board with a 48 to 4 multiplexer into 4 channels of 12-bit ADC. DSP chips with an average instruction time of 150 ns/operation are available as are ADCs with 12-bit accuracy and a digitization time of 1-2μs. A readout board would consist of a DSP with VME interface, multiplexer and 4 channels of ADC. The muon system requires only 30 such boards.

With the proposed DSP/ADC board, signals could be staged to permit the overlap of instructions and digitization. For the SAMUS case described above with 20 hit cells, we could expect 40μs to digitize and 300μs of program time. Even with 200 hit cells, the major increase would be due to digitization and the process could be complete in well under a millisecond. This would be within the requirements of the upgraded DØ data acquisition system at high luminosity.

Chapter 5 References

1. J.M. Butler et al., NIM A290, 122 (1990).

6. Trigger and Data Acquisition Upgrades

6.1 Introduction

Building the trigger to select interesting events at the upgraded Tevatron will be a formidable challenge. At the design luminosity of $10^{30} cm^{-2} s^{-1}$, the inelastic interaction rate is about 50 KHz with beam crossing times of 3.5 μsec. With the luminosity after the upgrade nearly $10^{32} cm^{-2} s^{-1}$, the raw interaction rate will approach 5 MHz with beam crossing times of 395 nsec. In contrast, the desired data rate to tape is a few (1–10) Hz. The DØ trigger is designed as a multi-stage trigger where each stage reduces the rate sufficiently so that subsequent stages which take longer times still have minimal deadtime. Level 0 is an inelastic interaction trigger based on hits in scintillator hodoscopes mounted on the End Calorimeters. The Level 1 trigger operates within the current bunch crossing interval of 3.5μs and uses hardware representations of calorimeter and muon chamber hits. The Level 2 trigger is built from a farm of microprocessors which also serve as the Event Builders. As implemented, some hardware triggers are found to require more than the 3.5 μs allotted to the dead-timeless interval between crossings; these are designated as Level 1.5 triggers.

6.2 Level 0 Trigger Upgrade

The Level 0 trigger consists of two hodoscopes of plastic scintillation counters with photomultiplier readout that surround the beam pipe on opposite ends of the detector. It is designed to identify beam-beam interactions, reconstruct the interaction vertex position, tag multiple interactions, and monitor the collider luminosity. Timing between the forward and backward ends can determine the position of the vertex to about ± 3 cm. The Level 0 electronics is capable of handling the bunch spacings being considered and should not require substantial changes. The photomultiplier readout will have to be replaced due to the high magnetic fields in the central detector; possible solutions include fiber optic light guides to remote photomultipliesrs or photodiode readout.

An intrinsic limitation of the Level 0 system is its inability to reconstruct the vertex position correctly for beam crossings with multiple interactions. Preliminary studies indicate that multiple interactions will reduce the accuracy of the Level 0 vertex position to 15-20 cm, and thus fast information on the vertex must be sought from the upgraded tracking system.

6.3 Level 1 Trigger Framework Upgrade

The Level 1 Trigger Framework,[1,2] has been used for the past several years. For each beam crossing the Framework makes a decision about whether or not a data acquisition cycle should be started. The Framework bases its decision on information supplied by the Level 0 , Level 1 Calorimeter, and the Level 1 Muon Triggers. Quantities measured by these systems, such as the number of muon tracks or the total E_T in the event, appear as input terms to an AND-OR network. Up to 32 Specific Trigger may be defined from combinations of the data presented to the AND-OR network. All processing by the Framework takes about 3 μs. The Framework treats the detector data acquisition systems as 32 independent Geographic Sections. The firing of a given Specific Trigger may cause the readout of any combination of these Geographic Sections.

The Trigger Framework supports Level 1.5 triggering. For Specific Triggers defined to operate in this mode, a data acquisition cycle is started when a Level 1 Trigger fires but after a few 10's of microseconds it may be stopped if the results of the Level 1.5 are negative. For example, the Level 1.5 TRD trigger uses the TRD information combined with the Level 1 EM calorimeter data to verify electron candidates.

The Trigger Framework includes facilities to control the flow of events through the various data acquisition systems and trigger systems. Monitoring of the flow of triggers through the data acquisition system is provided by the Framework. Scalers are provided to monitor individually all sources of dead time for each Specific Trigger, to count the number of each Specific Trigger, and to give the number of beam crossings for which each Specific Trigger was live. Monitor information and other information indicating why a Specific Trigger fired on a given beam crossing is read out in the event data stream in the same way as data from any of the DØ detector data acquisition systems. The Level 1 Trigger Framework is setup and managed by the COOR program running on the host computer.

Framework Resource Increase

We propose to increase the number of Specific Triggers and the programming flexibility for the Specific Triggers while maintaining the same general architecture and the same footprint in the counting house.

We expect a need for more than 32 Specific Triggers to allow for the various different combinations of AND-OR Network Input Terms. We are currently studying designs that would allow up to 16 combinations of AND-OR Network Input Terms to satisfy a given Specific Trigger.

To increase flexibility, we also have preliminary designs for doubling the number of Geographic Sections from 32 to 64 or doubling the number of AND-OR Network Input Terms from 256 to 512. We will need some running experience before it is known if we need to increase either of these resources.

Existing hardware/software interfaces and the Level 1 architecture will be kept for the upgraded triggers.

Level 1 Trigger Data Block Bandwidth

The second need for the upgraded Framework is to expand throughput to the Level 2 filter. There are a number of simple ways to increase from the current capability of 400 Hz to around 1KHz, so that the Level 1 Data Block bandwidth will not limit high $\mathcal{L}$operation. The list of ways to increase the Level 1 Trigger Data Block Bandwidth includes:

1. Use multiple paths in the Framework
2. Improve the driver cards, retaining the multiplexed address/data
3. Build the trigger data block in crate buffers
4. Double buffer the dual port memories
5. Double the number of dual port memories under 68K control

At this time the Level 1 Data Block is 8 kilobytes long (2K 32 bit long words). This includes data about the beam crossing that caused the Level 1 trigger and data from the proceeding beam crossing. If more history is desired, then the size of the Level 1

Data Block will increase and more bandwidth will be needed to maintain the desired number of events per second.

6.4 Level 1 Calorimeter Trigger Upgrades

The Level 1 Calorimeter Trigger[3,4,5] processes information from the 1280 projective trigger towers in the DØ uranium-liquid argon calorimeter. These Trigger Towers are 0.2×0.2 in η and ϕ. The Calorimeter Trigger receives an analog electromagnetic (EM) and a hadronic (HD) signal from each trigger tower. The Calorimeter Trigger uses these signals to calculate both global quantities and cluster quantities, any one of which can enter as entries to the AND/OR Network.

Global quantities include: the total EM E_T, the total HD E_T, the total E_T, the missing E_T, and the direction of the missing E_T. Trigger tower E_T's entering into global sums can be cut on predetermined thresholds and can be corrected for vertex z-location.

Cluster quantities involve local deposits of either EM or EM+HD energy. Counts of trigger tower E_T's above a set of thresholds are used to indicate electron, photon, or jet multiplicities.

The Level 1 Calorimeter Trigger is a pipelined digital system. With 6 bunch operation of the collider, the Calorimeter Trigger and the Framework finish in time to inform the front end electronics if latching is desired. Because of its pipeline design the Level 1 Calorimeter Trigger can operate with beam crossings as close as once every 132 nsec. The trigger takes about 2μsec to form. Accordingly, delay lines will be added to the calorimeter electronics as discussed in chapter 4. The Level 1 Calorimeter Trigger is also set up and controlled from the COOR program running on the host computer.

We propose to develop new tests that can be made on the calorimeter trigger signals so that the Calorimeter Trigger can operate at high luminosity to reject a high percentage of the beam crossings. Two examples are outlined below which would operate on a Level 1 or a Level 1.5 time scale.

<u>Electron Finder</u>

The Electron Finder would find EM energy"shared" between trigger towers by examining all 3 by 3 cells of trigger towers. It would make tests based on both the quantity of energy deposited and on the shape of the energy deposit.

A preliminary design has been made for a new circuit which requires a central hit cell and transverse energy shapes appropriate to electrons or photons.

The rest of the Electron Finder system, consisting of standard components from the current Level 1 Calorimeter Trigger, would count the number of cells reporting an electron and compare this count to a series of count thresholds.

Hadronic Cluster Finder

The Hadronic Cluster Finder would locate hadrons that have deposited the majority of their energy in a 4 by 4 array of trigger towers (0.8×0.8 in η and ϕ.). This eliminates the necessity of lowering single channel thresholds to trigger on hadrons whose energy is shared between trigger cells.

The first step in the processing would compare all of the Total E_T signals in the 4 by 4 cells of contiguous trigger towers to a low threshold. The results of this threshold comparison pass through a look up PROM which makes a selection based on the shape of the energy deposit. The outputs from this PROM enable the proper set of inputs of a 16 input digital Cluster Adder that forms the sum of the selected Total E_T signals. The output from this adder represents the energy in the hadronic cluster.

The sum signals from the Cluster Adders are compared to an hadronic cluster energy threshold. The number of Clusters above threshold are counted and compared to a count threshold. This processing can be done with cards that were developed for the current Level 1 Calorimeter Trigger.

This Hadronic Cluster Finder design will also provide information to the Level 2 system indicating the number of trigger towers hit and the location of the energy weighted center of mass.

6.5 Muon Level 1 Trigger Upgrade

The muon Level 1 trigger[6] is currently the slowest element in the DØ Level 1 trigger. Table 6.1 outlines the time spent on each part of the current configuration.

Table 6.1

Time for Muon Trigger Operations in Current Design

Activity	Time(μs)
Interaction to maximum drift	1.05
Trigger bit readout	0.40
Cable (max) from platform to MCH	0.44
Muon logic calculation	0.10
Cable in MCH	0.15
Calculation in trigger framework	0.46
Total to form trigger	2.60

The muon system must be reset before the next crossing if there is no trigger. With cable delay of 0.59μs and the reset assertion of 0.3μs, a total of 3.5μs is needed between triggers.

The existing trigger suffers in two ways as the bunch spacing is decreased. First, the crossing can no longer be identified with certainty, since the muon drift time is longer than the nominal 0.4μs bunch spacing proposed for the Tevatron. Second, the long time needed to form the trigger would force other subsystems to pipeline their signals a significantly greater amount of time until a muon trigger could be formed.

The muon system proposes to to add scintillator and other fast trigger elements to surround the detector by the 1993 run (see Chapter 5). This will unambiguously tag the crossing and provide a signal on the platform to initiate muon trigger. The existing muon front-end electronics provides for direct readout of chamber logic and the coarse centroid logic, now in the moving counting house, will be moved to the DØ platform. Table 6.2 shows the time then needed to form a muon trigger.

Table 6.2

Time for Muon Trigger Operations in Upgrade Design

Activity	Time(μs)
Interaction to maximum drift	1.05
Cable (max) from chamber to platform	0.14
Muon logic calculation	0.10
Fast cable to framework	0.25
Calculation in trigger framework	0.46
Total to form trigger	2.00

No return time will be needed as the muon chambers will reset based on scintillator firings. This limits muon readout to those events that have a muon trigger. Additional time can be saved by the addition of faster gas possibly reducing the maximum drift time in the muon chambers to $0.6\mu s$, as discussed in Chapter 5.

Another muon issue is the small angle chambers. The small tube size means the information will always be ready before the next crossing, but no pipelining was made on the chamber electronics. New ADLT front end cards will replace existing cards and provide sufficient pipelining to enable small angle data to be read out, even if there is no small angle muon trigger. In addition, to cope with the expected high occupancies in the SAMUS chambers, additional pad chambers will be added to provide space points to aid in triggering. More details can be found in chapter 5.

6.6 Level 1.5 Trigger

The aim of the Level 1.5 trigger is to reduce the Level 1 trigger rate by a factor 2 to 10. The output of Level 1 trigger will be used as an input to a Level 1.5 processor.

There are two possible sources of the trigger rate reduction:

(a) Combining information from different parts of detectors e.g. muon and calorimeter.

(b) A more precise measurement of the quantities used in the trigger, like jet energy, electron identification, missing energy etc.

Muon Level 1.5 Trigger

The current muon Level 1.5 trigger performs momentum calculations based on 5 cm resolution within each chamber. The muon momentum trigger currently needs 1-4 μs after the Level 1 trigger to make a decision. It is highly parallel, and adequate up to the highest luminosities considered for the upgraded Tevatron. The existing logic also already provides for fast output in the form of momentum, η and ϕ for each muon found. This can be integrated into a more sophisticated Level 1.5 processor.

New Calorimeter Level 1.5 Triggers

One of the shortcomings of the current Level 1 Calorimeter trigger is the small size of its basic triggering element, 0.2×0.2 in η and ϕ. This can lead to low triggering thresholds for jets if the E_T threshold is not set sufficiently low, even with the proposed Level 1 Hadronic Cluster Finder. At the luminosities expected with the upgraded collider, the trigger rate passed by Level 1 to Level 2 may be too large at some physically interesting thresholds. Ideally we would like to trigger on energies that are more like the full energy of a jet. We are investigating a number of approaches that would perform this function, as well as more general analyses of 'Lego' plot information.

A promising approach involves the use of large arrays of parallel computers with content addressable memories called Associative String Processors (ASP). A collaboration among the chip maker and several European groups exists with the aim of producing systems to solve problems like ours. The devices are programmable with high level languages and hence could be adapted to a variety of tasks. They are fast (5 - 6μs for cluster finding in a 64x64 array) and their development is well-advanced with finished systems due in 1991, which is consistent with the needs of the DØ upgrade. We are investigating how to apply these systems to very general problems in DØ calorimetry, including clustering of jets, electron identification, correlation of jets with electrons and muons and the calculation of secondary quantities such as effective masses. If the approach looks promising we would propose to proceed with high level modeling of the system performance in our environment.

2D Spatial Correlator

All of the calorimeter triggers that have been built so far or that have been proposed can provide spatial information about the location of hits in the calorimeters. This data could be used along with data from another detector trigger system (e.g. muon) for 2D spatial correlation. We are currently studying such triggers with the DØ Monte Carlo.

Hardware Track Finder

We propose a hardware track finder to verify that there is a high momentum track pointing at the calorimeter electron candidates. The exact form of the track finder will depend on choice of technologies for the tracking. We note that the information from the scintillating fibers will be available in the Level 1.5 time frame.

6.7 Software Triggers – Level 2

The Level 2 trigger uses high bandwidth data paths, a VME based highway to a processor farm, software filter algorithms to make the final event selection, and a high speed data path to the host computer for event recording and monitoring. Implementing the final trigger stage in software provides flexibility in setting trigger conditions, allows the use of the full event record to make the final trigger decisions, and allows extensive monitoring and testing of the Level 2 trigger. The current DØ Level 2 farm consists of 50 MicroVax computers. The DØ upgrade requires increasing the Level 2 bandwidth, processing power, and event recording speed. In addition, new software algorithms will need to be developed to provide more sophisticated event selection criteria.

Bandwidth Upgrade

The present Level 2 trigger is expected to handle a Level 1 trigger rate of 200 Hz, with a capacity for a 400 Hz Level 1 rate. The expected output rate is 1–2 Hz. With Level 1 Framework upgrades, the event transfer rate into Level 2 can be upgraded with an ultimate limit from digitization time and VME transfer speed limit of ≈ 1 kHz.

The Level 2 bandwidth will be increased in two stages. The first stage will involve increasing the transfer rate on the data cables from 40 MB/s to 60 MB/s. The existing VME Buffer Driver (VBD) and Multi-Port Memory (MPM) designs support the 60 MB/s transfer rate so no new electronics is required. The second stage will be to increase the number of data cables from 8 to 16. This requires either the purchase of 200 additional MPM boards or segmenting the Level 2 farm to reduce the bandwidth needed for any given processor. Figure 6.1 shows how two data cables from different parts of the detector can be combined to drive two farm segments. Each farm segment gets the data from both data cables for each event, but the events are divided between the two farm segments so that each segment gets half the events. Implementing both stages of the bandwidth upgrade will increase the bandwidth by a factor of 3 and provide capacity for ≥ 1 kHz Level 1 trigger rate.

Processor Farm Upgrade

The Level 2 processor farm will require substantial upgrades in its processing capacity to meet the demands of high luminosity. Besides having to accept a higher Level 1 trigger rate, the more stringent Level 1 trigger will exclude the "easy" events and require more sophisticated algorithms for the events that remain. Furthermore, the additional complexity of events with multiple interactions, uncertainty in the vertex position from Level 0, and the inclusion of B triggers with low p_T thresholds will further increase the required processing.

The VME based architecture of Level 2 provides a wide variety of upgrade paths, including upgrades to more powerful VAX family processors, the use of special function coprocessors based on DSP chip sets, the use of additional general purpose processors in a multiprocessor architecture, and increasing the number of nodes in the farm. Given our lack of running experience with the present Level 2 farm and the pace of change in the computing industry, it is premature to specify the mix of upgrade options that best provides Level 2 with sufficient processing power. However, the open architecture of Level 2 ensures a wide variety of choices will be available in the future that incorporate the leading edge of computing technology.

6.8 Event Recording and On–Line Computing

The upgrade of the DØ on-line system is driven by the need to record data more rapidly; the need to control, monitor, and calibrate new detector systems with significantly higher channel counts; and the need to perform a significantly more complex analysis on a fixed fraction sample of the larger quantity of data being taken.

Event Recording

Increase in recording densities and speeds for raw data are needed from 600 KBytes/s in 1991, to 1.5 MBytes/s in 1993, and to 3 MBytes/s in 1995. The upgrade for the 1993 run can be done within the currently planned framework. This means using a VAX 6000 machine with HSC-connected 8 mm tape drives (replacing the 1991 drives with higher rate and density drives) and a connection to the Level 2 processor farm which makes use of a BI bus connection through a variant of the DØ data cable. It may also be necessary to replace the HSC to 8 mm tape interface to obtain higher throughput and greater reliability. An additional 10 Gbytes of staging disk for data waiting to be written to the 8 mm drive will also be necessary.

For the 1995 upgrade we expect that there will have to be an upgrade in the link connecting the Level 2 processor farm and the host computer. This link is currently estimated to have a throughput of about 2 MBytes/sec. The intrinsic bandwidth of the data cable and both the BI and XMI bus are more than adequate to the 3 MBytes/s target rate, but a new connection from the DØ data cable to one of these VAX buses will be necessary. There will also have to be a change in the recording media. A new system available from Honeywell which uses VHS tapes for recording and is capable of 10 GBytes/Tape and 3 MBytes/s is already intended for use by some HEP experiments. This would be a possible choice in the immediate future, although clearly an optical disk system would be preferable, and in fact may be available by the time of the 1995 run. Approximately 20 GBytes of additional staging disk will also be required.

Additional Computing Power

Significantly more CPU cycles are needed, from the 1991 host cluster capacity of 75 MIPs, to a 1993 capacity of about 300 MIPS, to a final 1995 capacity of about 600 MIPS.

The CPU upgrade for the 1993 run consists of two parts. First, there will be an upgrade of the HSC connected cluster. The current 6000-410 will be upgraded to a dual processor version of the then top of the line 6000 class machine; in the immediate future that would mean a VAX 6000-520. This will enhance the ability to handle data on its way to tape and to more rapidly coordinate the activities associated with configuring the detector.

Second, the associated workstations will need to be upgraded. As now, we will need at least 16 separate activities, thus 16 workstations. Those involved in physics monitoring or other high level and relatively passive activities can probably use RISC/Unix workstations. The stations involved in active control operations will remain VAX/VMS in order to preserve the software investment in detector operating code. Assuming that the significant cost benefit advantage of RISC/Unix stations relative to VAX/VMS stations remains, the stations are likely to be divided approximately evenly between RISC/Unix and VAX/VMS.

The CPU upgrade for the 1995 run will again consist of upgrading the VAX 6000 with new and/or more processors. Anticipating the evolution of a computer line on a 4–5 year time scale is, of course, difficult and so what is being described here is a strawman, likely be modified on the basis of product developments. There will again be the need to upgrade the associated workstations. At this point the possibility of the entire new round of workstations of RISC/Unix stations exists. On this time scale it is hoped that the compliance of VMS and Unix to Open System Foundation standards will make practical inter-operability between the exiting online detector operating software running on the VMS host processor and Unix workstations.

<u>Data Storage</u>

Significantly more disk storage for raw data samples and various calibrations and databases will be needed.

DØ will need to double the amount of generally available disk space on the on-line host system for the 1993 run relative to the 1991 run which means 10 additional GBytes. The doubling will again be required for the 1995 run, thus 20 additional GBytes.

<u>Farm Bandwidth Upgrade</u>

Significantly higher bandwidth connecting the various processors which make up the on-line host system will be needed.

The workstation to host processor connections within the on-line system will be converted from Ethernet to FDDI. This conversion will be performed in time for the 1993 run. We expect all of the workstations we purchase for that run to have FDDI interfaces. This bandwidth upgrade will probably remain adequate for the 1995 run.

6.9 Off-line Computing

Off-line computing consist of two components. First, there are the facilities for production processing, reconstruction and Monte Carlo. Second, there are the facilities associated with the physics analysis of the data, repetitive cutting and plotting of data and comparing it to various models. Components of the physics analysis facilities are also commonly used for general interactive computing including software development, electronic mail, document preparation, etc.

The production off-line computing estimate for the 1991 run is 600 MIPS. The CPU requirement will increase somewhat faster than the volume of recorded data since the expected improved selection criteria will result in richer event samples, having fewer uninteresting events and requiring more complex analysis. The rate at which at which data is recorded will increase by a factor of 2-3 for each run so the 600 MIPS estimate for the 1991 run will rise to 2000 MIPS for the 1993 run and finally to 5000 MIPS for the 1995 run.

The physics analysis portion of the off-line computing has as its hub a file serving system which supports a large number of workstations on which the actual physics analysis is done. This system is not fully defined for the 1991 run but is believed to be equivalent to a HSC equipped VAX-6000 system heavily loaded with disk. This file server is then augmented by CPU servers and workstations. The load on this system is also driven by the number of interesting events and the complexity of the analysis applied. Its capability must also increase at approximately the same rate as the production processing farm, a factor of 3 in each run. The current estimate is that this part of the computing is likely to be of comparable cost to the production processing farm. There will be large numbers of associated workstations but, since significant fraction of these are expected to continue to supplied by the collaborating institutions, they are not being considered in detail here.

Chapter 6 References

1. M. Abolins et al., DØ Note 328.
2. M. Abolins et al., DØ Note 705.
3. M. Abolins et al., DØ Note 706.
4. M. Abolins et al., DØ Note 777
5. M. Abolins et al., Nucl. Instr. Meth. **A289**, 543 (1990).
6. M. Fortner, DØ Note 816

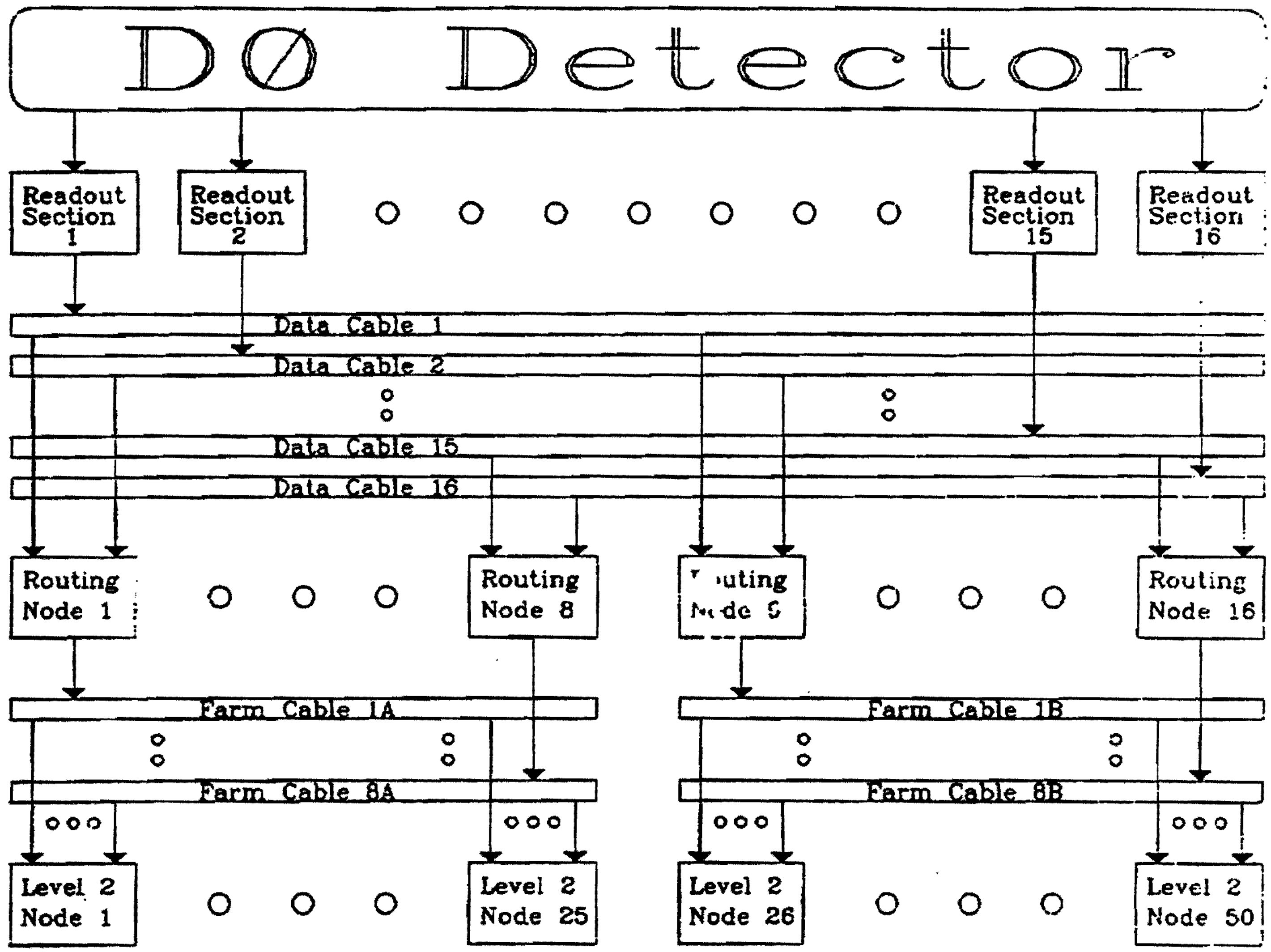

Figure 6.1 Data Cable to Farm Segment Connection

May 19, 1993

E823 (DØ Upgrade)

DØ$_\beta$

THE DØ COLLABORATION

The DØ upgrade is designed to adapt the detector to a higher luminosity Tevatron environment and to extend the DØ physics reach by replacing the current non-magnetic tracking system with a high-resolution, magnetic tracking and vertexing system. In addition, a preshower detector will be added to aid in electron identification and to compensate the response of the electromagnetic calorimetry for the effects of additional material within the magnetic volume. We present the results of simulation studies that demonstrate the performance characteristics of both track reconstruction and electron identification, and indicate some aspects of the anticipated increase in physics potential. We also present the current status of silicon microstrip and scintillating fiber R&D and note the progress on the magnet design. Having demonstrated the improved research power of the upgraded DØ, and having verified the feasibility of the detection techniques, we request Stage-1 approval for the full project.

Table of Contents

THE DØ COLLABORATION

B. Gomez, B. Hoeneisen, D. Mendoza, P. Nechev, J.P. Negret, O. Ramirez, J. Roldan, A. Serna
Universidad de los Andes, Bogota Colombia

J. Chen, D. Fein, G. Forden, E. James, K. Johns, P. Loch, L. Markovsky, B. May, A. Milder, J. Rutherfoord, M. Shupe, A. Smith, C. Zeitnitz
University of Arizona

S. Aronson, M. Fatyga, J. Featherly, B. Gibbard, H. Gordon, N. Graf, J.M. Guida, W. Guryn, S. Kahn, S. Protopopescu, P. Yamin
Brookhaven National Laboratory

J. Bantly, D. Cullen-Vidal, D. Cutts, T. Fahland,J. Hoftun, R. Lanou, F. Nang, D. Nešić, R. Partridge, H.W. Xu, R. Zeller
Brown University

J. Drinkard, A. Lankford, A. Lipniacka, D. Stoker
University of California, Irvine

K. Bazizi, B. Choudhary, J. Ellison, R. Hall, A. P. Heinson, T. Huehn, A. Kernan, S. Wimpenny
University of California, Riverside

G. Alves, G. Lima, A.K.A. Maciel, V. Oguri, A. Santoro, M. Souza, M. Vaz
LAFEX, Centro Brasiliero de Pesquisas Fisicas, Rio de Janeiro Brazil

H. Castilla, G. Herrera
CINVESTAV, Mexico City Mexico

I. Adam, P. Franzini, U. Heintz, P.M. Tuts
Columbia University

V. Kapoor, R. K. Shivpuri
Delhi University, Delhi India

S. Abachi, S. Ahn, J.F. Bartlett, P. Bhat, F. Borcherding, A. Brandt, A. Bross, J.M. Butler, J. Christenson, W.E. Cooper, M. Demarteau, K. Denisenko, N. Denisenko, H.T. Diehl, M. Diesburg, R. Dixon, D. Eartly, D. Elvira, H.E. Fisk, S. Fuess, C. Gao, K. Genser, C. Gerber, D. R. Green, H. Greenlee, H. Haggerty, S. Igarashi, A.S. Ito, M. Johnson, A. Jonckheere, H. Jostlein, B. Klima, S. Krzywdzinski, R. Li, Q.Z. Li-Demarteau, R. Lipton, L. Lueking, E. Malamud, I. Manning, H.-S. Mao, M. I. Martin, H. Melanson, X.-C. Meng, W. Merritt, S. Mishra, H.E. Montgomery, C.T. Murphy, M. Narain, N. Oshima, J. Ortmanns, A. Para, C. H. Park, A. Peryshkin, H. Prosper, Y. Que, P. Quintas, P. Rapidis, R. Raja, A.L. Read, W. Smart, R.P. Smith, A. Taketani, M. Tartaglia, D.-C. Wang, L. Wang, D. Wood, P. Xie, R. Yamada, M.-J. Yang, Y. Zhou, Y. Zhu
Fermi National Accelerator Laboratory

W. Dharmaratna, M. Goforth, S. Hagopian, V. Hagopian, A. Klatchko, S. Linn,
R. Madden, H. Piekarz, C. Shaffer, H. Wahl, D. Xiao, S. Youssef
Florida State University

J. Balderston, M. Cummings, M. Jones, M. Peters, C. Yoshikawa
University of Hawaii

M. Adams, D. Averill, M. Chung, H. Goldberg, S. Margulies, T. McKibben, J. Solomon
University of Illinois, Chicago

G. Alvarez, T. Marshall, H. J. Martin, C. Murphy, D. Zieminska, A. Zieminski
Indiana University

E. W. Anderson, P. Dervenagas, J. M. Hauptman, M. Pang, A. Zinchenko
Iowa State University

J. S. Kang, C. L. Kim, D. W. Kim, S. K. Kim, Y. M. Park
Korea University, Seoul, Korea

H. Aihara, J. Bendich, L.-P. Chen, A.R. Clark, O.I. Dahl, A. Goldschmidt,
P. Grudberg, L. Kerth, S.C. Loken, R.J. Madaras, E. Oltman, N.A. Roe,
A.L. Spadafora, M.L. Stevenson, M. Strovink, T. G. Trippe, P. Virador
Lawrence Berkeley Laboratory

A. Baden, W. G. Cobau, N. J. Hadley, S. Kunori, A. L. Lyon, D. Norman, K. Streets
P. Tamburello
University of Maryland

N. Amos, T. L. Geld, H.A. Neal, L. Oesch, D. Stewart, G.R. Snow, J. Qian, S. Zhang
University of Michigan

M. Abolins, R. Brock, D. Edmunds, S. Fahey, E. Flattum, K. Frame, R. Genik,
N. Grossman, S. Jerger, J. Linnemann, J. McKinley, P. Mooney, D. Owen, B. Pi,
B. G. Pope, H. Weerts, Y. Xia
Michigan State University

P. Ermolov, A. Leflat, S. Rusin, E. Shabbalina
Moscow State University, Russia

J. Kourlas, A. Mincer, M. Mudan, P. Nemethy, J. Sculli, J. Yang, Q. Zhu
New York University

E. Amidi, S.-M. Chang, R. Demina, H. Johari, J. Morimisato, M. Glaubman,
S. Reucroft, E. von Goeler, J. Wilcox, T. Yasuda
Northeastern University

M. Fortner, J. Green, D. Hedin, R. Markeloff, V. Sirotenko, S. Willis
Northern Illinois University

R. E. Avery, S. Blessing, D. Buchholz, B. Gobbi, Y.-K. Li, Y.-C. Liu, T. Joffe-Minor,
H. Schellman
Northwestern University

V. Balamurali, N. Biswas, J. Jaques, R. Kehoe, M. Kelly, R. Ruchti,
J. Warchol, M. Wayne
University of Notre Dame

S. Beri, V. Bhatnagar, S. Chopra, J. M. Kohli, J. B. Singh, P. M. Sood
Panjab University, Chandigarh India

Y. Antipov, B. Baldin, V. Bezzubov, N. Bozko, V. Burtovoy, S. Chekulaev, D. Denisov,
S. Denisov, A. Efimov, O. Eroshin, V. Evdokimov, A. Kirunin, B. Klochkov,
V. Klyukhin, I. Kotov, V. Kochetkov, E. Kozlovsky, A. Mayorov, Y. Pischalnikov,
V. Podstavkov, V. Riadovikov, A. Shkurenkov, D. Stoyanova, A. Suhanov, A. Vorobiev
Institute for High Energy Physics, Protvino, Russia

B. Abbott, D. Koltick,
Purdue University

D. Adams, G. Eppley, H. Miettinen, W. Oh, J. Skeens, P. Yepes
Rice University

G. Blazey, J. Borders, C. Cretsinger, S. Durston, G. Fanourakis, T.Ferbel,
S. Gruenendahl, R. Hirosky, K. Hodel, F. Lobkowicz, P. Slattery
University of Rochester

Y. Ducros, J. Glicenstein, J.R. Hubbard, P. Mangeot, B. Mansoulie, A. Pluquet,
J. Teiger, A. Zylberstejn
CEN Saclay, France

R. Astur, D. Chakraborty, W. Chen, D. Claes, J. Cochran, R. Engelmann, S. Feher,
G. Finocchiaro, M.L. Good, P. Grannis, J. A. Guida, T. Heuring, J. Jiang, C. K. Jung,
C. Klopfenstein, S. Lami, G. Landsberg, J. Lee-Franzini, H. L. Li, S. Lökös,
M. Marx, R. McCarthy, K. Ng, M. Paterno, D. Pizzuto, S. Rajagopalan, L. Rasmussen,
M. Rijssenbeek, P. Rubinov, R.D. Schamberger, S. Snyder, J. Thompson, C. Yanigasawa, J. Yu
State University of New York - Stony Brook

M. Botlo, P. Dingus, M. Diwan, H. Fenker, Y. Fisyak, S. Fredricksen, V. Glebov,
H. Johnstad, J. Kotcher, K. McFarlane, C. Milner, T. Regan, D. Schmid,
I. Sheer, F. Stocker, M. Takashima, E. Wang, J. Womersley
Superconducting Supercollider Laboratory, Dallas

B. S. Acharya, M. R. Krishnaswamy, N. K. Mondal, V.S. Narasimham, M. V. S. Rao,
H.C. Shankar, P. R. Vishwanath
Tata Institute of Fundamental Research, Bombay India

K. De, P. Draper, E. Gallas, J. Li, J. Perkins, L. Sawyer, M. Sosebee, A. White
University of Texas - Arlington

A. Boehnlein, M. Gui, R. Huson, J.T. White, J. Wightman
Texas A&M University

1. Introduction

The DØ detector was constructed to study proton-antiproton collisions at $\sqrt{s}$=2 TeV in the FNAL Tevatron Collider, with the prime physics focus being the study of high mass states and large p_T phenomena.[1] The current detector design has three principal features: muon detection using thick magnetized iron to provide muon momentum determination with small hadron punchthrough backgrounds; stable, unit gain, hermetic, finely segmented, radiation-hard calorimetry; and non-magnetic tracking with emphasis on suppressing backgrounds to electrons. The design and optimization of the DØ tracking system was very much influenced by the absence of a central magnetic field. After many years of construction and testing, the DØ detector is now approaching the end of its first and very successful run at the Collider.

The evolving upgrade in the Tevatron luminosity is proceeding rapidly, and the plans to upgrade the DØ detector for higher luminosity operation in the Tevatron runs of 1996 *et seq.* have been described in detail in earlier documents to the FNAL Physics Advisory Committee.[2–5] Briefly, in order to ensure a continuous and healthy physics program at DØ until and beyond the end of this century, the proposed upgrade consists of a two step process. In Step-1, the current vertex tracking (VTX) subsystem will be replaced by a combination of silicon microstrip barrel and disk detectors and a three super-layer scintillating fiber barrel tracker. The design and optimization of the Step-1 tracker has been described in detail in a DØ software note.[6] In the full upgrade (usually referred to as $DØ_\beta$ to distinguish it from the current detector, $DØ_\alpha$), the entire tracking system, consisting of Vertex Detector (VTX), Transition Radiation Detector (TRD), and Central and Forward Drift Chambers (CDC and FDC) is replaced by an expanded version of the silicon microstrip barrel and disk detectors of Step-1 along with a full scintillating fiber tracker. These detector systems are located inside a superconducting solenoid magnet, with a preshower detector located just outside the magnet.

The proposed full $DØ_\beta$ tracker is shown in Figure 1. The current scintillating fiber design consists of four super-layers arranged along cylinders at radii of 20, 33, 44, and 55 cm inside a 2 Tesla superconducting magnet. The outer three super-layers each contain eight 280 cm long scintillating fiber layers of single fibers on 0.87 mm center-to-center spacing. The inner super-layer is the same except its length along z is shorter, 256 cm, to allow room for forward silicon disks at each end. In each super-layer, the fiber layers are arranged in four doublets with half-fiber-width offsets. Two of the fiber doublets (axial) are oriented with fibers parallel to the beam axis, and the other two doublets (stereo) are oriented with offset angles to the axial layers of one to three degrees (*i.e.* a constant pitch of 0.001 rad/cm along z). This combination thereby provides track z information. In addition, the two axial doublets in each super-layer are separated by 1.5 cm to provide vector coordinates. This allows for enhanced discrimination of tracks during the track finding stage of reconstruction. There are a total of $\sim$90000 fibers in this system which are individually read out. The silicon disks and barrels are located inside the fiber barrels close to the beam axis. There are three barrels of single sided-silicon at radii of 3, 12 and 15 cm. The disks located in $|z| \leq 70$ cm are double-sided with inner radius 3 and outer radius 10 cm. The larger single-sided disks are located at the end of the inner fiber super-layer at ± 130 cm in z. There are about one million silicon strips in this system. The preshower detector consists of six 6 mm thick scintillator layers. The two middle layers are segmented in azimuth and are called z layers. The two top layers and the two bottom layers are segmented at an angle ($\pm 8°$) relative to the z direction, and are termed u and v layers. The two layers of the same orientation are staggered by a 1/2 strip-width. The total number of fibers to be read out in the preshower detector is ~5000.

In this document, we concentrate mainly on the improvements to the tracking system. We present the status of our simulation studies and the hardware R&D for the DØ$_\beta$ tracker, in addition to a brief discussion of the status of the current DØ$_\alpha$ tracking system. Our simulations show that the upgrade provides an excellent high-resolution detector capable of an exciting physics reach, and the hardware status indicates that we understand the techniques for the construction of the upgrade systems.

In the following, we describe the detector characteristics *vis − a − vis* track reconstruction efficiency, resolution and false track rates. We discuss the simulation of a variety of physics processes that DØ$_\beta$ will allow us to investigate. We present the status of the R&D projects associated with the silicon microstrip and scintillating fiber subsystems and we describe the status of the solenoid design.[+] Finally, we summarize our current overall situation and present the rationale behind our request for Stage-1 approval of the full DØ$_\beta$ upgrade.

2. Simulation Studies

We have made significant progress in our tracking simulation software packages for the DØ upgrade. We have developed software for combining the silicon and scintillating fiber detectors in the tracking simulation and have completed studies which are contributing to the design and expected physics potential of this detector.

The tracking simulation for DØ$_\beta$ is done in three steps. Physics processes are generated using ISAJET with full z-vertex smearing of the interaction region with a σ of 30 cm.[++] ISAJET events are then used as input to the DØ UPG_GEANT program, which is a version of DØGEANT (itself a DØ specific version of GEANT) that incorporates the proposed detector modifications. Provisions for either a uniform or realistic (*i.e.* non-uniform) magnetic field and digitized hits in the detectors are implemented in the program. A 2 T central field was used in the simulation discussed below. The generated information (ISAJET tracks and GEANT digitizations) for all tracks is stored in ZEBRA data banks and used to evaluate the

+ The choice of emphasis is driven by the comments received in the letter from John Peoples to Paul Grannis dated July 16, 1992.

++ Unless otherwise specified, the units used everywhere in this document are lengths in cm, angles in rad and momenta in GeV.

performance of the tracking program. The track finding and reconstruction package (BETA_TRACK[+]) has been integrated into the DØ software libraries. This program combines the digitized hits from GEANT to form clusters and calculates vector coordinates in each fiber super-layer and coordinates for each silicon detector layer. Tracks are reconstructed using these coordinates from the scintillating fiber and silicon detectors. Track finding starts with coordinates in the outermost layers and proceeds inward to the detectors nearer to the interaction region. Reconstructed tracks are checked against each other and where several have more than six clusters in common, the one with the better χ^2 is retained.

In order to evaluate the performance, reconstructed tracks are checked against ISAJET tracks at the cluster level. If no reconstructed track is found associated with an ISAJET track, then it contributes to the inefficiency. If extra reconstructed tracks are associated with an ISAJET track, then they are deemed spurious and termed ghost tracks.

In general, performance characteristics of the pattern recognition and track reconstruction procedures are evaluated in terms of the track reconstruction efficiency and the rate at which false tracks are reconstructed. Then for the successfully reconstructed tracks we calculate various resolution quantities plotted against kinematic quantities. In the following, we first discuss isolated track reconstruction in a constant magnetic field and then discuss the effect of implementing the full field map. In all the simulations, a representation of the material associated with the tracking detectors has been included. Figure 2 shows a plot of the amount of material (given in radiation lengths) versus η. The amount of material associated with the silicon detectors is given separately from that associated with the scintillating fiber super-layers. The results were generated for tracks originating in a realistic interaction envelope, and this has a smoothing effect on the distribution. Finally, to evaluate the tracker performance more realistically, we present the results of studying a variety of physics processes which become more accessible with $DØ_\beta$.

2.1 Isolated Track Reconstruction

In this section we present isolated track reconstruction characteristics as a function of pseudo-rapidity (η) and transverse momentum (p_T). Tracks with 5 discrete p_T values are generated uniformly in η with production vertex smeared in z. They are then input to UPG_GEANT where the $DØ_\beta$ detector response is fully simulated, including multiple scattering and interactions. A constant magnetic field is assumed. Pattern recognition and track reconstruction is performed in BETA_TRACK without any constraint from an assumed vertex of origin. This surely represents the simplest case from a tracking point of view and it is reassuring that the reconstruction efficiency is essentially 100% and the false track rate is vanishingly small for all values of η. This is shown in Figure 3, which gives the track reconstruction efficiency as a function of η, and Figure 4, which gives an η-z scatter

+ BETA_TRACK is the full $DØ_\beta$ detector tracking package developed for the studies described in this report.

plot of unreconstructed tracks. From a comparison of generated and reconstructed values we compute the resolutions (at the beam axis) in transverse distance (r), beam direction (z), azimuthal angle (ϕ), dip angle (θ) and transverse momentum (p_T). These are plotted versus η and p_T in Figures 5 through 9. Figure 9 demonstrates the improvement in p_T resolution, especially at high η, from applying a radial vertex constraint. The difference in Figure 9 between the behavior of the p_T resolution for $\eta \sim 2.2$ for high and low momentum tracks is due to the focussing effect of low p_T tracks into the silicon disks at large z, which would otherwise be missed. Table 1 summarizes the number of scintillating fiber super-layers, silicon disks, and barrels traversed by tracks emitted at different η-values from z=0.

Table 1

Number of fiber super-layers and silicon disks and barrels versus η from z=0

η	0.4	0.8	1.2	1.6	1.8	2.0	2.8
Fiber super-layers	4	4	4	4	3	2	0
Silicon disks	1	0	1	2	3	4	8
Silicon barrels	3	3	3	3	3	2	1
Total	8	7	8	9	9	8	9

2.2 Magnetic Field Effects

Using the full field map for the design magnet, we have investigated the effect on track reconstruction of the added complexity of having a non-uniform field. A Runge-Kutta technique, extracted from version 3.15 of GEANT, was adopted to step through the field in both simulation and reconstruction. In all the physics environments we have studied, both simple and complex, we have detected no significant effects on track reconstruction efficiency or resolution for any value of pseudo-rapidity. Figure 10 shows a set of typical examples. These plots give various track resolutions versus pseudo-rapidity for 2 GeV and 50 GeV muon tracks with both the constant field assumption and the non-uniform field.

These resolutions may be expressed as limits on the sign determination of fast charged particles. The 2 and 3 standard deviation limits in p_T as a function of η are shown in Figure 11 for single particles after reconstruction in the real field. This confirms that the sign determination for leptons is sufficiently good to perform the measurement of the forward-backward asymmetry, A_{FB}. In a previous study,[5] we showed that this determination will yield a 1% error on $\sin^2\theta_W$, assuming an integrated luminosity of 1000 pb^{-1}.

2.3 Electron Identification

In previous documents,[3,5] the results from Monte Carlo simulations on electron identification with the $D\emptyset_\beta$ detector, using a crude form of the preshower detector, have been reported. For the study reported on here, we have implemented a more realistic representation of the preshower detector in UPG_GEANT and repeated the study with the new program.

The preshower detector consists of six layers of 6 mm thick scintillator. Each layer is divided into approximately 5 mm wide strips. The two middle layers are segmented in the ϕ direction and are called z layers. The two top layers and the two bottom layers are segmented at an angle ($\pm 8^\circ$) relative to the z direction, and are termed u and v layers. The two layers of the same orientation are staggered by a 1/2 strip-width. Each scintillator segment is read out through a wave-length shifting fiber embedded in the scintillator, followed by a clear light-guide fiber and a Visible Light Photon Counter (VLPC).

The preshower detector geometry has been implemented in UPG_GEANT and a reconstruction program developed. The signals in any double-layer are combined and used as single hits of 2.5 mm segmentation. The hits are clustered in each double-layer using a straightforward algorithm. The clusters are then matched between u and z, and v and z projections using an energy matching algorithm and a z coordinate is calculated for each combination. The total energy, ϕ and z coordinates, are obtained for clusters in $u-z$ and $v-z$ that have a common z, and that satisfy the conditions for matching the energy and the z coordinate. The energy matching between clusters is an effective way of eliminating false combinations in the multi-particle environment. Figure 12 shows the position resolutions in ϕ and z, for isolated 50 GeV electrons, at the location of the preshower detector. The ϕ and z resolutions at η=0 are 0.9 mrad and 2.4 mm, respectively. The reconstruction efficiencies for isolated electrons and electrons from $t\bar{t}$ decays are both essentially 100%.

The number of photoelectrons generated by particles that go through the preshower detector has been estimated from measurements made in CDF/SSC R&D.[7] The mean number of photoelectrons for a minimum ionizing particle has been measured to be 3.3 using 2.5 mm thick scintillator (SCSN81) and 1 mm diameter wavelength shifting fiber (BCF91) with a bi-alkali photo-cathode tube. The number of photoelectrons for the preshower detector layer can be estimated using the above measured value and correcting for the known quantum efficiencies of 15 % and 70 % for a bi-alkali photo-cathode tube and VLPC, respectively. Assuming the attenuation lengths of the wavelength shifting fiber and clear fiber to be 3 m and 7 m, one can estimate the number of photoelectrons generated by a minimum ionizing particle at the far end, center and near end of the preshower detector as $\sim$6, $\sim$4 and $\sim$14, respectively (see Figure 13). The use of multi-clad fiber will increase these numbers significantly (see Chapter 5).

A covariance matrix method (the so-called H-matrix approach) has been developed for electron identification in $D\emptyset_\alpha$. We have generated a new set of H-matrices for $D\emptyset_\beta$, since the H-matrices for the current DØ detector are no longer relevant due to the changes in the detector configuration.

A set of 1000 single electron events were generated at 12 equally spaced η points in the range $0.05 \leq \eta \leq 1.15$ using UPG_GEANT. The precise plate geometry was used for the liquid argon calorimeter simulation. The UPG_GEANT code was adapted to the ULTRIX (DEC Unix operating system) platform and run on a DECstation farm. Output files were transferred to the FNALD0 cluster using the ZFTP package. The Monte Carlo events were then analyzed on the FNALD0 cluster.

For each η point an H-matrix was generated using the preshower signals, outputs from 40 calorimeter channels and the positions of the interaction vertices for single electron events with a continuous energy spectrum between 5 and 150 GeV. In addition, 3000 single electron events and 5000 single pion events were generated at each of four energies: 10, 25, 50 and 100 GeV. The electron events were used to establish the appropriate 95% efficiency electron cuts. Using these 42 x 42 element H-matrices plus the E/p cut and calorimeter/preshower position matching, criteria were established to discriminate between electrons and pions. The pion-to-electron rejection ratio is shown in Figure 14 versus pion energy (solid triangles). For comparison, the results from beam tests of the DØ end calorimeter (EC) are also shown in the plot as open squares and triangles. A set of Monte Carlo events was also generated for the preshower detector using UPG_GEANT, but without the presence of the solenoid material (black circles). The pion rejection ratio for this sample provides confidence in our study, since the results agree reasonably well with the beam test results. In fact, the agreement between this Monte-Carlo (solid circles) and the data (open squares and triangles) is remarkably good considering the extreme sensitivity of this particular measurement to both experimental and detector details. No attempt was made to simulate the detailed experimental layout, and we are only looking for qualitative agreement within, say, an order of magnitude.

The improvement observed in pion rejection at low energy for the DØ$_\beta$ detector is due to the E/p cut (compare the solid triangle to the solid circle at 10 GeV). The plot also shows that a possible drop in pion rejection at high energy due to the presence of extra material (the solenoid coil) is fully recovered using the preshower detector (compare the black circle to the black triangle at 100 GeV, which are essentially plotted on top of each other).

Events for three types of physics processes were generated with UPG_GEANT and the corresponding electron detection efficiencies were studied using the H-matrices and preshower criteria. The results confirm the essential conclusions of the earlier studies[3,5] based on a cruder preshower model and correspondingly crude H-matrices.

1000 $Z \rightarrow e^+e^-$ events were generated with ISAJET and used as input to the program UPG_GEANT. A pre-processing procedure was used to reduce computing time. This procedure selects high p_T ($p_T \geq 2.0$ GeV) electrons in the range $|\eta| \leq 3.0$. Only the particles within a cone of $\Delta R \leq 0.5$ around these electrons are kept. The resulting overall detection efficiency of electrons from Z's is found to be 80%.

1000 $t\bar{t}$ events were generated with ISAJET and again used as input to the UPG_GEANT program. The same pre-processing procedure as used for the $Z \rightarrow e^+e^-$ events was again used to reduce computing time. One t quark in each event was chosen to decay into $b + W$ with $W \to e + \nu$. The resulting overall detection efficiency of electrons from $t \to b + W, W \to e + \nu$ is found to be 70%.

About 3000 $b\bar{b}$ events were generated with ISAJET and also used as input to the UP-G_GEANT program. All the b quarks were chosen to decay into $c + e + \nu$. About 35 % and 16 % of electrons are lost by the H-matrix and E/p cuts, respectively. The hadrons that surround the b electron affect the H-matrix χ^2 and reconstructed energy. Approximately 32 % of electrons in the range $|\eta| \leq 3.0$ are found to survive all the cuts. This efficiency can be improved somewhat by tuning the H-matrix for non-isolated electrons.

These analyses and the major steps in the chain are summarized in Table 2.

Table 2

Summary of electron identification analyses

	e's from Z	e's from $t\bar{t}$	e's from $b\bar{b}$
Number in	1926	998	3800
Number after H-matrix cut	1626	783	1919
Number after position cut	1605	760	1770
Number after E/p cut	1557	732	1224

2.4 Physics Topics

In this section we present studies of the tracking system for a variety of physics topics. In many cases the topic has been on the menu for some time and some relatively complete studies, albeit missing the pattern recognition stage, have been presented. The goal of this section is to redress the balance and demonstrate the relevant track finding capability. Wherever possible, we have connected to the previous studies to complete the story. As a technical point it is often convenient when working with GEANT to choose a "muon" as the probe particle since its behavior in matter is fairly benign, unlike an electron. This makes the accounting problem in the program simpler. This is no more than a convenience tool; we are certainly not claiming, in the later b physics studies for example, that we have identification capability for muons with $p_T = 2$ GeV at $\eta = 0$.

2.4.1 Muon Reconstruction and $\mu\mu$ mass plots

Particles identified in the muon system have their momentum measured in the tracker. Thus, $D\emptyset_\beta$ provides a more precise measurement of muon properties than $D\emptyset_\alpha$. In order to investigate this, samples of $J/\Psi \rightarrow \mu^+\mu^-$, $Z \rightarrow \mu^+\mu^-$, and $Z' \rightarrow \mu^+\mu^-$ events were generated with ISAJET (or PYTHIA in the case of Z'). The events were then reconstructed with BETA_TRACK in the central tracker using fiber and silicon barrels, and the $\mu\mu$ effective mass obtained. In each sample, only those events which have both muons passing through the outer fiber super-layer were used to compute the invariant mass distributions.

The J/Ψ events were generated from $b\bar{b}$ events where the b's have a transverse momentum between 20 and 40 GeV. At least one b was required to produce a J/Ψ particle in each event, and the J/Ψ decayed to $\mu^+\mu^-$. From each J/Ψ at least one μ was required to have $p_T > 3$ GeV and $|\eta| < 1.8$. No vertex constraint was imposed in the track reconstruction. The reconstructed μ pair mass is shown in Figure 15. The mean of the distribution is 3.087 GeV and the σ of the gaussian fit is 0.072 GeV. This is to be compared to the current width of the J/ψ obtained with the $D\emptyset_\alpha$ data of 0.6 GeV.[8] The Z events were generated from quark annihilation and then forced to decay to μ pairs. The distributions of the generated and the reconstructed Z particle masses, and the mass difference between the two are shown in Figure 16. The mass difference plot gives a fit σ of about 3 GeV. Currently the $Z \rightarrow \mu\mu$ has a fit σ of 25 GeV using $D\emptyset_\alpha$ data. The Z' events were generated using a mass of 360 GeV and assuming a t mass of 160 GeV. The invariant μ pair mass distributions of the generated and the reconstructed Z' events, and the mass difference between the two are shown in Figure 17. The fit σ for the difference is about 35 GeV.

2.4.2 t-quark Physics and Isolated Leptons

In order to investigate the efficiency of finding isolated leptons from $t\bar{t}$ events, a sample of 100 $t\bar{t} \rightarrow W\overline{W}b\bar{b}$, $W\overline{W} \rightarrow \mu\mu$ events was studied. Unless otherwise specified, all t studies were made assuming a t mass of 120 GeV.

The pattern recognition program was run with a 0.5 GeV cutoff in p_T and, for these events, the fiber and silicon barrels were used to find tracks. The tracks were started using vector coordinates in the outer fiber super-layer and then extended to the inner barrel layers. Figure 18 shows the p_T distribution of the centrally produced μ's from this sample (by centrally produced, we mean that the tracks traversed the outer super-layer of the scintillating fiber portion of the tracker). 183 out of 200 of the μ's associated with the W's traversed that super-layer. A radial production vertex constraint was applied in the track fitting procedure.

The resulting μ reconstruction efficiency was 99-100% with no ghost tracks. Table 3 summarizes the numbers of generated and reconstructed muons, and ghost tracks, for the data noted above and for two other values of t mass.

Table 3

Number of generated and reconstructed central region μ tracks from $t\bar{t}$ events

t mass	120 GeV	160 GeV	200 GeV
Generated μ's	183	186	186
Reconstructed μ's	183	184	185
Ghosts	0	0	0

Figure 19 shows the resulting μ track resolutions, for the constant magnetic field and Figure 20 shows the same plots using a non-uniform field map. We see no appreciable difference in performance between the two cases. In addition, the track finding efficiencies remain the same.

An important question regarding our track finding package is whether or not the pattern recognition algorithms are robust. Specifically, one may ask what happens when the fiber digitization efficiencies are degraded by randomly reducing the hits throughout the scintillating fiber layers; there are provisions in the software for allowing for missed hits in any piece of the detector. The result is that we still find nearly all (99%) of the muon tracks with 10% of the digitizations randomly removed from every layer. Figure 21 shows the reconstruction efficiency of the muons as a function of the single fiber hit efficiency. It is very encouraging that we need only maintain a single fiber efficiency above 90% to provide a muon reconstruction efficiency of essentially 100%. Naturally enough, our zero ghost rate suffers as we relax the hit requirements in the barrels. For example, when allowing tracks to have vectors in only three fiber super-layers, we find six new ghost tracks associated with six of the 183 matched muon tracks.

2.4.3 t-quark Physics and b-quark Tagging

To investigate the efficiency of identifying $t\bar{t}$ events via b-jet tagging as a function of assumed t mass, two separate $t\bar{t}$ event samples (containing 100 events each) were generated for each assumed t mass. These $t\bar{t}$ samples consist of $W\overline{W}b\bar{b}$, $b\bar{b} \rightarrow \mu\mu$ and $W \rightarrow \mu +$ 4 (or more) jets. In addition, a background[9] W sample consisting of $(W \rightarrow \mu) + 4$jets was generated. In the following, these samples are referred to as $tb\mu$, $t\mu$j and Wj samples, respectively. VECBOS with ISAJET fragmentation was used to generate the Wj events. Jets in both $t\mu$j and Wj samples were required to have $E_T > 10$ GeV. Figure 22 shows the p_T distribution of the μ's from the $tb\mu$ sample.

The events were reconstructed as in the previous t physics section, except that in these samples it was not possible to use a radial vertex constraint (because of the displaced heavy flavor decay vertex). Again a 0.5 GeV p_T cut was imposed. The corresponding resolution plots for the μ tracks of the $tb\mu$ events are shown in Figure 23. Again, the resulting track reconstruction efficiency is 100% with no ghost tracks. For these muon tracks, the transverse distance (at the beam axis) resolution plot is shown in Figure 24a and the significance plot of r divided by σ_r is shown in Figure 24b.

Based on these results, we specify a b-quark tagging algorithm of 3 tracks with p_T>1 GeV and r/σ_r>3. Applying this algorithm to the $t\mu$j and Wj samples we obtain the $t\bar{t}$ tagging efficiency and false $t\bar{t}$ rate presented in Table 4. Note that this tagging efficiency does not depend on the muon; it applies to any b-jet.

Table 4

$t\bar{t}$ tagging efficiency versus t mass

t mass	efficiency
120 GeV	72%
160 GeV	78%
200 GeV	79%
Background	1%

Previously presented studies had estimated b-jet tagging efficiencies equivalent to the values obtained here.[3,5] At that time the importance of this technique for both the discovery of top and for the determination of the t mass was demonstrated.

2.4.4 New Physics Associated with High p_T τ's

The τ has the highest mass of all the known leptons. As a result, it often features in tests of postulated extensions to the standard model. Furthermore, τ decay offers the possibility of a polarization analysis. This feature has led to suggestions[10] that τ decay can be used to probe the couplings of higher mass bosons.

The simplest extensions beyond the minimal one-doublet standard model are those with two doublets of complex scalar fields which imply the existence of a charged Higgs (H^+). If $M_t > M_W + M_b$ and $M_t > M_H + M_b$, then $t \to H + b$ competes with $t \to W + b$ and H^+ decays into $\tau^+ + \bar{\nu}$ and $c + \bar{s}$. An excess of $\tau\bar{\nu}$ events over the standard model prediction (mainly from $t \to W \to \tau\nu$) will therefore signal new physics.[11] In SUSY-like models, the branching ratios can be written in terms of the three unknown parameters, M_t, M_H, and the ratio of vacuum expectation values tanβ. We have estimated the number of τ decays coming from H^+ bosons by varying these three parameters. As an example, a typical result is listed in Table 5 (Model I with tanβ=0.5) .[11]

Table 5

Number of $t \to H + b$ events with $H \to \tau + \nu$

$M_H \backslash M_t$	80	100	120	140	160	180	200
190	0	0	0	0	0	0	12
170	0	0	0	0	0	28	23
150	0	0	0	0	60	54	29
130	0	0	0	141	112	66	32
110	0	0	294	257	135	73	34
90	0	959	524	307	147	77	35
70	3428	1678	619	333	155	79	36
50	5899	1957	666	348	159	81	37

We assume 1000 pb^{-1} for the integrated luminosity and 0.1 for the overall detection efficiency of τ hadronic decays. The expected excess of $\tau\nu$ events can be small and depends strongly on M_t, M_H and tanβ. In order to detect this small signal, a careful analysis of τ hadronic decays is needed. Achieving an overall τ detection efficiency as high as 10% clearly depends on the ability of the pattern recognition to identify the τ decay products as such. In this respect, the analysis method using a magnetic tracking system as done by CDF[12] is superior to the analysis using jet event shape as done by UA2.[13]

In previous sections of this report, we have demonstrated the ability to find tracks efficiently and with minimal background in a range of different event topologies and from low to high p_T. This excellent performance promises good access to the τ physics arena.

2.4.5 $WW\gamma$ Coupling and the W Magnetic Moment

The $W\gamma$ production process probes the $WW\gamma$ vertex[14] and a non-standard model effect will appear as an anomalous magnetic moment or anomalous electric quadrupole moment of the W. We have generated ISAJET events for both $W\gamma$ and W-jet processes and studied the p_T spectrum of the γ, the rapidity spectrum of the γ, the p_T spectrum of the electron, and the $W\gamma$ invariant mass. The W-jet process is the major source of background and a series of cuts are applied[14] to reduce this background. Figure 25 shows the expected distributions for the ISAJET $W\gamma$ event sample. These plots were generated assuming an integrated luminosity of 1000 pb^{-1}. An anomalous magnetic moment effect would appear as an excess of events with high $W\gamma$ effective mass containing γ's with high p_T and low η. By scaling from the UA2 result,[15] which was based on 10 events, we obtain the 95% confidence level contours shown in Figure 26 for κ and λ, where the W magnetic moment is given by $\mu_W = e/2M_W(1+\kappa+\lambda)$ and the W electric quadrupole moment is given by $Q_W = -e/M_W^2(\kappa-\lambda)$.

The excellent DØ calorimetry plus upgraded tracker and preshower detector gives us the opportunity to have high efficiency for identifying these $W\gamma$ events.

2.4.6 b-quark Physics

Copious production of hadrons containing the b quark at the Tevatron permits a very broad range of studies. Recent results from CDF and from DØ show that it is possible to select high statistics clean samples of B states and J/ψ's. These achievements, taken together with the simulations reported previously for $DØ_\beta$, give good promise for detecting CP violation in the B-sector at the upgraded DØ. However, it should be stressed that many more crucial measurements are possible with $DØ_\beta$, many of them inaccessible to experiments in a e^+e^- collider. Among these unique studies are (1) B_s mixing and determination of V_{ts}; (2) Study of the B_c meson (with its unique spectroscopy of two heavy dissimilar quarks); (3) Exploration of the b-baryon spectroscopy; (4) Rare decays involving flavor changing neutral currents.

While a major thrust of the DØ Upgrade has been towards the high mass, high p_T physics, we have shown previously that, in principle, the acceptances and resolutions for tracks are adequate to make a significant contribution to b-physics. The phase space of the B-meson decay products fully populates the acceptance of the tracking system to $|\eta| = 3$ and beyond, and down to very low p_T. In particular, for b-quark physics one must have a high reconstruction efficiency for tracks which traverse all components of the tracking system: scintillating fiber barrels, silicon barrels and silicon disks. Thus, tracking in the b environment necessitates a deeper level of tracking system integration than does the t-quark physics discussed earlier.

We have generated $b\bar{b}$ events and selected $b \to \mu$ decays in two distinct η regions:

$\eta \simeq 2.0$ and $\eta \simeq 2.5$. In the first case, the muon traverses 4 silicon disks, 2 silicon barrels and 2 fiber barrels; in the second case it traverses 7 silicon disks and one silicon barrel. In either case we find a track finding efficiency of 100% and no distortion of the resolution functions compared to those shown earlier for isolated muon tracks.

We have then generated a sample of $b\bar{b}$ events and forced one of the B-mesons to decay to J/ψ and subsequently to a muon pair. The b-quark p_T was between 10 and 20 GeV and that of the muons greater than 2 GeV with $|\eta| \leq 4.0$. Figure 27 shows the distributions of the reconstructed minus the generated parameters for those tracks. They are very similar to the isolated muon distributions. In Figure 28 we show the difference between reconstructed and generated radial distance from the beam axis along with that radial difference divided by its error. The latter is a quantity analogous to that used to measure the significance of detachment of a secondary vertex from the primary which we have shown in previous studies. A cut of 3 in the radial quantity would give a 65% efficiency for identification of the muon as a b-quark decay product.

Finally, in Figure 29 we show the J/ψ mass resolution in two different η regions; the first has both muons accepted in the scintillating fiber barrels the second not. The resolution obtained in the mass is entirely compatible with that used in our previous, more simplistic, simulation studies of CP violation. The study presented here uses full pattern recognition in both disks and barrels. With the demonstration that the real field causes no degradation, we have confirmed the veracity of our earlier claims as to the properties of this tracking design for b-quark physics.

3. Existing Tracker Status

In a previous document,[3] we described how the existing $D\emptyset_\alpha$ tracking detectors were expected to respond as the integrated luminosity increased. The critical quantity is the charge deposited per unit length of sense wire. In general, deposits of 0.1-1 C/cm have been observed to kill or dramatically reduce the efficiency of chambers. A clear symptom of this effect is a reduction of pulse height for a given high voltage.

This effect has been monitored in $D\emptyset_\alpha$ and already we see measurable effects in chambers close to the beam. We will use the FDC Θ chambers as the example. Currently, a decrease of about 1.5 %/pb^{-1} in pulse height is observed for the inner cell (innermost 6 wires). Extrapolating linearly to 100 pb^{-1} would lead to pulse heights of less than 1% of their initial values rendering the inner cells useless.

Using the hit rates and pulse heights observed we have estimated the relationship between luminosity and charge deposition for the current operating parameters. We find that 100 pb^{-1} corresponds to approximately 0.2 C/cm. This is in agreement with our previous estimates.[3] The reduction in pulse height is also not dramatically different from the projections. The CDC, FDC Φ and FDC Θ cells at large radius show no measurable effect. So, although extrapolations of this nature are notoriously difficult, it appears that we should indeed be worried about the performance of the innermost tracking during Run Ib, by the end of which, we anticipate having accumulated 100 pb^{-1}. Further studies will be conducted during summer 1993.

4. Solenoid Design Status

A working group has completed the design and is preparing a design report, to be completed this month, for a thin, 2 Tesla superconducting solenoid to be inserted in the existing clear inner volume of the Central Calorimeter. A preshower detector will be installed in a narrow annulus outside the magnet cryostat to correct for electromagnetic energy lost in the coil and to give additional electron identification and pion rejection complementing the E/p resolution afforded by the field.

The magnet extends to $|\eta| \leq 1.6$ and the winding current density is enhanced at the magnet ends to increase the volume of uniform field, especially in the forward direction. The solenoid and cryostat have an overall radial thickness of 15.8 cm and 0.9 X_0 at $\eta = 0$, as shown in Figure 30. Figure 31 shows that the solenoidal field is quite uniform in the central region. A lead radiator of tapering thickness is installed on the outer diameter of the cryostat to make the total preshower radiator thickness 2 X_0 uniformly in η.

The design report for the solenoid details a base-line design for the magnet, cryogenic system, and operation and control system which meets all the detector and installation-dependent requirements that have been specified or identified.

The magnet is 2.75 m long x 1.45 m in diameter, with a clear bore of 1.13 m diameter, and it stores 5 MJ at 2 T central field. The stored energy is modest in comparison with the stored energy per cold mass of other existing thin superconducting solenoids (see Figure 32). It will operate at 4800 amperes and will be passively safe in the event of a quench. An energization, protection, and control system will enable the magnet to be charged in approximately 5 minutes and to be discharged without inducing a quench in about 10 minutes. No faster discharge system is required for magnet protection. The control system will regulate the operating current to better than 0.1%. A reversing switch is provided to permit convenient reversal of the field as desired. The control computer will be an extension of the existing process controller which operates the calorimeter cryogenic system.

The solenoid is wound with an aluminum-stabilized copper and NbTi superconductor supported by an aluminum bobbin. The cryostat is also aluminum. The magnet is quite far from the existing muon steel both radially and axially, and although the field will fringe strongly in the volumes occupied by the calorimeters and the innermost muon chambers, the forces between the magnet and the muon steel are quite small. The magnet cold mass support system will provide precision coil location following thermal cycling and energization, and will permit simple augmentation for shipping from a vendor's fabrication facility.

The coil is indirectly cooled by helium flowing in a cooling tube attached to the bobbin; the helium is supplied from a refrigerator/liquifier and is subcooled in a control dewar located on the existing cryobridge of the detector. The control dewar also supports the gas-cooled leads of the magnet at the interface between the water-cooled current buses and the superconducting leads of the magnet which run from the control dewar to the coil itself. These current leads and the cryogen lines for the magnet are conducted from the control dewar to the coil in a long vacuum-insulated chimney which threads its way in the existing gap between the CC and the EC cryostats to reach the coil.

A cryogenic system which also supports the cryogenic needs of the anticipated VLPC system of the scintillating fiber tracker will be installed in an annex to the DØ Assembly Building service building. The system will permit the independent cool-down, warm-up, and operation of either or both the VLPC or magnet systems. A convenient interface will be provided to the Tevatron helium system with compressor augmentation at DØ. Connection points in the cryogenic lines and electrical buses for the magnet are provided to permit operation of the magnet in both the assembly hall and the collision hall. The cryosystem will be able to cool the magnet from room temperature to operating temperature in about 120 hours.

Because the magnet system embodies the type of technical and industrial technology that is by now common, its procurement is expected to be straightforward and is estimated to provide delivery of a fully-tested magnet about two years after placement of the order.

5. Fiber R&D Status

The DØ collaboration has chosen, for both steps of the upgrade, to complement the inner silicon tracking detector with an outer tracker based on scintillating fibers. The attractive features of fiber tracking are well known: intrinsically prompt response, uniform detector coverage, the absence of active components in the detection volume, and overall simplicity of design. A fiber tracker can also provide an efficient charged particle trigger.

A schematic of a scintillating fiber tracking detector is shown in Figure 33. Concentric cylinders surrounding the interaction region are covered uniformly with plastic optical fibers doped with scintillating dyes. The light produced when a charged particle traverses a fiber is transported to the end of the cylinder where the scintillating fiber is mated with a clear optical fiber of similar construction. The light is "piped" along the clear fibers out of the detection volume to a photodetector. The photodetector output is amplified, shaped and discriminated, providing signals for both the readout and trigger.

The geometry of the fiber tracking design for the $DØ_\beta$ detector is given elsewhere in this document. In the rest of this section we will discuss the current status of the various components making up the fiber tracker, followed by a description of the upcoming large-scale test of the fiber tracking technology.

5.1 Current Status

Many advances have been made towards the development of a successful fiber tracking detector over the past year, and nowhere more importantly than in the optical fiber itself. Figure 34 shows the benefit of adding an outer cladding of fluorinated polymer to the "standard" fiber constructed of a polystyrene core surrounded by PMMA acrylic cladding. A 70% increase in light trapping is predicted and has been realized in tests performed earlier this year. In the DØ detector the scintillating fiber will be made up of a $775\mu m$ diameter polystyrene core surrounded by PMMA and then fluoro-acrylic claddings, each with a $15\mu m$ wall thickness (Figure 35). The scintillating core has been optimized to have a 1% concentration of p-terphenyl along with 1500 ppm of 3-hydroxyflavone, which fluoresces with a peak wavelength of 530 nm. The net result is an efficient scintillating fiber with high light yield and an attenuation length of roughly 5 meters. Large quantities of this fiber have been fabricated in industry (Kuraray Corp.). Typically the overall diameter of $835\mu m$ is held to better than 2% tolerance.

Before being placed on their support cylinders, individual fibers are fabricated into doublet ribbons, 128 fibers wide with a center-to-center spacing of $870\mu m$ as follows: a single layer of 128 fibers is placed into precision grooves, after which a thin fiberglass sheet, followed by a thin mylar sheet, are laid over the fibers. The whole assembly is glued together to make a single layer. The final doublet ribbon is made by gluing two singlet layers together, while maintaining a 1/2 fiber-diameter space offset between the two fiber layers. This results in a fiber ribbon which is durable, yet flexible enough to be molded onto a cylinder. The ribbons are also accurate. Figure 36 shows that the variation of the center-to-center spacing across a ribbon is controlled to $\sim 10\mu m$. Thus the contribution to the resolution of a fiber ribbon doublet from uncertainty in fiber location is negligible.

The support cylinders for the scintillating fiber ribbons are required to be rigid and precise, while maintaining as low an effective mass as possible. A prototype cylinder which achieves these goals has been purchased from Hercules Corporation. The prototype consists of a paper honey-comb mesh sandwiched between 7-mil thick cylindrical carbon fiber sheets. The total structure presents only 0.5% radiation lengths to a particle traversing at 90^o to the cylinder axis. Measurements comparing the prototype to an ideal cylinder yield $\sigma_r \leq 100\mu m$ for all points and $\sigma_r \leq 20\mu m$ locally (see Figure 37); well within the required tolerance.

To insure that the scintillating fiber ribbons are accurately placed onto their support cylinders, a technique has been developed which utilizes a large Coordinate Measuring Machine (CMM). This allows an essentially continuous monitoring of the fiber ribbon position relative to the cylinder, throughout the ribbon laying process. Ribbons can be accurately placed in the axial and stereo views. The procedure has been tested with a CMM large enough to accommodate the full DØ fiber tracker, and results are shown in Figure 38. The axial view fibers are parallel to the cylinder axis within approximately $30\mu m$ over the 2 meter length of the ribbon. Spacing between adjacent ribbons is also controlled with comparable precision. Thus, the uncertainty in position resolution will be dominated by the finite fiber size, rather than any uncertainty in fiber location.

Several options for mating the scintillating fibers with clear fiber waveguides are being investigated. In the DØ$_\beta$ detector, the connection will likely be achieved with mating connectors into which fibers will be glued and then highly polished with a diamond finishing tool. This technology can polish both individual fibers and fairly large surfaces with a flatness precision of better than 1μm. Several tests with individual fiber couplings have shown that light transmission greater than 90% can be obtained. Figure 39 shows one such result. To further improve light transmission, the clear fibers will have a 965μm diameter. This step-up in diameter makes the alignment within the connector less critical and has the added benefit of improved attenuation length over 835μm diameter fiber. The Step-1 version of the fiber tracker will probably require a different connection scheme due to the limited available space. Possible solutions include thermally fusing clear fibers to their scintillating counterparts, or fusing short clear "pigtails" which are subsequently connected to longer clear fibers in the region between the fiber tracker and the forward drift chamber. The technique of thermally fusing fibers is well understood and also provides a better than 90% light transmission.

The photodetector of choice for the DØ fiber tracker is the Visible Light Photon Counter, or VLPC. This solid-state device, manufactured at Rockwell International, is capable of high-rate, single photon counting with a quantum efficiency greater than 70%. Figure 40 shows the layout for an 8x1 pixel VLPC array mounted on its substrate. Each of the eight 1 mm diameter pixels is connected via a wire-bond to the substrate, which in turn is connected to the downstream electronics via low-capacitance flat-ribbon cable. Typically the VLPC has a gain of about 10^4 at an operating voltage of 7-8 volts.

Rockwell has produced some 100000 channels of VLPC devices as part of an R&D program to explore the relevant parameter space. DØ and Rockwell agreed on a specification for 5000 channels purchased by DØ. These devices have now been fabricated. Sample devices from each production wafer have been characterized at Rockwell. The 8-channel arrays have been cut from the wafers, prepared with a back-side metallization, and are now being delivered to FNAL. The first chips have arrived within the past month. Arrays will be mounted onto substrates, wire bonded, and then characterized as a function of operating bias and temperature before installation in the system test.

Design of the electronics downstream of the VLPC is under way. Tests have shown that the VLPC works well with a room-temperature amplifier, which enables the amplifier to be combined with shaping and discrimination circuitry in a single card at the warm end of the cassette. This ASD card will send the digital signals from hit fibers to the VME-based readout via an optical link. Efforts are being made to keep the design as close to the silicon electronics as is feasible.

One of the challenges of using VLPC readout is that the devices must be operated at a temperature around 6-8 K, requiring a helium cryogenic system. A great deal of progress towards the development of such a system has been made at DØ . A total of 128 VLPC channels are packed into a 25cm-long cylindrical container known as a "cassette", shown in Figures 41 and 42. Light is brought to each pixel via short lengths of clear fiber inside the cassette. These short fibers are optically coupled at the top of the cassette to the long clear fibers piping the light from the detector. Each of the 16 VLPC arrays is mounted on a copper structure which acts as an isotherm to guarantee that all channels are at the same temperature to within tens of milli-Kelvin. Twenty-four such cassettes are contained in a single cryostat, which is shown schematically in Figures 43 and 44. The cryostat operates as a two-phase system. A reservoir of liquid helium sits at the bottom of the cryostat, while a cold layer of gaseous helium surrounds each cassette and maintains the VLPC's at their operating temperature. The temperature can be controlled by adjusting the flow rate of the gaseous helium up the cassette, or with the use of small heating resistors mounted in the copper isotherm. A prototype cryostat, using the same two-phase concept, but holding a single cassette, has been fabricated and tested at FNAL with excellent results. A stable temperature was achieved and controlled to better than 10 milli-Kelvin. Design of a full-scale cryostat is complete, and the first unit is being assembled with operation expected in June.

We believe that the key technological, mechanical and design issues associated with a scintillating fiber tracking detector are now well understood. The next important step is the demonstration that such a detector can be operated smoothly and stably over an extended period of time. This summer we will operate a 3072-channel scintillating fiber detector, tracking cosmic ray muons. The test is discussed in detail below.

5.2 Cosmic Ray Test

Several tests of scintillating fibers read out by VLPC's have already been performed. Results have been published from the UCLA cosmic ray test[16] and from a FNAL beam test T-839.[17] The cosmic ray test showed that sufficient light yield for fiber tracking was achievable, while in the beam test clear tracks were seen in fibers read out by 32 channels of VLPC. In a subsequent beam test performed at BNL in summer 1992, approximately 1 million events were recorded and analyzed. In this test, 96 fiber ribbons were read out by 96 channels of VLPC. Spatial resolutions of $\sim 130\mu m$ were obtained for doublet layers of $835\mu m$ fibers.

A cosmic ray test at FNAL is planned for this summer. Figure 45 shows a schematic view of the cosmic ray test setup. Approximately 3000 scintillating fibers, assembled into ribbons, will be precisely placed on top and bottom portions of a support cylinder, with a third plane of fibers inside. The scintillating fibers cover the entire cylinder length of 2 meters and are arranged in the standard super-layer structure (two stereo doublets sandwiched between two axial doublets). Each of these fibers will be connected to an 8-meter-long clear fiber via optical connectors coupling 128 fibers per connector. The support cylinder sits atop a 2-meter stack of iron which will provide a minimum momentum cut of about 2.5 GeV for triggering muons. The iron is also segmented to allow some selection of lower momentum tracks. A system of Iarocci tubes will be added to help determine tracking resolution. The entire structure resides in a dark house in Lab 6 at FNAL.

The readout system for the cosmic ray test will incorporate the VLPC cassette and cryostat exactly as described above. A 3000-gallon dewar will supply liquid helium for the cryostat, allowing steady operation of the detector for 4-6 weeks. Amplification of the

VLPC output is done at the top, warm end of the cassette. Each cassette will contain four 32-channel amplifier cards based on the QPA02 chip. Prototypes of this card have been manufactured and successfully tested, and a full production run is under way. The amplifier outputs are fed to a LeCroy 1885 ADC system which in turn is read out via FASTBUS. The complete data acquisition system is up and running in Lab 6, along with a variety of display and monitoring programs. Figure 46 shows one view of a simulated cosmic ray traversing the detector.

An additional feature of this test will be the incorporation of an LED- based calibration and monitoring system. The non-readout ends of the scintillating fibers will be coupled to arrays of LEDs. The LEDs will be under computer control which will enable light to be injected into any combination of fibers. This system will be very useful in the debugging phase of the cosmic ray test, and more importantly, will enable us to measure quickly the relative gain and long-term stability of each of the 3072 channels.

The cosmic ray test will be the major focus of the fiber tracking effort for the next several months. This test will exercise, over an extended time, nearly all the key elements which make up a fiber tracking detector. This large scale test is the final step needed to prove the viability of scintillating fiber tracking for the DØ upgrade.

6. Silicon R&D Status

The $D\O_\beta$ silicon tracker is designed to maintain good impact parameter resolution over the full η coverage of DØ . It consists of interleaved disk and barrel detectors surrounding the interaction region. This disk/barrel geometry provides a solution to the problems imposed by the combination of a long interaction region and complete η coverage. Many of the electronic and mechanical issues have been considered and preliminary designs have been developed. Prototypes exist for the internal supports, cooling systems, external spaceframe and detectors.

6.1 Detectors

The $D\O_\beta$ tracker design requires both single-sided and double-sided silicon detectors. Single-sided detectors are used for the large area "H" disks at large z, which provide momentum resolution for tracks at large values of η. Double-sided detectors are used for the "disk" planes, which provide vertex resolution for the high and intermediate η tracks. The barrels will also use single-sided detectors. Pairs of these detectors, one with two layers of metallization, may be used to provide stereo information in the barrel.

6.1.1 Single-Sided Detectors

The single-sided AC coupled detectors proposed for the barrels and H disks are now standard technology for manufacturers. Our studies to date have concentrated on testing of prototypes provided by Moscow State University (MSU) and Micron Semiconductor.

MSU has begun a program of working with Russian industry to produce silicon detectors for DØ . The first detectors arrived at FNAL last summer and we have performed tests for leakage current, depletion voltage, and breakdown voltage. Probe test results for typical detectors are shown in Figure 47. In general we find about 5% of the strips have problems with either high leakage current or shorts in the AC coupling dielectric.

We have also tested MSU detectors using a Ru-106 source and an SVX readout system. The source is collimated and the trigger consists of a 1 mm diameter scintillating fiber and a thick counter with an upper cut on the pulse height to ensure that we are counting energetic Ru decay electrons. The data were analyzed by looking for clusters of summed pulse height greater then 1/3 minimum ionizing, with strip pulse heights greater than 1/10 minimum ionizing. Figure 48 shows our results for position, pulse height, cluster size and number of clusters for normal incidence.[18] These tests are encouraging and we feel that with some improvement in quality control and new masks, the MSU detectors will be acceptable for the H disks.

6.1.2 Double-Sided Detectors

We have received the first shipment from SINTEF-SI of AC coupled double-sided detectors. The processing of these detectors is much more complex than single-sided devices, with more than double the number of mask steps and much more careful handling required. Figure 49 is a photomicrograph of the p-side of one of the SI detectors, showing the guard rings and polysilicon bias structures. Some preliminary probe tests of the detectors have been done, which indicate that the total leakage currents in the current shipment are higher than our specifications.

We are also investigating the option of providing stereo information in the barrels. We are constrained by cooling and geometry considerations to place the readout chips at the edges of the barrels. In this geometry an additional layer of interconnectivity (double metallization) has to be added to bring the signals from the wide side to the edge where the readout occurs. One option is a double sided double metal design. Such a detector is technically difficult to construct and is likely to be expensive. A more conservative option is to use a back-to-back 250μm thick single-sided detectors, where the $r-z$ detectors have double metallization. This can be achieved with current technology at a lower cost than the double-sided double metal option, but with a penalty in mass.

6.2 Mechanical

Much of our mechanical design work has been in the context of the approved Step-1 silicon tracker. We expect that the designs for the Step-1 disk modules and the barrel ladders will be unchanged for the full upgrade. We also expect to retain our basic cooling (water using laminar flow) and assembly and alignment philosophy. We expect the detailed design of the barrel support bulkheads and spaceframe to change due to requirements for interspersed disk and barrel modules and the different radii involved.

6.2.1 Cooling and Readout Support

Silicon detectors are read out by SVX-II chips mounted on the detectors. Each of the 128 channel SVX-II chips is expected to dissipate about 400 mW of power. The detector itself must be kept at room temperature or below to control the effects of leakage currents on the noise. We have chosen a design using water cooling in the laminar flow region. This choice allows for good cooling efficiency with low pressure drop, allowing a sub-atmospheric pressure water system design. The laminar flow system imposes geometric constraints on the disk and barrel supports since the cooling efficiency is determined by the aspect ratio of the rectangular water channel.

Another important aspect of the design is the readout support system (Figure 50). The design that we have chosen draws heat from the chips through a 300μm Be plate which is in thermal contact with the cooling channel. The detector is thermally isolated from the heat sources. Electrically-insulating, thermally- conducting connections are made with diamond film epoxy. We are in the process of producing prototype mounts and testing the epoxy for mechanical stability and effects on the detector surface.

6.2.2 Barrel Ladders

The barrel detectors are supported in "ladders"; the ladder support is constructed out of both carbon fiber reinforced plastic (CFRP) and Rohacell. The Rohacell acts as a carrier for the CFRP, where a large part of the ladder stiffness is derived from the distance between the CFRP pieces. A number of ladders have been made for mechanical and thermal testing. The basic design will work well for both single and double-sided barrels. We plan to build a working single-sided ladder this summer using SVX-H chips and the expected readout support structure.

6.2.3 Disk Supports

Like the barrel bulkheads the disk supports are expected to fill the dual roles of cooling and support. The current design consists of a simple ring with a rectangular water channel. Water flow tests have been performed on prototypes.

6.3 Electronics

6.3.1 SVX-II Chip

Both the CDF and DØ$_\beta$ silicon detectors will use the SVX-II chip now being developed by a FNAL-LBL collaboration. This chip will include a preamp which can be optimized for several beam crossing intervals, including 132 and 396 ns, an analog delay line, and an ADC. Prototypes of each subsection are now in the final design stage or being fabricated. The readout and control protocol has been specified. We expect that the first fully integrated rad-soft chip will be available by the end of this calendar year.

6.3.2 Interconnections

A compact, high density, system such as the silicon tracker requires reliable, high density interconnections. Structures such as the one on which the SVX-II integrated circuits are mounted are known in the electronics industry as multichip modules (MCM). We have decided that copper on kapton (flex circuit) technology laminated on a beryllium plate will provide the best low mass thermal, and electrical performance. Prototype MCM's designed for the current generation of SVX chips have been fabricated for detector prototype work. MCM design for the higher speed SVX-II will proceed as the pinout of the chips are specified.

The silicon tracker will consist of approximately 1000000 channels. Careful consideration of cable design and signal multiplexing is crucial to a successful design. We plan to avoid the need to make a direct mechanical connection to the detector modules by including a microstrip pigtail on the edge of the detector MCM's. Multiple MCM pigtails are connected to a bus cable using a demountable unidirectional (Fujipoly) connector. We are currently in the process of fabricating and testing microstrip cables and interconnects.

6.3.3 Readout System

The SVX-II circuit requires a complex control and readout system. There are two major components, the "port card", and the VME interface card. Our design calls for a microstrip cable connection between the detector and the port card and a high speed optical link between the port card and the VME readout card located in the movable counting house.

The VME card includes buffers for incoming data and outgoing commands, optical links to the port cards, and a high speed port used to transfer data to an external level 1.5 trigger processor. The design for this card is almost complete, pending final specification of the trigger port.

The port card will be mounted on the detector and contains the logic to generate commands and clock signals for control of the SVX-II chip. Signals are transferred to the port card from the VME via optical cable. Commands and clock control for the SVX are generated by a state machine in a gate array on the port card. Data from the chip is sent to VME through a port card interface which includes a high speed parallel to serial converter and optical fiber drivers.

7. Conclusion

In this document we have discussed the status of both hardware and software components of the proposed DØ tracking system upgrade.

The solenoid design meets all our requirements. The FNAL Research Division is in the process of conducting a review of the Solenoid Design Report. Procurement could commence within a few months.

The silicon system design has progressed well with much of the original design concept holding up; advanced prototyping and engineering design is well under way.

The scintillating fiber tracking technique has made several important advances over the past year or so. Excellent double clad fibers are now commercially available and the latest batch of VLPC devices appears to meet our design specifications. All technical measures relating to specific subsystems of the fiber tracker have now been shown to meet our prior specifications and the simulations show that the resulting tracking detector will perform efficiently and with the desired resolution. We regard the cosmic ray tests over the summer as the final step needed to demonstrate that all these subsystems can work effectively and reliably together for extended periods of time.

We have developed advanced simulation, track reconstruction and analysis software and all of our studies unambiguously indicate that we can achieve high efficiency and excellent resolution in the challenging high-rate Tevatron environment. In particular, we have responded to the specific comments received from the PAC one year ago.

The progress reported here on hardware and simulated performance of the proposed DØ upgrade, taken together with the remarkable achievements of the detector now in place, represent a unique opportunity for physics in the latter part of this decade. The potential is large for advances in understanding the top quark, testing the SU(3)×SU(2)×U(1) Standard Model, exploring the quark-mass matrix parameters, and searching for new phenomena outside the minimal SM in the years before the SSC and LHC. We have demonstrated the ability of the $D\emptyset_\beta$ detector to lead the way in all of these high-priority and fundamental physics issues.

Since the original proposal for the DØ upgrade in Fall 1990, we have shown that the $D\emptyset_\beta$ detector will fulfill these broad physics goals. The proposed upgrade is based upon detector techniques which have been thoroughly studied and documented over the past two and a half years of the proposal process. It builds upon the inherent strengths of the DØ detector – namely, its hermetic, uniform coverage calorimeter and muon detection systems. Limiting the main elements to be upgraded to the small tracking volume has the benefit of controlling the overall cost of the upgrade.

With the conclusion of the successful R&D program and the simulation of the DØ upgrade, we believe that it is time to begin building this detector. We request Stage-I approval for the full upgrade at this time. Delay in starting the DØ upgrade, accompanied by the aging of the existing tracking detectors and the completion of much of the physics program accessible with the present detector, would diminish the Tevatron potential. We believe that the upgrade project should be completed in late 1997, in time for Run II with high luminosity and shortened bunch time interval. We expect that following the Stage-I approval, there will be FNAL technical reviews of those subsystems not yet approved for detector equipment funds. This Laboratory review should be taken as the opportunity for final check and verification that the technical developments (such as the large-scale system tests now underway for the fiber tracking) remain positive.

REFERENCES

1. The DØ Detector, S. Abachi et al., to be published in NIM (1993).
2. The DØ Upgrade, unpublished (1990).
3. P823 (DØ Upgrade): Responses to the Physics Advisory Committee, DØ note 1148 (1991).
4. E823 (DØ Upgrade): R&D and Optimization Progress Report, DØ note 1322 (1992).
5. E823 (DØ Upgrade): Step-1 and Beyond, DØ note 1421 (1992).
6. Optimization of the DØ Step-1 Fiber Tracking System, DØ Note 1619 (1993).
7. R&D Results on Scintillating Tile/Fiber Calorimetry for the CDF and SDC Detectors, P. de Barbaro et al., SDC Note SDC-91-168 (1992).
8. C. R. Murphy, DØ note 1703 (1993).
9. F. A. Berends et al., Fermilab-Pub-90/213-T (1990).
10. J. D. Anderson et al., Phys. Rev. Lett. 69 (1992) 25.
11. J. F. Gunion et al., The Higgs Hunter's Guide, Addison-Wesley (1990).
12. F. Abe et al., Phys. Rev. Lett. 68 (1992) 3398.
13. J. Alitti et al., Phys. Lett. B280 (1992) 137.
14. U. Baur and E. L. Berger, Phys. Rev. D41 (1990) 1476.
15. J. Alitti et al., Phys. Lett. B277 (1992) 194.
16. M. Atac et al., NIM A320 (1992) 155.
17. B. Abbott et al., NIM A327 (1993) 319.
18. A. Leflat et al., DØ note 1709 (1993).

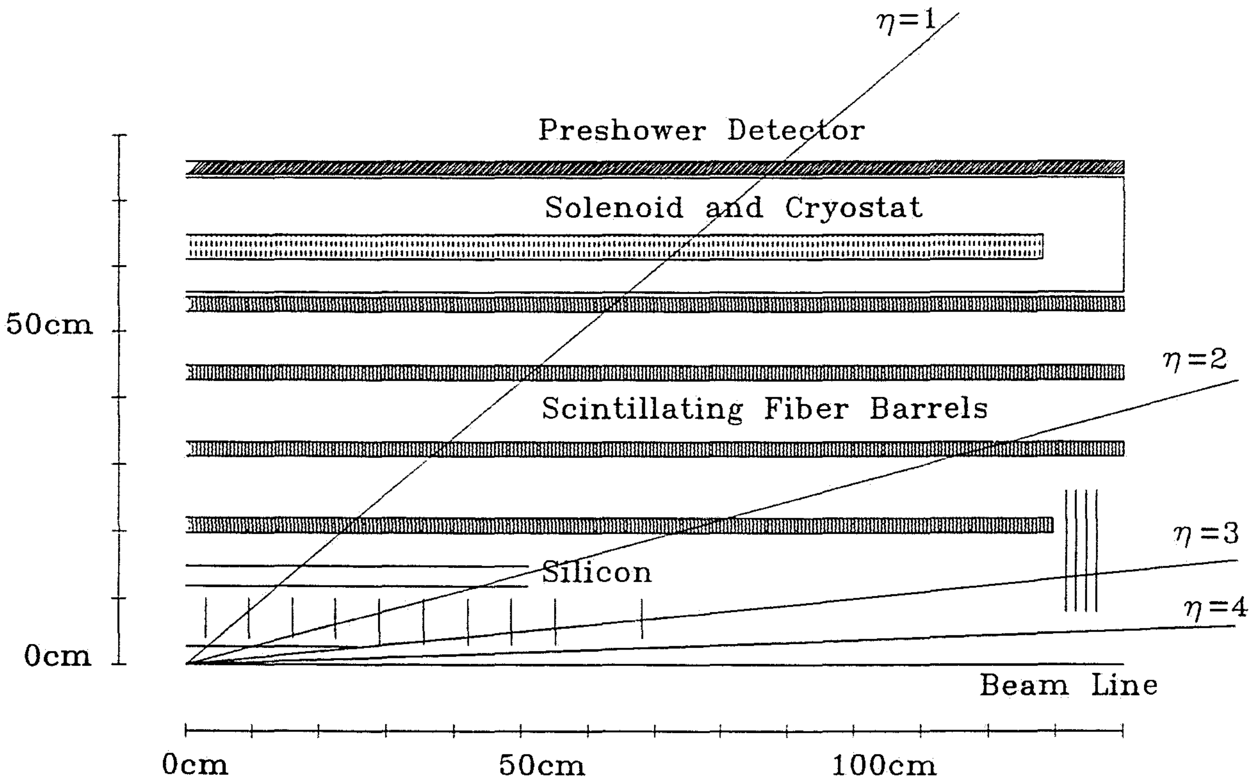

Figure 1 Layout of the DØ upgrade showing solenoid, scintillating fiber super-layers, silicon barrels and disks and the preshower detector.

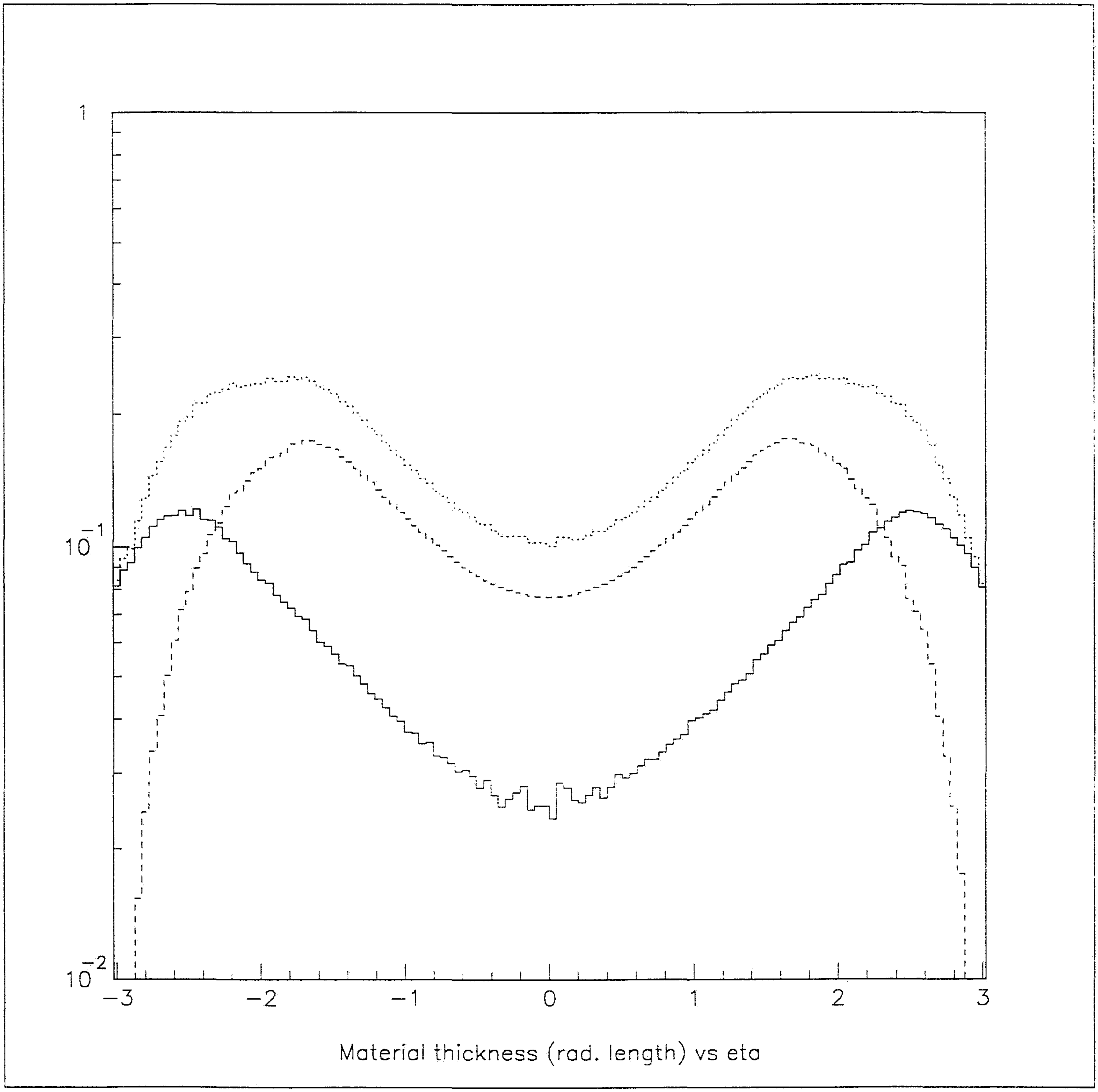

Figure 2 Tracking volume material versus pseudo-rapidity. The lower curve shows material associated with the silicon detectors, the middle curve the scintillating fiber super-layers and the upper curve shows the sum of the two.

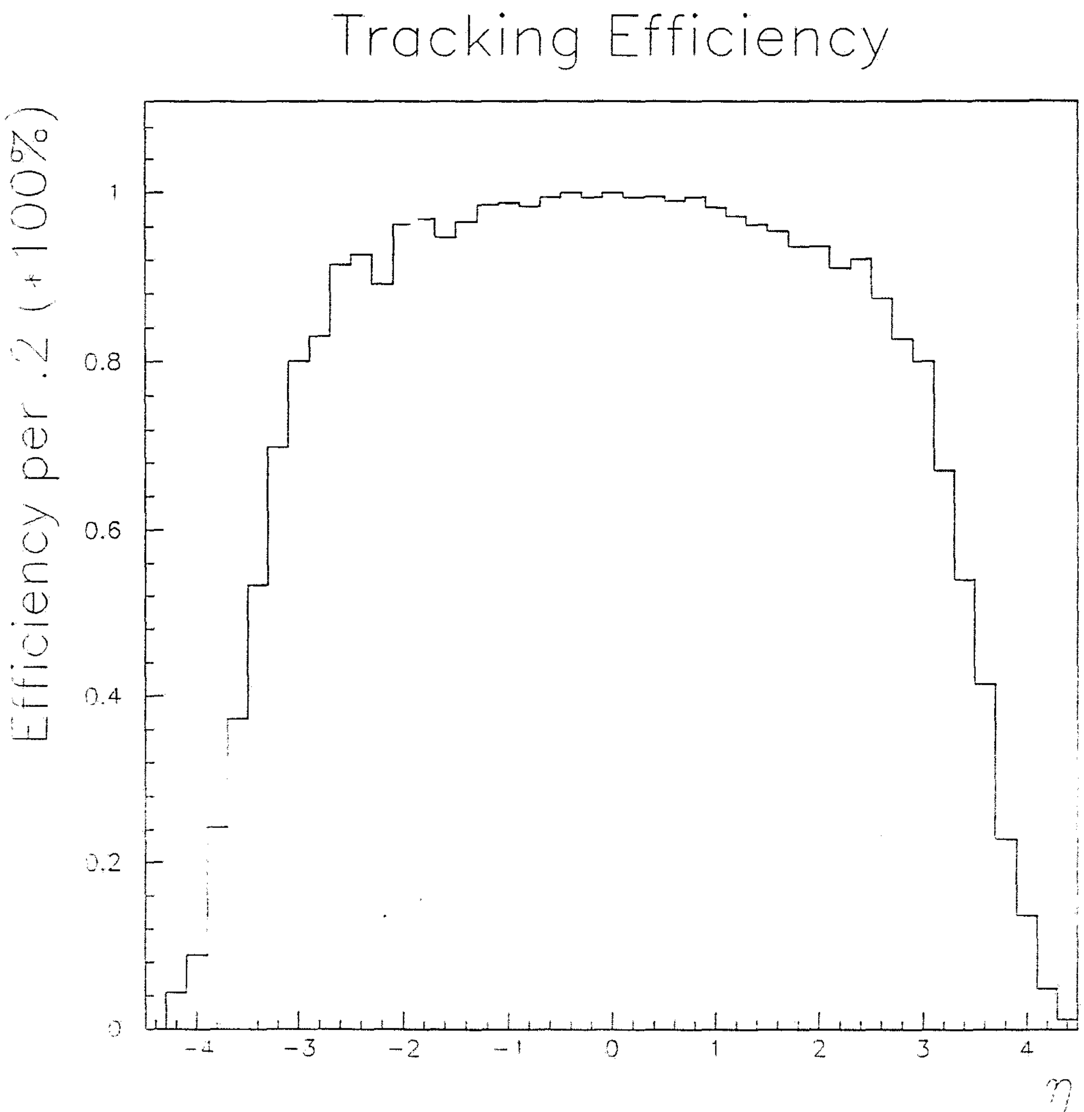

Figure 3 Isolated track reconstruction efficiency versus pseudo-rapidity.

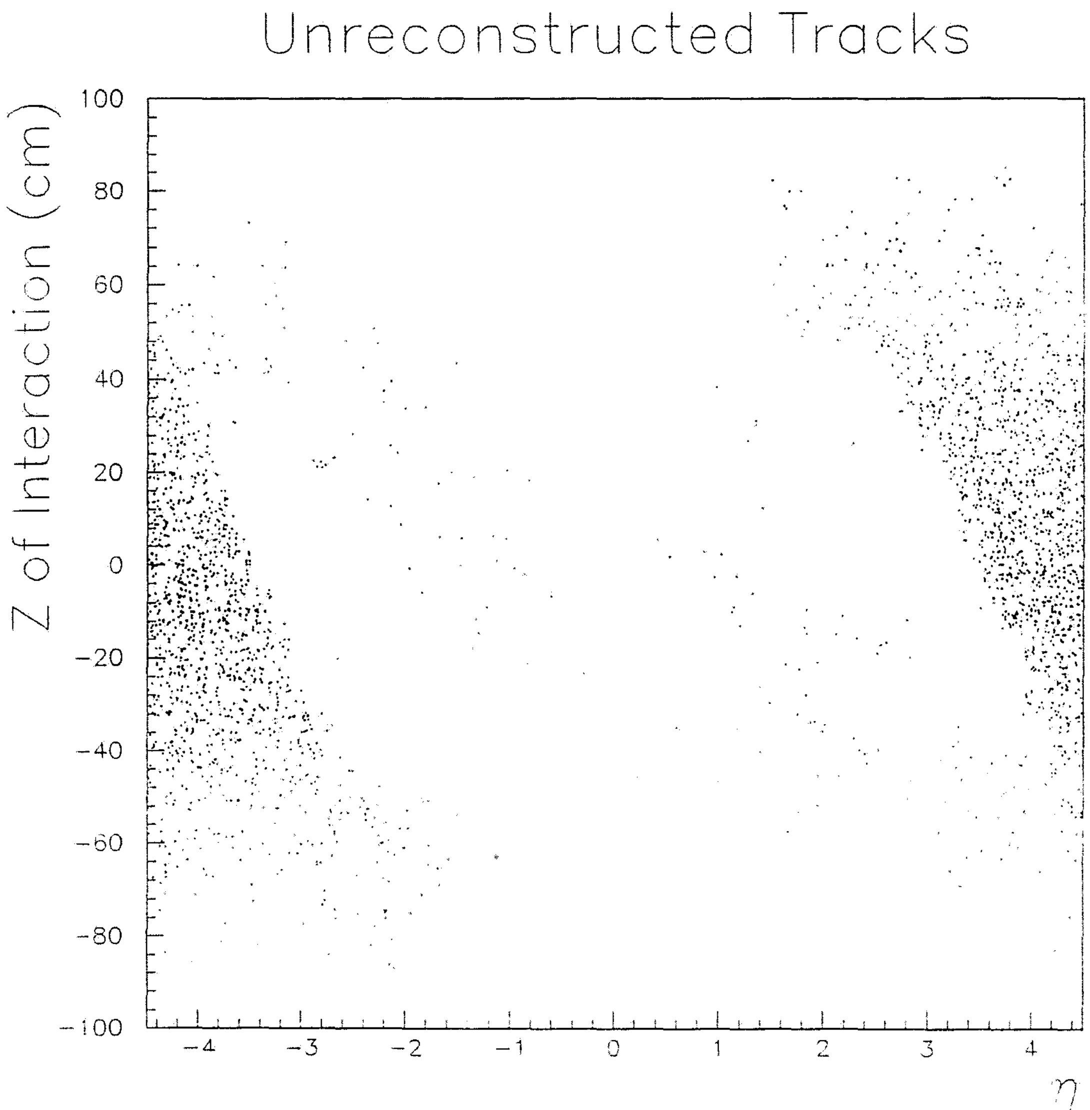

Figure 4 Scatter plot in η-z of isolated tracks which fail to be reconstructed.

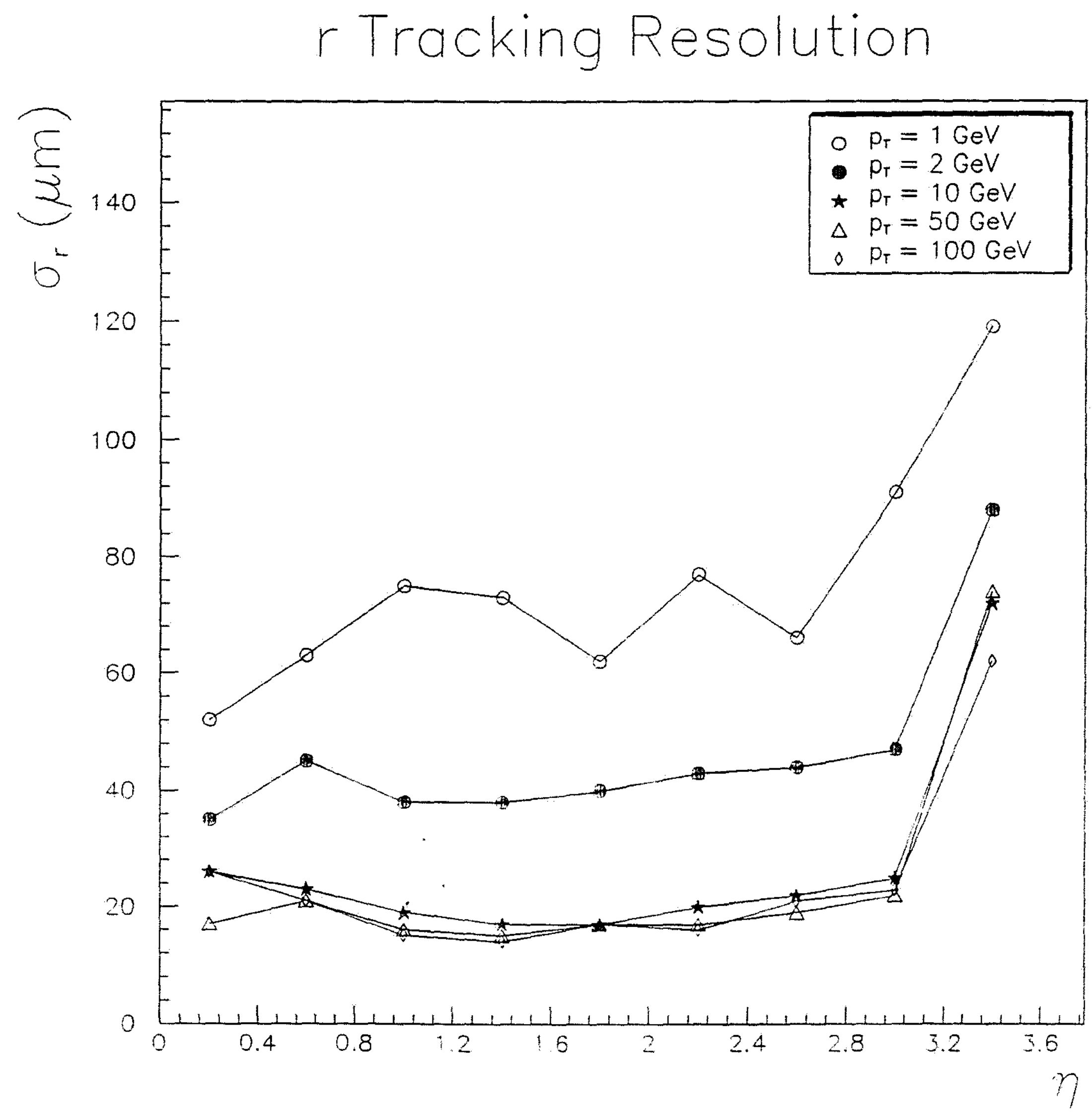

Figure 5 Isolated track transverse coordinate (r) resolution versus pseudo-rapidity.

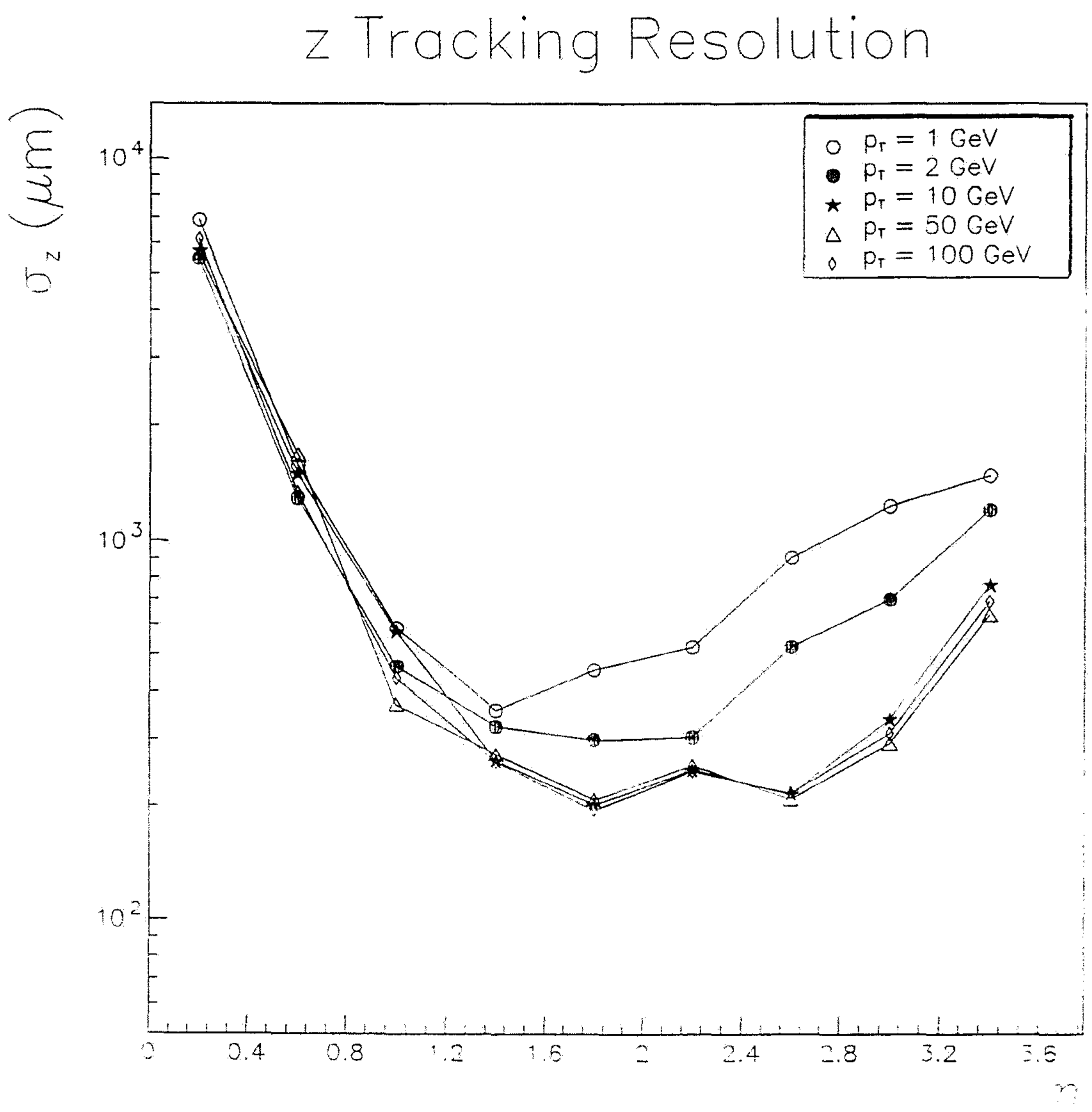

Figure 6 Isolated track beam axis coordinate (z) resolution versus pseudo-rapidity.

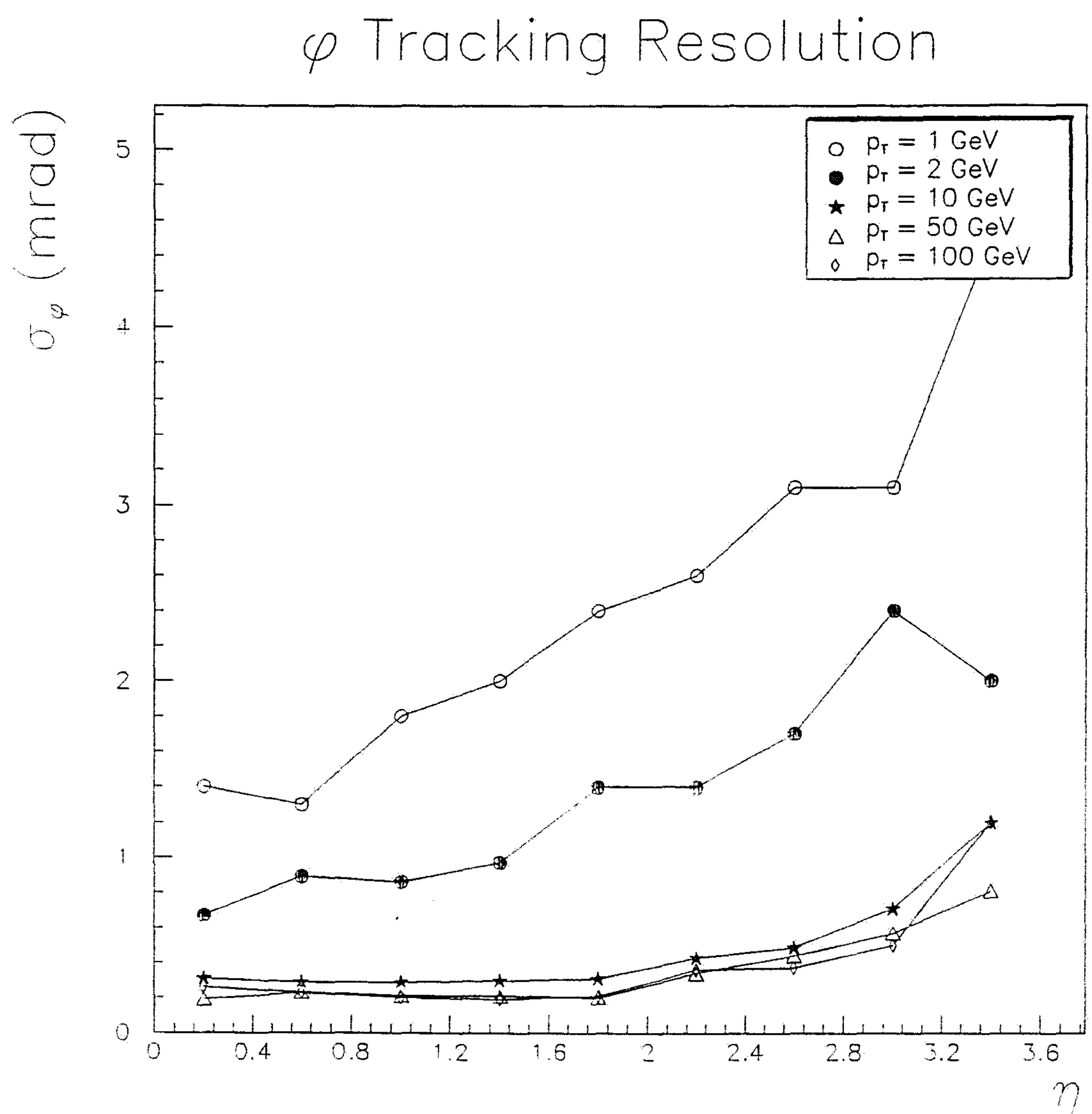

Figure 7 Isolated track ϕ angle resolution versus pseudo-rapidity.

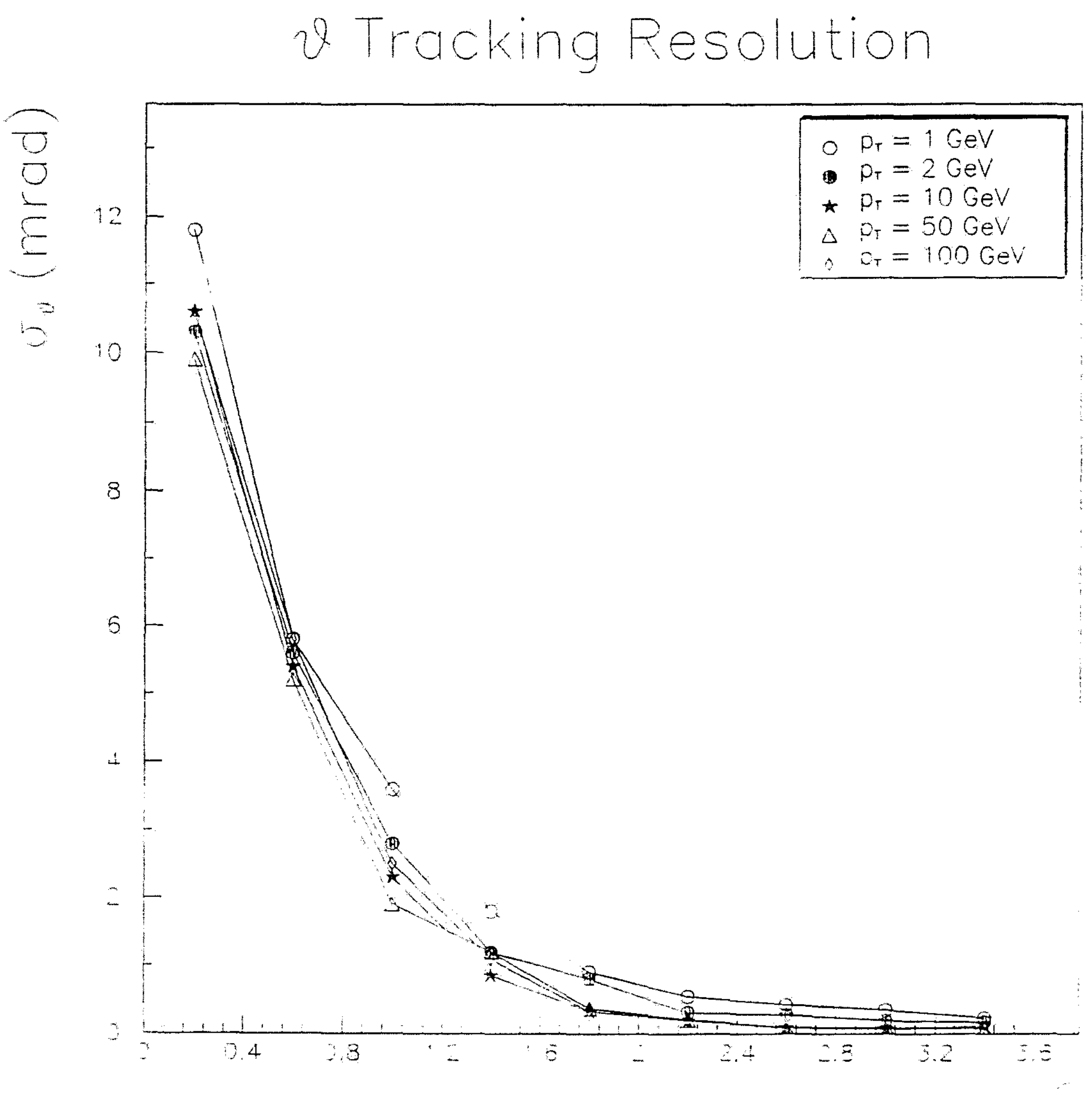

Figure 8 Isolated track θ angle resolution versus pseudo-rapidity.

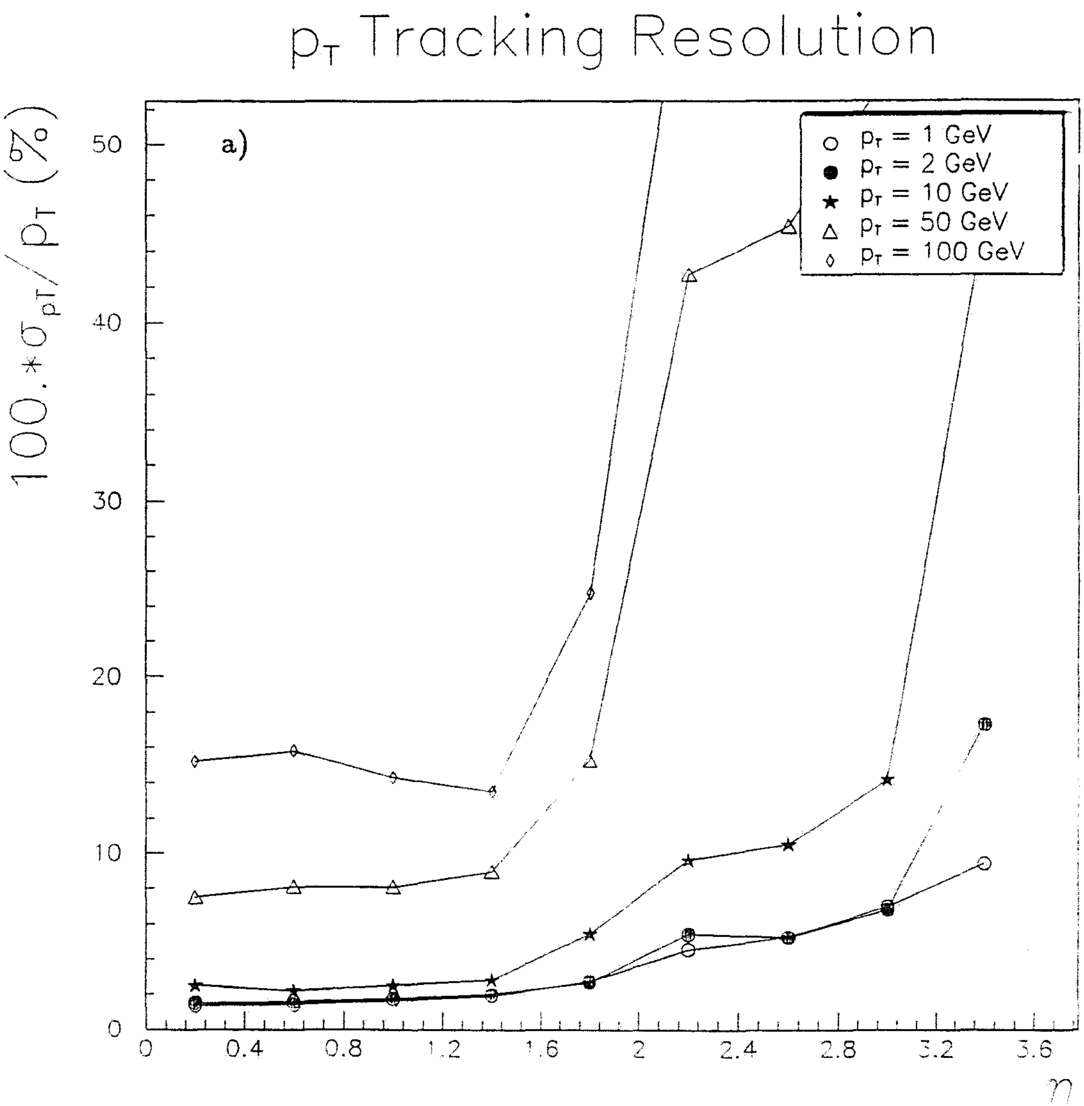

Figure 9 Isolated track transverse momentum (p_T) resolution versus pseudo-rapidity:

a) without radial vertex constraint;

b) with radial vertex constraint.

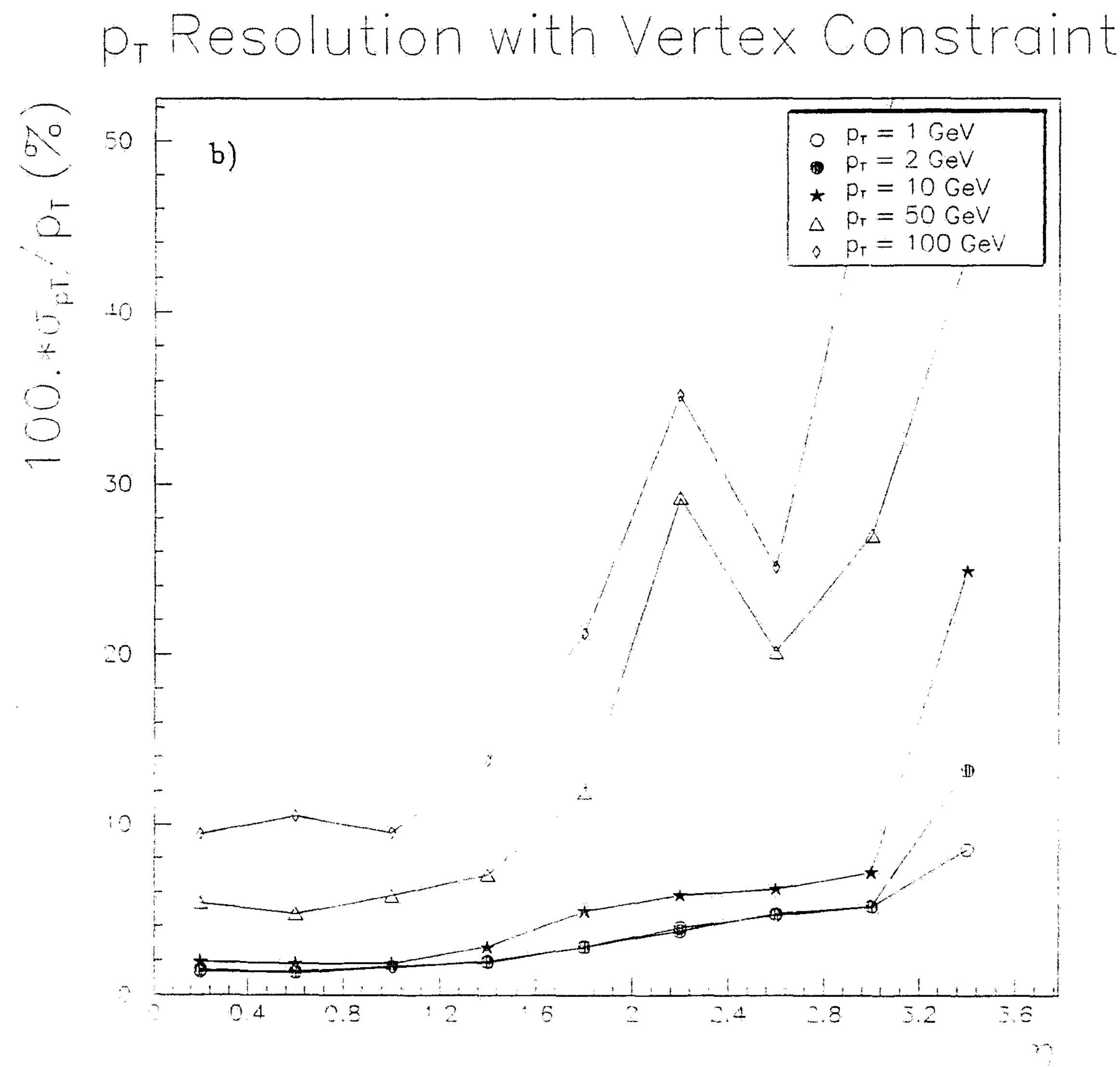

Figure 9 b) with radial vertex constraint.

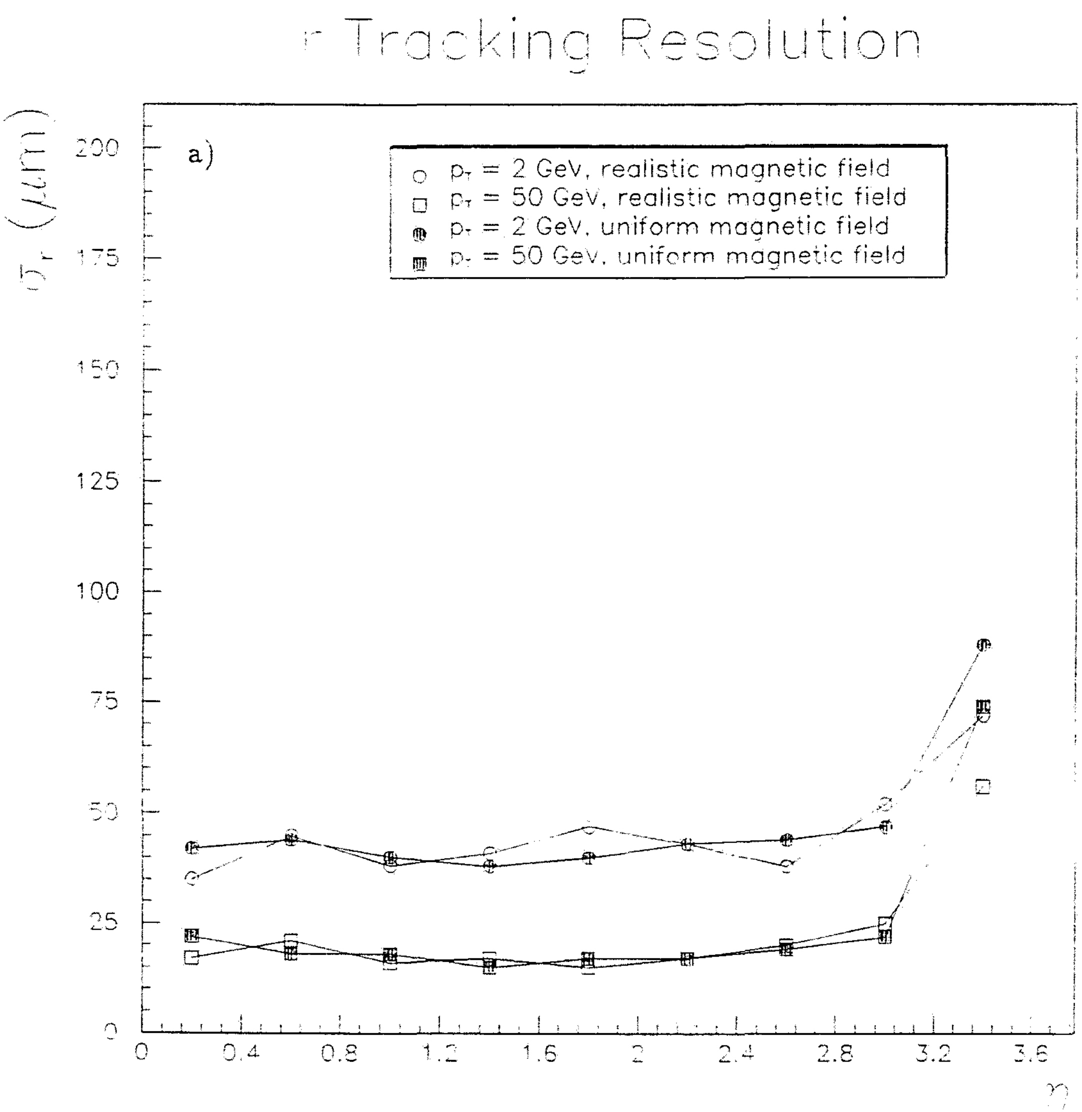

Figure 10 Comparison of single track reconstruction characteristics for 2 GeV and 50 GeV tracks with constant magnetic field and with the full, non-uniform magnetic field map:

a) r resolution versus pseudo-rapidity;

b) z resolution versus pseudo-rapidity;

c) ϕ resolution versus pseudo-rapidity;

d) θ resolution versus pseudo-rapidity;

e) p_T resolution versus pseudo-rapidity.

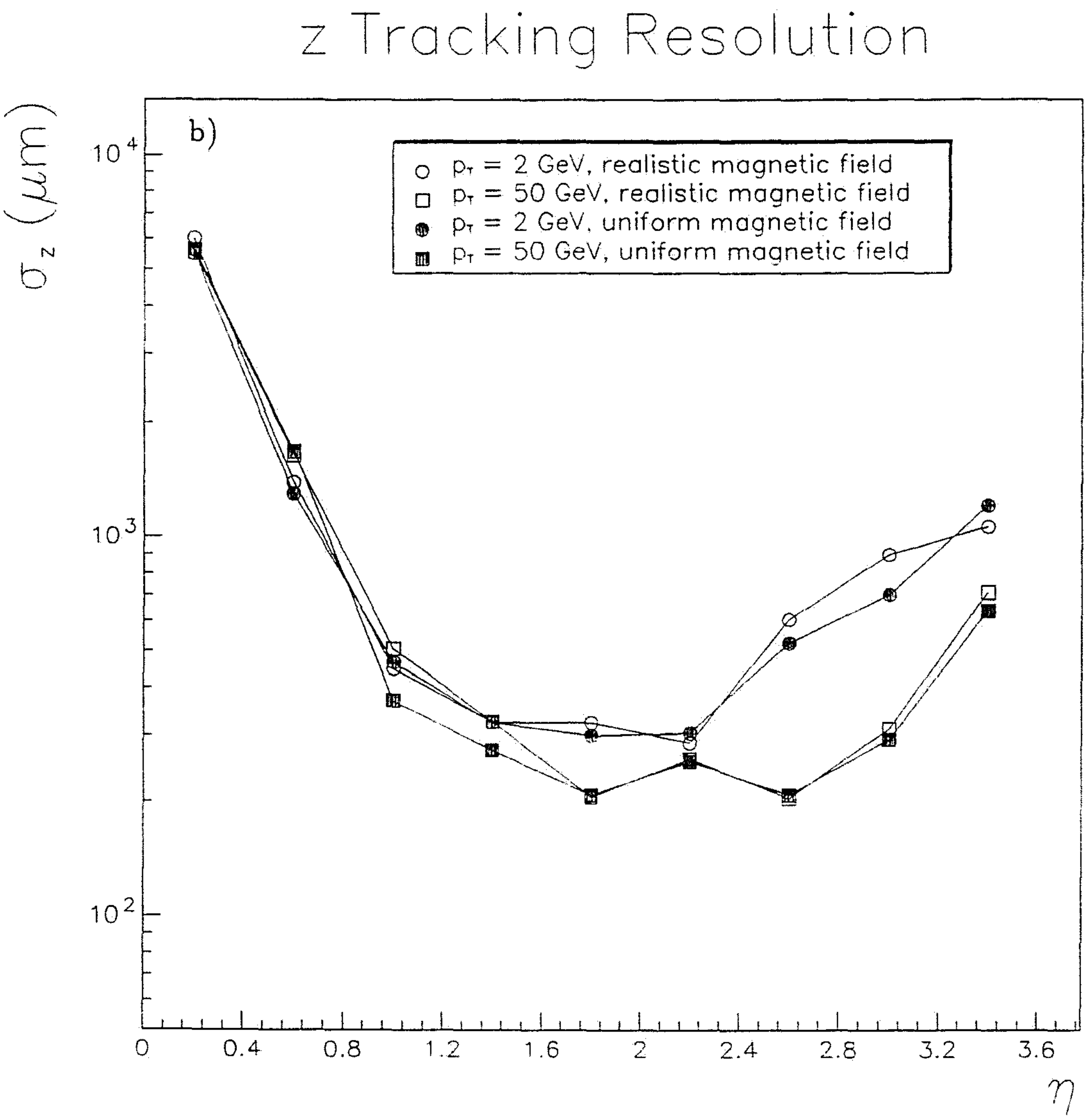
z Tracking Resolution
b)
p_T = 2 GeV, realistic magnetic field
p_T = 50 GeV, realistic magnetic field
p_T = 2 GeV, uniform magnetic field
p_T = 50 GeV, uniform magnetic field
σ_z (μm)
10^4
10^3
10^2
0
0.4
0.8
1.2
1.6
2
2.4
2.8
3.2
3.6
η

Figure 10

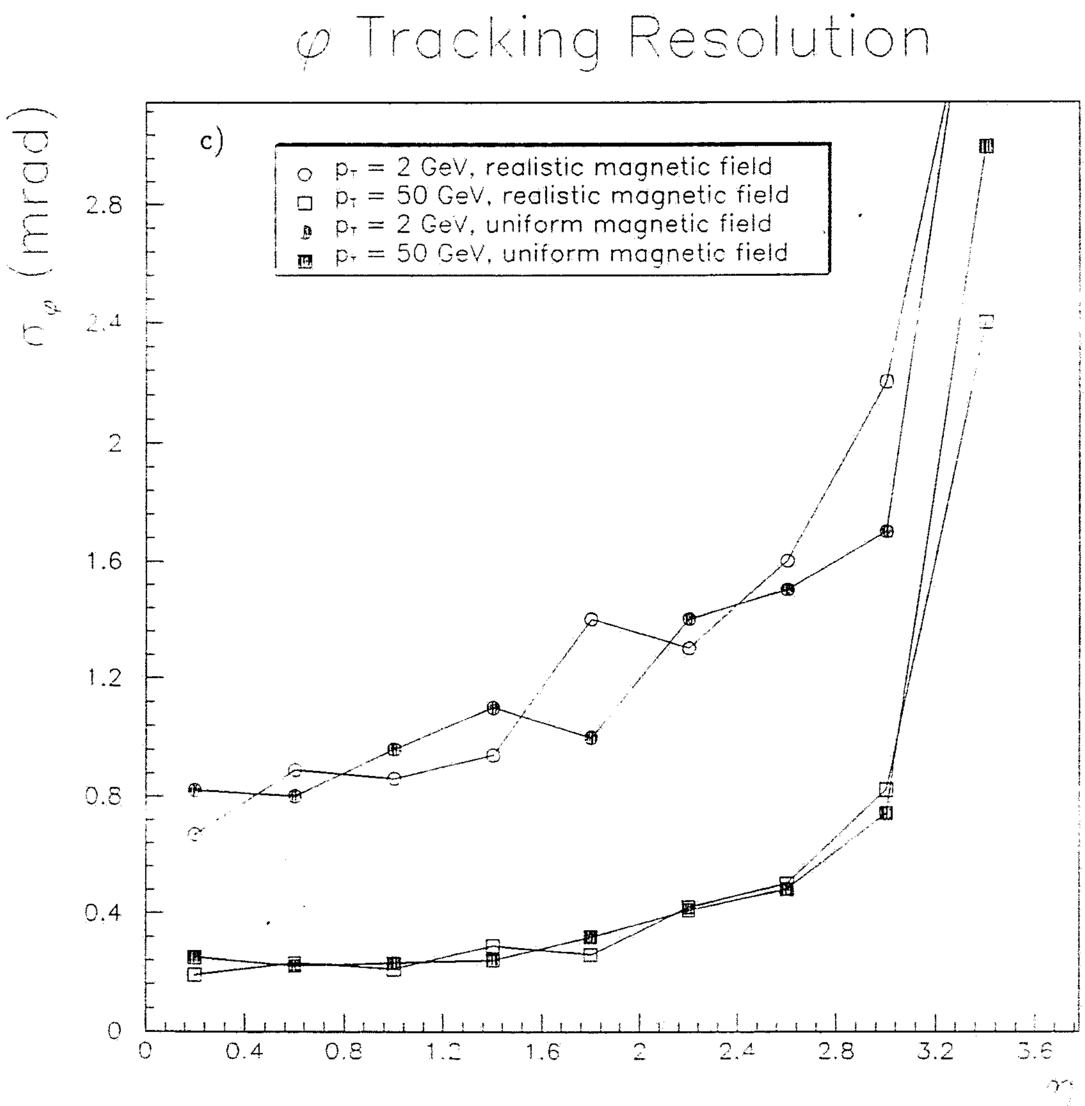

φ Tracking Resolution
σ_φ (mrad)
c)
p_T = 2 GeV, realistic magnetic field
p_T = 50 GeV, realistic magnetic field
p_T = 2 GeV, uniform magnetic field
p_T = 50 GeV, uniform magnetic field
2.8
2.4
2
1.6
1.2
0.8
0.4
0
0
0.4
0.8
1.2
1.6
2
2.4
2.8
3.2
3.6
η

Figure 10

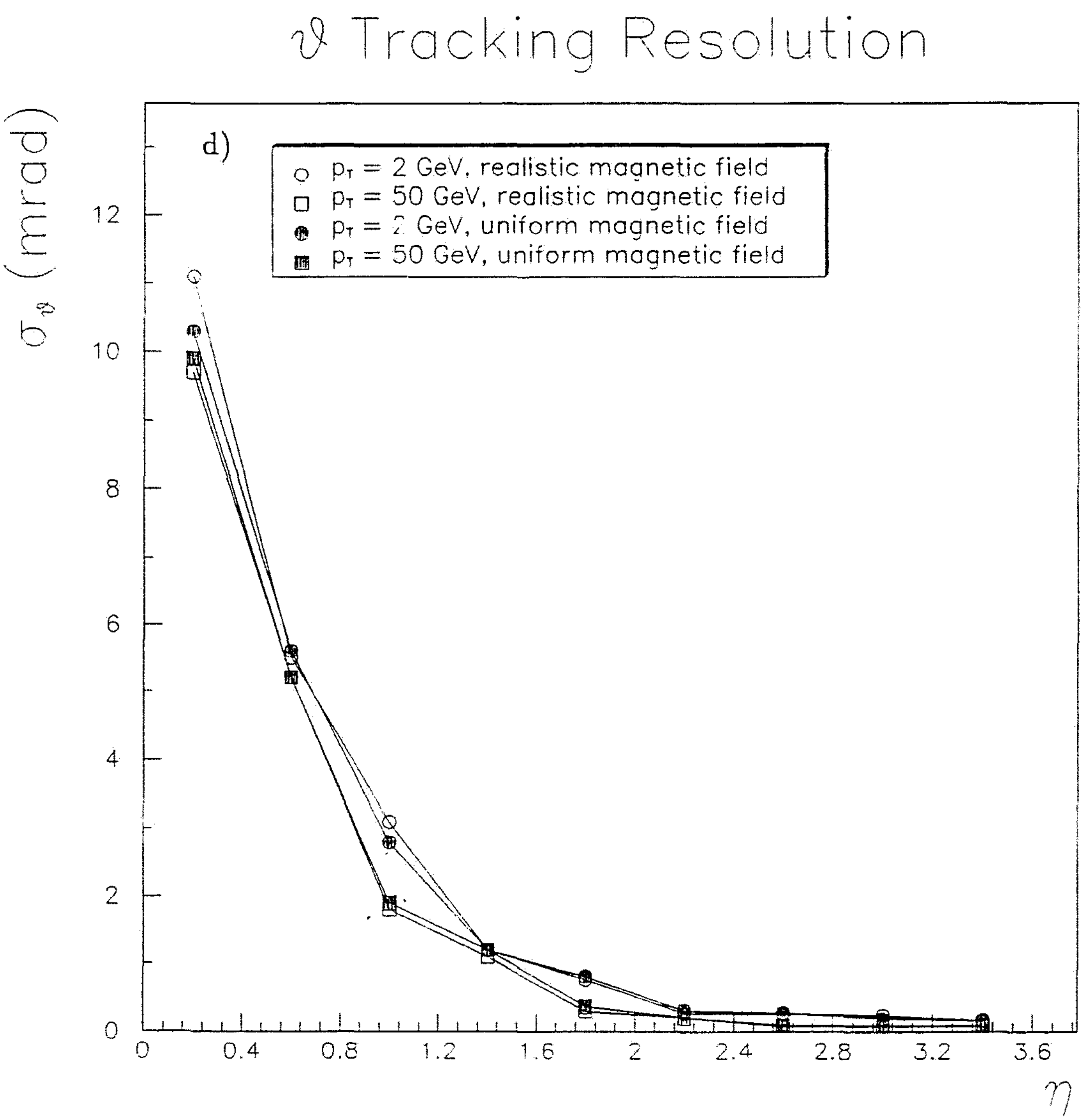

ϑ Tracking Resolution
σ_ϑ (mrad)
d)
p_T = 2 GeV, realistic magnetic field
p_T = 50 GeV, realistic magnetic field
p_T = 2 GeV, uniform magnetic field
p_T = 50 GeV, uniform magnetic field
12
10
8
6
4
2
0
0
0.4
0.8
1.2
1.6
2
2.4
2.8
3.2
3.6
η

Figure 10

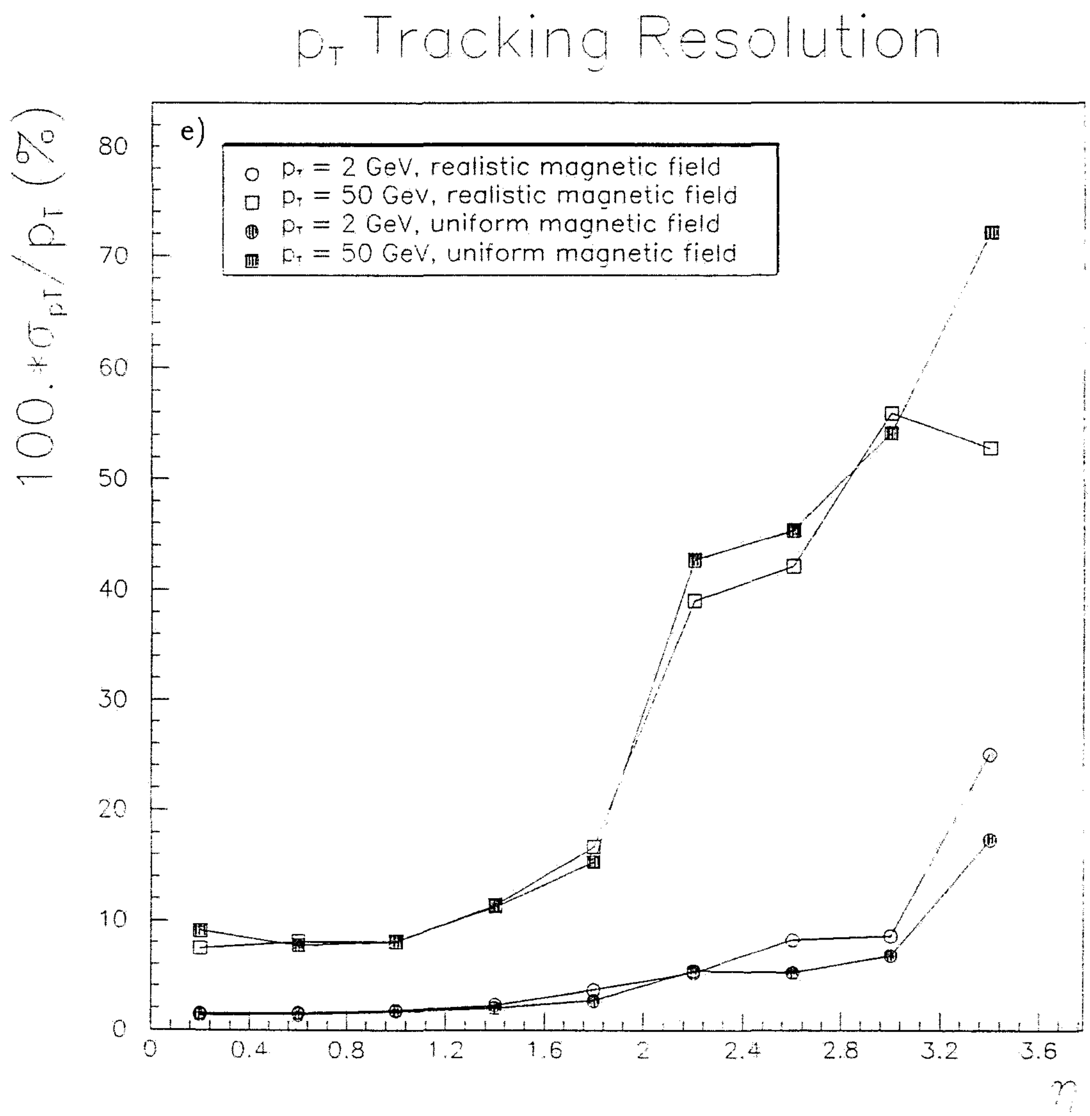

p_T Tracking Resolution
e)
p_T = 2 GeV, realistic magnetic field
p_T = 50 GeV, realistic magnetic field
p_T = 2 GeV, uniform magnetic field
p_T = 50 GeV, uniform magnetic field
$100.*\sigma_{pT}/p_T$ (%)
0
10
20
30
40
50
60
70
80
0
0.4
0.8
1.2
1.6
2
2.4
2.8
3.2
3.6
η

Figure 10

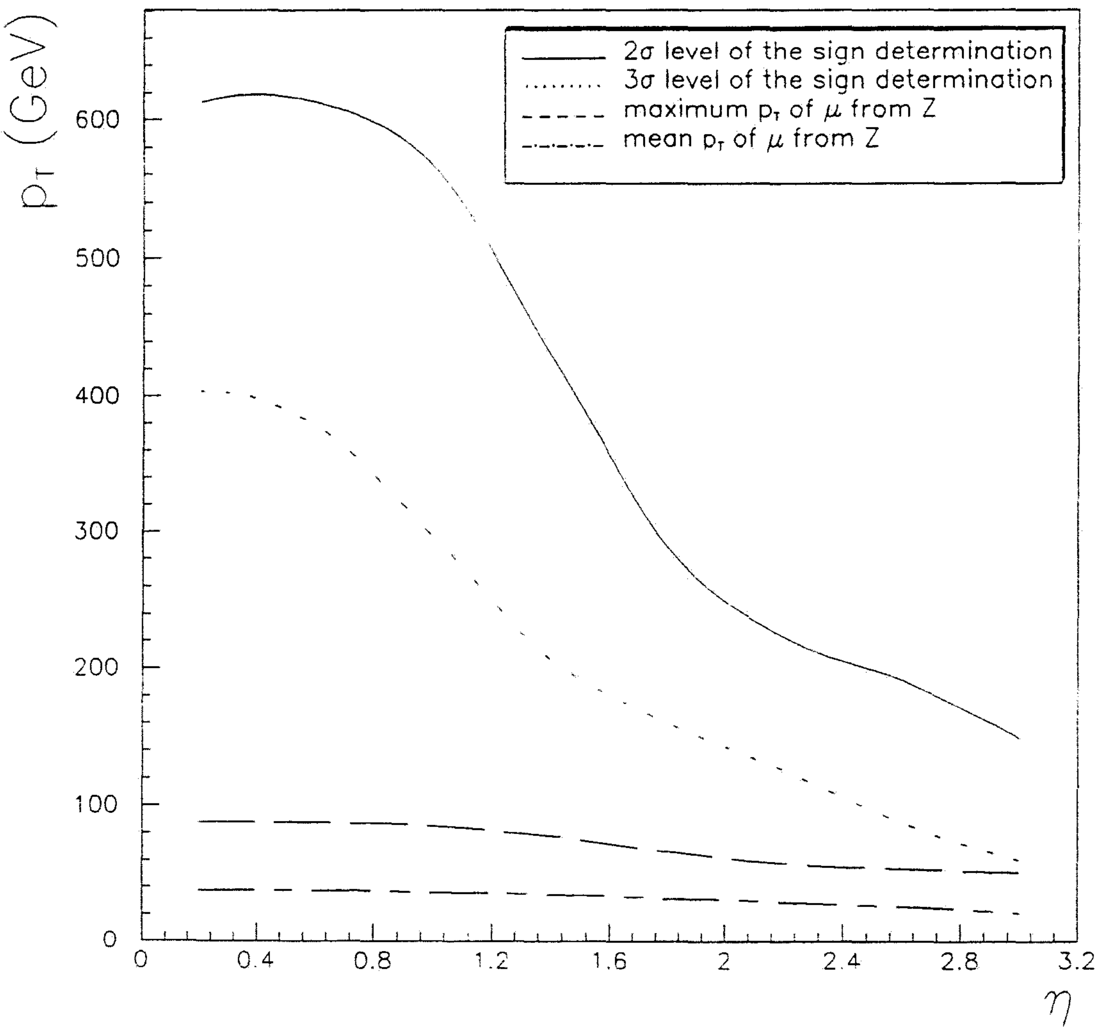

Figure 11 Limits at the 2 and 3 standard deviation level versus η for determining the sign of charged particles in $D\O_\beta$. Also shown are the mean and maximum p_T of μ from Z decay.

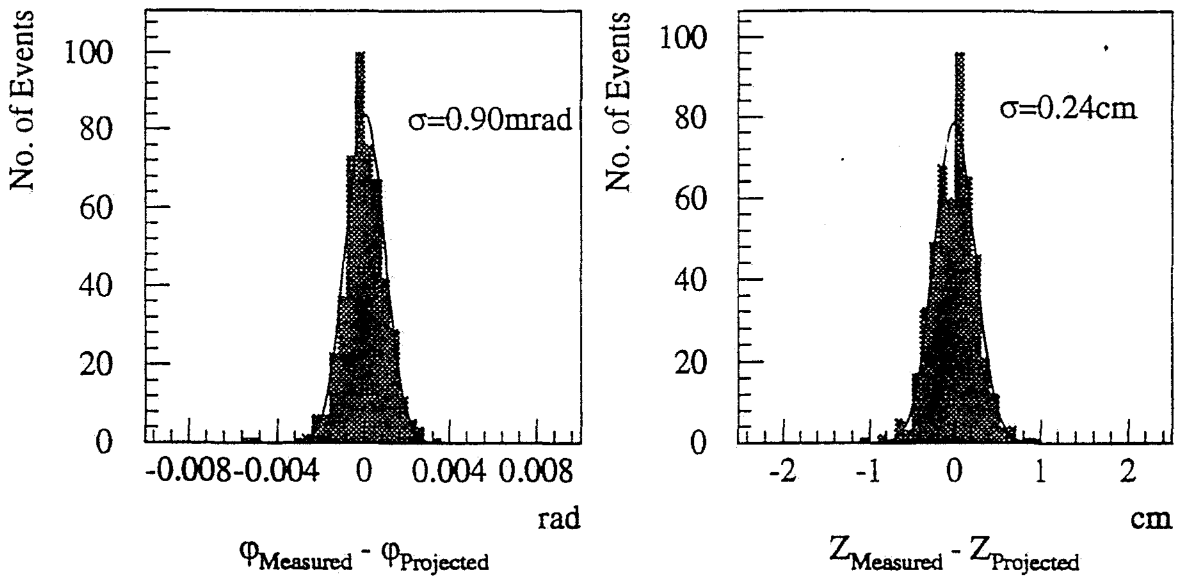

Figure 12 Preshower position resolutions in ϕ and z for 50 GeV isolated electrons.

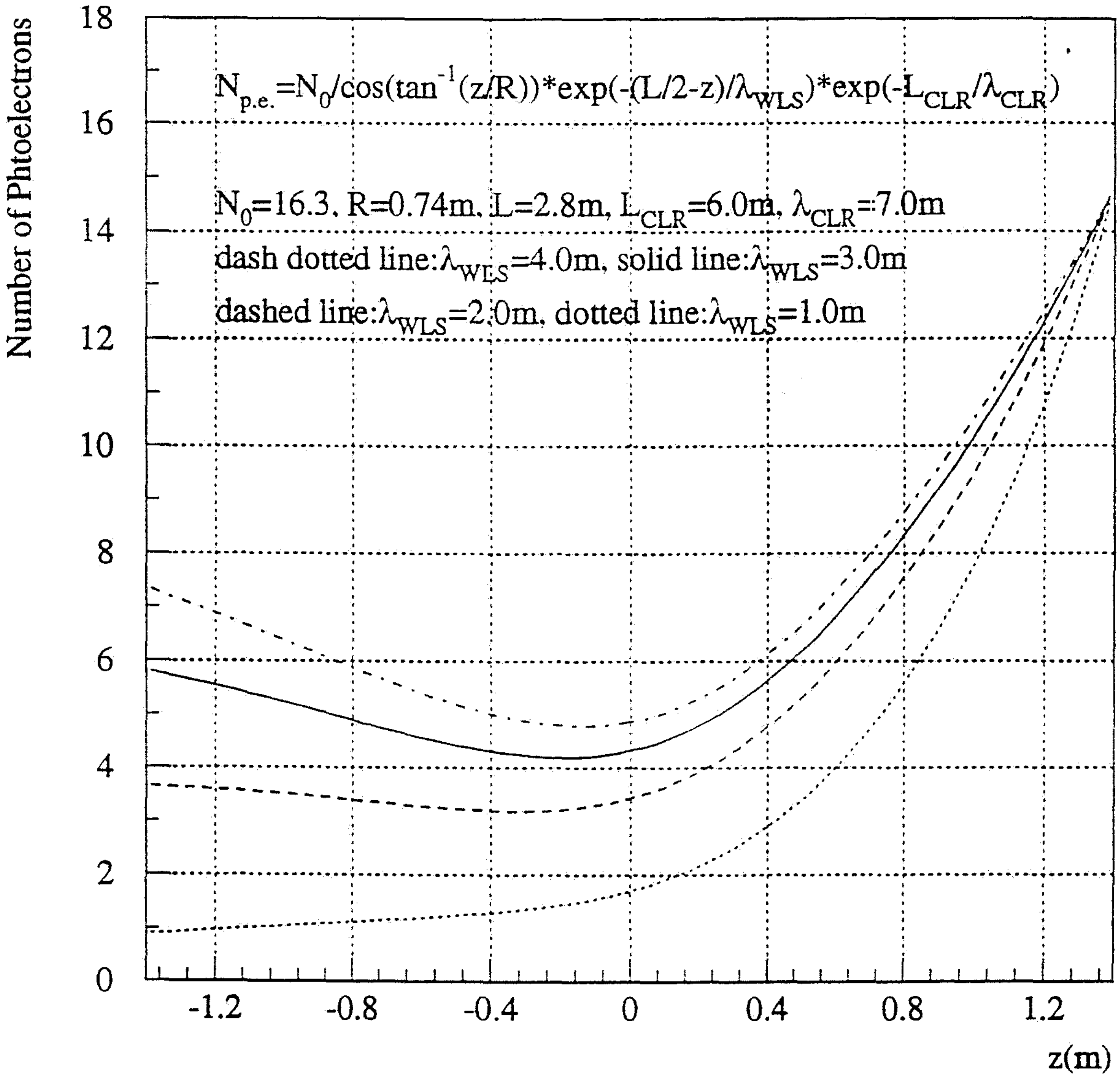

Figure 13 Estimated number of photoelectrons for a minimum ionizing particle which traverses one layer of the preshower detector.

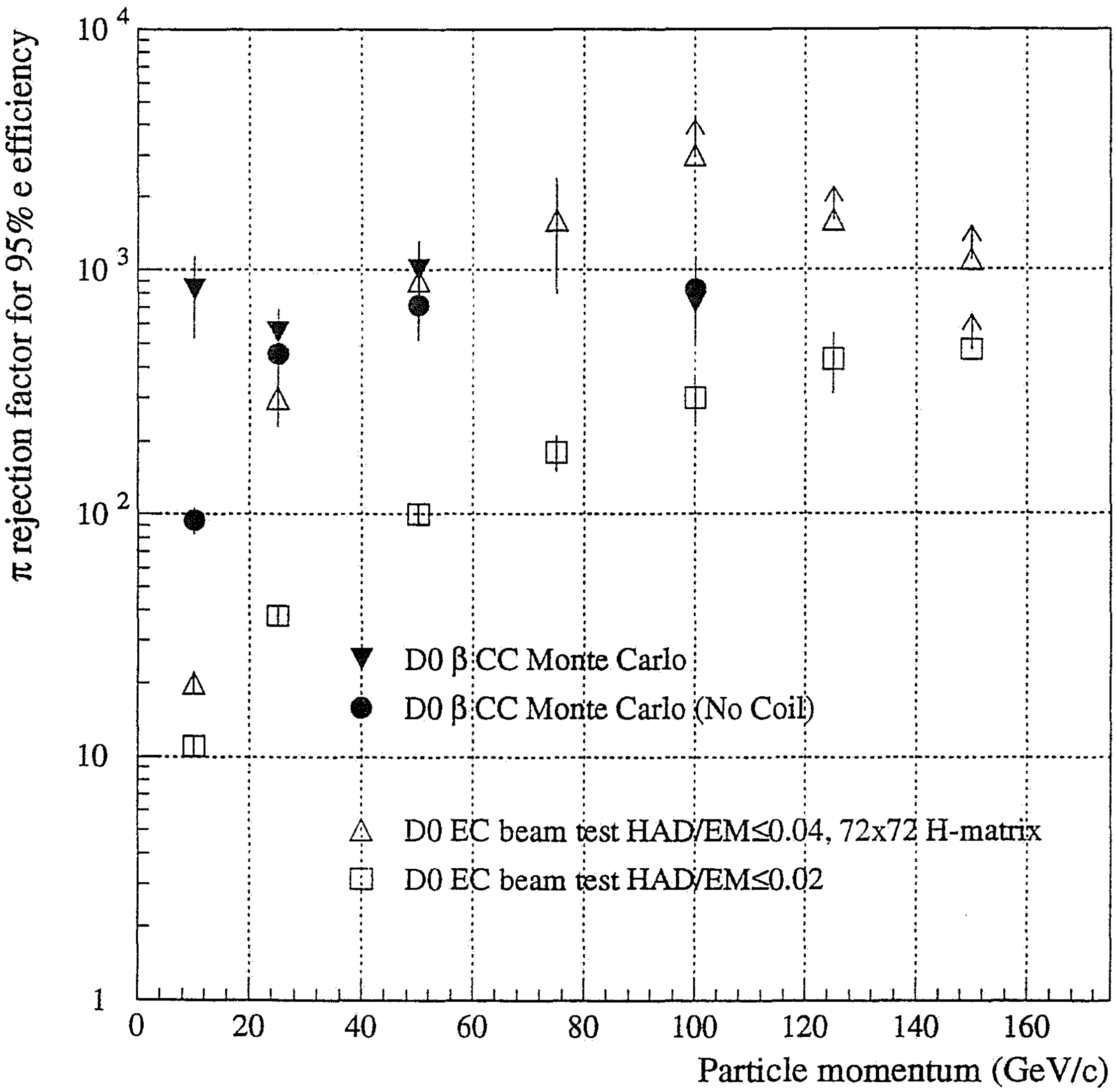

Figure 14 Preshower pion rejection ratio. See text for details.

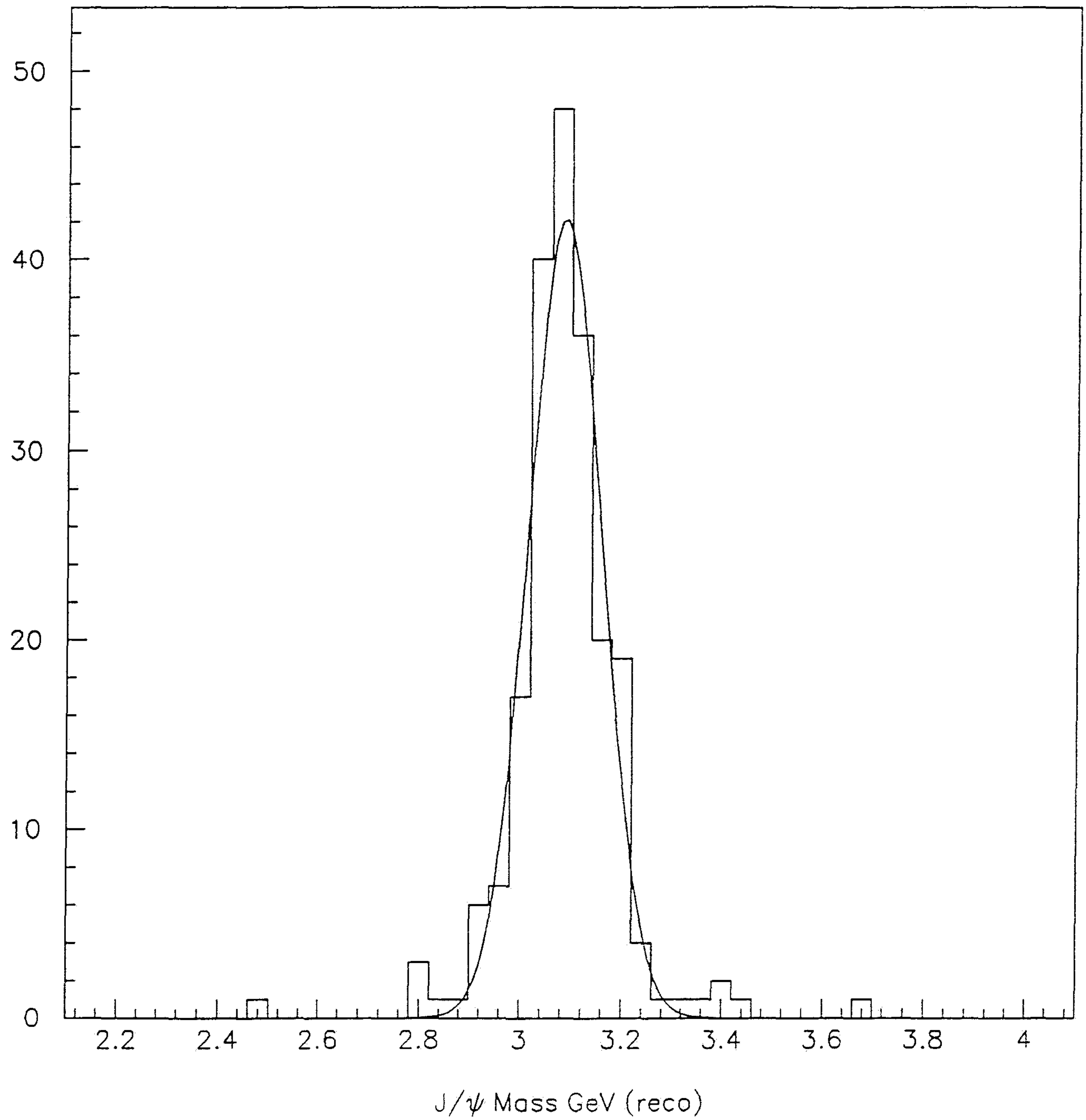

Figure 15 Di-muon mass plot in the J/Ψ region.

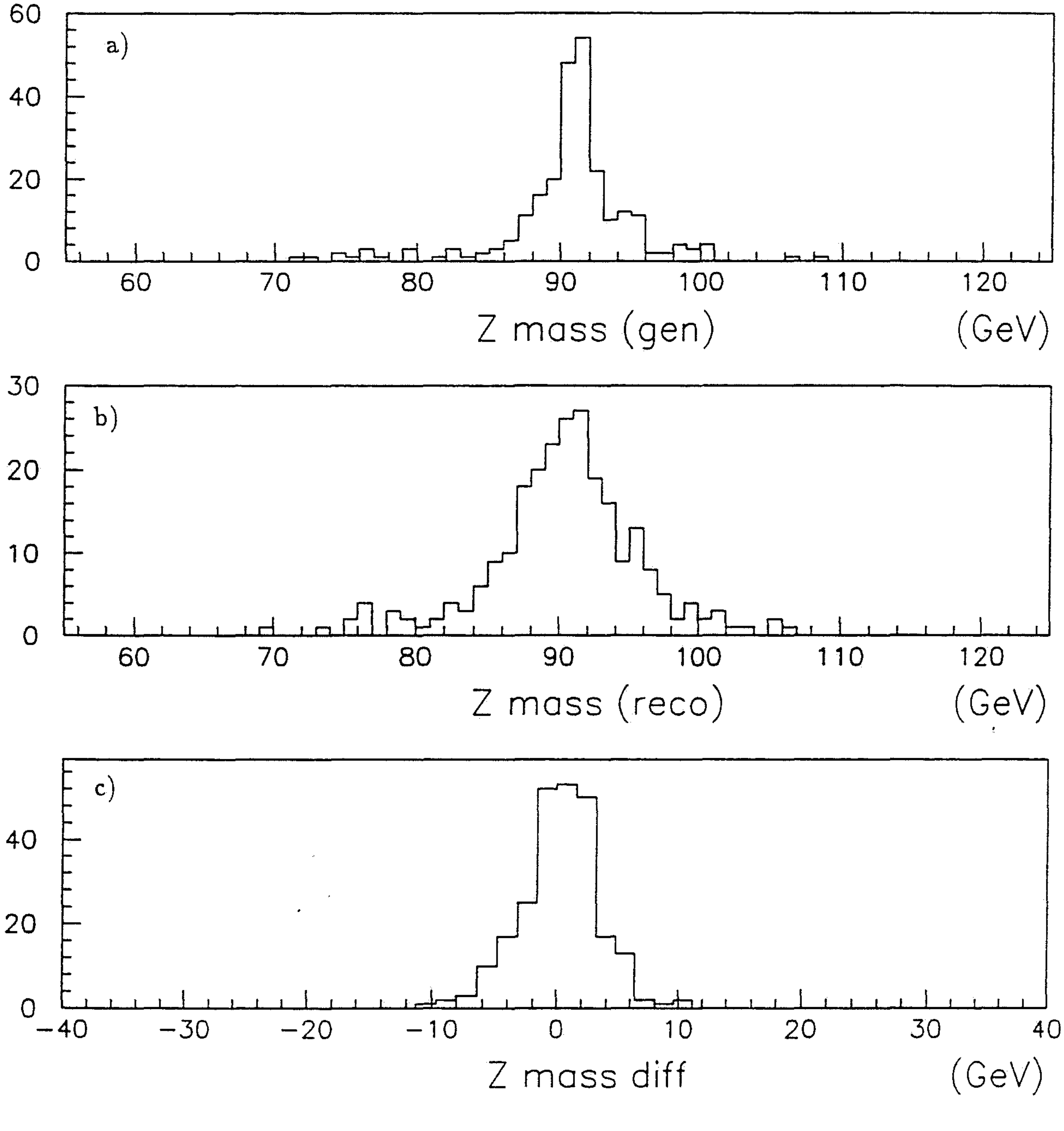

Figure 16 Di-muon mass plot in the Z region:

a) Generated muons;

b) Reconstructed muons;

c) Difference between generated and reconstructed $\mu\mu$ mass.

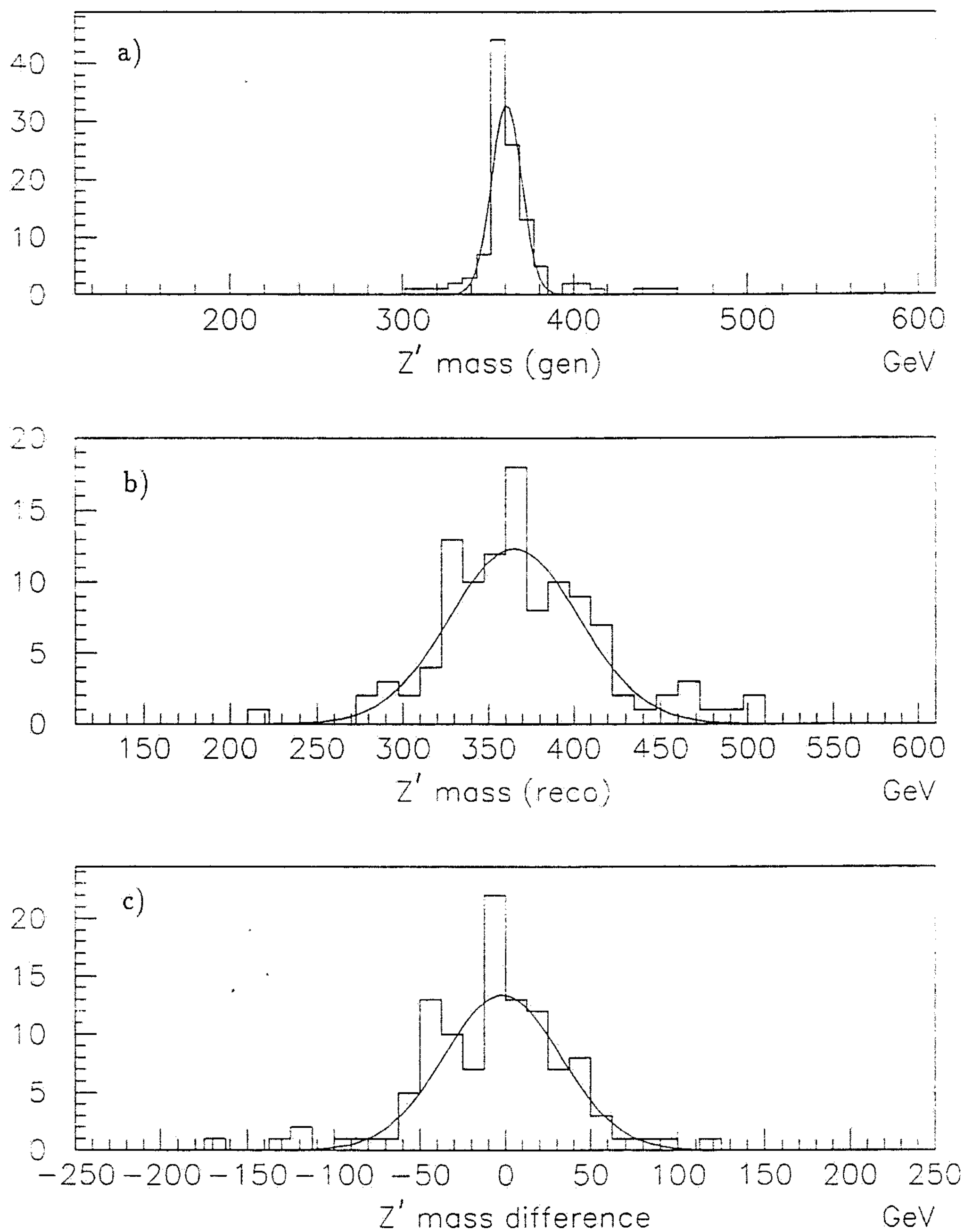

Figure 17 Di-muon mass plot in the region of a hypothetical 360 GeV Z' particle:

a) Generated muons;

b) Reconstructed muons;

c) Difference between generated and reconstructed $\mu\mu$ mass.

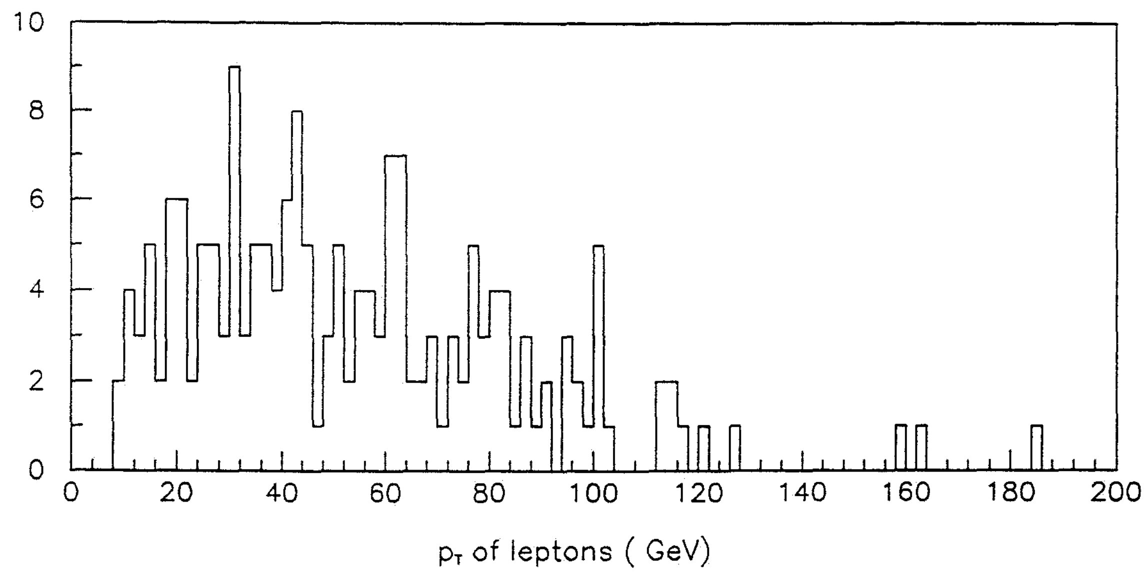

Figure 18 Transverse momentum distribution of μ from W from t.

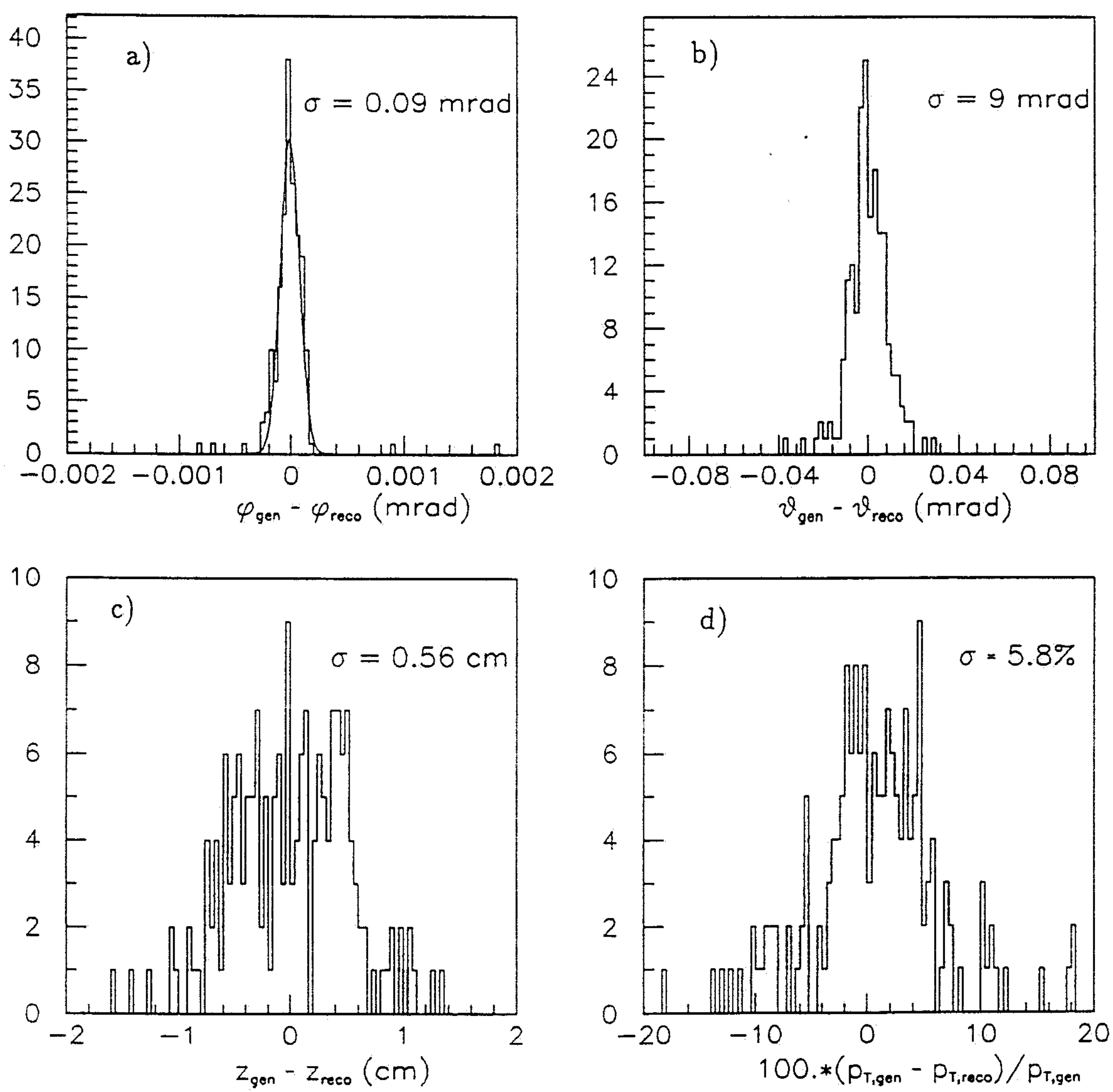

Figure 19 Resolution of the μ from W from t, assuming a constant magnetic field:

a) ϕ angle;

b) θ angle;

c) z coordinate;

d) p_T.

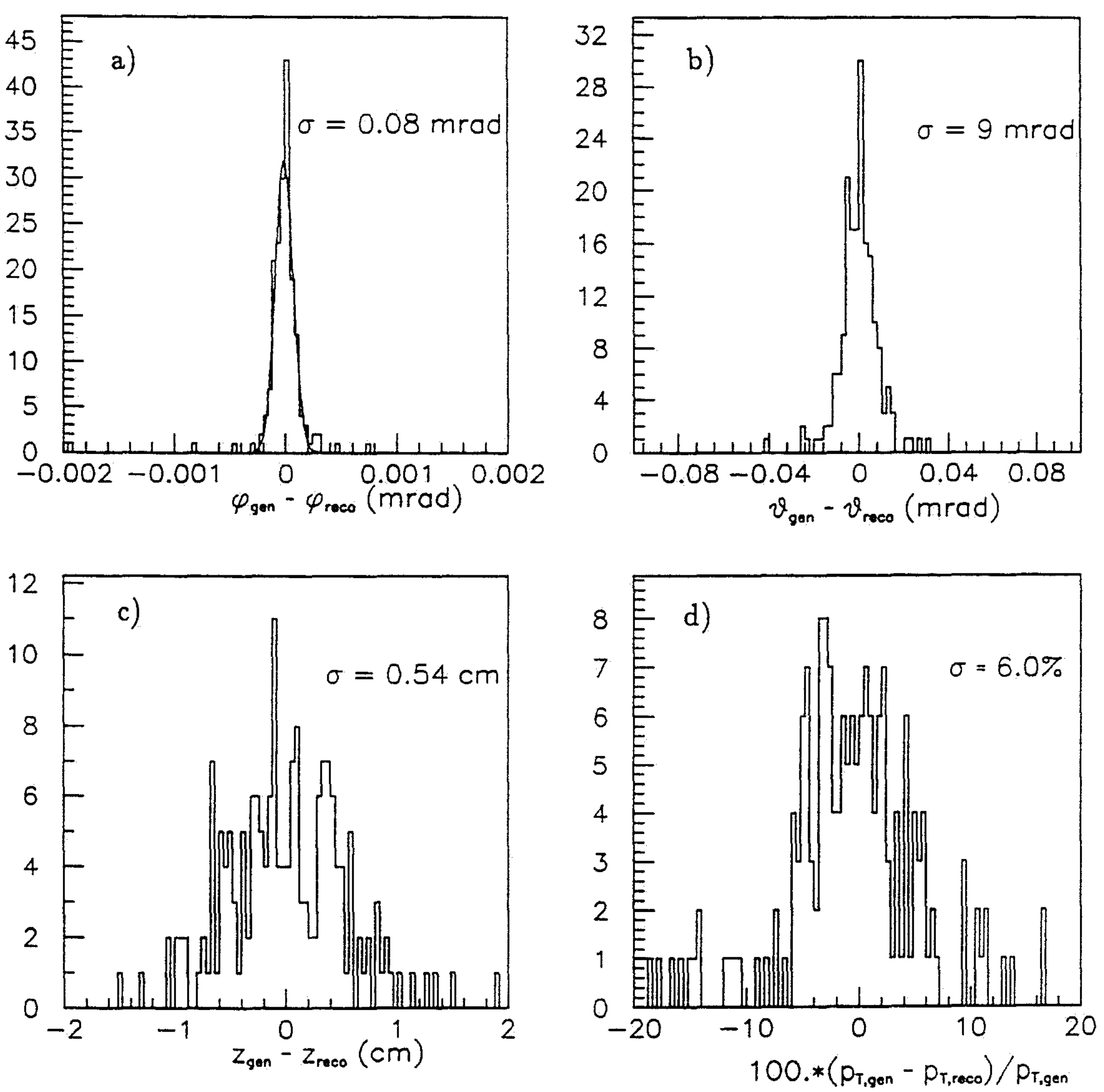

Figure 20 Resolution of the μ from W from t, assuming a non-uniform magnetic field map:

a) ϕ angle;

b) θ angle;

c) z coordinate;

d) p_T.

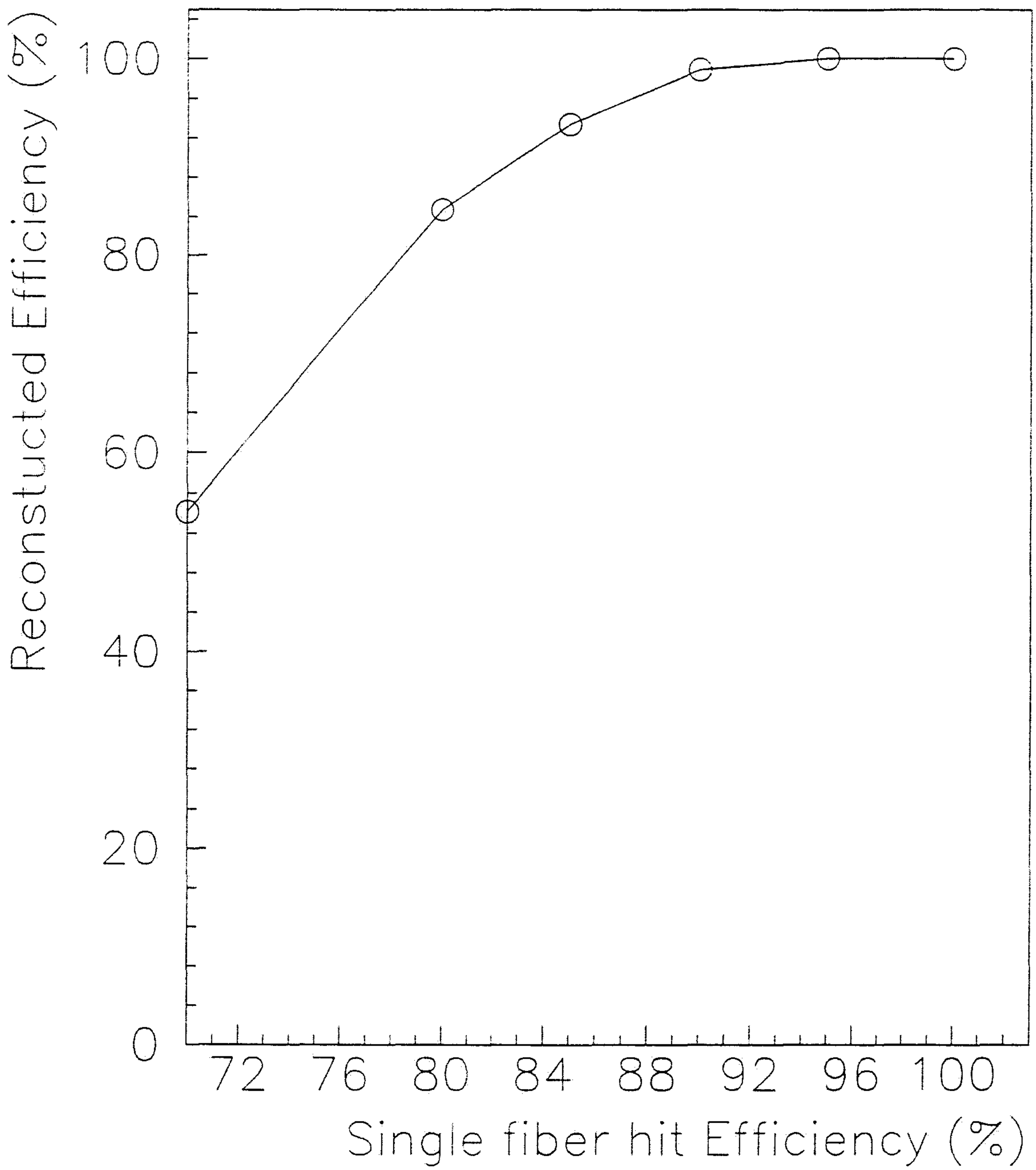

Figure 21 Track reconstruction efficiency of μ from t versus single scintillating fiber hit efficiency.

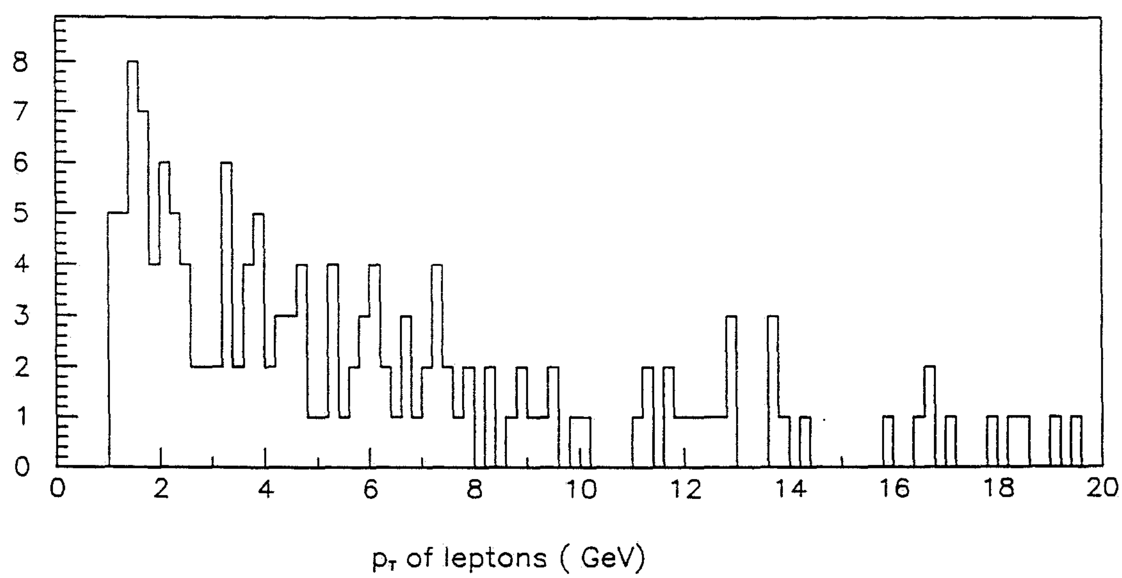

Figure 22 Transverse momentum distribution of μ from b from t.

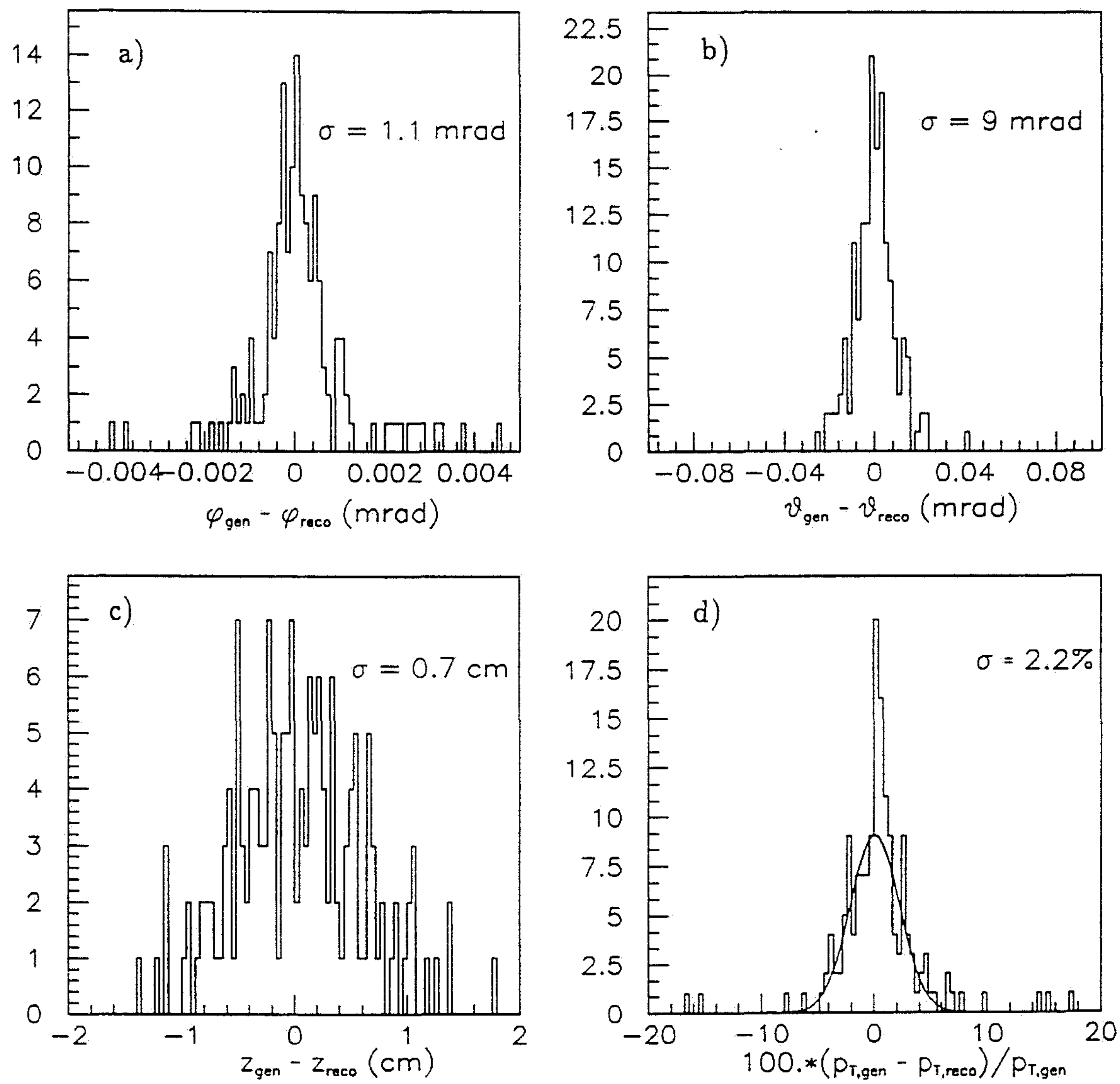

Figure 23 Resolution of the μ from b from t

a) ϕ angle;

b) θ angle;

c) z coordinate;

d) p_T.

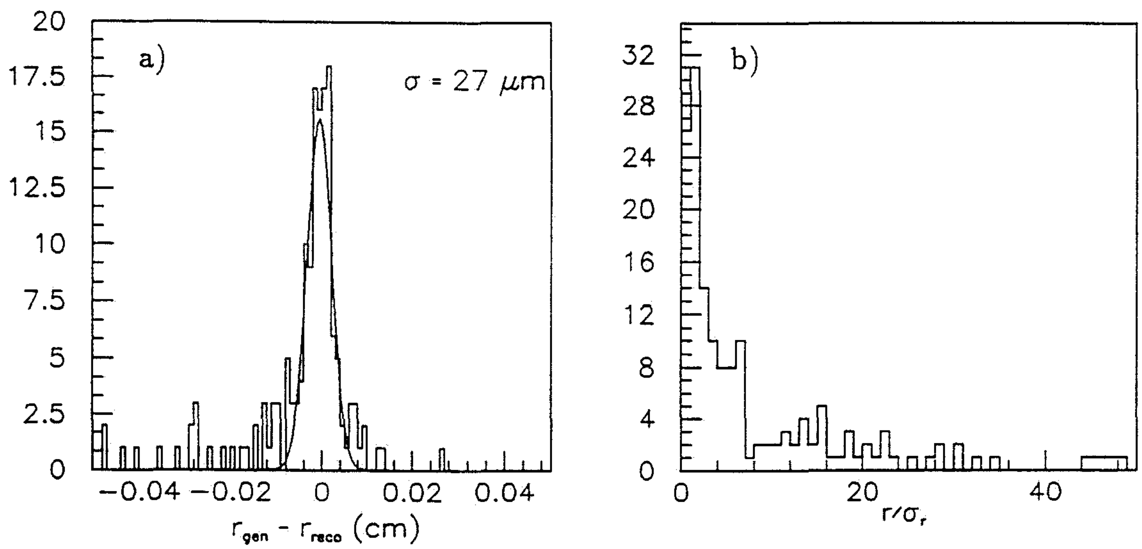

Figure 24 Resolution characteristics of μ from b from t:
a) Transverse distance resolution distribution at the beam axis;
b) Significance distribution (transverse distance r divided by σ_r.)

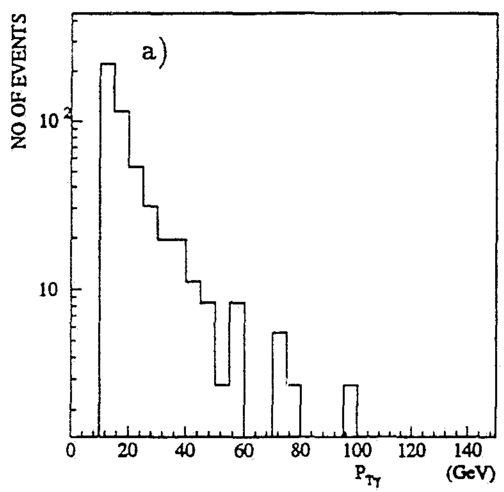

(a) p_T spectrum of γ

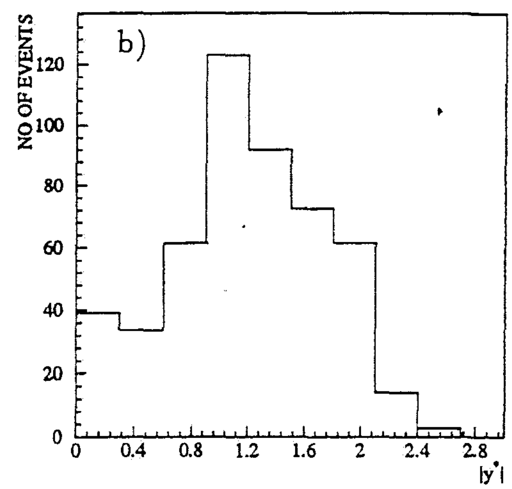

(b) rapidity spectrum of γ

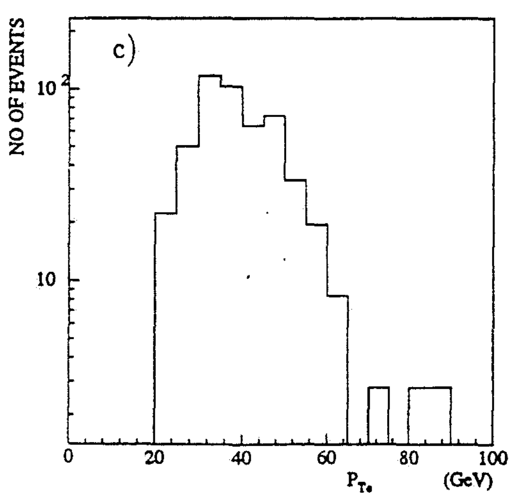

(c) p_T spectrum of electron

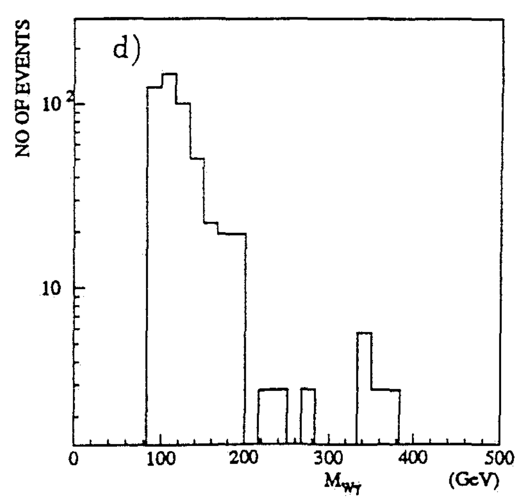

(d) $W-\gamma$ invariant mass

Figure 25 Expected kinematical distributions for $W\gamma$ events with integrated luminosity $1000\mathrm{pb}^{-1}$.

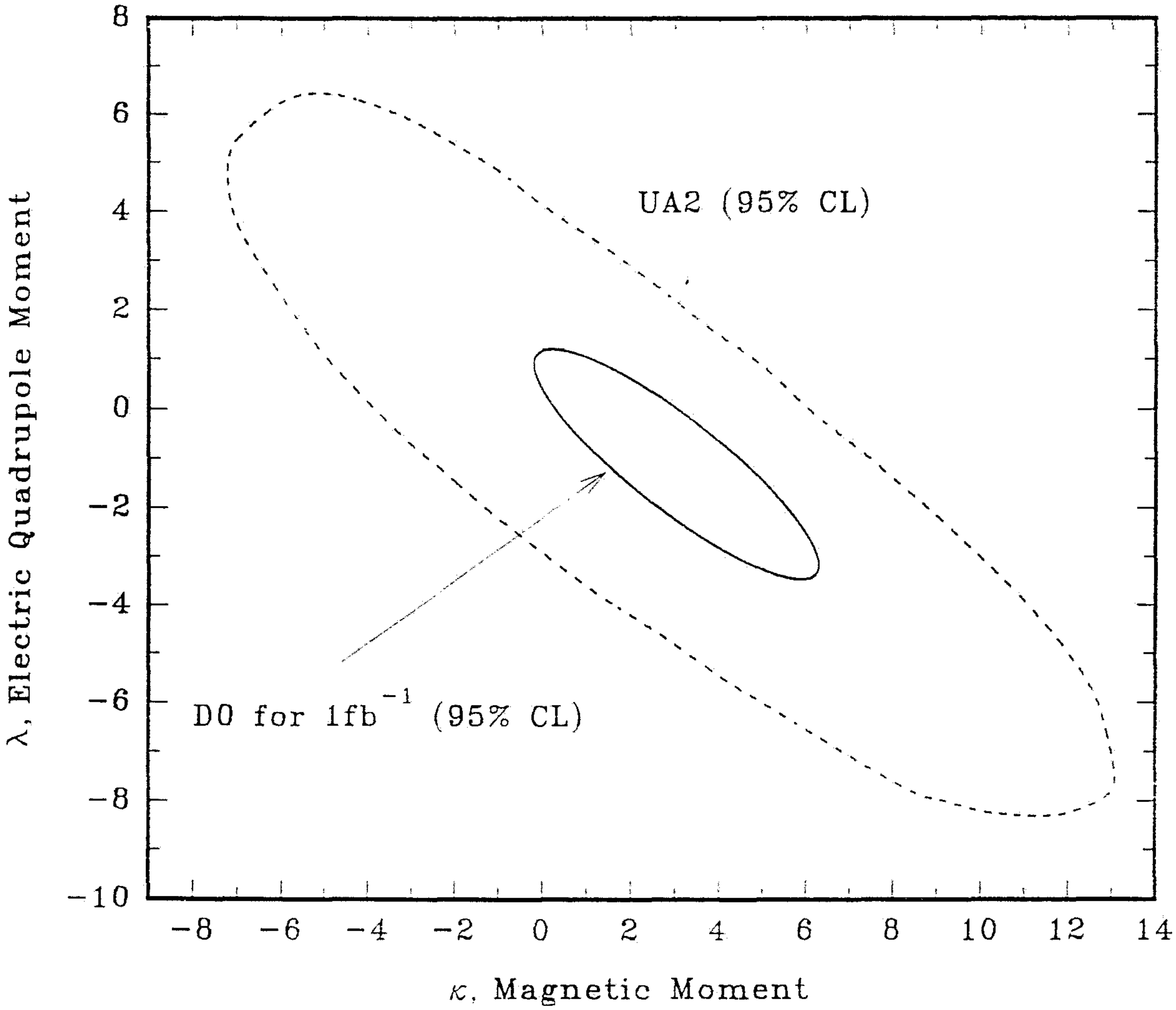

Figure 26 Plot of W anomalous magnetic moment (κ) versus anomalous electric quadrupole moment (λ) with 95% confidence level contours of UA2 data and potential DØ$_\beta$ with integrated luminosity of 1000 pb^{-1}.

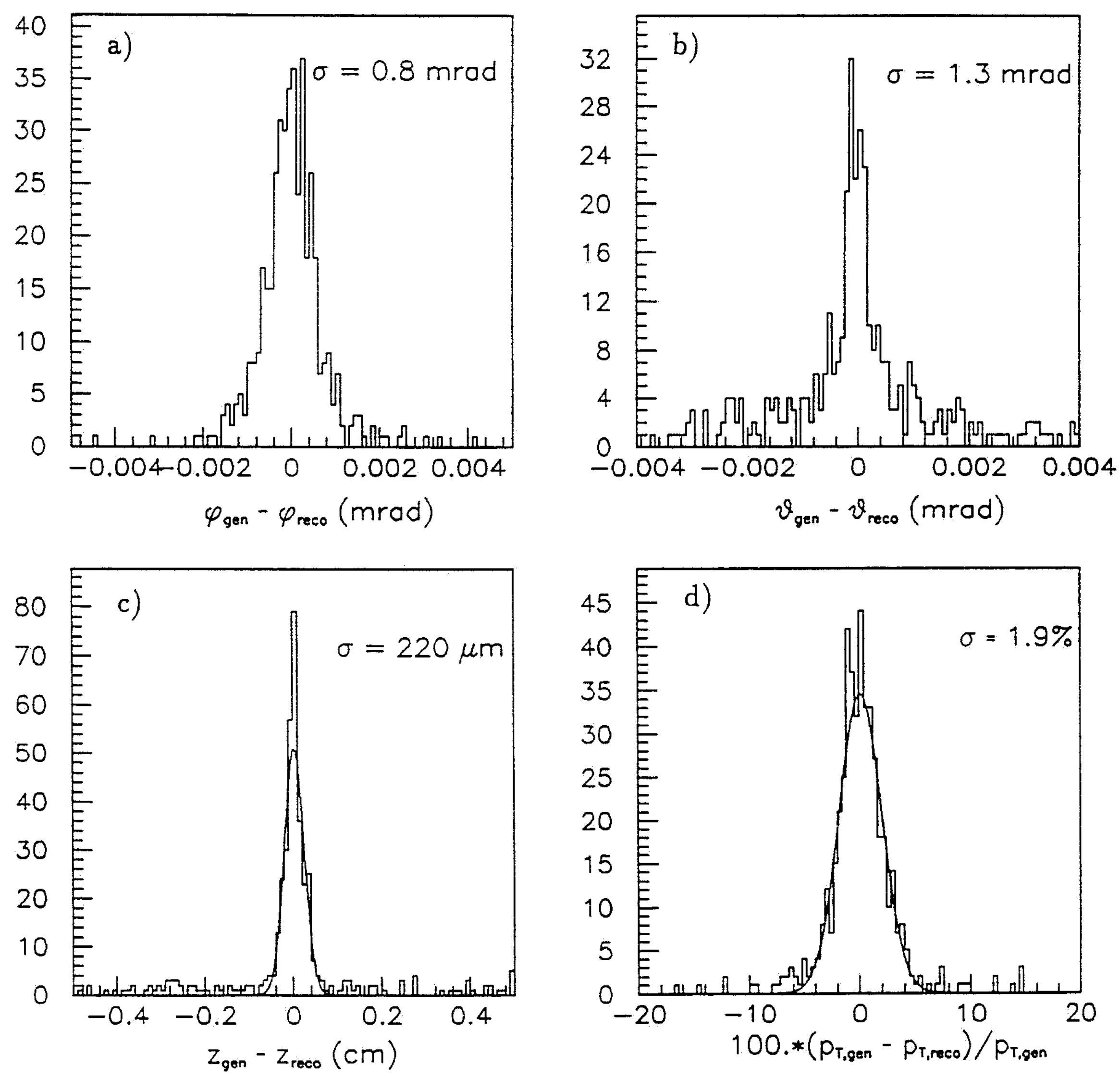

Figure 27 Resolution characteristics of μ from J/ψ from b:

a) ϕ angle;

b) θ angle;

c) z coordinate;

d) p_T.

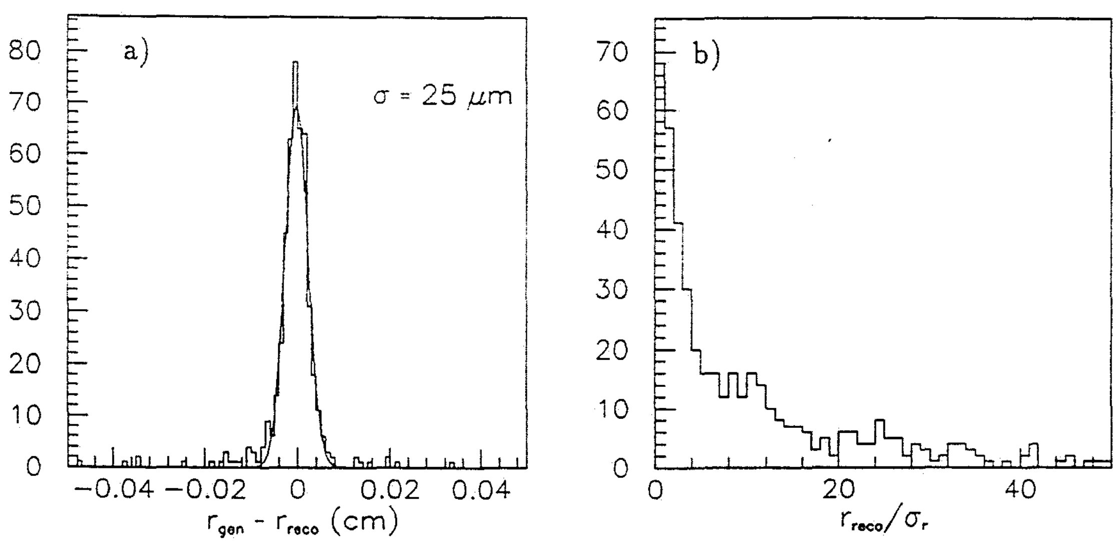

Figure 28 Resolution characteristics of μ from J/ψ from b:

a) Transverse distance resolution distribution at the beam axis;

b) Significance distribution (transverse distance r divided by σ_r.)

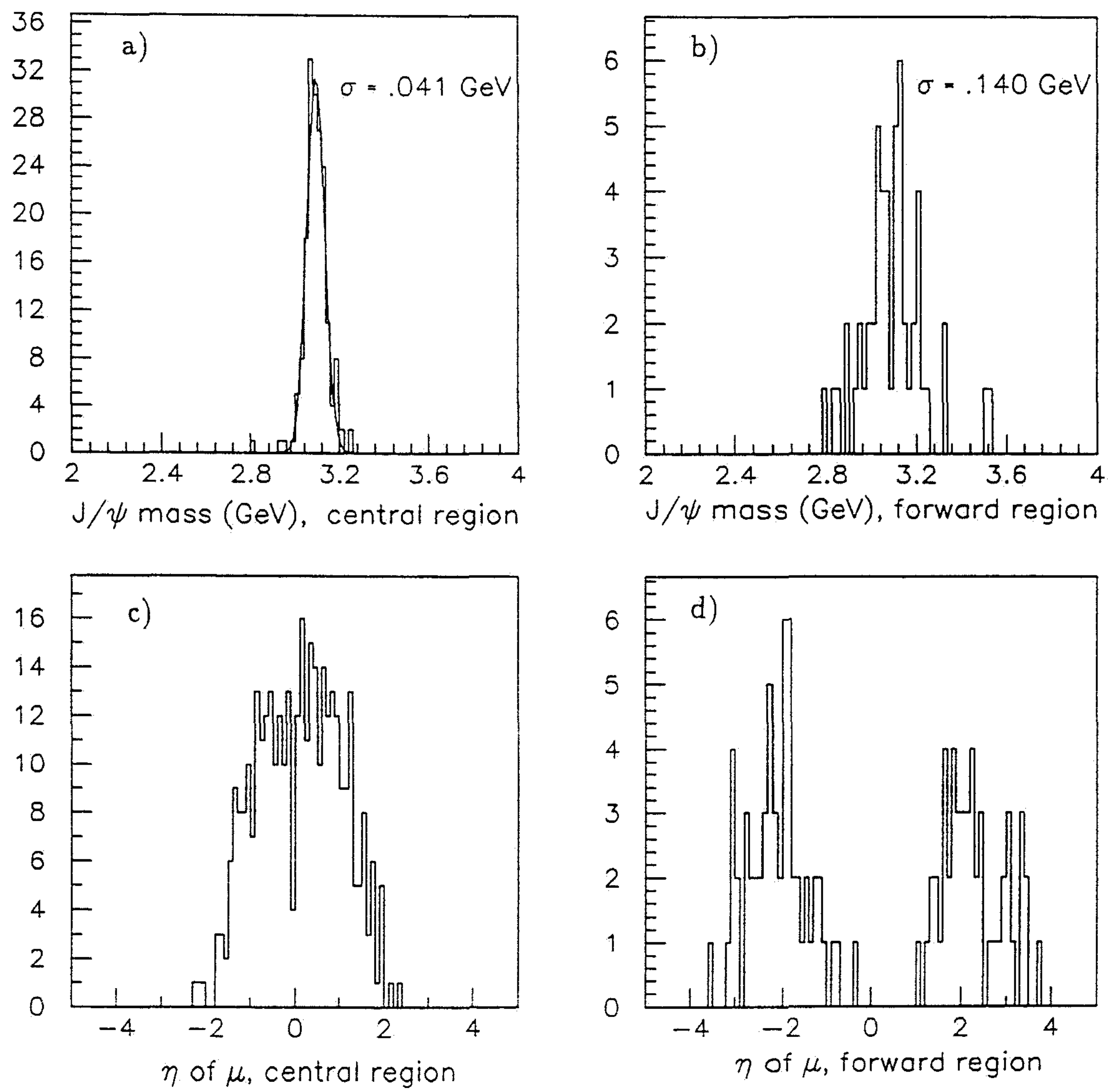

Figure 29 J/ψ characteristics from $B \to J/\psi$ events, with $J/\psi \to \mu\mu$:
a) $\mu\mu$ mass plot for μ's in central region (defined by the fiber tracker);
b) $\mu\mu$ mass plot for high η μ's;
c) η distribution for central region μ's;
d) η distribution for high η μ's.

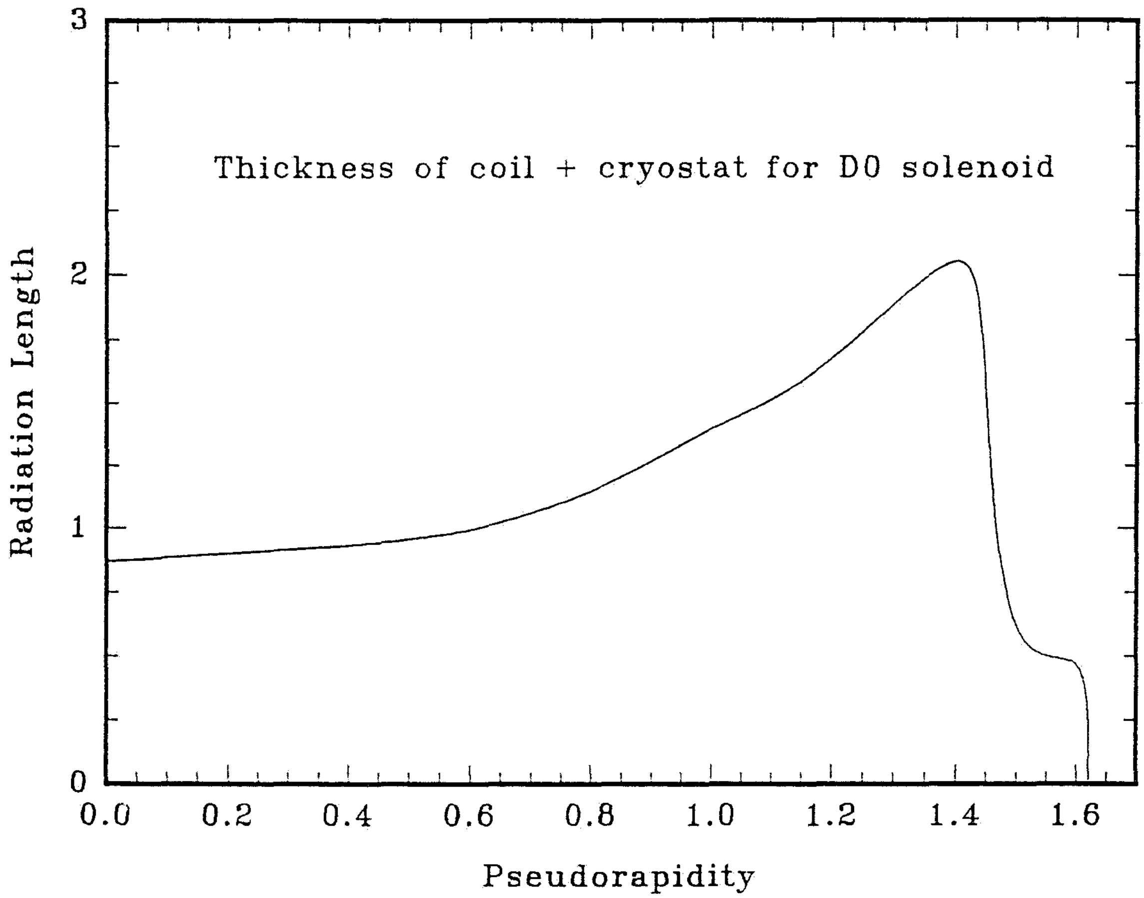

Figure 30 The thickness of the solenoid and cryostat in radiation lengths versus pseudo-rapidity.

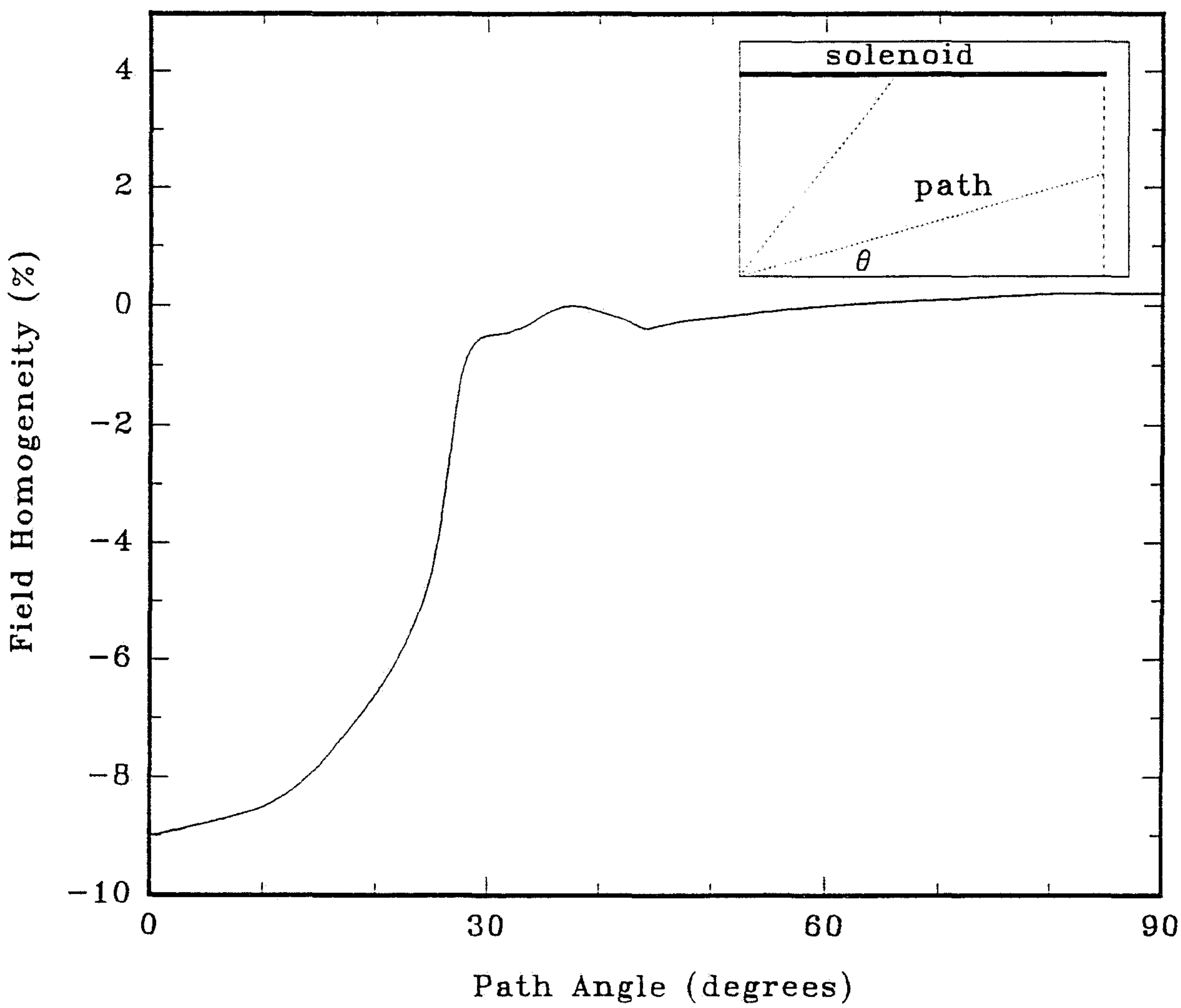

Figure 31 Field homogeneity measured as the average deviation of B along a path from the origin to the edge of the solenoid. The inset defines the angle for two typical paths.

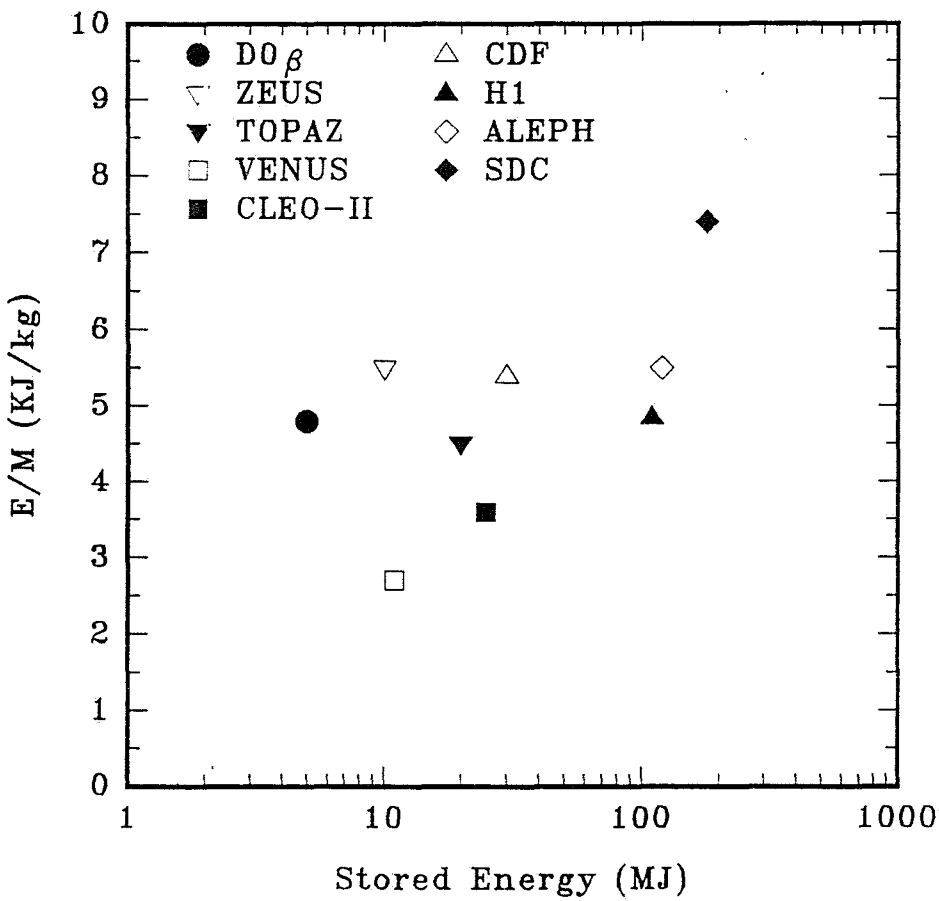

Figure 32 The value of the stored energy per cold mass (E/M) versus stored energy for existing and planned thin superconducting solenoid magnets.

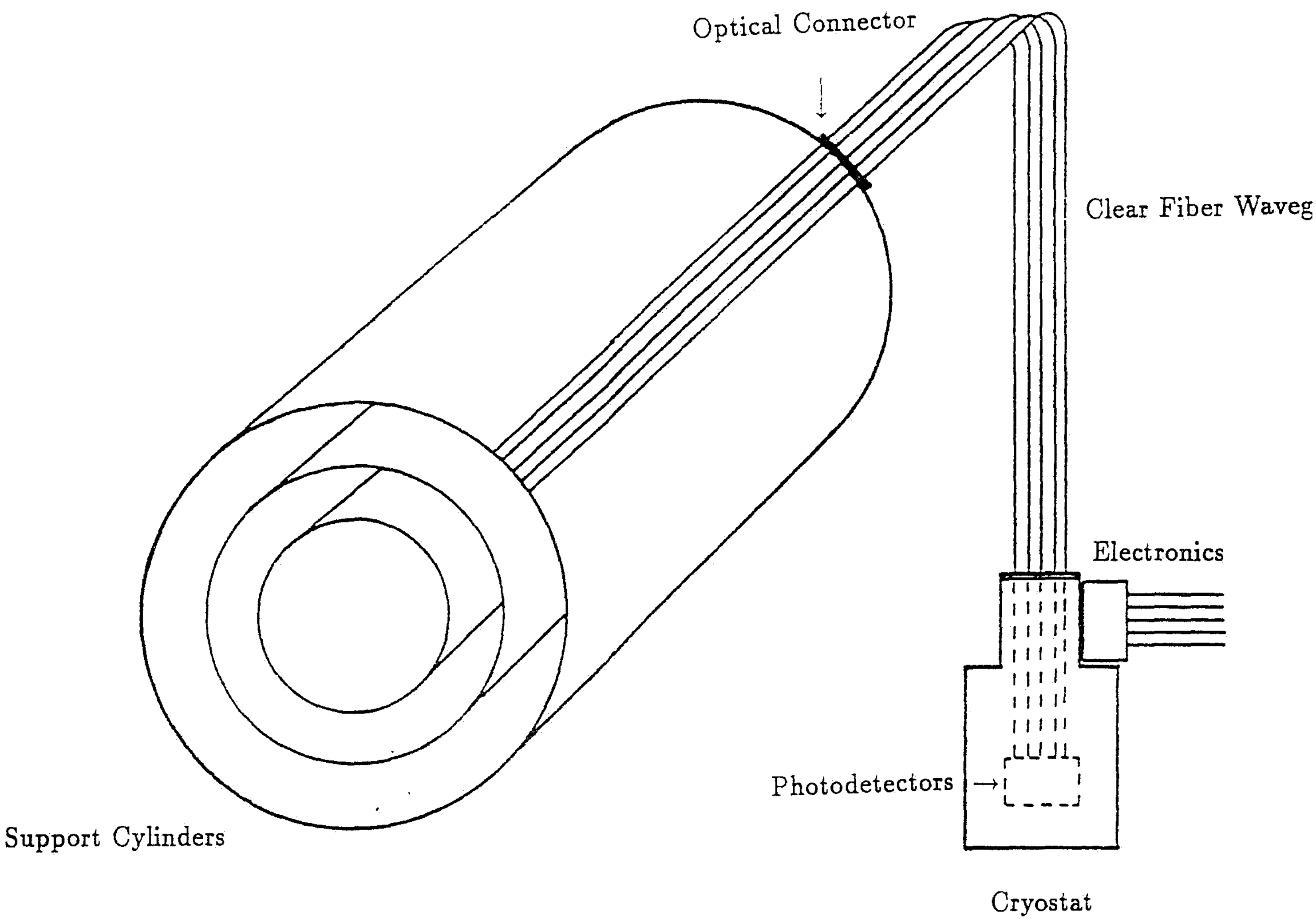

Figure 33 Schematic view of a generic scintillating fiber tracking detector.

Multiclad Fiber Analysis

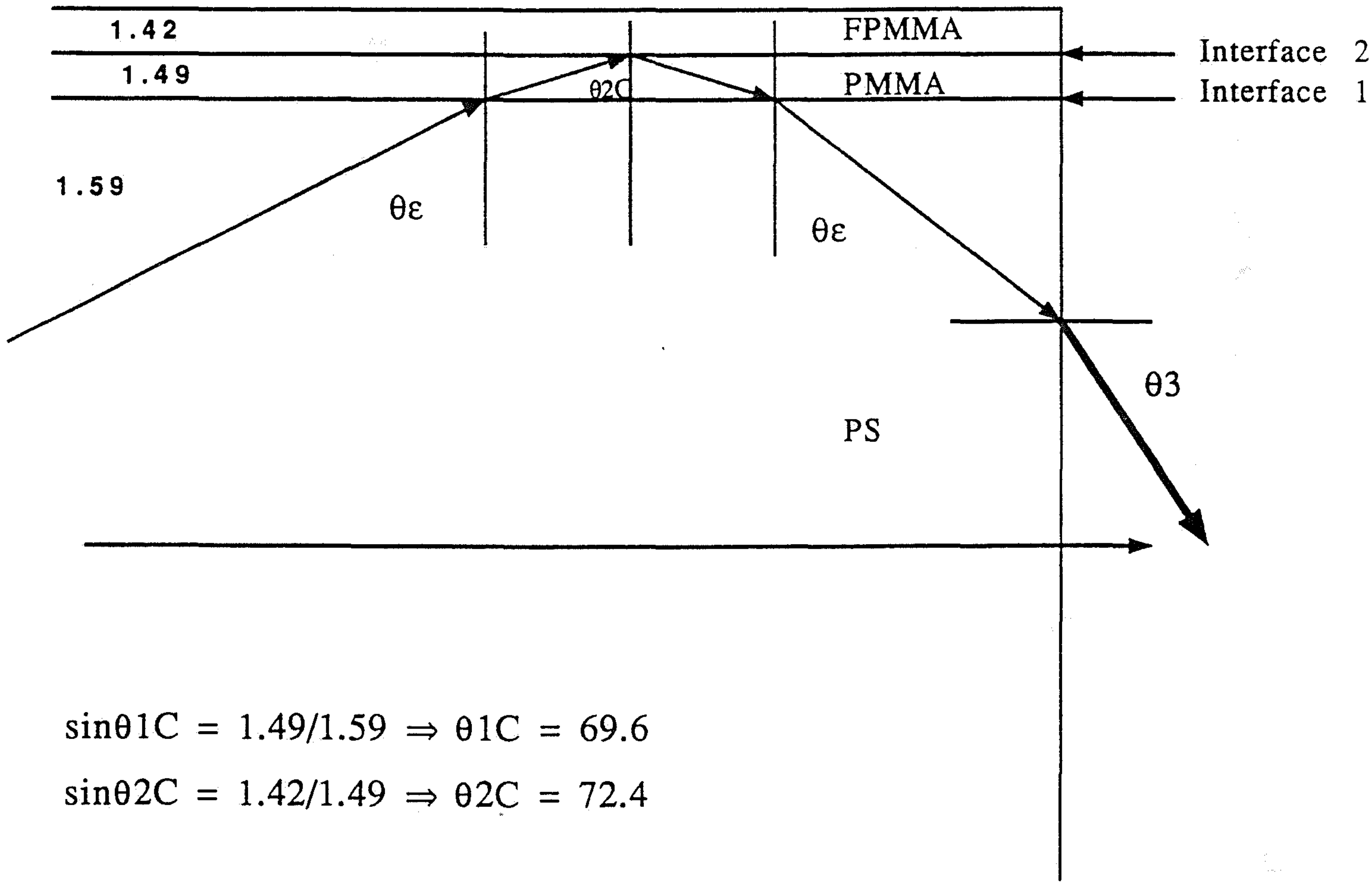

$\sin\theta 1C = 1.49/1.59 \Rightarrow \theta 1C = 69.6$

$\sin\theta 2C = 1.42/1.49 \Rightarrow \theta 2C = 72.4$

Trapping effciency:

PS/PMMA: $\varepsilon = (1-\cos(90-\theta 1C))/2 = (1-1.49/1.59)/2 = 3.1\%$

PS/FPMMA: $\varepsilon = (1-\cos(90-\theta\varepsilon))/2 = (1-1.42/1.59)/2 = 5.3\%$

$R = 5.3/3.1 = 1.71$

Figure 34 Sketch of a light ray trapped in a multi-clad optical fiber, illustrating the enhancement in light-trapping efficiency.

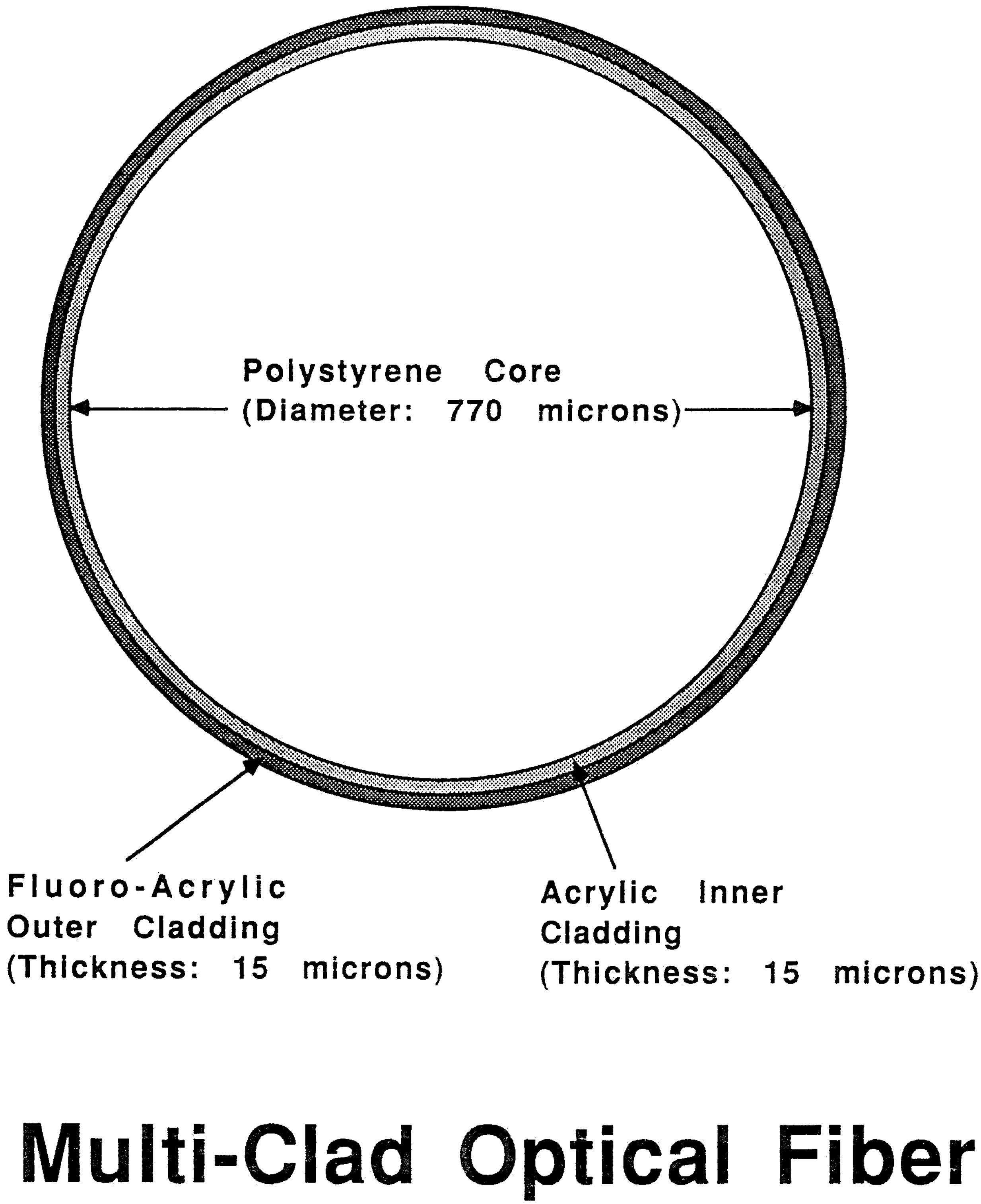

Figure 35 Cross-sectional view of multi-clad optical fiber.

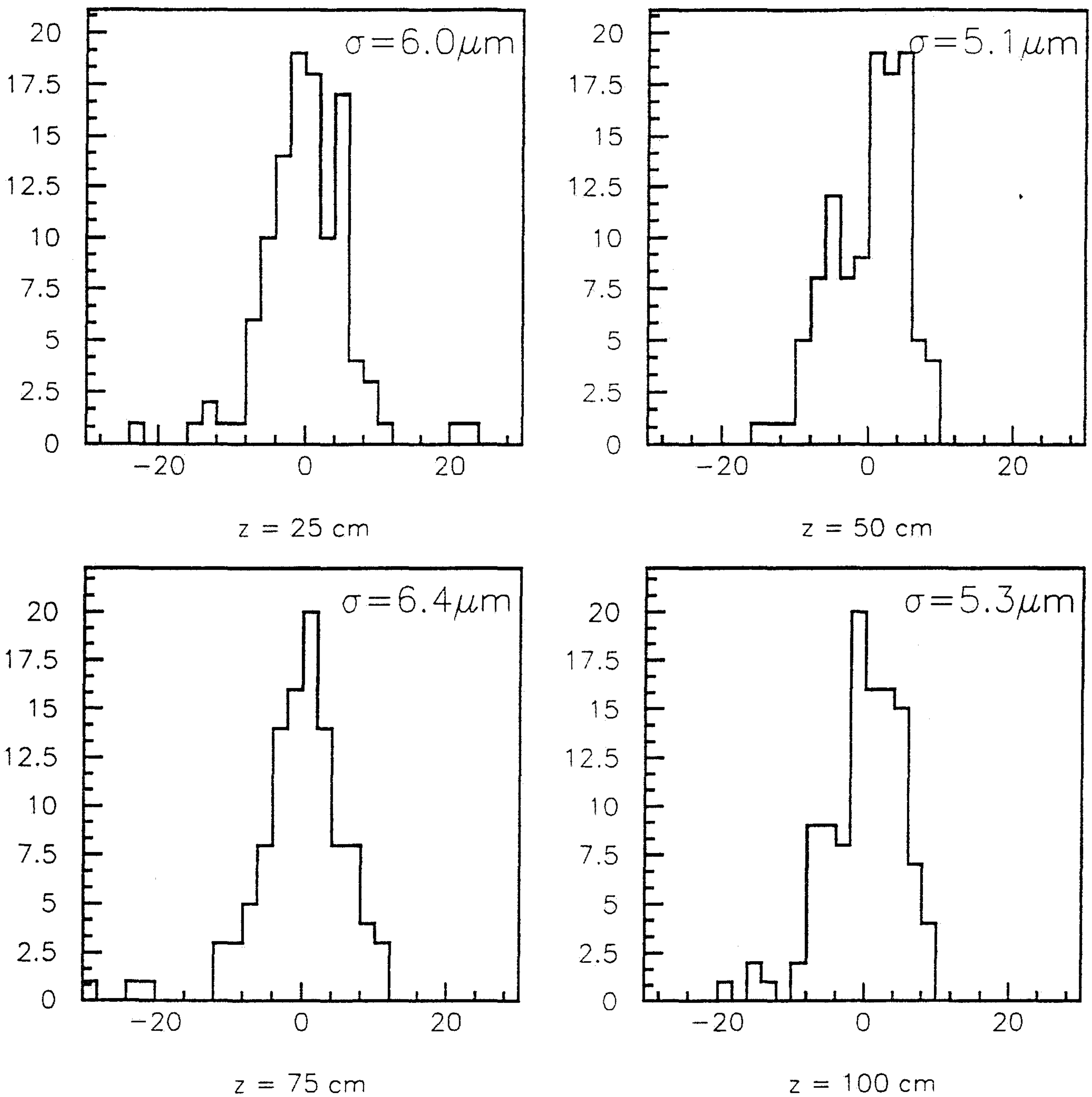

Figure 36 Residual plots of center-to-center spacing in optical fiber ribbons. The different plots correspond to measurements taken at 25 cm intervals along the ribbon length.

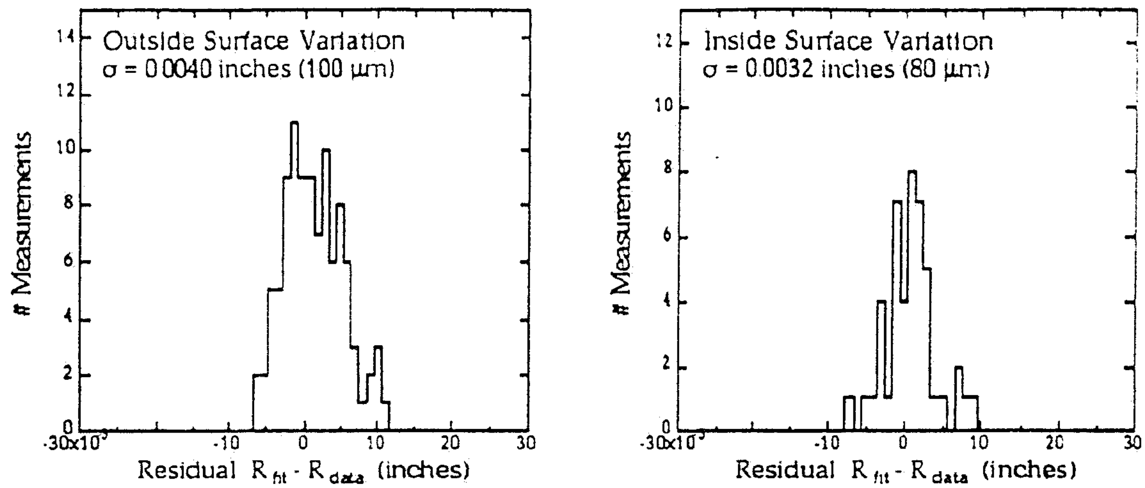

Figure 37 Residual plots comparing the prototype cylinder radius to an ideal cylinder, for both inner and outer cylinder surfaces.

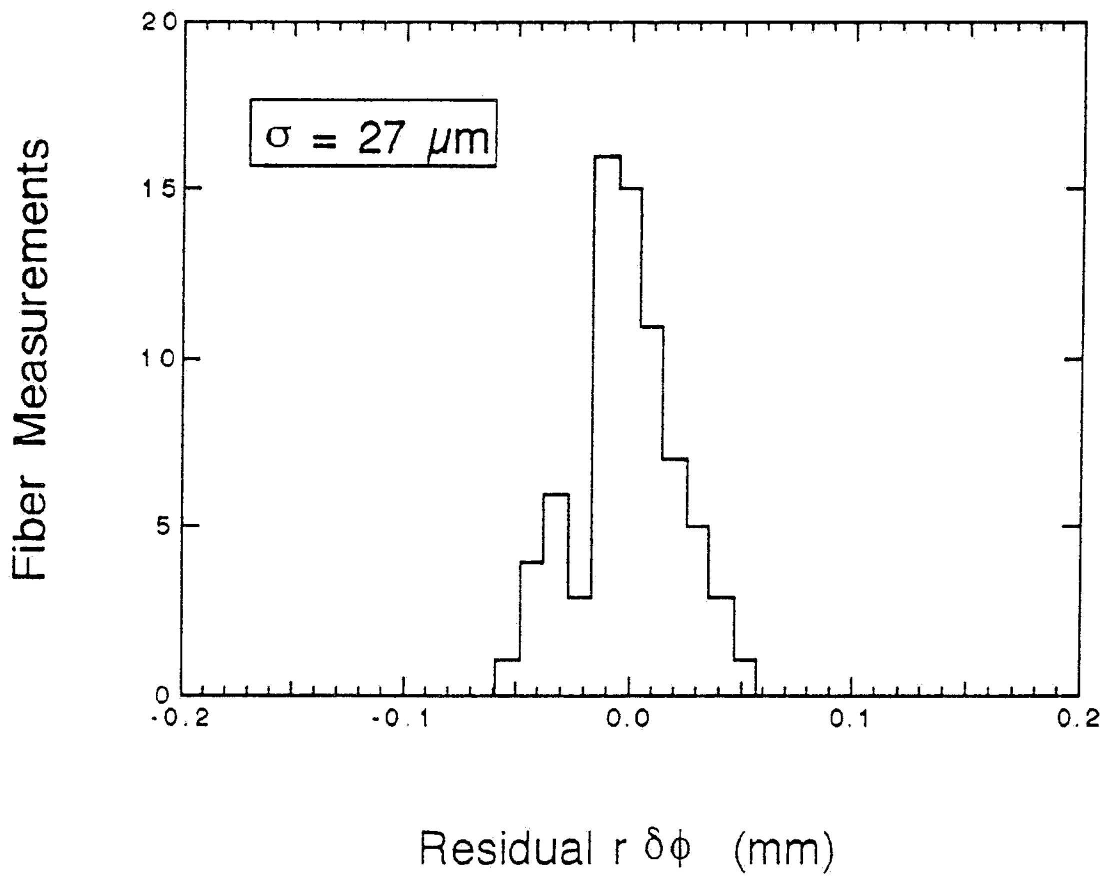

Figure 38 Residual plot comparing the direction of axial-view fibers fibers mounted on a cylinder with the cylinder axis.

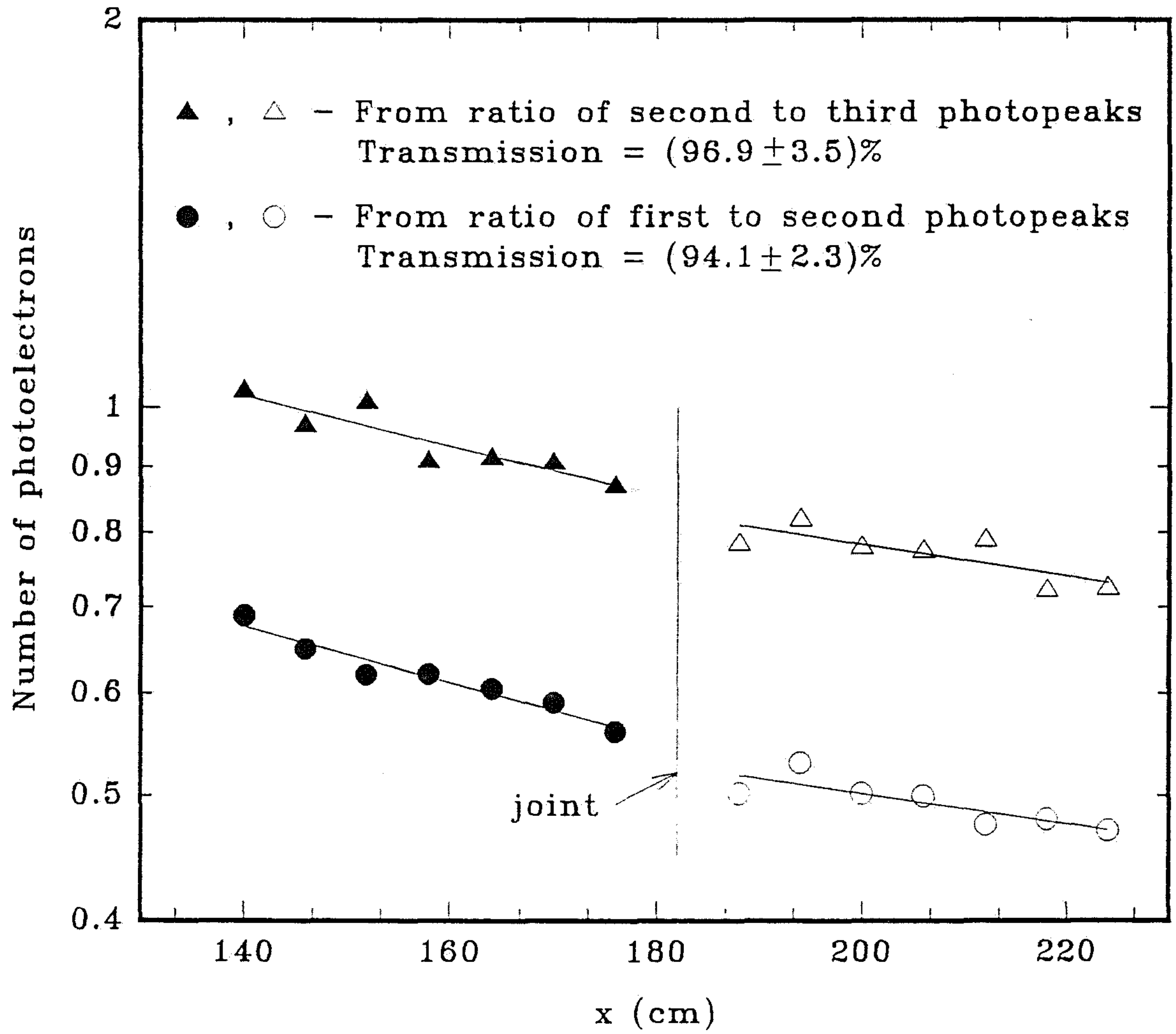

Figure 39 Results of a measurement of light transmission through a joint between two fibers with diamond-polished fiber ends.

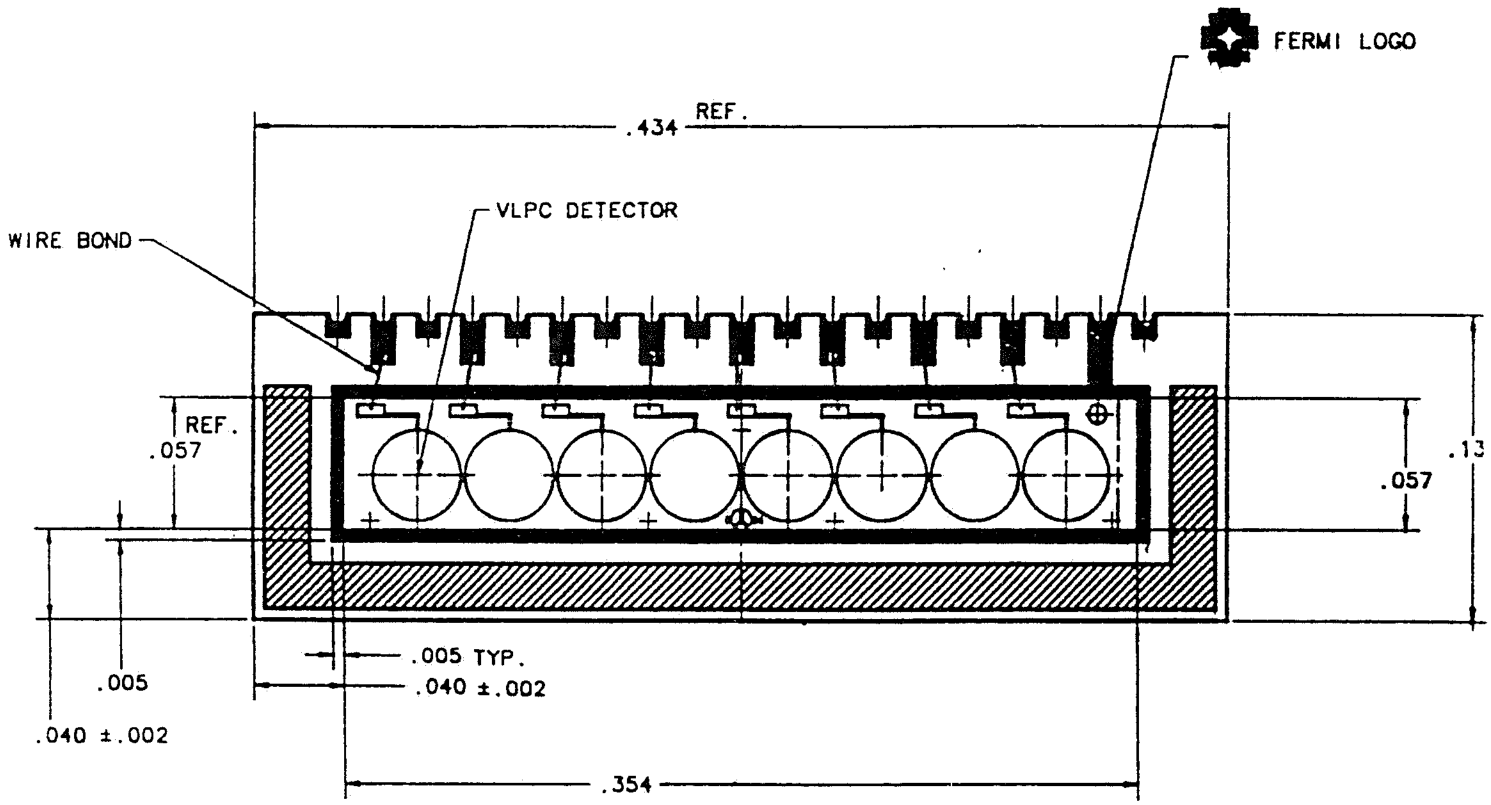

Figure 40 Layout of 8-channel VLPC array mounted on its substrate. The small pads adjacent to each pixel are for wire bonds which take the output signal to castellations at the top of the substrate.

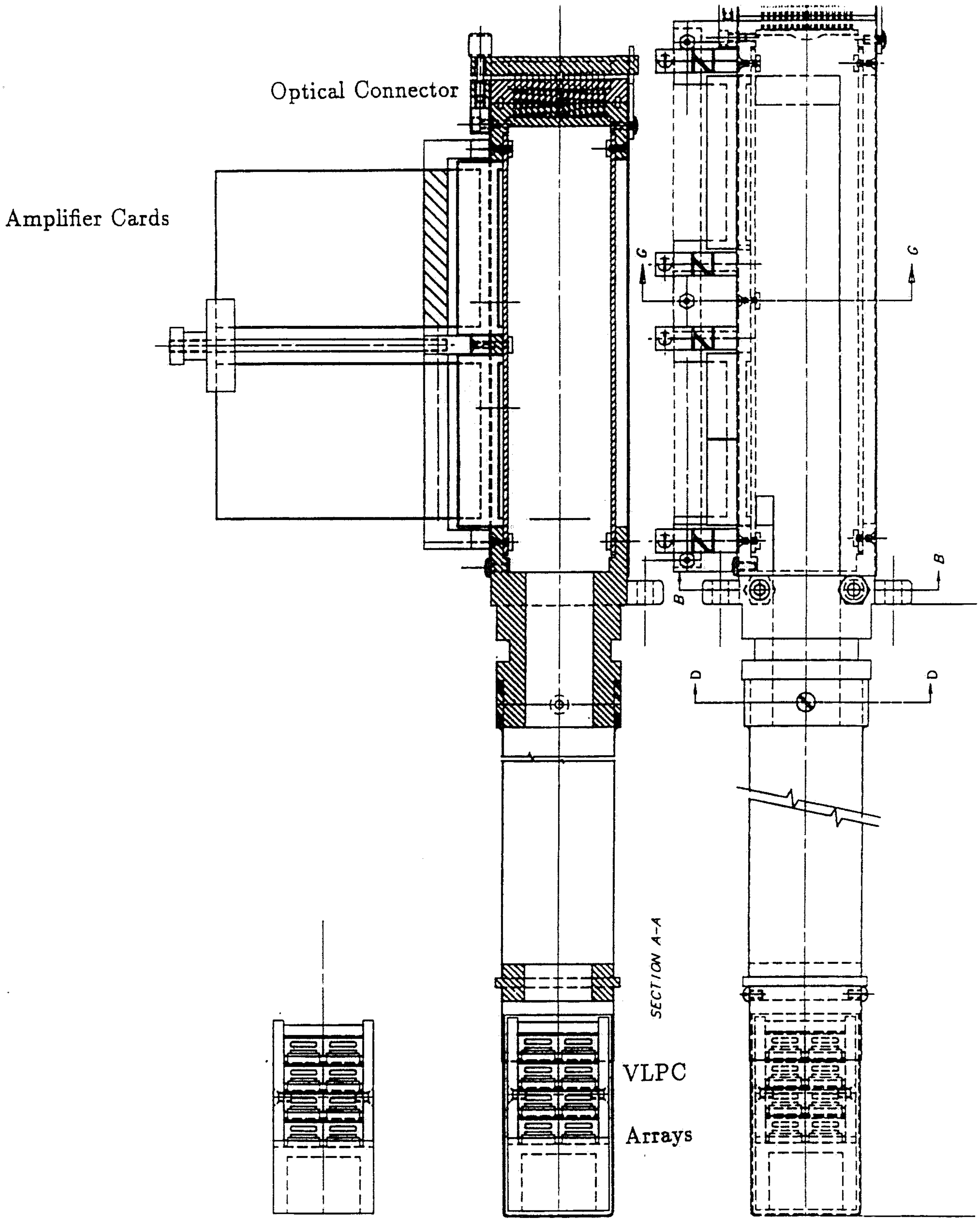

Figure 41 View of VLPC cassette containing 128 channels. The cassette is ~25 inches long.

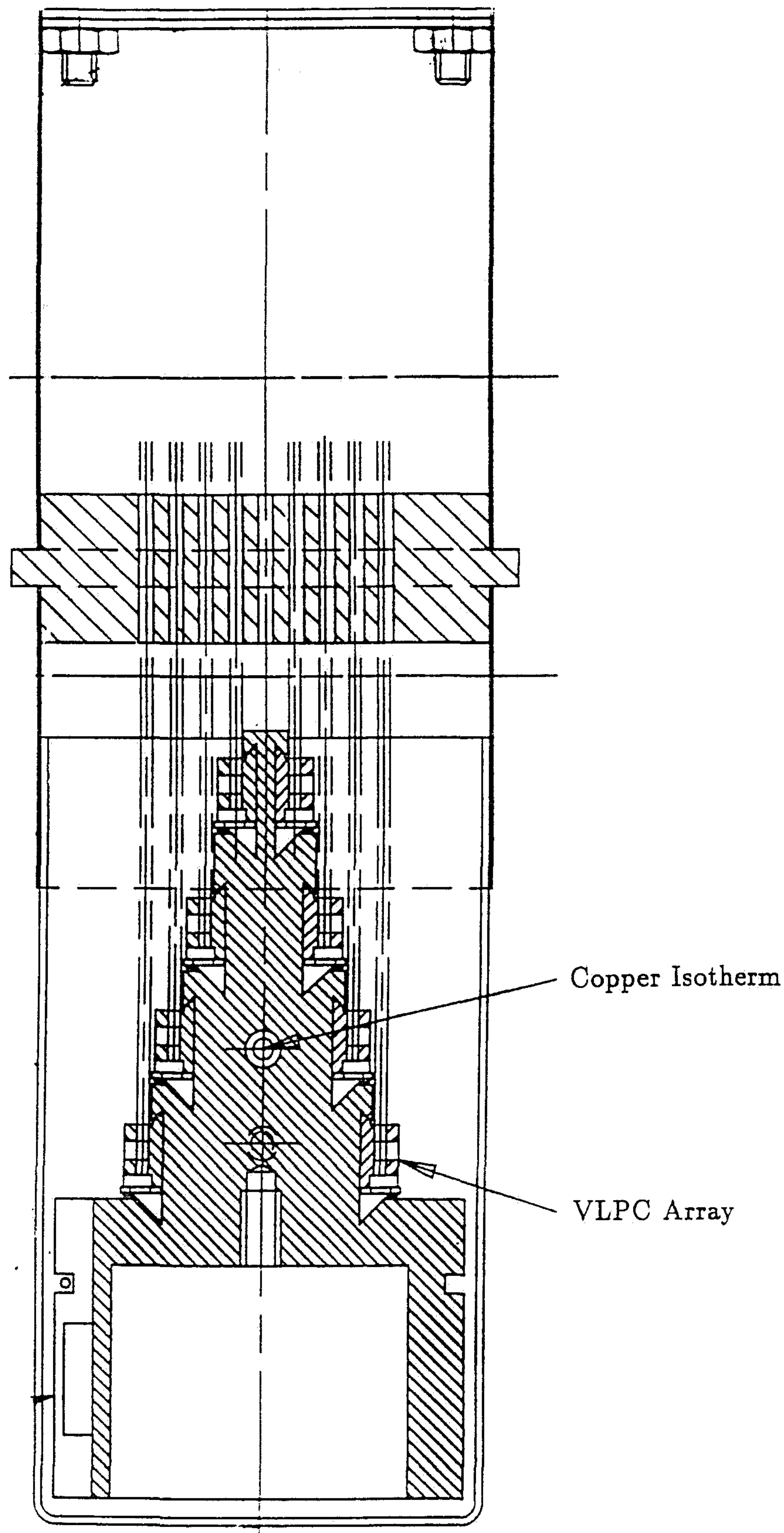

Figure 42 Close-up of the bottom of a VLPC cassette showing the copper isotherm containing VLPC arrays.

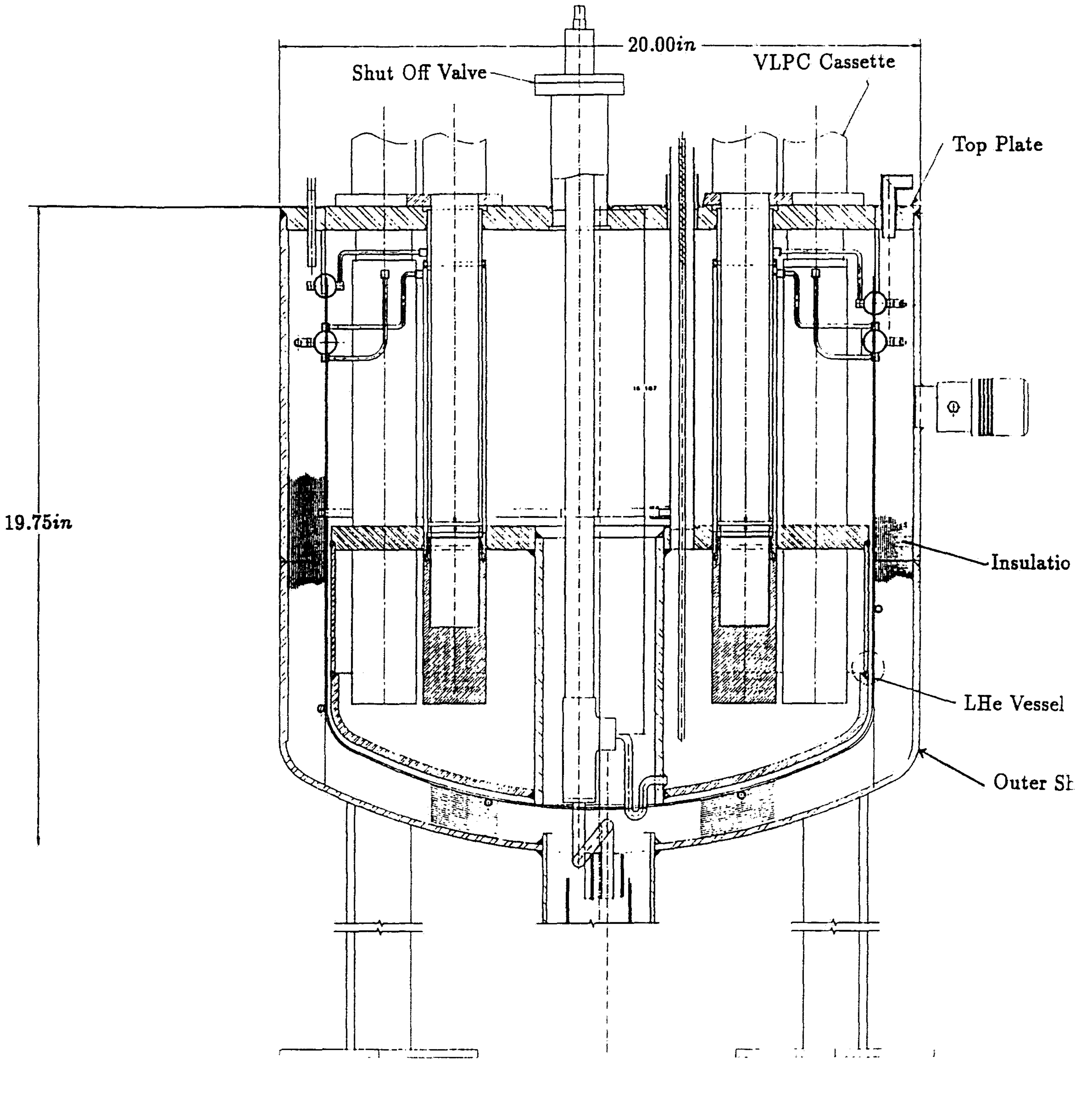

Figure 43 Side view of the DØ VLPC cryostat designed to operate a total of 3072 VLPC channels.

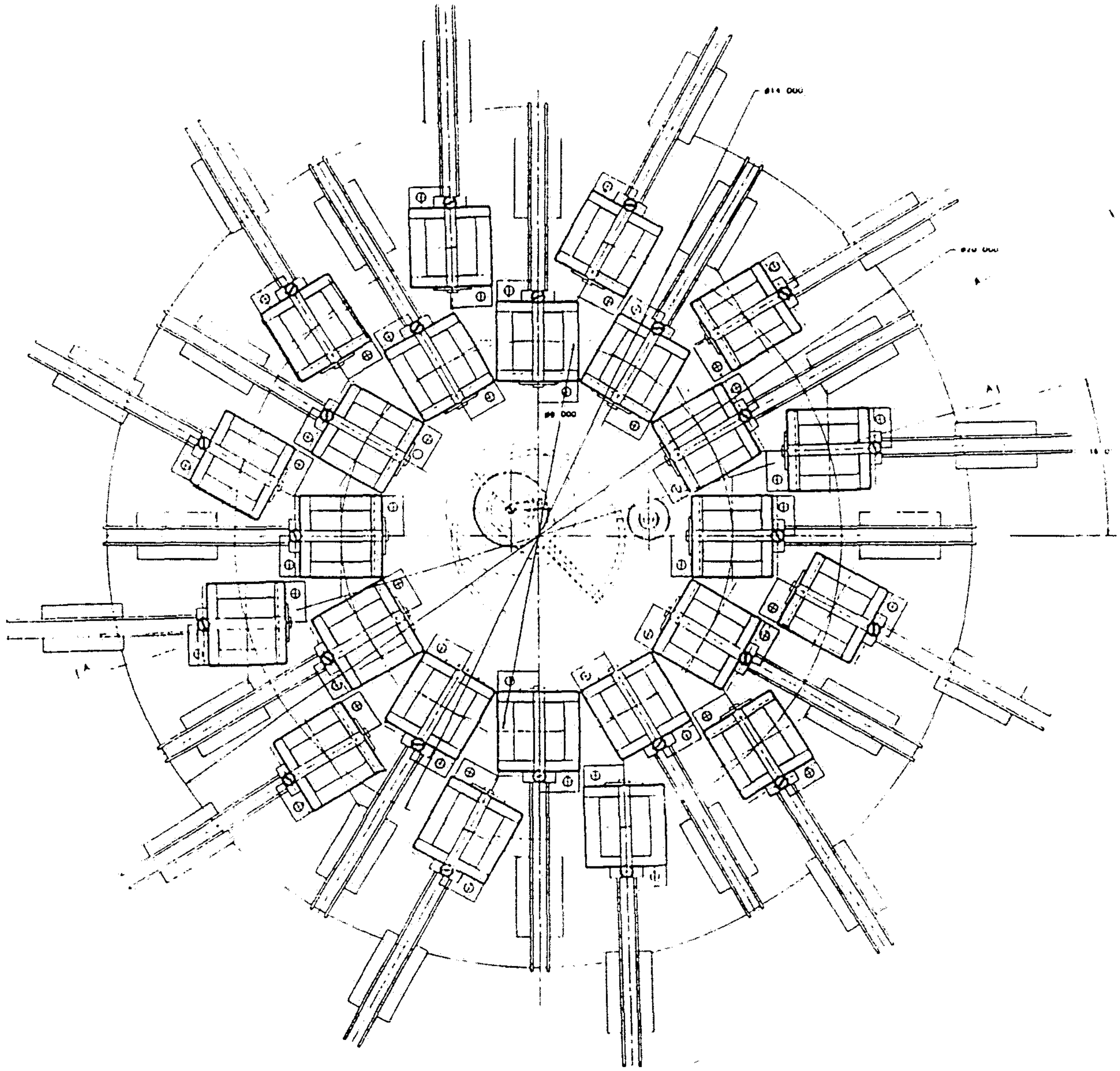

Figure 44 Top view of the DØ VLPC cryostat designed to operate a total of 3072 VLPC channels.

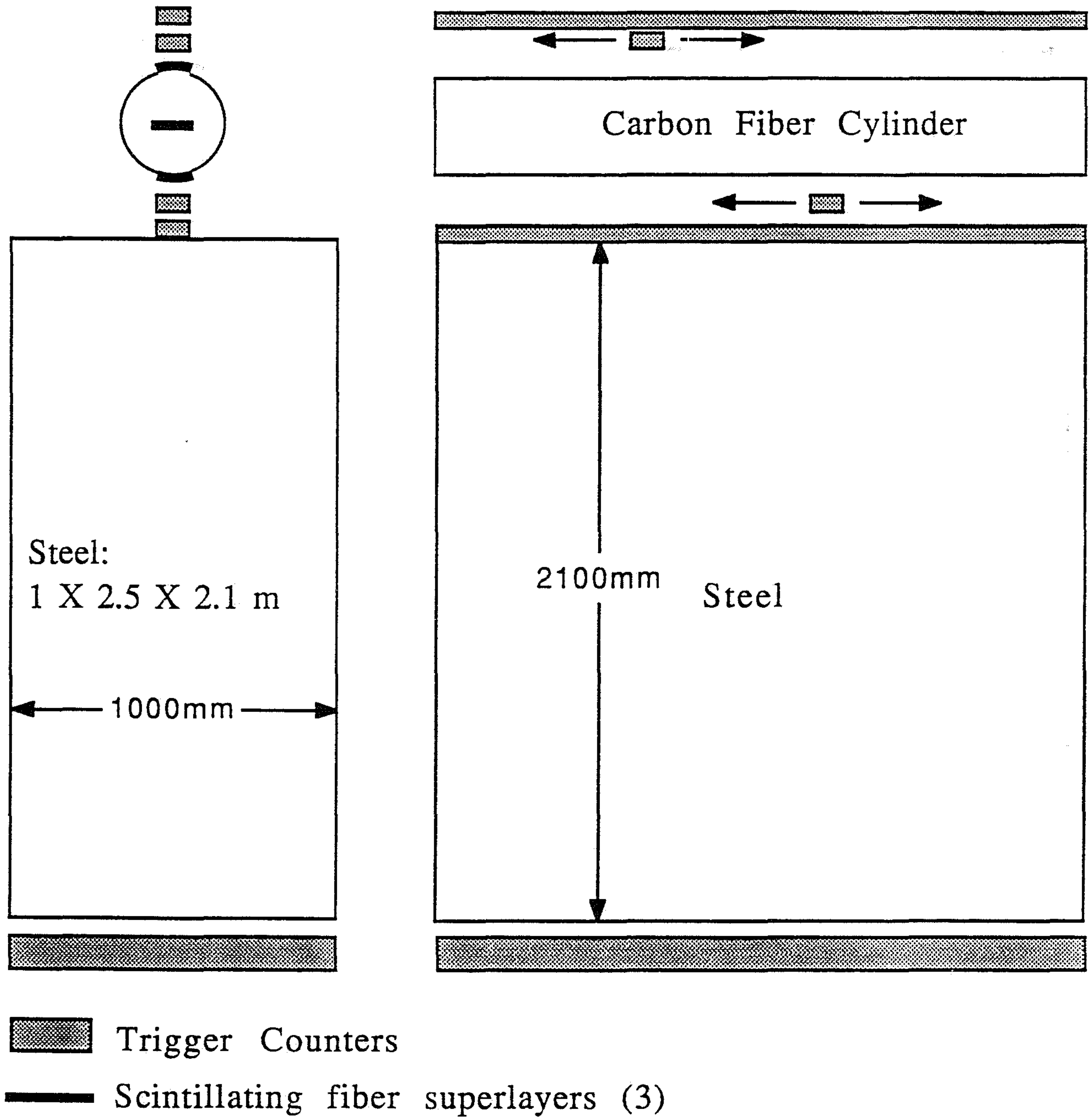

Figure 45 Schematic of the DØ scintillating fiber cosmic ray test setup.

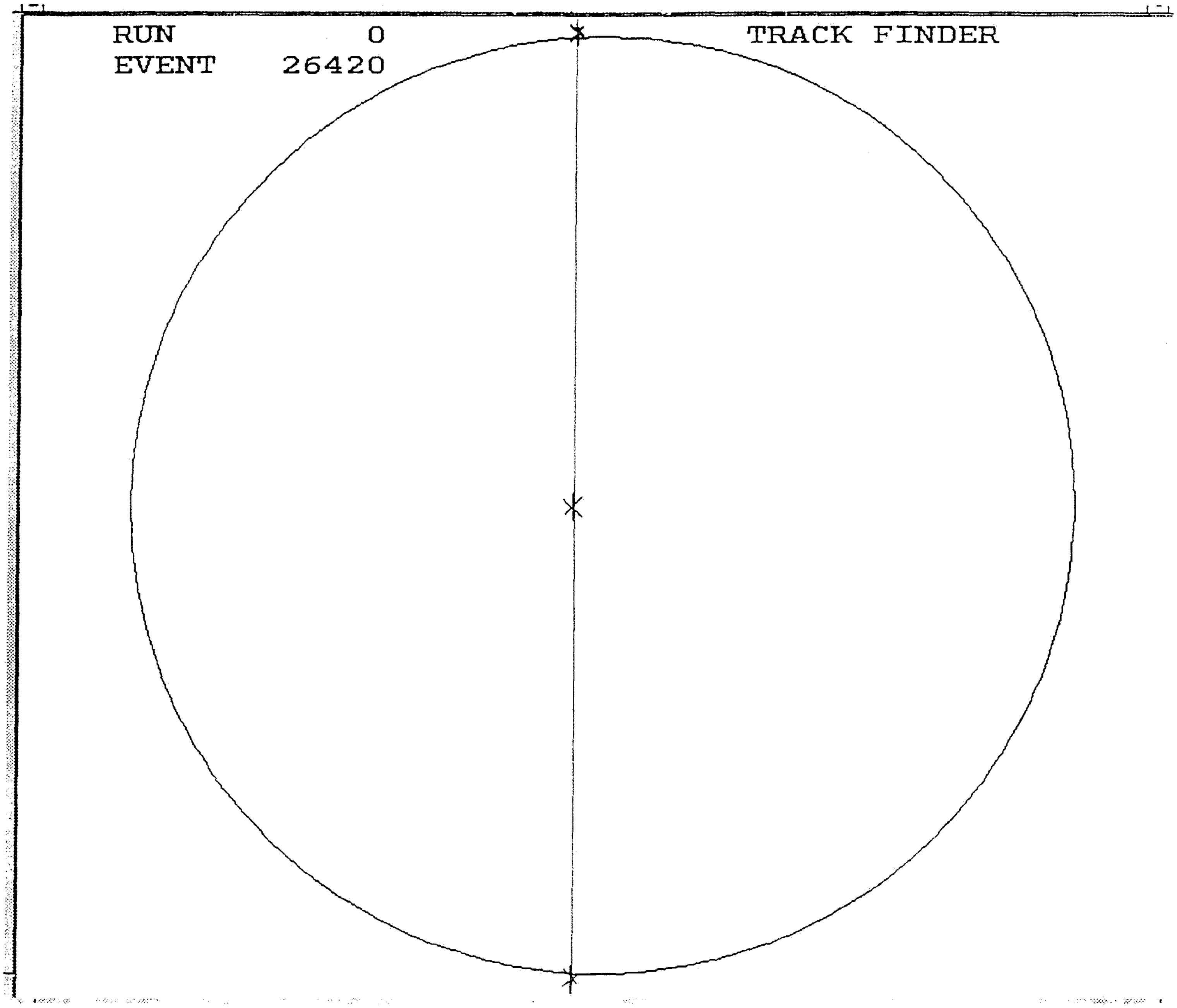

Figure 46 Simulated cosmic ray track traversing the scintillating fiber cosmic ray setup.

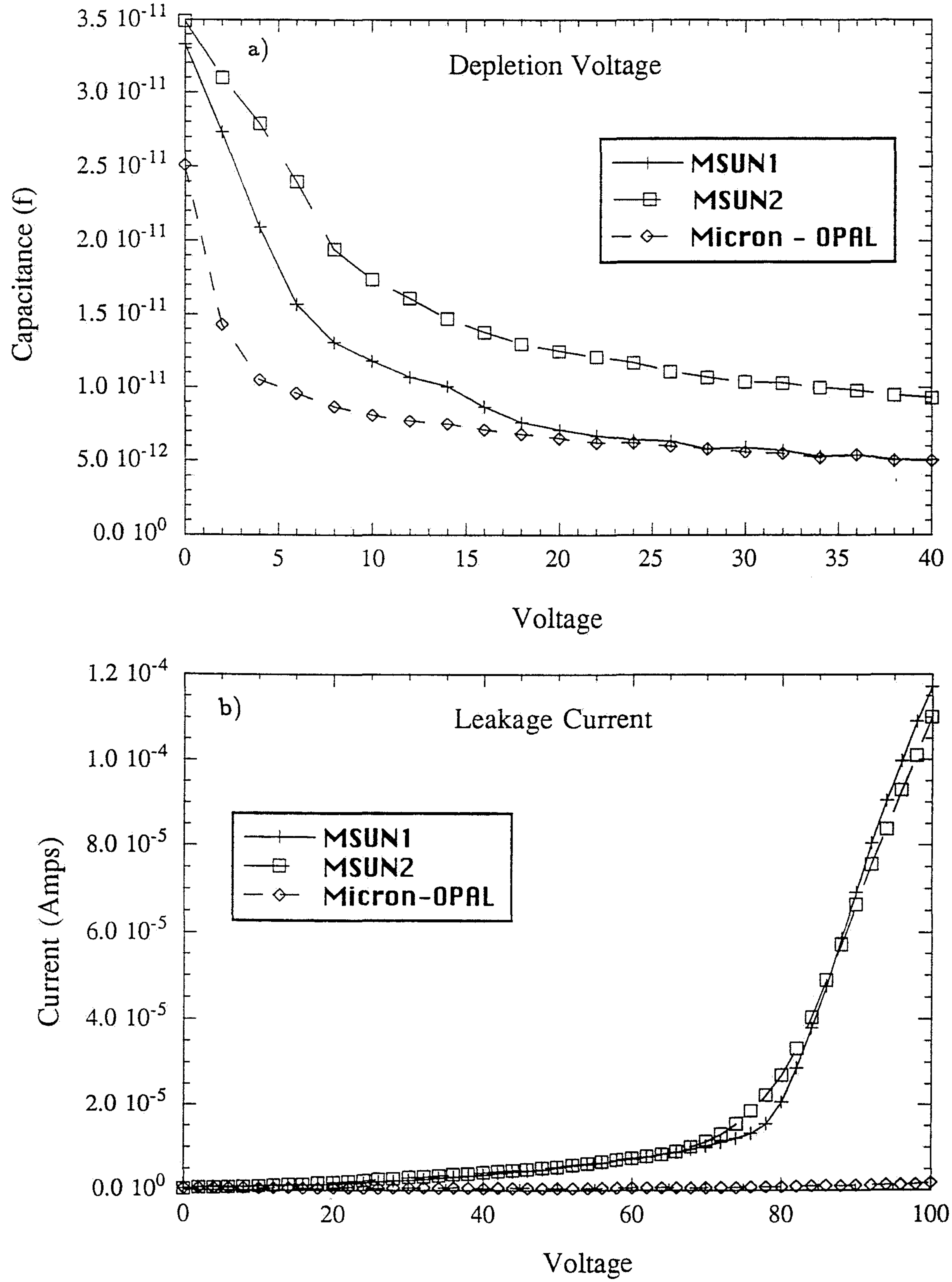

Figure 47 Probe test results for a typical single-sided detector:

a) Depletion voltage;

b) Leakage current.

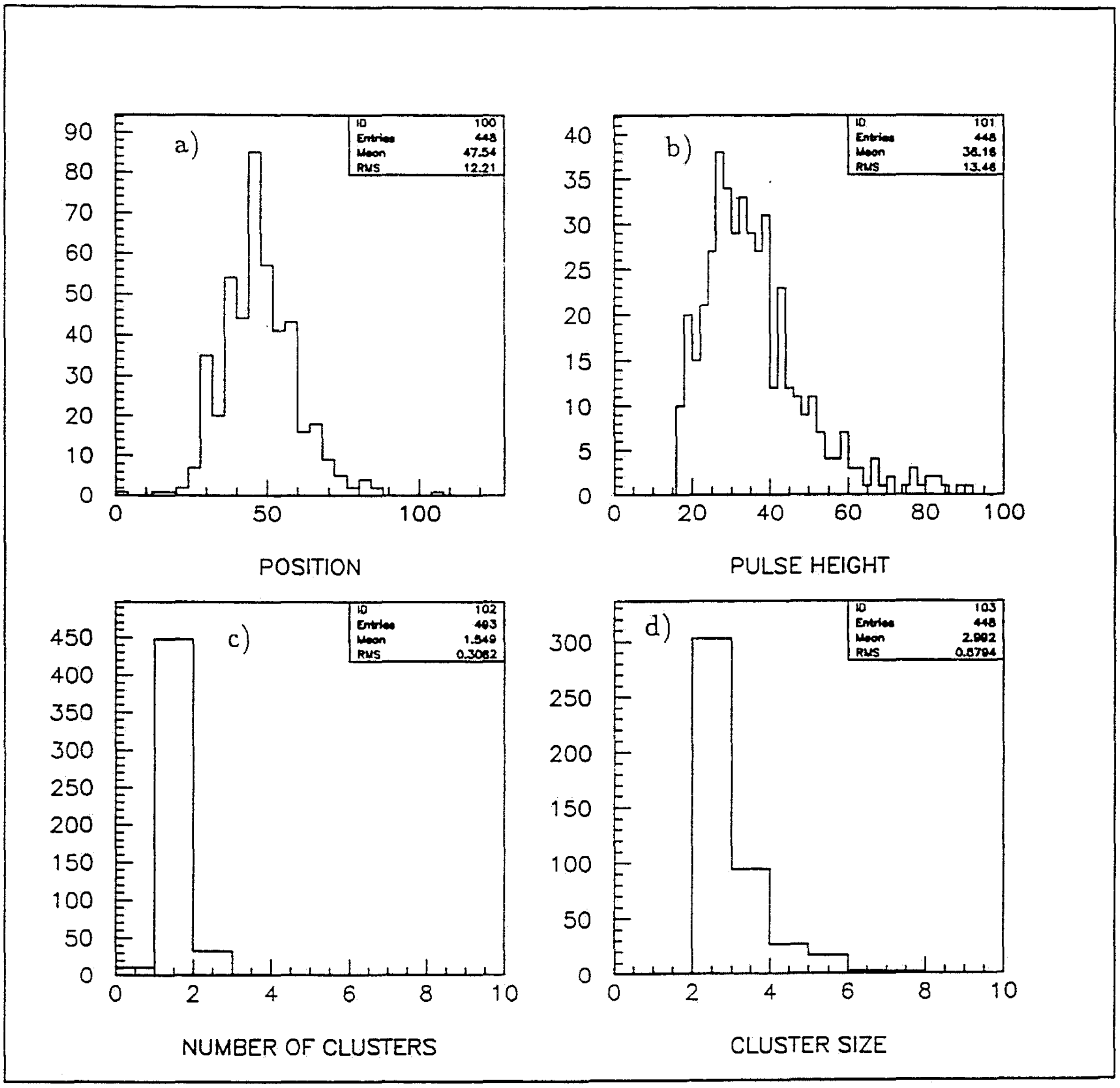

Figure 48 Test results of single-sided detector using energetic electrons from a Ru-106 source:

a) Position distribution;

b) Pulse height distribution;

c) Number of clusters;

d) Cluster size distribution.

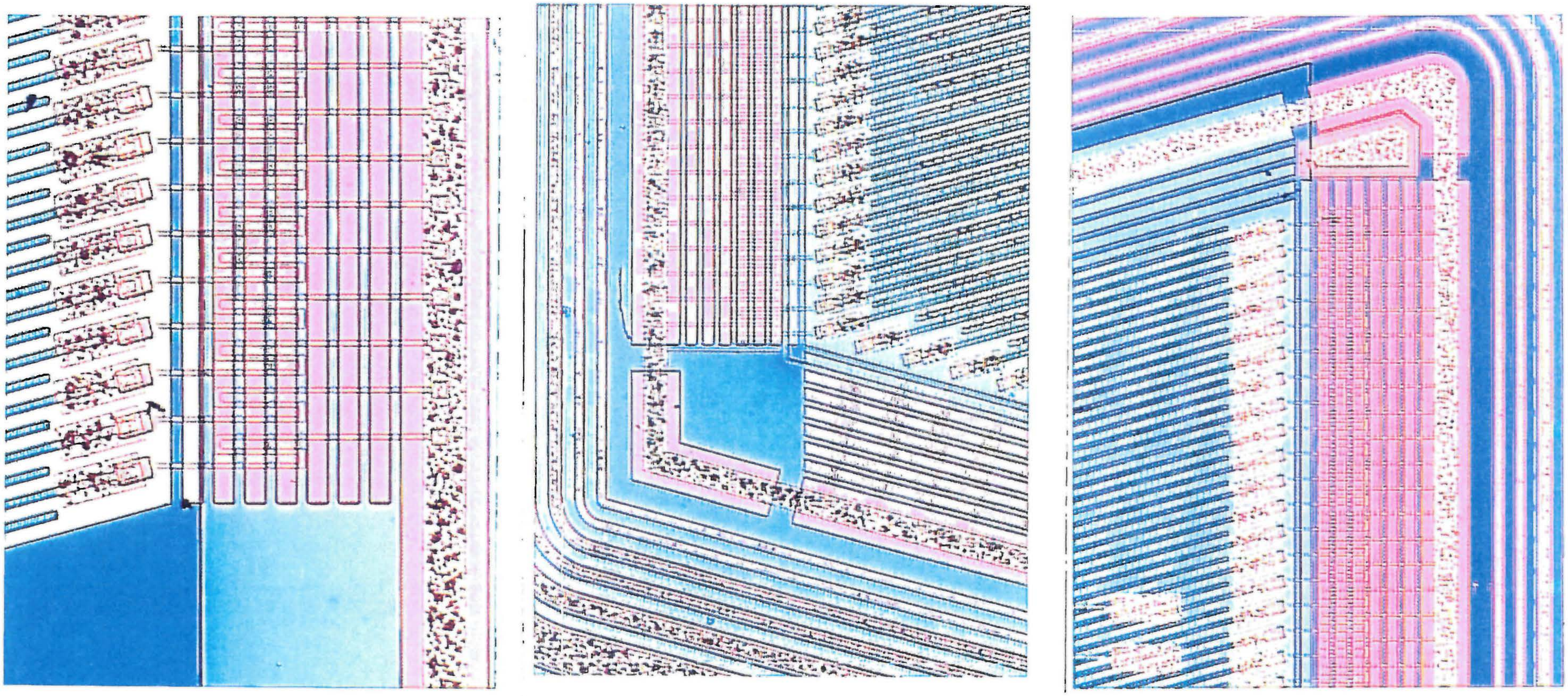

Figure 49 Photomicrograph of the p-side of a double-sided detector:

a) Top left corner showing the DC probe points, multi-guard ring structure, and p^+ implants;

b) Bottom right corner;

c) Close-up of the bias structure showing the *s*-shaped polysilicon resistors, p^+ implants (blue strips), and aluminization (speckled white regions).

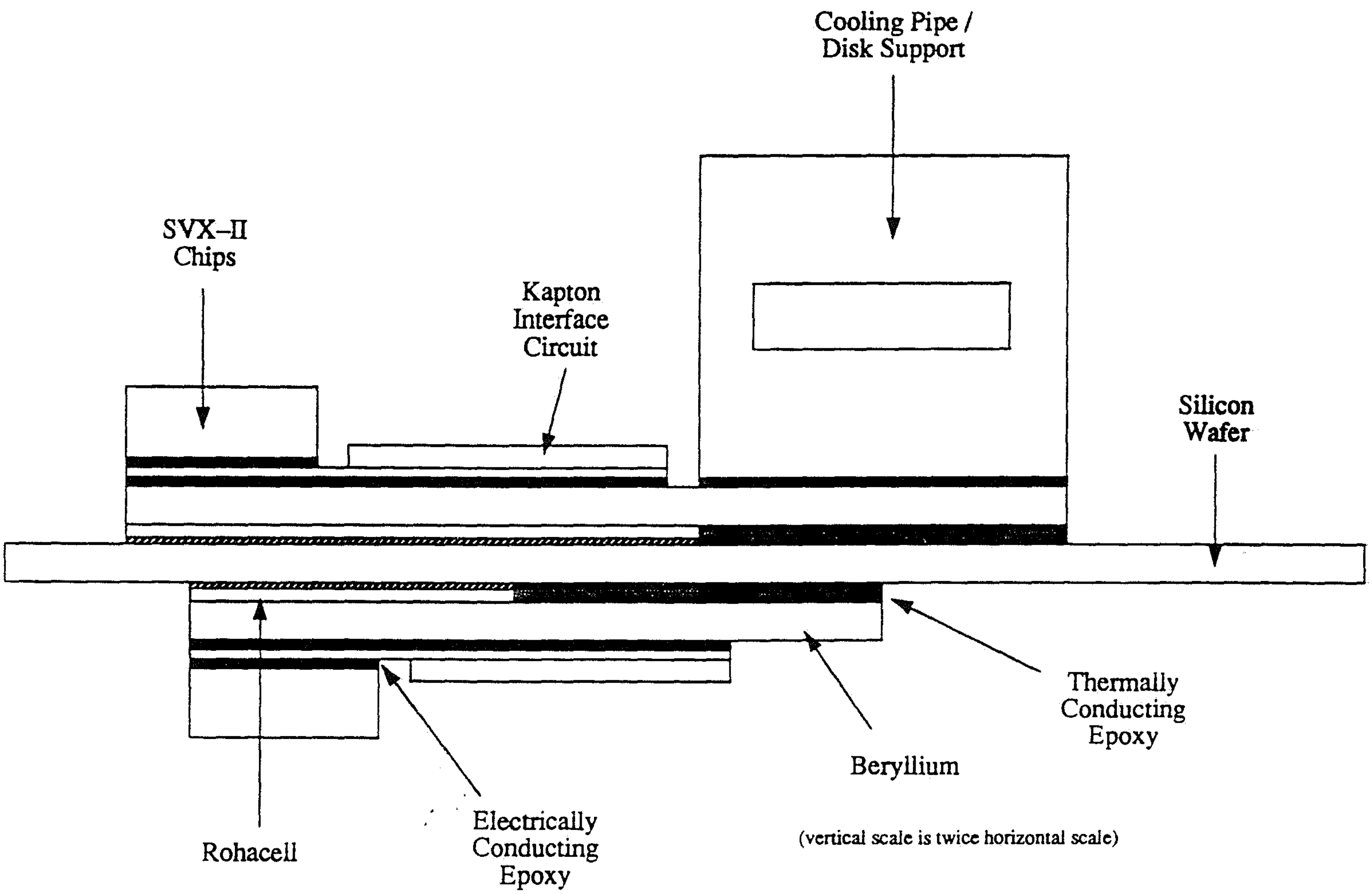

Figure 50 Silicon detector readout support system.

October 12, 1993

E823 (DØ Upgrade): Magnetic Tracking

THE DØ COLLABORATION

The full DØ upgrade is designed to adapt the DØ detector to a new and higher luminosity Tevatron environment, and to extend the DØ physics reach by replacing the present non-magnetic tracking system with a high-resolution, integrated magnetic tracking and vertexing system. In addition, a preshower detector will be added to maintain the excellent electron identification and electromagnetic energy resolution of the DØ calorimeter. Performance characteristics of the full DØ upgrade were presented in an earlier report to the PAC. Here, we present a reoptimization of the tracker which matches the expected resources and schedules, and which has resulted in a slightly different design for the silicon portion of the tracker and a staging scenario for both silicon and scintillating fiber detectors. The changes also reflect the evolution of our understanding of issues related to the construction of the detectors. Simulation studies demonstrate the feasibility of this new design. We also present the current status of the scintillating fiber cosmic ray test, note the progress on the magnet design and briefly discuss our consideration of tracker techniques other than the scintillating fiber technique.

Table of Contents

THE DØ COLLABORATION

B. Gomez, B. Hoeneisen, D. Mendoza, P. Nechev, J.P. Negret, O. Ramirez, J. Roldan, A. Serna
Universidad de los Andes, Bogota Colombia

J. Chen, D. Fein, G. Forden, E. James, K. Johns, P. Loch, L. Markovsky, B. May, A. Milder, J. Rutherfoord, M. Shupe, A. Smith, C. Zeitnitz
University of Arizona

S. Aronson, M. Fatyga, J. Featherly, B. Gibbard, H. Gordon, N. Graf, J.M. Guida, W. Guryn, S. Kahn, S. Protopopescu, P. Yamin
Brookhaven National Laboratory

J. Bantly, D. Cullen-Vidal, D. Cutts, T. Fahland, J. Hoftun, R. Lanou, F. Nang, D. Nešić, R. Partridge, H.W. Xu, R. Zeller
Brown University

S. Glenn, S. Mani, D. E. Pellett
University of California, Davis

J. Drinkard, A. Lankford, A. Lipniacka, D. Stoker
University of California, Irvine

K. Bazizi, C. Boswell, B. Choudhary, J. Ellison, R. Hall, A. P. Heinson, T. Huehn, A. Kernan, S. Wimpenny
University of California, Riverside

G. Alves ,G. Lima, A.K.A. Maciel, J.R.T. de Mello Neto, J. Miranda, V. Oguri, A. Santoro, M. Souza, M. Vaz
LAFEX, Centro Brasiliero de Pesquisas Fisicas, Rio de Janeiro Brazil

H. Castilla-Valdez, G. Herrera-Corral
CINVESTAV, Mexico City Mexico

I. Adam, P. Franzini, U. Heintz, P.M. Tuts
Columbia University

M. Bhattacharjee, V. Kapoor, R. K. Shivpuri
Delhi University, Delhi India

S. Abachi, S. Ahn, B. Baldin, J.F. Bartlett, P. Bhat, F. Borcherding, A. Brandt, A. Bross, J.M. Butler, J. Christenson, W.E. Cooper, M. Demarteau, K. Denisenko, N. Denisenko, H.T. Diehl, M. Diesburg, R. Dixon, D. Elvira, H.E. Fisk, S. Fuess, C. Gao, K. Genser, C. Gerber, D. R. Green, H. Greenlee, N. Grossman, H. Haggerty, S. Igarashi, A.S. Ito, M. Johnson, A. Jonckheere, H. Jöstlein, B. Klima, S. Krzywdzinski, R. Li, Q.Z. Li-Demarteau, R. Lipton, L. Lueking, H.S. Mao, M. I. Martin, H. Melanson, X.-C. Meng, W. Merritt, S. Mishra, H.E. Montgomery, C.T. Murphy, M. Narain, N. Oshima, A. Para, C. H. Park, A. Peryshkin, Y. Que, P. Quintas, P. Rapidis, R. Raja, A.L. Read, W. Smart, R.P. Smith, A. Taketani, M. Tartaglia, D.-C. Wang, L. Wang, D. Wood, P. Xie, R. Yamada, Y. Zhou, Y. Zhu
Fermi National Accelerator Laboratory

W. Dharmaratna, M. Goforth, S. Hagopian, V. Hagopian, T. Heuring, A. Klatchko, S. Linn, R. Madden, H. Piekarz, H. Prosper, C. Shaffer, H. Wahl, D. Xiao, S. Youssef
Florida State University

J. Balderston, M. Cummings, M. Jones, M. Peters, C. Yoshikawa
University of Hawaii

M. Adams, D. Averill, M. Chung, H. Goldberg, S. Margulies, T. McKibben, J. Solomon
University of Illinois, Chicago

G. Alvarez, T. Marshall, H. J. Martin, C. Murphy, D. Zieminska, A. Zieminski
Indiana University

E. W. Anderson, P. Dervenagas, J. M. Hauptman, M. Pang, A. Zinchenko
Iowa State University

J. S. Kang, C. L. Kim, D. W. Kim, S. K. Kim, Y. M. Park
Korea University, Seoul, Korea

H. Aihara, J. Bendich, L.-P. Chen, A.R. Clark, O.I. Dahl, A. Goldschmidt, P. Grudberg, L. Kerth, S.C. Loken, R.J. Madaras, E. Oltman, N.A. Roe, M.L. Stevenson, M. Strovink, T. G. Trippe, E. Varnes, P. Virador
Lawrence Berkeley Laboratory

A. Baden, W. G. Cobau, N. J. Hadley, S. Kunori, A. L. Lyon, D. Norman, K. Streets, P. Tamburello
University of Maryland

N. Amos, H.A. Neal, L. Oesch, D. Stewart, J. Qian, S. Zhang
University of Michigan

M. Abolins, R. Brock, D. Edmunds, S. Fahey, E. Flattum, K. Frame, R. Genik, S. Jerger, J. Linnemann, J. McKinley, P. Mooney, D. Owen, B. Pi, B. G. Pope, H. Weerts, Y. Xia
Michigan State University

E.E. Boos, P. F.Ermolov, Yu.V. Fisyak, A.K. Leflat, A.M. Rusin, E.K. Shabbalina, E.G. Zverev
Moscow State University, Russia

G.R. Snow
University of Nebraska

J. Kourlas, A. Mincer, M. Mudan, P. Nemethy, J. Sculli, J. Yang, Q. Zhu
New York University

E. Amidi, S.-M. Chang, R. Demina, H. Johari, J. Morimisato, M. Glaubman, S. Reucroft, E. von Goeler, J. Wilcox, T. Yasuda
Northeastern University

M. Fortner, J. Green, D. Hedin, R. Markeloff, V. Sirotenko, S. Willis
Northern Illinois University

R. E. Avery, S. Blessing, D. Buchholz, B. Gobbi, Y.-K. Li, Y.-C. Liu, T. Joffe-Minor, S.Y. Jun, H. Schellman, T. Taylor
Northwestern University

V. Balamurali, N. Biswas, J. Jaques, R. Kehoe, M. Kelly, R. Ruchti, J. Warchol, M. Wayne
University of Notre Dame

S. Beri, V. Bhatnagar, S. Chopra, J. M. Kohli, J. B. Singh, P. M. Sood
Panjab University, Chandigarh India

Y. Antipov, V. Bezzubov, N. Bozko, V. Burtovoy, S. Chekulaev, S. Denisov, A. Efimov, O. Eroshin, V. Evdokimov, A. Kirunin, B. Klochkov, V. Klyukhin, I. Kotov, V. Kochetkov, E. Kozlovsky, A. Mayorov, Y. Pischalnikov, V. Podstavkov, V. Riadovikov, A. Shkurenkov, D. Stoyanova, A. Suhanov, A. Vorobiev
Institute for High Energy Physics, Protvino, Russia

B. Abbott, D. Koltick,
Purdue University

D. Adams, I. Bertram, G. Eppley, H. Miettinen, W. Oh, J. Skeens, P. Yepes
Rice University

G. Blazey, J. Borders, C. Cretsinger, G. Fanourakis, M. K. Fatyga, T.Ferbel, S. Grünendahl, R. Hirosky, S. Durston Johnson, F. Lobkowicz, P. Slattery, J. Yu
University of Rochester

Y. Ducros, J. Glicenstein, J.R. Hubbard, P. Mangeot, B. Mansoulie, A. Pluquet, J. Teiger, A. Zylberstejn
CEN Saclay, France

R. Astur, D. Chakraborty, W. Chen, D. Claes J. Cochran, R. Engelmann, S. Feher, G. Finocchiaro, M.L. Good, P. Grannis, J. A. Guida, J.Z.-Y. Jiang, C. K. Jung, C. Klopfenstein, S. Lami, G. Landsberg, J. Lee-Franzini, H. L. Li, S. Lökös, M. Marx, R. McCarthy, M. Paterno, D. Pizzuto, S. Rajagopalan, L. Rasmussen, M. Rijssenbeek, P. Rubinov, R.D. Schamberger, S. Snyder, J. Thompson, C. Yanagisawa,
State University of New York - Stony Brook

M. Botlo, D. Denisov, P. Dingus, M. Diwan, H. Fenker, S. Fredricksen, T. L. Geld, V. Glebov, H. Johnstad, J. Kotcher, K. McFarlane, C. Milner, P. Padley, T. Regan, D. Schmid, I. Sheer, A.L. Spadafora, F. Stocker, M. Takashima, E. Wang, J. Womersley
Superconducting Supercollider Laboratory

B. S. Acharya, M. R. Krishnaswamy, N. K. Mondal, V.S. Narasimham, M. V. S. Rao, H.C. Shankar, P. R. Vishwanath
Tata Institute of Fundamental Research, Bombay India

K. De, P. Draper, E. Gallas, J. Li, J. Perkins, L. Sawyer, M. Sosebee, A. White
University of Texas - Arlington

A. Boehnlein, M. Gui, R. Huson, J.T. White, J. A. Wightman, J.V.D. Wirjawan
Texas A&M University

1. Introduction

The DØ detector was constructed to study proton-antiproton collisions at $\sqrt{s}$=2 TeV in the FNAL Tevatron Collider, with the prime physics focus being the study of high mass states and large p_T phenomena.[1] The current detector has three principal features: muon detection using thick magnetized iron to provide muon momentum determination with small hadron punchthrough backgrounds; stable, unit gain, hermetic, finely segmented, radiation-hard calorimetry; non-magnetic tracking with emphasis on suppressing backgrounds to electrons. The design of the DØ tracking system was very much influenced by the absence of a central magnetic field. The evolving upgrade in the Tevatron luminosity is proceeding rapidly, and the plans to upgrade the DØ detector for higher luminosity operation in the Tevatron runs from 1996 onwards have been described in detail in earlier documents to the FNAL Physics Advisory Committee.[2–6] In the full upgrade (usually referred to as $DØ_\beta$ to distinguish it from the current detector, $DØ_\alpha$) the entire $DØ_\alpha$ tracking system, consisting of Vertex Detector (VTX), Transition Radiation Detector (TRD), and Central and Forward Drift Chambers (CDC and FDC) is replaced by a combination of silicon microstrip barrel and disk detectors and a four superlayer scintillating fiber barrel tracker. These detector systems are located inside a superconducting solenoid magnet, with a preshower detector located just outside the magnet.

Since presenting the earlier design and the associated tracking characteristics at the June 1993 meeting of the PAC, we have embarked upon a reoptimization exercise intended to produce a design which better matches the anticipated resources and schedules. We have also incorporated features which match our current thinking on how to construct the detectors. Here we present the new $DØ_\beta$ design which has resulted from that exercise, and describe the proposed staging scenario. This new design is shown in Fig. 1(a). In the following we distinguish between the full upgrade ($DØ_\beta$), which will be ready for operation in FY99, and a staged version (referred to here as $DØ_\beta$-), which is intended to start operation in early FY97. The $DØ_\beta$- layout is shown in Fig. 1(b).

After a brief reminder of the $DØ_\beta$ characteristics extracted from the earlier PAC report,[6] we concentrate, in this document, on the new design. First we give details of the design itself and the staging process that allows us to develop a powerful tracking system ready for operation by early FY97. We then underline appropriate performance features of this new design. We discuss the status of the scintillating fiber cosmic ray test and the solenoid design and present a brief discussion of alternate tracker possibilities. Finally we give some cost and schedule details.

2. The Initial DØ$_\beta$ Design

In this section we present a summary of the performance characteristics of the full DØ$_\beta$ tracker as presented to the PAC in June 1993. This is mainly intended as a reminder, and more details can be found elsewhere.[6] On the other hand, after the staging process is complete, the current design will be essentially identical to the earlier version in the scintillating fiber sector and should have very similar tracking and vertexing characteristics in the silicon sector. This reminder therefore also yields an excellent approximation to the behavior of the current tracker design.

2.1 Tracking Performance

A variety of physics processes were simulated, most of which involved the tracking of muons. These included: low and high transverse momentum isolated single tracks; μ from W from t decay and μ from b from t decay (for a variety of assumed t masses in the range from 120 to 200 GeV); μ from J/ψ from b decay. For all of these processes, the efficiency of reconstruction of the muon track, the false track reconstruction rate and a variety of track parameter resolutions were determined. All of these performance parameters were found to be essentially independent of physics process and event complexity; isolated track results are the same as one finds for even the most complex physics process. The study of isolated tracks has the advantage of giving the possibility of investigating the track parameter dependence on quantities such as pseudorapidity and transverse momentum.

In all cases studied, the track reconstruction efficiency was very close to 100% and the false track rate very close to 0%. In the central region ($|\eta| < 2$), the resolution in p_T was a few % in the low (few GeV) p_T region, rising to ~10% at 50 GeV. The resolution in the ϕ angle was in the range 0.1 to 1 mrad and the resolution in θ was in the range 1 to 10 mrad. The resolutions in r and z at the beam axis were ~25 μm and in the range 200 μm to a few mm, respectively. All of these resulted in: t-identification via b-quark tagging with efficiency above 70% and background rejection by a factor ~100; good $\mu\mu$ mass resolution in both J/ψ and Z mass regions, and for hypothetical very high mass effects (such as Z').

2.2 Electron Tracking Characteristics

In many of the above studies, we utilized muons as the measure of performance. The passage of electrons through the detectors can result in perturbations through energy loss via brehmstrahlung, which yield the potential for significant deterioration of track finding for electrons as compared to muons. We have investigated this using the process $t \to bW$ with both b and W decaying into electrons. For the electrons from W decay the track finding efficiency is reduced to 97% and for electrons from b decay it is reduced to 96%. The reconstructed track parameters are perturbed by a negligible amount. We are therefore confident that our tracking design is adequate for electron track reconstruction.

3. The Magnetic Tracker Design

The full magnetic tracking system is referred to as DØ$_\beta$ and consists of a superconducting solenoid containing a 4 superlayer scintillating fiber tracker and a silicon tracker composed of a combination of 4 barrels and 22 disks. A preshower detector is located between the solenoid and the DØ calorimeter system. Fig. 1(a) shows a diagram of DØ$_\beta$. The staged version of DØ$_\beta$ is referred to as DØ$_{\beta^-}$ and consists of the solenoid and the preshower detector with an incomplete tracker composed of the 3 inner scintillating fiber superlayers, all 4 silicon barrels and only 6 of the 14 small silicon disks. Fig.1(b) shows a diagram of DØ$_{\beta^-}$.

3.1 Physics Considerations

Our basic strategy is to first maintain and strengthen our excellent capabilities for high p_T physics, and secondly to extend our reach into lower p_T phenomena as the detector evolves. The first stage of the DØ upgrade will be ready in early FY97. This detector, dubbed DØ$_{\beta^-}$ in this report, is fully compatible with 36 bunch operation in all subsystems. In addition, we will include a solenoidal magnetic field and precision tracking devices which will give us a momentum measurement with a resolution of $\sigma(p_T)/{p_T}^2 \sim 0.2\%$ over the region $|\eta| < 2$. The coil of the magnet also functions as an absorber for a preshower detector to aid in electron identification, and a silicon vertex detector will give us precise impact parameter information. These additional capabilities complement and enhance our existing strengths, namely our excellent calorimetry and muon systems.

The DØ$_{\beta^-}$ detector is well-designed to exploit high p_T physics at high luminosity. For example, the tracking volume of $|\eta| < 2$ contains 90% of the electrons from W decay, and the use of E/p and preshower information will enhance our already strong electron identification. The W mass measurement will also be given another handle on systematics through comparison of calorimetric and tracking measurements. For W decays to μ and τ leptons, the distributions are similar but the benefits are even greater, since these channels will be greatly improved with the availability of precison momentum information. For Z's, the presence of 2 electrons puts a greater premium on tracking coverage: only 65% of all $Z \to e^+e^-$ decays are contained within $|\eta| < 2$. However, we have found from our present data sample that we can require a good track for only one of the 2 electrons, and simply require that the second electron be contained within the electromagnetic calorimeter, which extends out to $|\eta| < 3.2$. Therefore we do not anticipate that the staging of the detector will statistically limit our Z sample.

For $t\bar{t}$ decays to di-leptons, 95% of all events have both leptons within $|\eta| < 2$, and the additional requirement that a b-jet be within the tracking volume only reduces the acceptance to 92%. Other high p_T processes, such as the production of heavy exotics, are centrally produced and will also have high acceptances.

With the completion of the full upgrade to DØ$_\beta$ in early FY99, the momentum measurement will improve due to the instrumentation of the fourth and outermost scintillating fiber superlayer, and will be extended forward with additional silicon disks to $|\eta| < 3$. The full upgrade will improve some high p_T physics analyses, such as the charge asymmetry in Z decays, which peaks at high pseudorapidity and will benefit from improved electron identification in the forward direction. The production of di-boson events, such as $W\gamma$, $Z\gamma$, WW and WZ will also benefit from the extended tracking coverage, due to the additional multiplicity of the final states. For example, 70% of all $W\gamma \rightarrow e\gamma$ events are contained within $|\eta| < 2$, but this increases to 98% for $|\eta| < 3$. Another physics topic which will benefit is direct photon production, which probes the gluon distribution function at low-x. The uncertainty in gluon distributions at low-x results in a large uncertainty in direct photon production in the region $|\eta| > 2$. The forward tracking system for DØ$_\beta$ presents much less mass in this region than the present tracker, and this will reduce conversions and allow us to extend our study of this process into a very interesting region.

In addition to strengthening our high p_T physics program, the full DØ$_\beta$ upgrade will allow us to greatly extend our reach into low p_T physics, specifically in the area of b physics. Because b-quarks are lighter than t-quarks, they are produced over a much broader η region, and with lower p_T. For example, only 50% of the di-lepton events produced from $B \rightarrow J/\psi X$ are contained within $|\eta| < 2$, but this increases to 80% for $|\eta| < 3$. This forward coverage is particularly important in DØ , because the central muon system iron requires a minimum p_T of about 3.5 GeV for penetration, while in the forward system, the minimum p_T is only about 0.5 GeV. Thus, our potential acceptance for b physics could be greatly enhanced in the forward region through the use of muon triggers. As a follow-on to participation in this year's SNOWMASS workshop, we recently held a workshop on B physics with DØ$_\beta$. There is presently a great deal of activity in the area of triggering and data acquisition to give us the capability to write a large fraction of interesting $b\bar{b}$ events to tape. Due to the very large rate of $b\bar{b}$ production at the Tevatron, we believe that DØ could contribute to many topics in B physics, including the spectroscopy of B mesons and baryons, rare decays involving leptons, B_S mixing and CP violation.

To summarize, we have staged the DØ tracking upgrade so as to maintain our excellent capabilities for high p_T physics throughout the evolution of the detector. The DØ$_\beta$- tracker gives us good momentum and impact parameter resolution which extends out to $|\eta| = 2$. This is sufficient for all high p_T physics, which tends to be centrally produced, and the momentum determination and vertex tagging will greatly enhance our physics reach. For the full DØ$_\beta$ upgrade, not only do we greatly improve pattern recognition and resolution in the central region, but we extend this performance into the forward region. This will aid in a variety of special topics such as direct photon production, di-boson production and the Z charge asymmetry, and will greatly improve our ability to study b quark production and decay.

3.2 Tracker Components

The broad performance characteristics of the full D$\emptyset_\beta$ tracker described in the previous section were determined by the end of 1991. Detector R&D based on this design occupied most of 1992, and we have made significant technical progress on the mechanical and electronic aspects of the detector design. During a series of workshops begun in early 1993, we have reviewed this design in the light of experience gained during Run Ia.

We have incorporated some changes which reflect our present understanding of the appropriate physics emphasis, the availability of resources and the schedule. We have retained the strong features of the 1991 design and incorporated the technical advances in detector R&D. Finally, we have adopted a staged approach which will allow us to fully exploit the physics potential of Run II within the given fiscal limitations.

The result of this review is the D$\emptyset_\beta$ Magnetic Tracker presented in Fig. 1 and Table 1. Proceeding outward in radius, as in the 1991 design it consists of a multilayer silicon microstrip tracker containing both barrel layers and small and large disks (the so-called F- and H-disks); a four superlayer scintillating fiber outer tracker with two stereo and two $r - \phi$ measurements per superlayer; a 2 Tesla superconducting solenoid; and a six layer preshower detector with two axial and four stereo measurements. The main new feature is a modified silicon tracker geometry.

Philosophically, the new silicon geometry remains similar to the originally proposed configuration. The modifications will further strengthen track pattern recognition in concert with the outer tracker, and, as resources and time permit, will allow D$\emptyset$ to extend more smoothly the pseudorapidity range within which the pattern recognition, vertex reconstruction and momentum determination are excellent.

3.2.1 Silicon Tracker

The main points of comparison between the new silicon geometry and its 1991 counterpart are:

- A powerful and distinctive feature of the 1991 design was its inclusion of silicon disks distributed along the interaction region, integrated with a multilayer silicon barrel. This feature is retained, as the silicon disks are needed for pattern recognition out to $|\eta| = 3$ to match D$\emptyset$'s excellent forward lepton identification. Recent advances in D$\emptyset$'s disk and barrel designs now make it natural for the disks to be interspersed axially between barrel segments, rather than trapped between barrel layers. The total number of small disks is reduced from 20 to 14. To compensate, the minimum radius of the interspersed disks is reduced by more than one third while leaving the maximum radius unchanged.

- For enhanced pattern recognition, the modified silicon barrel has four rather than three layers, and the second and fourth layers are instrumented with small-angle stereo strips in addition to the axial strips in the 1991 design. The stereo strips also improve the ability to separate multiple interaction vertices. In the modified barrel, all layers share the same active length of 84 cm, compared to 48 or 96 cm in the 1991 design, for greater uniformity of acceptance.

Table 1(a) DØ$_\beta$ Si and fiber tracker parameters.

Silicon Detectors										
Barrels	Average radius (cm)									Length (cm)
Barrel 1	3.1									84
Barrel 2	5.0									84
Barrel 3	7.1									84
Barrel 4	9.0									84
Segments(7)	Minimum z (mm)									Length (mm)
	-423	-302	-181	- 60	+ 60	+181	+302			120
Disks	R_{min} (cm)	R_{max}(cm)	$\|z\|$ (cm)							
F (14)	2.6	10.0	6.1	18.2	30.3	43.0				
			48.0	53.0	58.0					
H (8)	9.5	26.0	120.0	122.5						
			125.0	127.5						

Scintillating Fiber Detectors		
Barrels	Average radius (cm)	Length (cm)
Superlayer 1	20	220
Superlayer 2	30	254
Superlayer 3	40	254
Superlayer 4	50	254

Table 1(b) DØ$_\beta$ Si and fiber tracker parameters.

Silicon	1-sided	2-sided	Total
No. of barrel layers	2 (layers 1 and 3)	2 (layers 2 and 4)	4
No. of disks	8 (H)	14 (F)	22
Barrel detector area (m^2)	1.34	1.83	3.17
Disk detector area (m^2)	1.26	0.45	1.71
No. of barrel channels	103,940	286,720	390,660
No. of disk channels	245,760	344,060	589,820
Scintillating Fiber	Number of Fibers	Stereo angle(deg)	
Superlayer 1	11,556	1.3	
Superlayer 2	17,333	2.0	
Superlayer 3	23,111	2.7	
Superlayer 4	28,888	3.3	
Total	80,888		

Nevertheless, because the geometrical modifications permit the barrel to become radially more compact, both the total silicon area and the total number of silicon readout channels remain the same relative to the 1991 design.

- The portion of the silicon tracker to be completed by the start of FY97 includes six disks beyond the ends of the barrel silicon, but defers eight disks interspersed among the seven 12 cm long barrel segments. When the interspersed disks are installed, it will be necessary only to displace the intact barrel segments by small distances in the axial direction. In contrast, the transition between the Step I and full DØ$_\beta$ versions of the 1991 silicon tracker required reconfiguration of the barrel detector ladders within a new mechanical support system. Further discussion of the mechanical design and staging are deferred, respectively, to Sections 3.2 and 4 below.

The advances in DØ's disk and barrel designs which make it possible to intersperse the disks axially between barrel segments share one essential aspect: each reduces the axial distance between active regions of barrel segments. With careful choices of barrel ladder average radii (3.1, 5.0, 7.1, and 9.0 cm) and of number of ladders around the azimuth (12, 12, 16, and 20), it is possible to bring all support, cooling, electrical and electronic services for each segment out radially rather than axially, using a single beryllium bulkhead for all four layers. As in the 1991 design, detectors for the 12-sector small disks have parallel strips on either side set at $\pm 15°$ to the radial direction. By bussing the strip signals from side B of each detector to side A, and locating all the electronics and cooling on side A, one can reduce the total disk thickness to 6 mm.

The parameters of the silicon tracker are presented in Table 1. As in the 1991 design, the silicon barrel provides xy vertex finding and contributes axial-strip hits to the overall pattern recognition. The present design adds one layer of axial and two layers of stereo strip information for enhanced pattern recognition and multiple vertex separation. The small F-disks, all identical, provide pattern recognition and three dimensional vertex detection of high-$|\eta|$ tracks. The large H-disks, or similar, are essential for magnetic analysis of high-$|\eta|$ tracks and contribute further to their pattern recognition.

3.2.2 Scintillating Fiber Tracker

Outside the silicon system is the outer tracker, consisting of four barrel superlayers of scintillating fibers at average radii of 20, 30, 40 and 50 cm. Each superlayer consists of eight fiber layers. Within one superlayer, each of the four pairs of layers, or doublets, shares the same fiber orientation with a pair offset of one half of the 870 μm fiber spacing. Proceeding from minimum to maximum radius within a superlayer, the doublet orientations are z, z, u, and $-u$, where the u orientation maintains a constant pitch $d\phi/dz$ with respect to the (axial) z orientation. This results in stereo angles of 1.3°, 2.0°, 2.7°, and 3.3° for superlayers 1 through 4, respectively. The ~1.5 cm separation between axial doublets makes it possible to determine within each superlayer not only a three-dimensional space point, but also the track angle projected in the xy plane.

The design of these elements has changed only incrementally since early 1993. The lengths of the fiber barrels have been reduced by 5-10% to accommodate more easily our plans for service and access. Based on recent measurements, (conservative) parameters used for the simulations include a scintillating fiber attenuation length of 5 m. Based on our latest Visible Light Photon Counter (VLPC) measurements, we expect to detect at least ~30, ~10, or ~20 photoelectrons from one charged particle passing from the interaction region through the diameter of one fiber at its near, middle or far ends, respectively.

3.2.3 Superconducting Solenoid

A thin solenoidal coil establishes a central field of 2 Tesla within a clear bore of 1.13 m diameter. The 2.54 m long × 1.20 m diameter coil is augmented by a tapered lead radiator on its outer diameter to present a uniform 2 X_0 to particles as they enter the preshower detector.

3.2.4 Preshower Detector

The preshower detector is a single superlayer consisting of six 6 mm thick layers of scintillator, divided by grooves into 5 mm wide elements. As in the outer tracker, pairs of layers are arranged in parallel doublets with adjacent elements offset by half the characteristic spacing. In the preshower detector, the inner, middle and outer doublets are oriented along the u, z and $-u$ directions, where the u orientation maintains an angle of 8° with respect to the axial (z) orientation. Clusters of hits in the three doublets are matched both geometrically and with the aid of the recorded pulse heights.

3.3 Mechanical Considerations

The DØ$_\beta$ tracker fits within the bore of the inner cryostat of the DØ calorimeter, which has a radius of 76 cm. A list of the various detectors and their gross dimensions is shown in Table 2, and a cross-section indicating the support structures is shown in Fig. 2.

The outermost element is the preshower detector which consists of a shaped lead radiator, such that particles traversing the solenoid and this lead radiator see a constant amount of material equal to approximately two radiation lengths. The active elements of this detector are six layers of scintillator, each 0.6 cm thick, read out by waveshifter fibers. The segmentation is quite coarse (0.5 cm strips) and the positioning of this detector does not pose any significant constraints on the mechanical plant. It will be built around a large G-10 cylinder and placed around the solenoid's cryostat. The solenoid/preshower will form a subassembly which will be installed in the bore of the calorimeter.

The superconducting solenoid is 17.5 cm thick. It is rigidly attached at one end to the inner wall of the inner cryostat of the calorimeters. At this time we envision that all of the tracking detectors will be rigidly attached to the end plates of the solenoid's cryostat. Nevertheless, a detailed study of the stability of these end plates as the solenoid's cryostat is evacuated and the coil is cooled down needs to be performed, before this choice can be adopted. Alternatively, the tracking detectors can be mounted directly on the inner cryostat of the calorimeter.

The tracking system will provide measurements of space points on tracks with submillimeter resolution, and therefore the requirements of alignment and stability are quite stringent. Both rigid and kinematic mounts will be employed to allow the tracking detectors to maintain their position in space, while stresses due to movements of the support points will not be transmitted to the detectors themselves. In this way we expect that there will be no significant time dependent distortions of the detectors.

An arrangement of rings and struts located ± 127 cm in z from the interaction point will support superlayers 2, 3 and 4 of the scintillating fiber tracker. At a radius of approximately

Table 2 Detector Dimensions

	Radius(cm)	Length(cm)
Calorimeter cryostat	76	>275
Preshower Detector	74	265
Superconducting Solenoid	71.6 inner	265
	54.0 outer	
Fiber Barrel 4	50	254
Fiber Barrel 3	40	254
Fiber Barrel 2	30	254
Fiber Barrel 1	20	220
Silicon Support Spaceframe	16	220
Silicon Barrel 4	9.0	84
Silicon Barrel 3	7.1	84
Silicon Barrel 2	5.0	84
Silicon Barrel 1	3.1	84
Beam Pipe	2.0	

27 cm two cylindrical inserts each 17 cm long (one at each end) are used to support the inner layer of the scintillating fiber system. Since the fiber layers for DØ$_{\beta}$- and DØ$_{\beta}$ are identical, the only difference between the two stages being the number of layers read out, the support structure for the scintillating fibers is the same for both stages. The scintillating fiber tracker will form a subassembly that will be installed inside the solenoid bore.

A spaceframe structure constructed of thin wall aluminum tubing with a radius of 16 cm and a length of 220 cm is used to support the silicon tracker. It is in turn attached to the rings that support the outer layers of the scintillating fiber tracker, in a fashion similar to the one used to support the innermost scintillating fiber layer, but as an independent system. The silicon tracker forms the last subassembly to be mounted inside the scintillating fiber tracker.

The silicon detector for DØ$_{\beta}$- consists of 7 barrel segments, each barrel segment consisting of four layers of silicon detectors. In addition three double-sided disk detectors at each end of the barrels complete the DØ$_{\beta}$- detector by providing coverage at large η. The silicon detector for DØ$_{\beta}$ will have an additional six disks interleaved between the seven barrel segments, and two additional disks, one at each end, for a total of 14 disk detectors. Another set of three larger annular tracking detectors, the H-disks, located at larger z

($\sim \pm 120$ cm) complement the inner silicon tracker for D$\emptyset_\beta$. At this time we are exploring a variety of technologies for the H-disks such as silicon strip detectors or gas microstrip chambers.[7]

The SVX II amplifiers mounted on top of the silicon detectors are the primary heat producing element inside the active volume of the tracker and they need to be cooled. A water cooling system will carry away the generated heat, which for the full D$\emptyset_\beta$ silicon detector will be slightly more than 2 kW. By comparison, the heat generated in the cables for this detector is insignificant. Dry air will be flowing through the tracker volume.

The step-like structure in the silicon tracker spaceframe at $z = \pm 110$ cm is included in order to be able to incorporate the forward tracking H-disks. Since the insertion of the interleaved disks of D$\emptyset_\beta$ to the silicon tracker will anyway require the removal and disassembly of the entire subsystem, it may be possible for D$\emptyset_{\beta^-}$ to use a simpler spaceframe structure. The final decision will depend upon details of the exact routing of cables and the fiber light guides of the scintillating fibers. Water cooling lines for the silicon, cables carrying signals and power for the silicon tracker and the fiber light pipes from the scintillating fiber tracker vie for space in the forward region.

The monitoring of the stability of the position of the various tracking detectors is an important task for a precise detector. Even though the ultimate alignment and monitoring will be provided by the data itself (*i.e.* by fitting tracks), a system capable of detecting shifts in the various detectors is a prerequisite. Experience with the LEP detectors and with the design studies for SSC detectors has yielded several possibilities (such as capacitive proximity probes and laser monitoring systems) that satisfy our requirements.

3.4 Electronics Considerations

The present plan is to develop readout electronics for the tracking system with the higher level being similar to the existing DØ VME readout. Where possible, common systems are used. An overview of the tracker electronics readout system is shown in Fig. 3.

The SVX II will be the basic data acquisition part for the DØ silicon detector. It has 128 channels and 32 stages of pipeline delay and an 8 bit ADC for each channel. It can be reset between every crossing (at 132 ns) and has a sparse data readout system.

Since the gain of the VLPC is around 25,000 and the capacitance (determined mostly by the output cable) is around 12 pf, a VLPC output is very similar to a silicon strip. Thus, a standard SVX II chip should work for all the non-trigger scintillating fiber channels. Even if the ADC in the SVX II is not needed, the facts that the chip has a pipeline delay, 128 channels per chip and low power consumption make it very attractive. A 512 channel cassette is similar in size to a readout string for a silicon detector.

The DØ design allows strings of up to 64 SVX II chips to be connected serially together. The read out of up to 4 strings of these chips is controlled by a special readout controller card ("port" card) located on the detector in the silicon case and close to the cryostats in the VLPC case. Data from the port card is sent to a VME readout card via a 1 Gigabit/sec fiber optic link. There are 2 fiber links per port card and 2 (possibly 3) fiber links per VME card. The VME card provides 2 high speed ports for level 1.5 trigger processors. Data is sent over these ports as soon as it arrives over the fiber cable. A design of all the relevant new boards in the system is complete and prototypes are expected within a few months. This is a large system (980,000 silicon channels and 80,000 VLPC channels) so much design effort is being spent on diagnostics. We plan to have one VME microprocessor (commercial) per crate to monitor system performance. This will include data acquisition hardware monitoring and histogramming pulse heights for every channel in the crate. Techniques for detecting bad channels from these histograms are under development.

Scintillating fiber channels that would participate in a level 1 trigger will need a prompt discriminator output as well as a delayed discriminator or ADC output. Space for the trigger cabling and logic is at a premium. We are looking for a system that has a minimum of 16 channels per IC, onboard delay, sparse data readout, and a prompt trigger pickoff. The choices under consideration are as follows:

- LeCroy has a discriminator-only wire chamber system that will probably work,
- U.Pennsylvania has developed a shaper discriminator for the SDC that will also work with minor modifications (removing shaping circuit) but would require the addition of a digital delay.

The drawback for both of these systems is that they consist of only 8 channels per chip and they have significant power requirements. Preliminary designs show that either system requires parts on both sides of a PC board, and local water cooling in order to operate at the density required. The system components could be made to fit.

- A derivative of the SVX II has been examined and the preliminary indications are positive.[8]

As shown in Fig. 3, the silicon system would participate in the trigger only at level 1.5 or level 2.

4. Staging

Budgetary and schedule constraints force us to implement a downscaled version of the full $D\emptyset_\beta$ detector for early FY97. This detector, $D\emptyset_{\beta}-$, is shown in Fig. 1 (b). We have designed the $D\emptyset_\beta$ detector so as to allow a viable staging scenario.

As emphasized in the description of the silicon tracker, the new design takes account of possible budgetary restrictions that cause a portion of the entire silicon system to be completed later than the beginning of FY97. Provided that an irreducible kernel of the silicon tracker can be completed by that date, the new design provides for orderly and efficient addition of the remaining elements.

The silicon kernel consists of the central barrel (4 layers × 7 axial segments each 12 cm long) and 6 of the 14 small disks, 3 on either end of the barrel. The large disks at the ends of the tracking region, as well as 8 of the 14 small disks, are deferred. This is the minimum system needed for full tracking at central pseudorapidities, providing only stubs for electron and muon identification out to the calorimeter and muon system limits near $|\eta| = 3$.

The staging of the scintillating fiber tracker is achieved by installing all four fiber barrels, but delaying the readout electronics for one superlayer and the tracking trigger system. Since the dominant cost of the fiber tracker is in the electronics, postponing some of the readout channels allows us to obtain the maximal cost savings for the FY97 detector while maintaining the most flexible upgrade path in terms of taking advantage of improved funding opportunities or schedule delays. We propose to defer the instrumentation of the outer scintillating fiber superlayer, which comprises about 36% of the channels. The preshower detector and the solenoid are fully implemented for the FY97 detector. This staging plan provides the minimum tracking capabilities required to carry out the central region physics, at the expense of tracking at large pseudorapidities. The performance of this initial stage, the DØ$_{\beta^-}$ detector, and the full DØ$_\beta$ detector are described in the following sections.

5. Performance Characteristics

We have continued our studies of performance to include the evolution of the proposed DØ tracker from the DØ$_{\beta^-}$ staged detector to the full DØ$_\beta$ tracker, which will be ready in time for the start of physics with the Main Injector. Our studies include both a fast simulation which gives us acceptance, momentum resolution and impact parameter resolutions, and a CPU-intensive, full GEANT Monte Carlo simulation which allows us to study pattern recognition.

5.1 Resolution and Acceptance

The results of the fast simulation[9] will be presented first. This simulation takes into account the intrinsic resolution of the detectors as well as multiple scattering, energy loss and fluctuations in energy loss.

For the silicon detector we have assumed an intrinsic detector resolution of 8 μm in the direction perpendicular to the strips, and we have doubled the detector thickness from 300 to 600 μm to take into account mechanical support, cooling and electronic readout. The resolution of the silicon is degraded for tracks which cross the strips at an angle, causing the charge to be divided among several channels. For the small-angle stereo of the barrel detectors (2°) the effect is negligible. For the disks there can be an appreciable effect for central tracks which cross a disk at a grazing angle. We assume an efficiency of 97% for the active silicon detectors, and we have included all of the inactive regions due to gaps in the detector geometry. For $D\O_{\beta}-$ the 6 disks interleaved with the barrel segments are left out, as well as 1 additional disk at each end and the large disks which provide coverage at large pseudorapidity.

For the scintillating fiber detector, we assume the fibers have a center-to-center spacing of 870 μm and that they are arranged in four superlayers at radii of 20, 30, 40 and 50 cm. Each superlayer consists of four fiber doublets, two axial and two stereo with a pitch of 0.001 rad/cm. The fraction of dead fibers is taken to be 2%. For $D\O_{\beta}-$, the outermost fiber superlayer is not included.

For the purpose of these studies, we have assumed that the interaction region has a Gaussian distribution along the beamline characterized by $\sigma(z)=$ 22 cm. The detector performance is then evaluated as a function of track angle, expressed in units of pseudorapidity, $\eta = -\ln(\tan\theta/2)$. In Fig. 4 the transverse momentum resolution, $\sigma(p_T)/p_T$ is plotted versus η for the staged detector and for the full upgrade, for a track with $p_T = 50$ GeV. In Fig. 5 we see the transverse momentum resolution plotted versus η for a 2 GeV track. If we characterize the momentum resolution as the quadratic sum of two terms, $\frac{\sigma(p_T)}{p_T} = a \oplus b \cdot p_T$, where the first term is due to the multiple scattering contribution and the second is due to the intrinsic resolution, then from Fig. 4 we see that $b = 0.0022$ for the staged detector for $|\eta| \leq 1.5$, improving to 0.0016 for the full upgrade. The improvement is due primarily to the inclusion of the outermost scintillating fiber superlayer. There is also a noticeable improvement in the momentum resolution of the full upgrade for $|\eta| > 2.2$. This is due to the addition of H-disks in the forward and backward regions. These results are consistent with previous studies of the DØ upgrade tracking resolution, given the small decrease in the radius of the outermost superlayer to accomodate the increase in the thickness of the superconducting coil.

The impact parameter resolutions for the $D\O_{\beta}$ and $D\O_{\beta}-$ are shown in Fig. 6 and Fig. 7 , for $p_T = 50$ GeV tracks. We obtain good resolution in transverse impact parameter (10-20 μm) all the way out to $|\eta| = 3.0$ for the full upgrade; for the $D\O_{\beta}-$ detector there is some loss of precision at large pseudorapidity due to the fact that the large H-disks are not implemented. The distributions of the z impact parameter are shown in Fig. 7. The choice of small-angle stereo in the silicon barrel limits the precision to $\sim 500\mu$m for $D\O_{\beta}-$ whereas in the full upgrade, the silicon disks extend the z precision into the forward region. This z information is very valuable in pattern recognition, and in distinguishing multiple interaction vertices.

The impact parameter resolutions in both the transverse plane and along the beam axis are shown in Fig. 8 and Fig. 9 for $p_T = 2$ GeV. In this momentum range, multiple scattering is more important. This effect is readily apparent, especially at large pseudorapidities.

5.2 Pattern Recognition

We have studied the pattern recognition characteristics of the $D\O_{\beta}$ and $D\O_{\beta}-$ detectors to look for any problems as compared with the design presented to the PAC in June 1993. In a similar manner to the previous studies, the detector geometrical representation is quite detailed, with the actual structure of both the silicon and scintillating fibers included. For example, there is a 5% geometrical inefficiency in any silicon surface due to detector details and gaps between wafers. The amount of material is also representative of the actual trackers.

Initially, we examine the low-η performance in which the tracks traverse all of the available scintillating fiber barrels. GEANT is used to propagate tracks through the detector accounting for multiple scattering, hadronic interactions, decays and energy loss. The response of the scintillating fiber detectors is simulated at a detailed level; however with the current understanding of photon yields, VLPC quantum efficiency and doublet ribbons the calculated inefficiencies are quite negligible. Similarly, the silicon detectors are intrinsically highly efficient. However, to account for imperfection in construction and operation, 1% of the channels are randomly turned on to account for noise and 2% of the channels are randomly turned off to account for dead channels in both silicon and scintillating fibers. We believe that current construction techniques and electronics reliabilities in large systems tend to make these worst case rather than typical.

Several high p_T event samples were generated, including single 100 GeV muons and also $t\bar{t}$ events, with 1000 events in each sample. The assumed t mass was 150 GeV. Leptonic decays to muons were forced in each sample. The observed occupancies for the $t\bar{t}$ events with and without the random noise are shown in Table 3. While the noise is comparable to the pure physics occupancies in the scintillating fibers it dramatically increases the occupancies in the silicon, because the silicon intrinsic occupancy is so small.

Table 3 Tracking Detector Occupancies

Event Sample	$t\bar{t}$ evts, no noise	$t\bar{t}$ evts, 1% noise
Barrel 1 Silicon	0.005	0.015
Barrel 2 Silicon	0.003	0.013
Barrel 3 Silicon	0.003	0.013
Barrel 4 Silicon	0.002	0.012
Superlayer 1 Scintillator	0.06	0.07
Superlayer 2 Scintillator	0.04	0.05
Superlayer 3 Scintillator	0.03	0.04
Superlayer 4 Scintillator	0.02	0.03

The first step in the reconstruction is clustering. Adjacent hit fibers in a layer are merged to form a single cluster. Overlapping clusters in the two layers forming each doublet are merged to form a supercluster. The track finding is performed with a road-following technique. A starting track is assigned parameters with very large errors and then this track is propagated along predefined paths through the detector. Each path consists of a list of detector surfaces which are traversed. If the next surface is to be crossed, then an attempt is made to extend the track using each of the nearby hits on the surface. A new track is created for each such hit starting with the parameters of the parent track and then updating them for the new hit information using a Kalman filter algorithm. If the new χ^2 is too large or the new track parameters are inconsistent with the path, the new track is deleted. For the work here, we have carried out the track finding in two passes. On the first pass we proceed from the outermost to the innermost ϕ measuring elements. We then go back and add the stereo measurements, again from outside to inside.

On completion of the track finding, we compare the individual tracks in the reconstructed sample to those in the initially generated monte carlo sample. The reconstructed tracks are divided into two categories. The first, so-called *efficient* category, are reconstructed tracks which can be identified with a generated track. The second category, *fakes*, are reconstructed tracks which cannot be identified with a generated track. Some of the *efficient* sample are not perfectly reconstructed and we can sub-divide this sample into *good* and *misreconstructed* using a χ^2 comparison between reconstructed and generated tracks.

With the $D\O_\beta$ detector we find that even for the most complicated events studied, $t\bar{t}$ events with detector noise included, more than 92% of the test tracks are in the efficient category. Of these, 3-4 % appear initially to be misreconstructed. We have looked further at the characteristics of these few % and observe that the misreconstruction is mainly in the z dimension. They may be tracks which have no (or few) real hits in the silicon, in which they have picked up false hits. There appears to be room for optimism that this particular defect could be remedied by implementation of a repechage process in which individual bad hits are removed from the found tracks. It is also clear that the track finding algorithm may not be optimal. When the noise is taken to be zero, the misreconstructed fraction is almost halved. In all the samples examined the ratio of fake tracks to real is negligible.

For the $D\O_{\beta^-}$ detector, the efficiency for track finding remains high. However, the fraction which is misreconstructed rises by about 1%. In this case, with the outer scintillating fiber superlayer not instrumented, the *fakes* also start to be measurable at the few per thousand level in the more complicated event samples. Further reduction of the number of instrumented layers, for example by removing the stereo doublets of superlayer 3, increases further the level of the *fakes*.

In the preceding paragraphs we have concentrated on the track finding at low η. At higher η, the silicon disks play a significant role and the changes from the June 1993 design have led to an increase in the distance between disks. We have examined the effect of this change using a modification of the June 1993 simulation and studying b production with subsequent decay via J/ψ into two muons in the disk region. In particular, alternate disks were removed so that the distance between successive disks was approximately the same as in the current design. Due primarily to geometrical effects, which are partially alleviated in the current design by reducing the inner radius of the disks, about 10% of the J/ψ were lost. There was no deterioration of the explicit track finding performance; no increase in the *fakes* or *misreconstructed* samples was observed.

5.3 Physics Performance

We have used the fast detector simulation to study our capabilities for some physics processes which are of special interest for Run II and beyond. Most of these studies duplicate previous work and were intended to simply confirm that the evolution of the detector design has not had a negative impact upon our physics capabilities.

5.3.1 b-tagging for t Physics

The ability to tag a b-quark by measuring the impact parameters of its decay products is an attractive technique which will aid in the identification of t-quark decays. To study this we have used ISAJET to generate the decay $t \to Wb$, then allowed the b-quark to hadronize and decay. The decay products of the b-quark were then passed through the fast simulation, and the impact parameter significance (transverse impact parameter divided by its error) was calculated for each track. As in previous studies, we required that at least three tracks in the b-jet with $p_T > 1$ GeV have impact parameter significance greater than three. The tagging efficiency, defined as the probability that at least 1 b-jet in a $t\bar{t}$ event be identified, was found to be 79% for the full upgrade, for a t-quark mass of 150 GeV. (The primary loss of efficiency is simply the kinematic requirement of 3 charged tracks with $p_T > 1$ GeV in the b-decay; once this is satisfied the impact parameter cuts are 91% efficient on each b-jet.) Again, this is consistent with previous studies. Since the t quark is produced centrally, this tagging efficiency is the same for both $D\emptyset_\beta$ and $D\emptyset_{\beta}-$.

5.3.2 Mass and Impact Parameter Resolution for $b\bar{b}$ Events

We have generated $b\bar{b}$ events using ISAJET, and required one b to hadronize as a B_S and subsequently decay to $J/\psi\phi$. The decays $J/\psi \to \mu^+\mu^-$ and $\phi \to K^+K^-$ were also forced. We then selected events in which both muons were within the acceptance, defined by $|\eta| < 3.0$, and $p_T > 1.0$ GeV. The resulting $\mu^+\mu^-$ invariant mass distribution, shown in Fig. 10 , is fit to a Gaussian with $\sigma = 42$ MeV. The $\mu^+\mu^-K^+K^-$ invariant mass distribution is shown in Fig. 11 (a) and the B_S mass resolution is 56 MeV. If we perform a mass-constrained fit, using the known J/ψ and ϕ masses (see Fig. 11 (b)), we obtain a much better resolution of 29 MeV. We have also studied the impact parameter resolution for muons from semi-leptonic B-meson decays. A cut requiring impact parameter significance > 5 results in 50% efficiency for tagging a $B \to \mu X$ decay.

5.4 Conclusions

Based on the studies presented in this chapter we see that our new $D\emptyset_\beta$ design indeed has comparable performance characteristics to that presented to the PAC in June 1993. The staged detector $D\emptyset_{\beta}-$ which will be ready in FY97 has adequate performance characteristics for $|\eta| \leq 2$ and so can address the majority of archetypal high p_T physics. On the other hand, its limitations for $|\eta| > 2$ are manifest and, in particular, progress in attacking the b-physics potential unfortunately will be deferred.

6. Scintillating Fiber Cosmic Ray Test Status

As a final step towards demonstrating the viability of a scintillating fiber tracker for the DØ upgrade, we are installing a tracking system cosmic ray test containing approximately 3000 channels of scintillating fibers read out with Visible Light Photon Counters. Details of this test, along with the status of several important R&D issues associated with the fiber tracker, were presented in the previous report to the PAC.[6] At this time we update the progress of several key elements of the cosmic ray test.

Fourteen doublet ribbons of 2 m scintillating fibers have been fabricated at FNAL and are being mounted on the carbon-fiber support cylinder. Each doublet contains 256 fibers for a total channel count of 3072. Each end of each ribbon is terminated with two 128-hole connectors made of Delrin plastic, all of which have been optically polished with a diamond polishing machine. Tests of the light transmission through mating connectors polished with this machine gave excellent results, with mean transmission of 95%. The 24 bundles of 8 m clear fibers which pipe the light from the scintillating fibers to the VLPC's are also complete and are terminated with the appropriate connectors, as are the 24 bundles of shorter clear fibers which couple the scintillating fibers to the LED-based calibration system.

The scintillating fiber ribbons are currently being mounted on their support cylinder at FEPCO, a company near Indianapolis. The mounting process takes place inside a large CMM machine which enables constant monitoring of the procedure. This machine also provides a complete set of calibration constants describing the locations of the ribbons. The entire procedure is expected to take less than two weeks and the cylinder should be ready for installation in the cosmic ray test before the end of October.

A great deal of progress has been made towards the implementation of VLPC's in the cosmic ray test. A total of 5000 channels have been delivered to FNAL from Rockwell International. We obtain the VLPC's in the form of bare die, with each chip containing eight 1 mm diameter pixels. Each chip is soldered and wire bonded onto its substrate. The substrate and chip assembly are aligned precisely and glued into a Torlon plastic holder, which gives an accurate registration of each pixel to its clear fiber waveguide. Finally, each pixel is characterized by measuring its response as a function of operating temperature and bias. This entire procedure is now operational. At the time of writing, a total of 400 channels have been studied and the device performance agrees with Rockwell data from a sampling of devices from this lot. Approximately 98% of the channels operate successfully.

A cryostat capable of holding up to 3,072 VLPC channels has been fabricated and was under test in LAB-6 at FNAL when a helium leak was discovered. To expedite the repair of the leak, the cryostat was removed from the cosmic ray setup. The problem has been solved and reinstallation of the cryostat is well underway. The overall liquid helium system, complete with 3000 gallon supply dewar and helium recovery system, is operational at LAB-6.

The rest of the cosmic ray test system is complete and operational, both hardware and software. Trigger, data acquisition and event reconstruction are being exercised with the use of several planes of Iarocci detectors. The fiber tracker will be commissioned in stages once enough VLPCs have been tested and characterized.

7. Solenoid Issues

A key element of the integrated tracker is the addition of a thin 2T superconducting solenoid, which was encouraged by the PAC in its June 1993 meeting. The solenoid is fully described in a design report,[10] and while it poses no significant technical challenge, it does require that the procurement process begin now, in order to meet an early FY97 schedule for the first phase of the integrated tracking upgrade. A review took place at FNAL in August 1993 which considered the conceptual design for technical quality, suitability to the upgraded detector, and adequacy as a basis for procurement from an outside vendor. After responding to the review committee's report, a procurement specification document is in preparation, which will also be reviewed by the review panel before release of the request for quotation.

In summary, the review panel found the mechanical design of the coil to be sound, the cryostat design to be well thought out, and the decision to use existing cryogenic machinery for the refrigeration system to be appropriate. Overall the panel judged that the design choices selected in the conceptual design are conservative. The performance goals for the magnet place it well within the state-of-the-art.

As a result of the review, and in response to the panel's recommendations, we have made some modifications to the design report as follows:

- The interlayer electrical insulation was increased, without seriously compromising the thermal integrity of the magnet.
- The overall radial thickness of the magnet cryostat was judged unduly thin, carrying with it the risk of thermal shorts between the various elements inside the vacuum vessel. Therefore we have established mechanical tolerances for all the pertinent elements which increase the package thickness by 1.7 cm. As part of this effort, we have also decreased the overall radial size of the magnet in order to increase the preshower detector space tolerance and to allow adequate clearance to install the magnet inside the CC warm bore. As a result of these changes, the radii of the outer fiber barrels have been reduced slightly.
- We have prepared a three dimensional drawing of the mechanical detail of the outlet where the service chimney connects to the vessel, in order to check for any possible mechanical or thermal interference.
- We have added an additional valve to our separate piping runs for the radiation shield and support link cooling.
- Calculational detail on the quenching behavior of the magnet and the routing of instrumentation leads out of the cryostat has been added.

The addition of a magnetic field in DØ could potentially affect the various existing detector elements. We have compiled a list of all elements of the detector that potentially are affected by the fringe field of the solenoid and the rapid field decay expected when the magnet discharges or quenches. The fringe field also makes an impact on the Main Ring (particularly at injection). Working with members of the accelerator department we have designed a soft iron shield for the Main Ring that appears to adequately shield the proton beam from the solenoid.[11] With the anticipated tolerance on the positioning of the magnet, the effect on operation of the Tevatron is also expected to be benign.

In response to the panel's suggestion, we have developed a procurement strategy that minimizes the constraints placed on the specific design, as we judge that industrial experience by now is relatively mature for magnets of this type.

8. Alternate Tracker Possibilities

Great progress has been made this past few years with the scintillating fiber technique, especially regarding the light-yield characteristics of the fibers themselves, and we are now confident that we can build the tracker described in this report and that it will perform as reliably and as well as the simulation results indicate. The cosmic ray test described earlier is very close to providing the required proof-of-principle; however, there does not yet exist a fully operational tracker using the VLPC readout technique and several thousand fiber channels.

Under these conditions, it is prudent to consider alternate tracker techniques and indeed we have invested some effort into investigating and evaluating the alternatives. Possibilities that we have considered include:

- extending the silicon detector beyond its current maximum radius to $r \sim 20$ cm by the addition of two more double-sided barrels,
- building a small-cell cylindrical drift chamber between $r \sim 15$ cm and $r \sim 50$ cm,[12]
- filling the region between $r \sim 15$ cm and $r \sim 50$ cm with either interpolating pad chambers,[13] or gas microstrip detectors,[7][14]
- filling the region between $r \sim 15$ cm and $r \sim 50$ cm with $\sim$2.5 m long straw tubes.

This latter option is our alternate system of choice. It was described in detail in a DØ note[15] and in an earlier DØ upgrade report to the PAC[5] and we do not repeat the detailed description here.

We have successfully tested prototypes in a test-beam,[16] produced two detailed designs and performed simulation studies.[15] The performance characteristics are somewhat inferior to those of our proposed scintillating fiber tracker. In particular, the occupancy rate is higher and the two-track resolution is worse. Nevertheless, we remain confident that we could build such a tracker in a timely fashion, should we discover some unexpected and unforeseen scintillating fiber problem, and that it would represent a useful and valuable tracking complement to the silicon detector.

9. Cost and Schedule

The staging plan for the DØ$_\beta$ detector (which is to be running in early FY97) was developed to allow for the maximum flexibility and optimal use of resources. Since the FY97 detector is a proper subset of the full FY99 DØ$_\beta$ detector, there is a minimal amount of perturbation in making the transition to the full detector. This document describes a DØ$_\beta$ detector that has been designed to cost, matching the funding guidelines provided at the June 1993 Aspen PAC meeting. The costs presented in the following table are for: the M&S spending to date for FY92-93; the projected M&S spending for FY94-96 required to complete the DØ$_{\beta^-}$ detector; the projected M&S spending required to complete the full DØ$_\beta$ detector beyond the DØ$_{\beta^-}$ completion cost. We note that offline computing costs and the superconducting solenoid, which is to be constructed with AIP funds, are not included in the table.

Table 4 M&S costs for the DØ$_{\beta^-}$ detector (in M$).

Detector System	Spent FY92-93	DØ$_{\beta^-}$ FY94-96	DØ$_\beta$ Completion
Integrated Tracker	0.00	8.09	4.16
Calorimetry	0.58	3.25	0.00
Muon System	0.90	1.50	1.65
Trigger	0.31	0.76	2.18
Base Cost	1.79	13.60	7.99
Contingency (25%)	0.00	3.40	2.00
Total Cost	1.79	17.00	9.99

In constructing Table 4, we have taken into account our experience with DØ$_\alpha$ and the evolution in our understanding of the costs associated with upgrading other DØ$_\beta$ detector subsystems. These changes will be incorporated in more detail in the upcoming version of the Project Management Plan.

10. Conclusion

This report has summarized a rather complete review of the DØ Upgrade tracking design which has taken place since the consideration by the Physics Advisory Committee in June 1993. The design rests upon the rather detailed understanding of the capabilities of the existing DØ detector from operation in Run Ia and through the large range of physics analyses reported in conferences and in the process of publication. The detector enhancements or replacements needed to sustain operation at $\mathcal{L}= 10^{32}\mathrm{cm}^{-2}\mathrm{s}^{-1}$ and to extend the study of fundamental short distance studies of strong and electroweak interactions are by now quite well understood.

We agree with the conclusion of the PAC and the FNAL Director that the primary focus for DØ in the intermediate term future should be grounded in studies of high mass, high p_T physics – with extensions to other interesting topics (hard diffraction, gluon structure, b quark production and decays, *etc*) as permitted, without jeopardizing the high p_T physics or impacting financial or schedule constraints. This focus has guided our redesign throughout and we do not in fact see many areas of conflict.

A central feature of this redesign has been the inclusion of the solenoidal magnet at the start of the tracking upgrade. We are pleased with the technical progress in review and ratification of the magnet design, the preparation of a procurement document, and the successful conclusion of studies of the effect of the magnetic field on accelerator operation. It has been of great help to the DØ collaboration to be able to optimize the upgrade on the basis of an early appearance of the solenoid and we are grateful for the encouragement of the PAC in this regard.

Various elements of the upgrade discussed and approved earlier (re-optimization of the calorimeter signal shaping electronics, addition of more powerful hardware trigger logic for electron and jet recognition, coverage of the periphery of the detector with scintillators for cosmic ray protection, improvements to the readout speed in digitizers and data acquisition) have proceeded well. Many of these upgrades (cosmic ray shield, fast electron triggers, data-flow speed-up) have in fact been incorporated in time for Run Ib. The others are now into the full-scale system test or procurement stages.

Considerable progress has been made toward the large scale test operation of the scintillating fiber system, though at the time of writing this test was not operational. However, we are very much encouraged by the succesful test and operation of each individual portion of the fiber detector system (fibers, VLPC's, photodetector packaging, cryo-systems, connections and readout). Progress has also been made to assure ourselves that workable and affordable arrangements are available for the procurement of the critical elements of the system.

The DØ$_\beta$ tracking detector design and its first stage implementation presented here (DØ$_\beta$–) have been optimized to satisfy the sometimes conflicting demands of physics performance, cost and budget constraints, construction schedules and flexibility for subsequent improvement and expansion. The design to cost has led us to defer much of the forward tracking detectors, in part because of the focus on high p_T and in part because adding detectors for smaller angle tracking is more gracefully accomplished in a short shutdown than reconfiguring the large angle tracking detectors. Similarly, we have deferred deployment of more scintillating fiber readout channels than we might like, since these elements are far simpler to add at the last minute, or during a run, than the detector elements themselves. We have reluctantly deferred portions of the upgraded trigger and data acquisition systems, since we judge that the high p_T physics can survive at a few $\times 10^{31}\text{cm}^{-2}\text{s}^{-1}$ without tracking triggers, or more powerful event topological triggers. We do note that the lack of these upgrades will somewhat limit the data samples for studies involving J/ψ, Υ and b-tagging through leptonic decays, and that these samples are often crucial for understanding t and W/Z physics.

Nevertheless, the simulations reported here show that the DØ$_\beta$- detector operating in early FY97 will reliably improve our ability to study most important high p_T questions. These studies have been done with the full complexity expected in real-life, with programs which simulate our experience with the present detector quite well. They have included real magnetic fields, low energy particles, realistic detector effects, and the effects of dead channels and extra noise hits. We have shown a good capability for reconstruction and identification of both electrons and muons in the most complex events expected ($t\bar{t}$). Thus, we are confident that although we have somewhat limited the physics scope in the DØ$_\beta$- detector, this first stage detector will work well.

We have also considered rather carefully the constraints imposed by the rather short interval expected between the first and final stages of the DØ upgrade. Installation of those additions needed to complete the upgrade are understood well enough to assure us that a one year interval between the end of the DØ$_\beta$- detector run and the full upgrade is sufficient.

We are pleased with the successful completion of most R&D on detector, electronics and magnet systems and the conclusion of the detector re-optimization. The upgraded DØ detector will permit substantial and incisive advances on many physics fronts in the late 1990's. The DØ Collaboration has continued to grow and now includes 425 physicists from 40 institutions, with the recent additions committed primarily to the upgrade. We reiterate our request to the PAC for approval of the remaining portions of the upgrade proposal and look forward to a continued vigorous physics program throughout this decade.

REFERENCES

1. The DØ Detector, S. Abachi et al., to be published in NIM (1993).
2. The DØ Upgrade, unpublished (1990).
3. P823 (DØ Upgrade): Responses to the Physics Advisory Committee, DØ note 1148 (1991).
4. E823 (DØ Upgrade): R&D and Optimization Progress Report, DØ note 1322 (1992).
5. E823 (DØ Upgrade): Step-1 and Beyond, DØ note 1421 (1992).
6. E823 (DØ Upgrade): $DØ_\beta$, DØ note 1733 (1993).
7. A Tracking System for the DØ Upgrade based on Gas Microstrip Chambers, G. Finocchiaro, B. Gobbi, S. Lami and M. Martin, DØ note 1612 (1993)
8. Scintillating Fiber Readout and Triggering Considerations for the DØ Upgrade, S. Glenn, R.L. Lander, S. Mani and D.E. Pellett, DØ note 1907 (1993).
9. The fast simulation is based on the program TRACKERR, developed by W. Innes. It uses the method of Billoir (P. Billoir, NIM 225 (1984) 352) to calculate the track-fit error matrix assuming an optimal fit.
10. Design Report of the 2T Superconducting Solenoid for the DØ Upgrade, J. Brzezniak et al. (1993).
11. R. Yamada, G. Goderre, F. Ostiguy and A. Mesin, DØ note 1888 (1993) and J. Marriner (to S. Holmes) FNAL Internal Memo (1993).
12. H. Schellman, DØ internal memo (1991).
13. H. Fenker, private communication (1993).
14. J. Moromisato, submitted to Nucl. Instr. and Meths. (1993).
15. M. R. Krishnaswamy, DØ note 1419 (1992).
16. Test of Microstrip Gas Chambers, S. Lami, DØ note 1762 (1993).

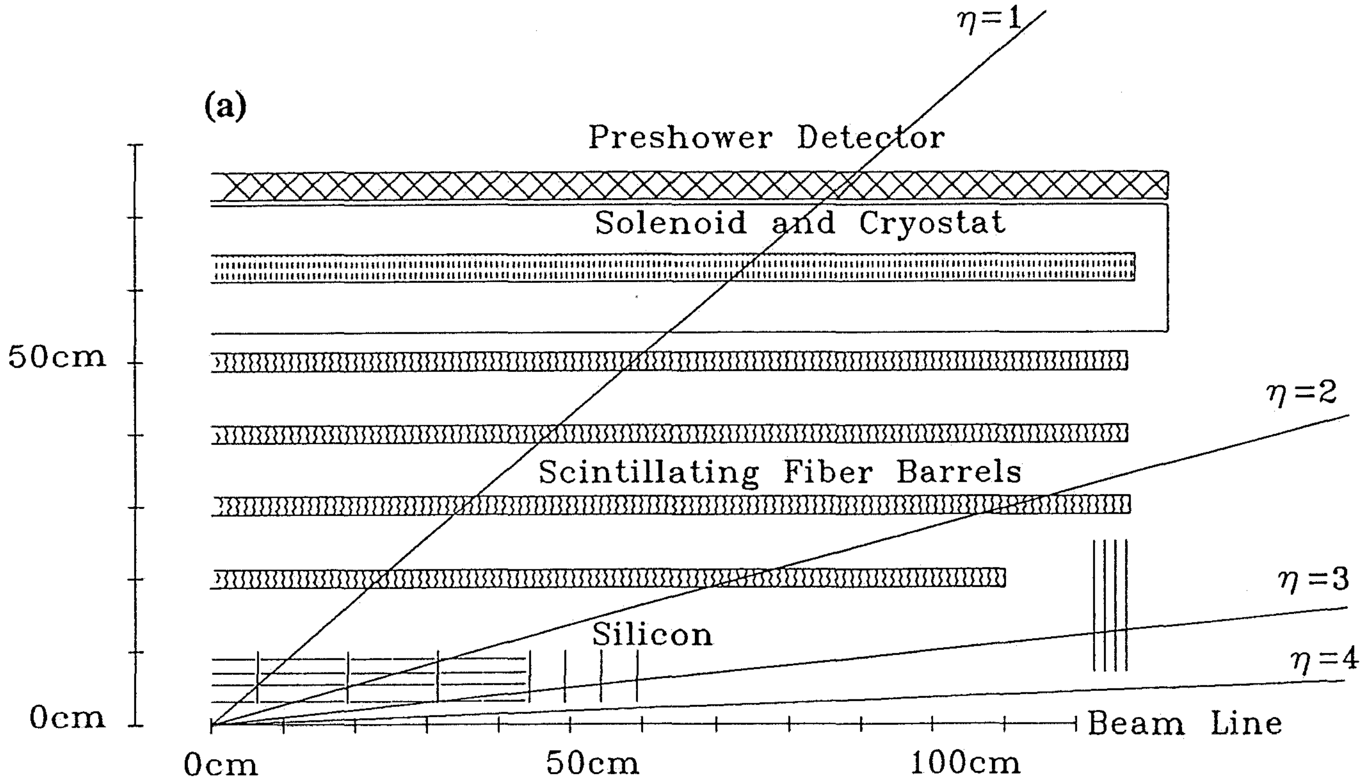

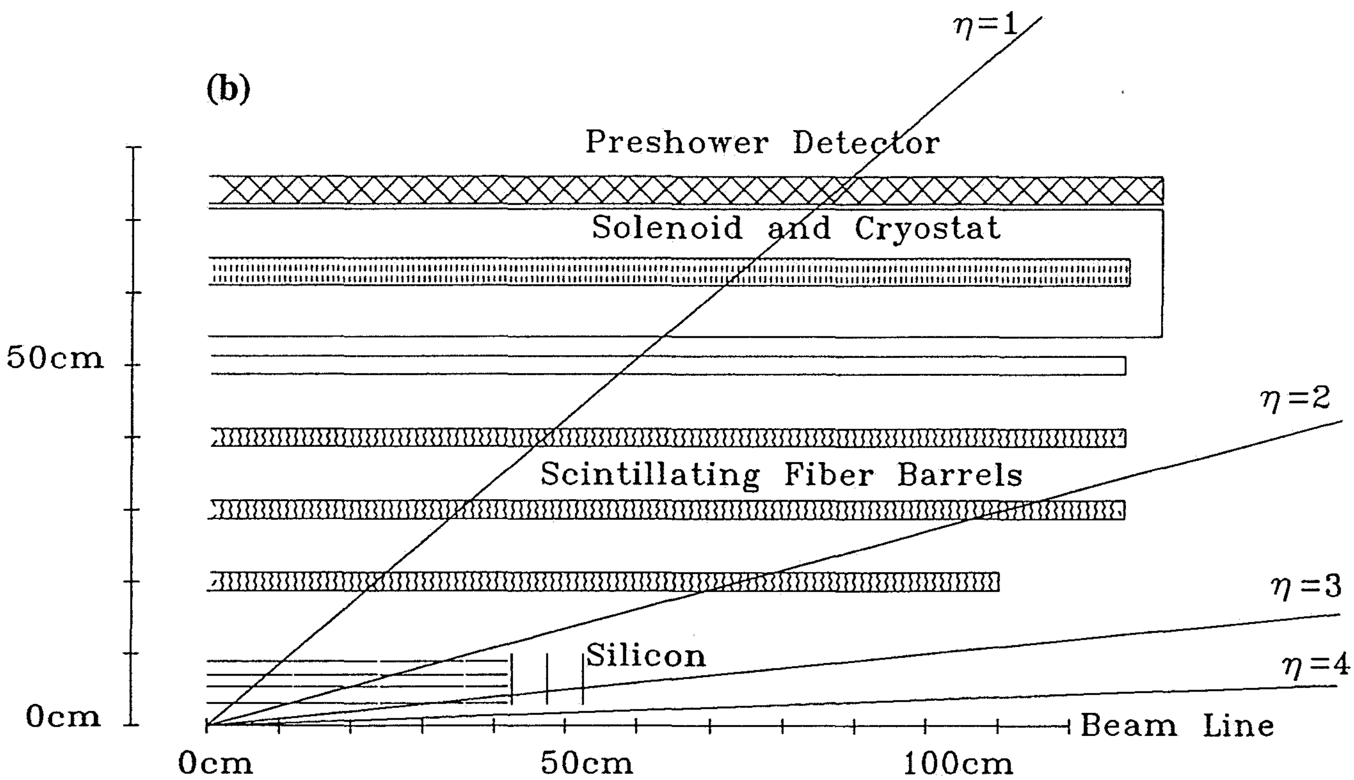

Fig. 1. Layout of the DØ tracking upgrade showing superconducting solenoid, scintillating fiber superlayers, silicon barrels and disks and the preshower detector (see text for details): a) D$Ø_\beta$; b) D$Ø_{\beta}$- .

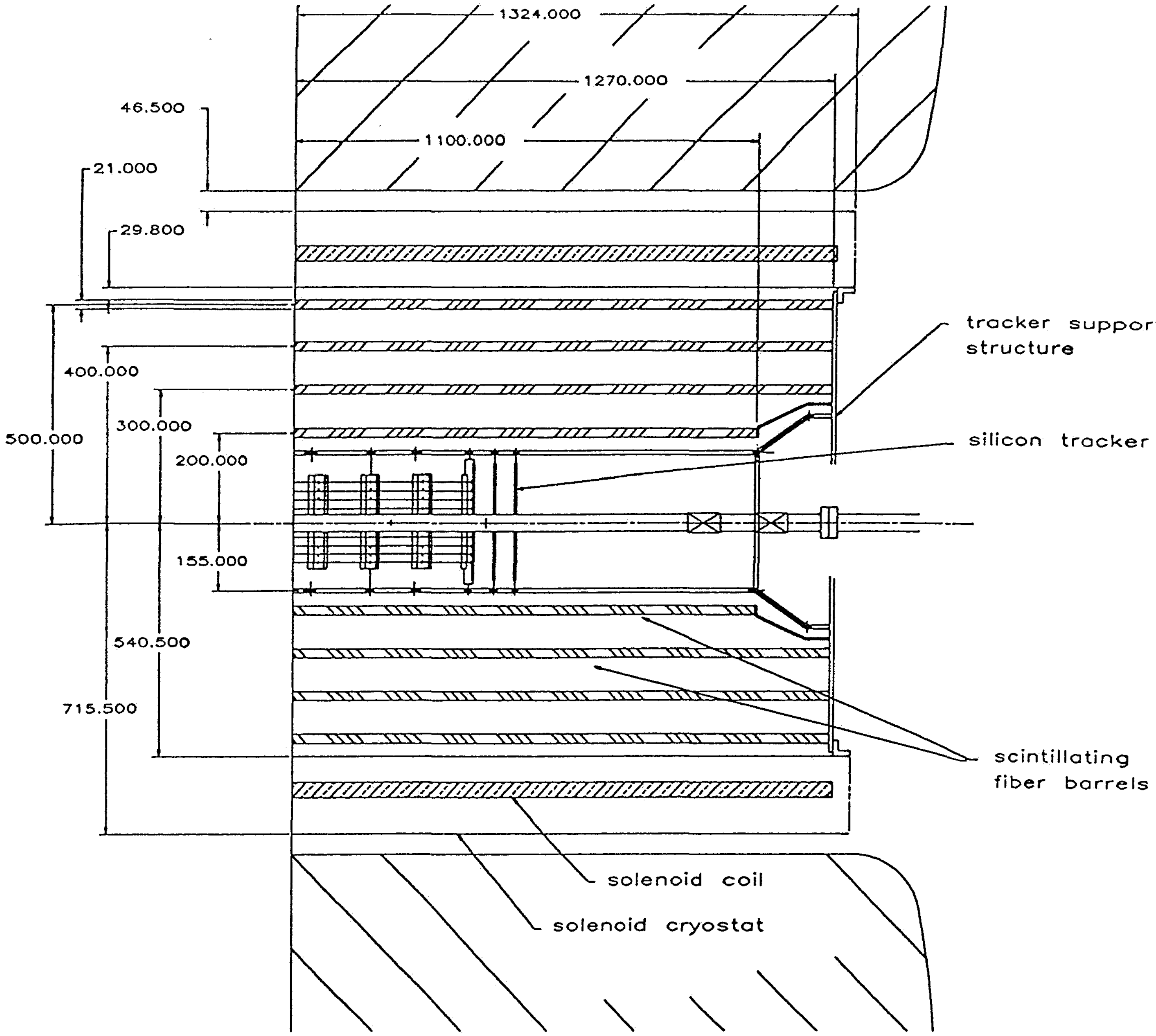

Fig. 2. Tracker cross-section indicating mechanical support structures. All dimensions are in mm.

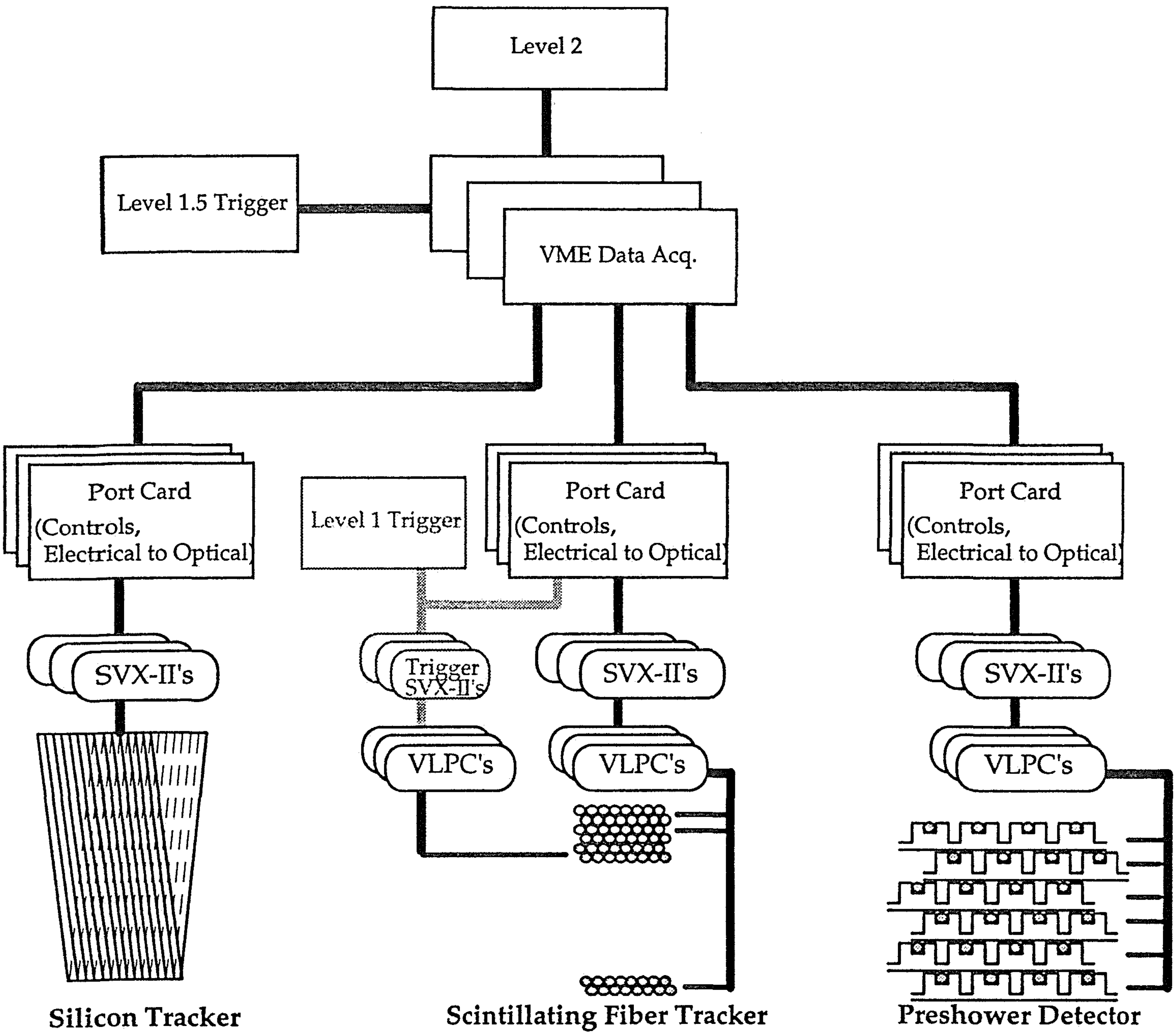

Fig. 3. Block diagram of the tracker readout electronics.

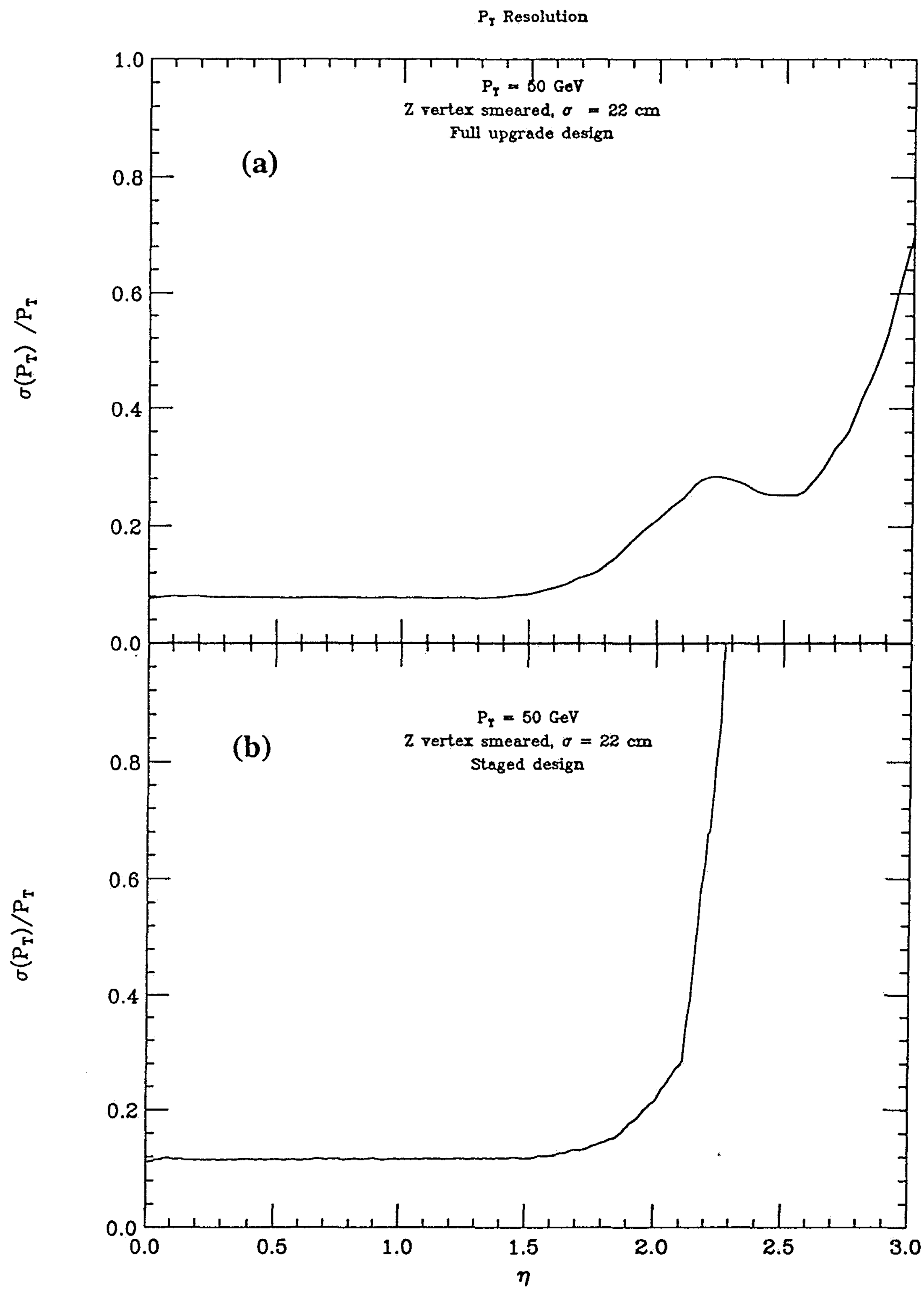

Fig. 4. Transverse momentum resolution versus η for a p_T=50 GeV track: a) D$\O_\beta$; b) D$\O_{\beta^-}$.

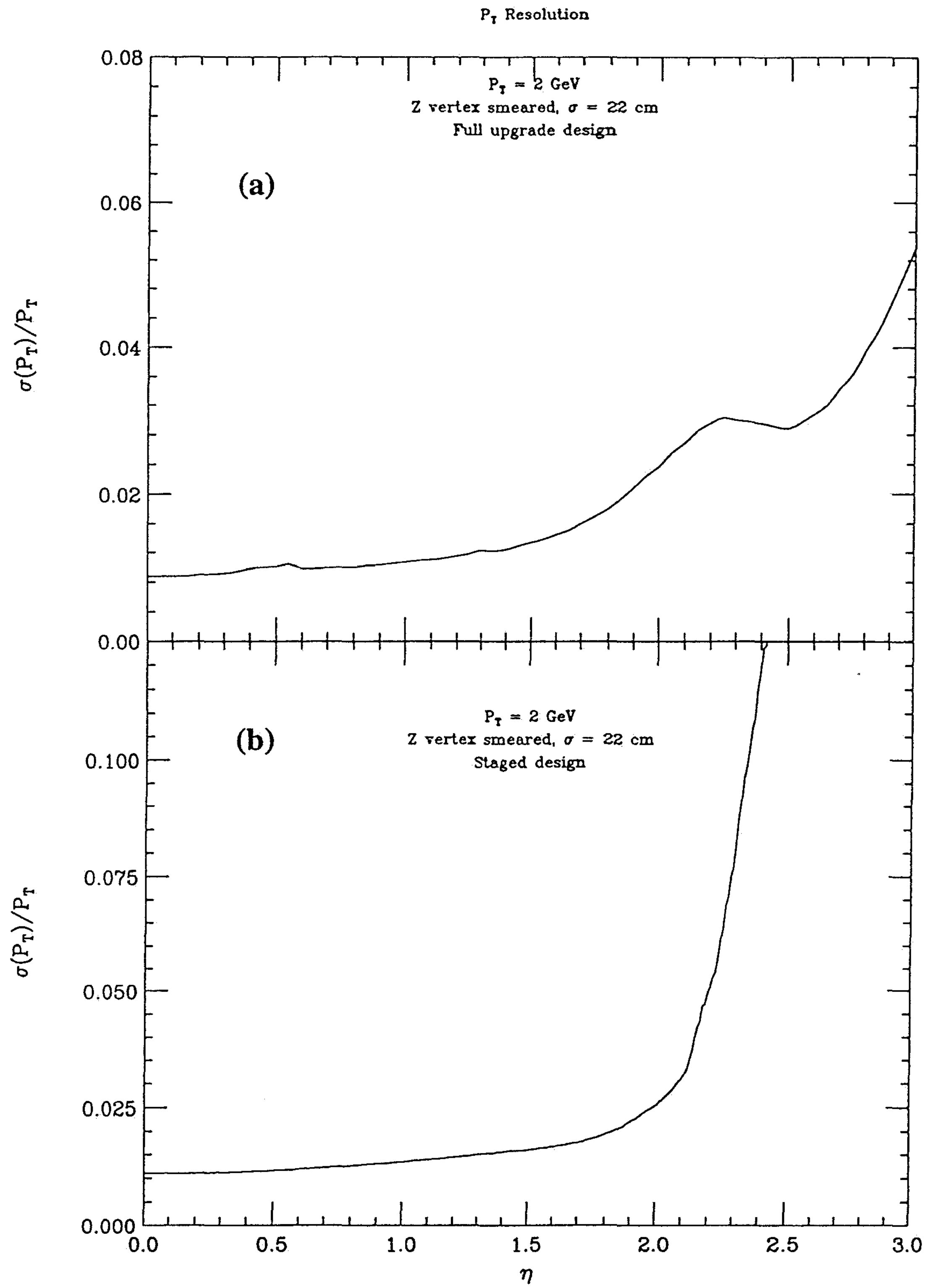

Fig. 5. Transverse momentum resolution versus η for a p_T=2 GeV track: a) D$\emptyset_\beta$; b) D$\emptyset_{\beta-}$.

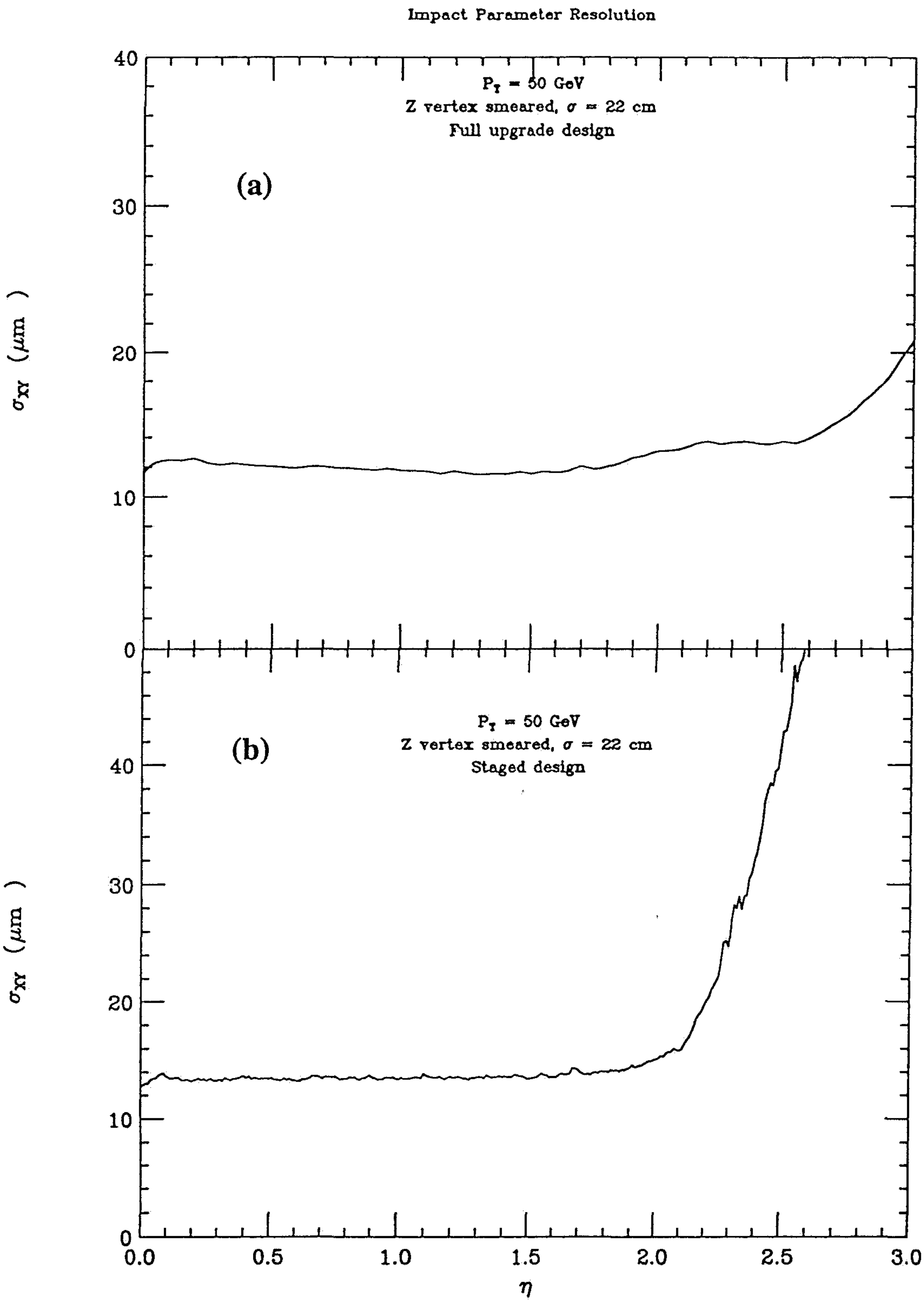

Fig. 6. Transverse impact parameter resolution versus pseudorapidity, η, for a p_T=50 GeV track: a) D$\emptyset_\beta$; b) D$\emptyset_{\beta^-}$.

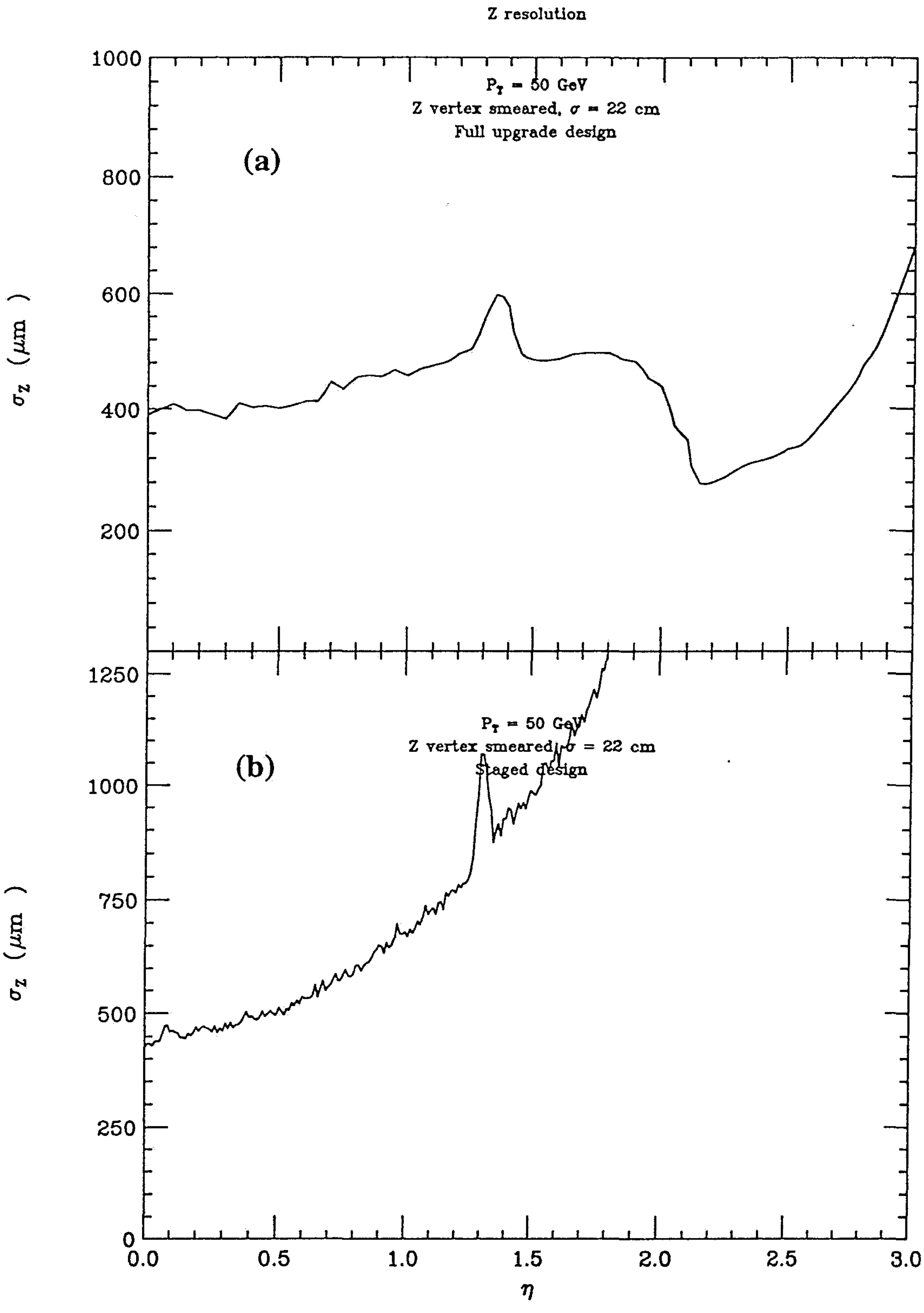

Fig. 7. Beam axis impact parameter resolution versus pseudorapidity, η, for a p_T=50 GeV track: a) $D\O_\beta$; b) $D\O_{\beta\text{-}}$.

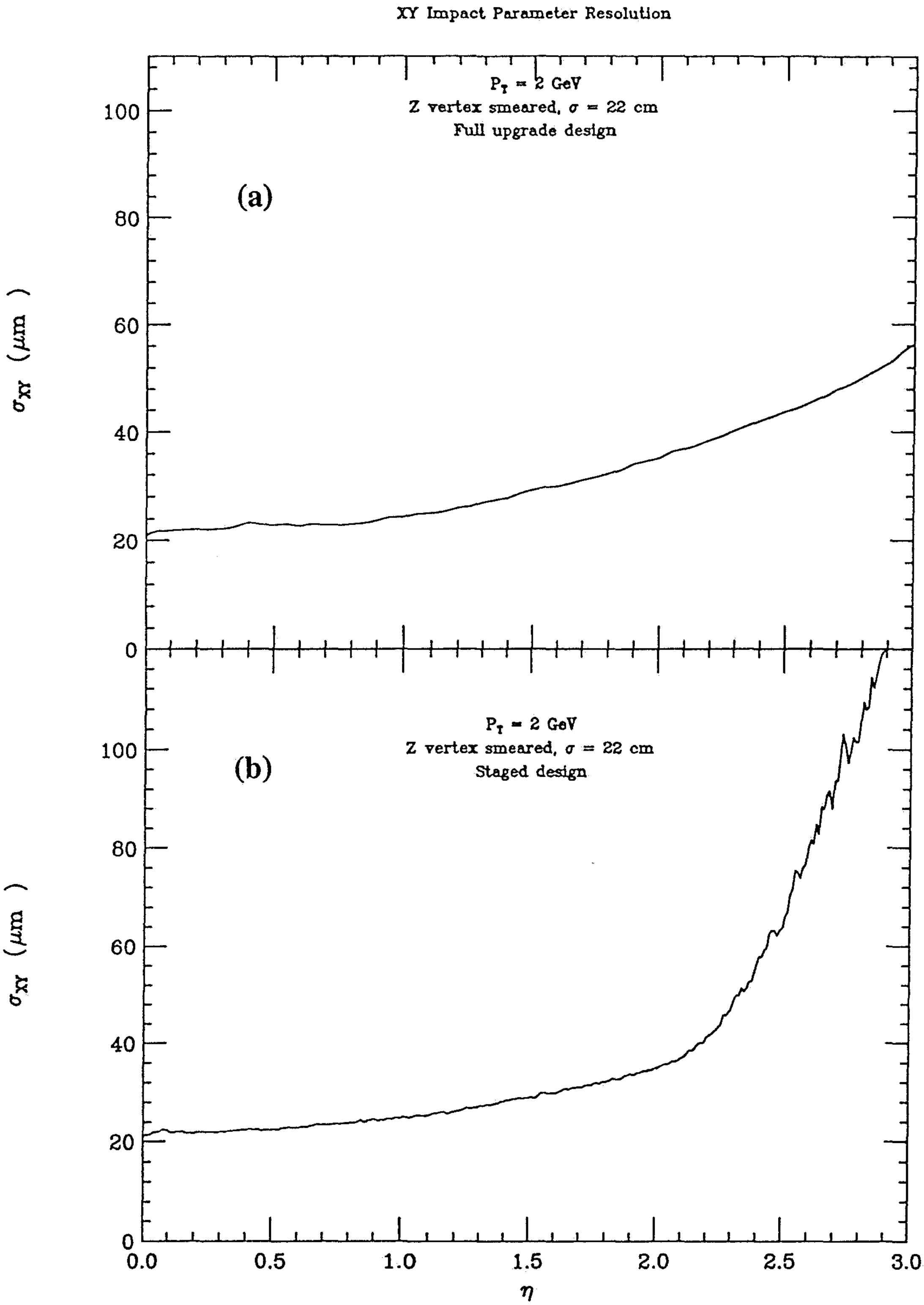

Fig. 8. Transverse impact parameter resolution versus pseudorapidity, η, for a p_T=2 GeV track: a) D$\emptyset_\beta$; b) D$\emptyset_{\beta^-}$.

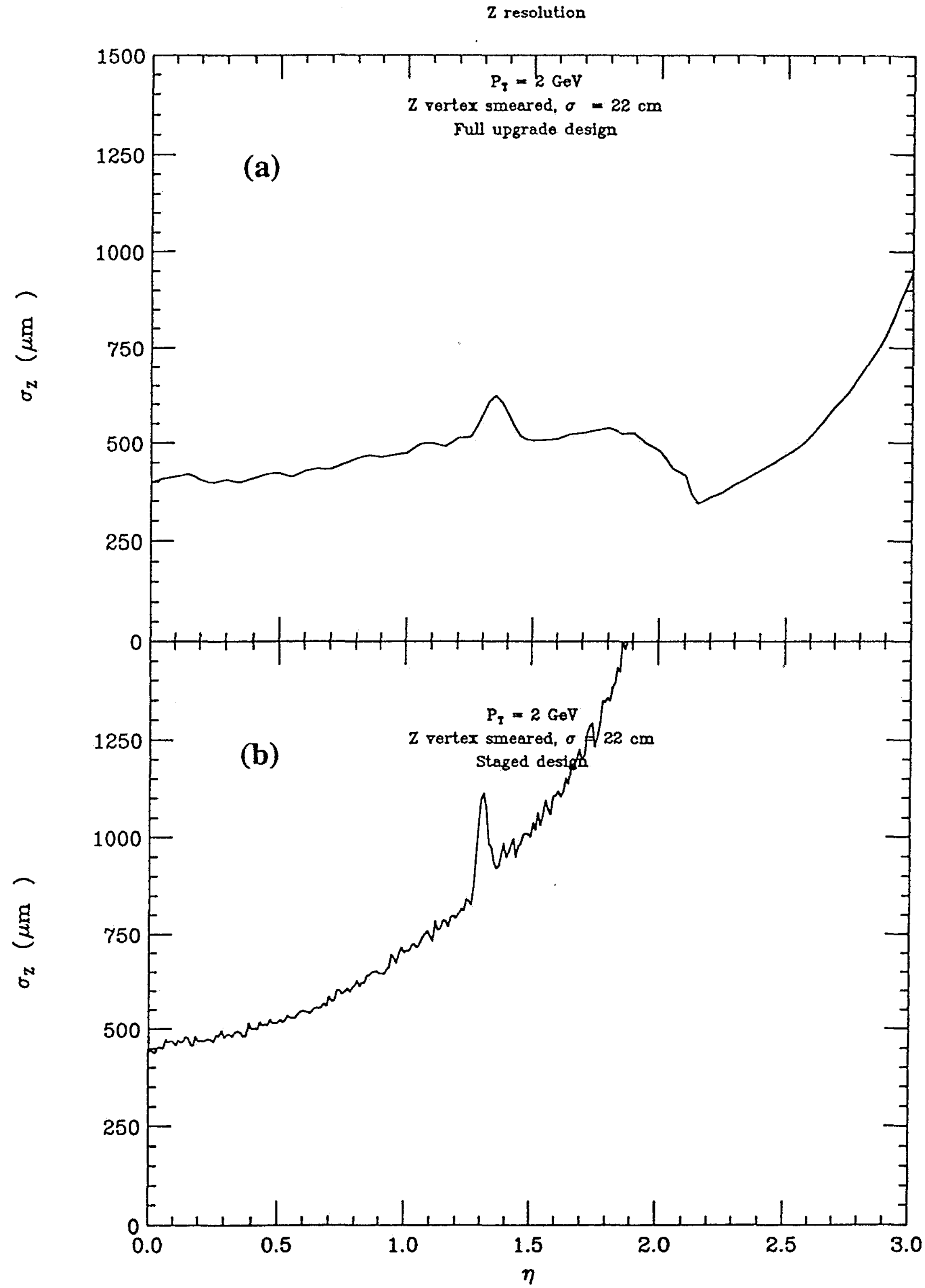

Fig. 9. Beam axis impact parameter resolution versus pseudorapidity, η, for a p_T=2 GeV track: a) $D\O_\beta$; b) $D\O_{\beta-}$.

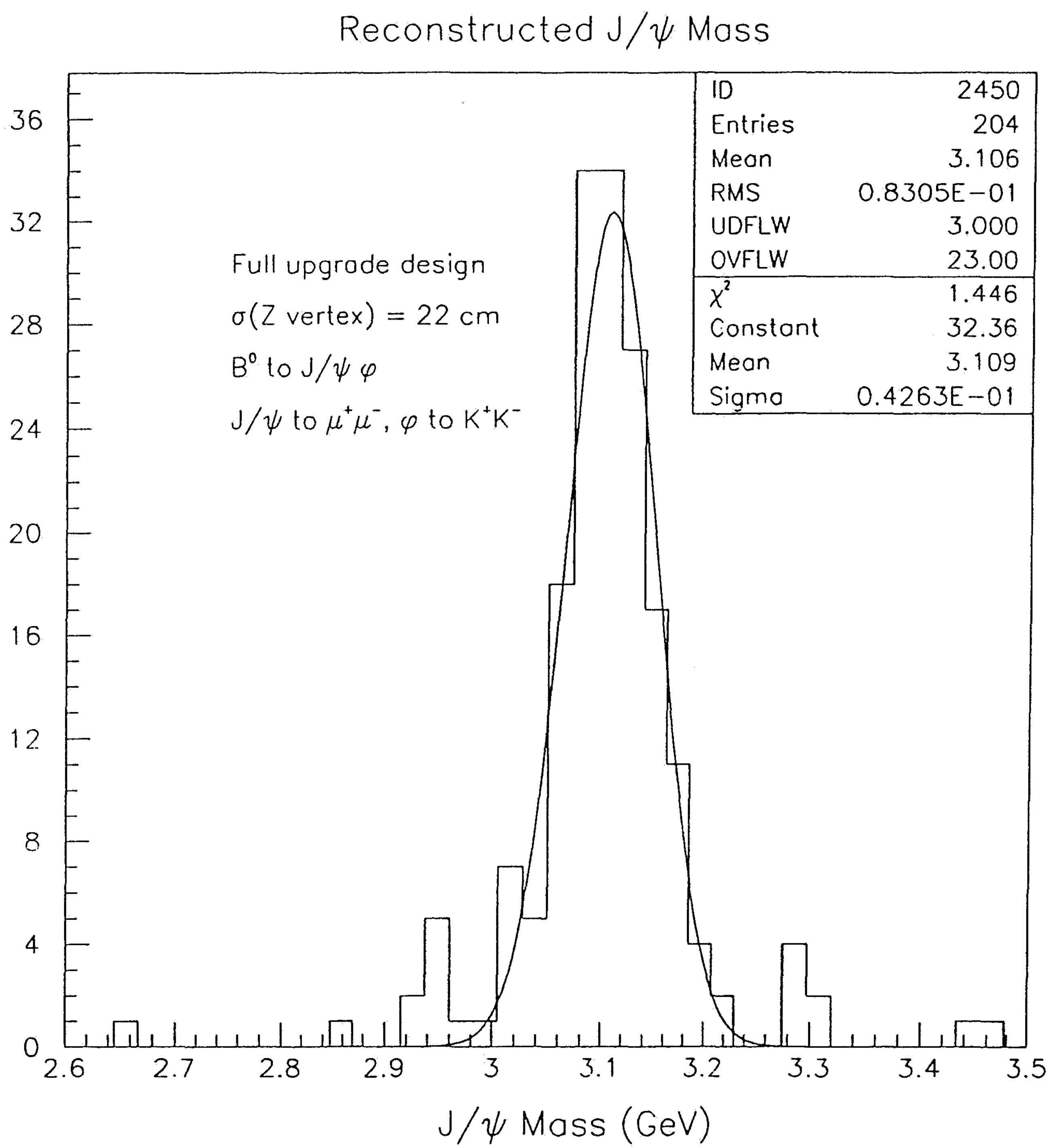

Fig. 10. Di-muon mass distribution in the J/ψ mass region.

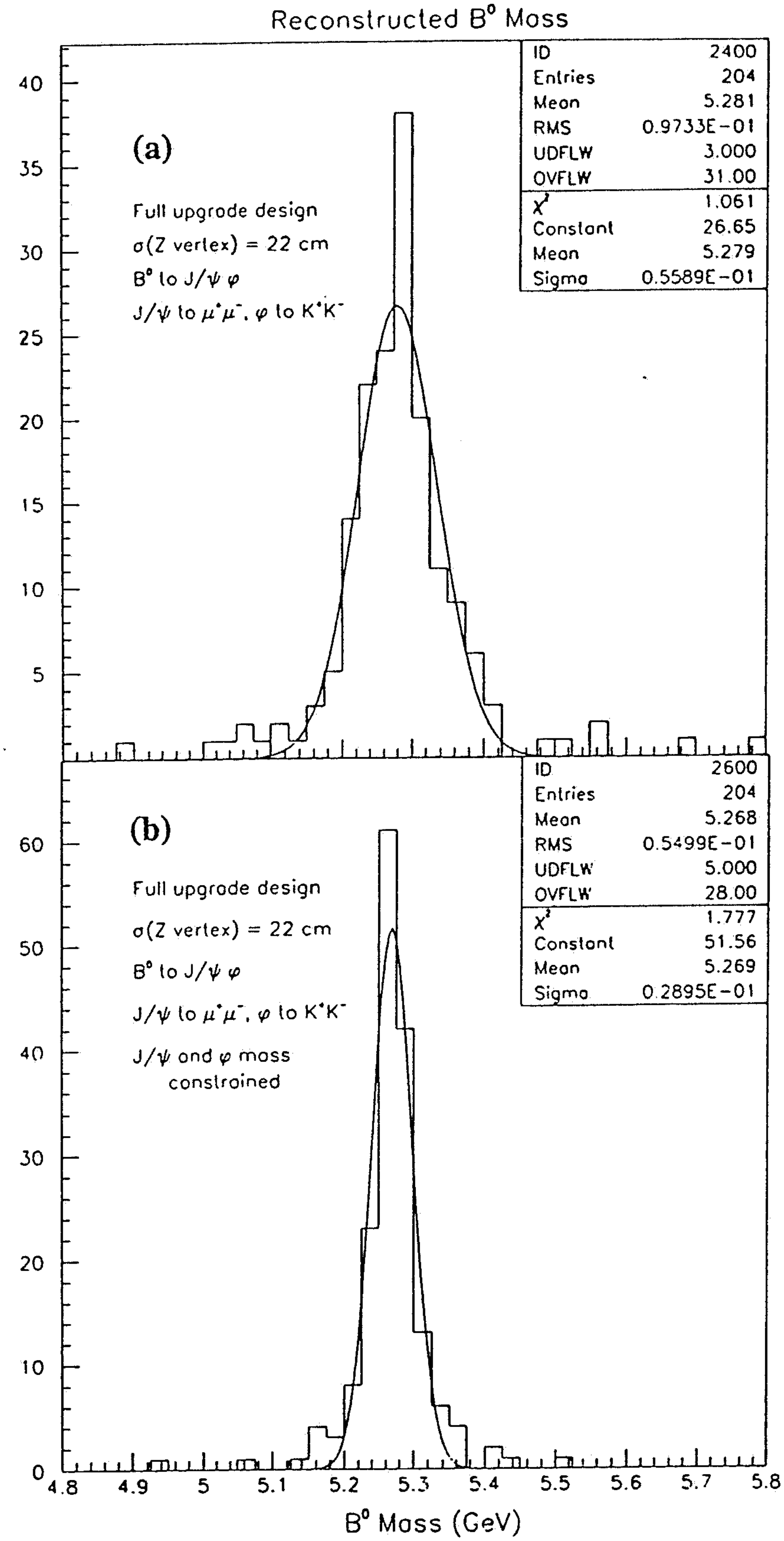

Fig. 11. $\mu^+\mu^-K^+K^-$ effective mass distribution in the B_S mass region: a) No J/ψ or ϕ mass constraints; b) Both J/ψ and ϕ mass constraints applied.